UNIVERSITY OF BIRMINGHAM

INVESTIGATING THE MECHANICAL PROPERTIES OF PERFUME MICROCAPSULES AND THEIR PERFORMANCE IN LAUNDRY APPLICATIONS

by

Andrew Trevor Gray

A thesis submitted to the University of Birmingham for the degree of

Doctor of Engineering

School of Chemical Engineering
College of Physical and Engineering Sciences
University of Birmingham
September 2019

Abstract

Perfume microcapsules (PMCs) are commercially used as perfume delivery agents in laundry products, and greater insights into the properties of the PMCs that influence performance, and development of new techniques to predict and monitor performance are sought as tools to give more guidance to the design process.

This thesis characterises Polyacrylate (PAC) PMC samples, to understand how physicochemical and structural characteristics relate to mechanical properties. The work then proceeds to outline a new validated methodology to complete a mass balance of PMCs in a washing machine, enabling quantification of PMCs, intact or broken, at any time or place during the wash. Performance of PMCs showed strong correlation to the PMC volume weighted rupture stress, providing a new quick screening method in PMC design. A new tribological methodology for analysing PMC rupture under friction is introduced, showing that friction as a force causing PMC rupture is impactful alongside compression, and requires further study, given the prevalence of friction as a force for PMCs embedded within fabrics.

It is believed that the collection of findings and techniques can be used as valuable tools to guide not only current PAC PMC design, but also future architectures, given the transferrable nature of the work.

Acknowledgements

I would first like to express my wholehearted gratitude to my primary supervisor, Professor Zhibing Zhang, for his excellent supervision over the course of the project. From getting me settled into doctoral research at Birmingham to his unwavering support once I had moved to work on the project in industry, I owe a lot of my development to him. I would also like to thank my secondary supervisor Professor Serafim Bakalis for his guidance during the project. I would also like to express my gratitude to Dr Richard Greenwood for his continued support throughout the EngD programme.

From my industrials sponsor, P&G, I would like to acknowledge the efforts of Stefan Egan in helping to get the project underway and for being my initial industrial support. I would like to thank Nathalia Guillard and Dr Pierre Verstraete for their supervision during my time based in P&G, especially for their efforts in trying to navigate the intertwined nature of academic and industrial components of the project. Also, from P&G I would like to thank Olivier Fasbender, Dr Carlos Amador, and Dr Johan Smets for valuable discussions over the course of the project.

From back in Birmingham I would like to thank Paul Stanley and Theresa Morris from the School of Electron Microscopy in Birmingham for their assistance in studies with the Transmission Electron Microscope

To John, Lynn, and all of the administrative staff at Birmingham, I am extremely grateful for your assistance in smoothing over all of the complications that arise in an EngD. In a similar vein I must thank Kathleen Hynes for all that she did for myself and all of the other EngD students during the programme.

To my close friends in the micromanipulation group; Javier, Mariana, Bingyu, Toni-Bianca and Teddy, I owe an enormous amount of gratitude for not only supporting me through the years, but also for contributing to a vibrant research environment within which many excellent ideas were conceived.

Finally, I must acknowledge the support of my family. To all of my grandparents, who, over the years have always been rooting for me. To my sister, secretly the best scientist in the family, who always keeps me on my toes. From an early age I have always been supported in everything I do, and I reserve the final acknowledgement for my parents, whose unrelenting efforts have been key to helping me reach for my aspirations. I hope you will always share happiness in any achievements I may have, as they are as much yours as they are mine.

Contents

List of Figures

List of Tables

List of equations

Nomenclature

a	Acceleration due to gravity	$m.s^{-2}$
a_p	Radius of contact between probe and a substrate	m
A	Contact area radius	m
C_0	Initial concentration of analyte in the sample	$mol.m^{-3}$
C_{COM}	Compliance of force transducer	$m.N^{-1}$
C_{ext}	External concentration	$mol.m^{-3}$
C_f	Concentration of analyte on the fiber	$mol.m^{-3}$
C_g	Concentration of analyte in gaseous phase	$mol.m^{-3}$
C_h	Concentration of analyte in the headspace	$mol.m^{-3}$
C_{int}	Internal concentration	$mol.m^{-3}$
C_s	Concentration of analyte in sample phase	$mol.m^{-3}$
d	Displacement of a flat surface	m
D	Diffusion coefficient	$cm^2.s^{-1}$
D_{10}	10 % cumulative percentile of PMC size	m
d_{32}	Sauter mean drop diameter	m
D_{50}	Mass-median-diameter	m

D_{90}	90 % cumulative percentile of PMC size	m
D_m	Diameter of PMC before compression	m
E	Young's modulus	Pa
E^*	Combined Young's modulus of two surfaces	Pa
E_w	Young's modulus of microcapsule shell material	Pa
F_k	Dynamic friction force	N
F_{max}	Static friction force	N
F_n	Normal force	N
F_R	Rupture Force	N
h	Shell thickness	m
H	Partition coefficient between PMC core and solvent	
h_{TEM}	Shell thickness measured by TEM	m
K_{hs}	Partition coefficient between headspace and sample	
K_{fh}	Partition coefficient of the analyte between fiber and headspace	
k_s	Transducer sensitivity	$mN.V^{-1}$
L	Impeller diameter	m
$\overline{m}$	Mean gradient used to calculate transducer compliance	V

M	Mass	kg
M_w	Molecular weight of a polymer	Da
n	Number of moles	Mol
N	Force	N
p_o	Maximum contact pressure	Pa
P_{ow}	Partition coefficient between octanol and water	
$p(r)$	Distribution of contact pressure	Pa
r	Microcapsule radius	m
R	Radius of a sphere	m
T_a	Micromanipulation probe travelling time	s
T_R	Nominal wall tension	$N.m^{-1}$
u	Linear speed of impeller	$m.s^{-1}$
V	Voltage	V
V_h	Volume of headspace	m^3
V_f	Volume of SPME fiber	m^3
V_s	Volume of sample	m^3
We	Weber number	

Greek symbols

α	Significance level	
δ	Half of total compressive displacement	m
δ_h	Energy from hydrogen bonds between molecules	J
δ_p	Energy from dipolar intermolecular forces between molecules	J
ε_B	Fractional deformation at rupture	
ε_{LE}	Elastic limit of the microcapsule	
Θ	Volume fraction of dispersed phase	
ν	Poisson ratio	
v_s	Probe compression speed	$m.s^{-1}$
ρ	Density of dispersed phase	$kg.m^3$
σ	Interfacial tension between dispersed and continuous phase	$N.m^{-1}$
σ_R	Nominal rupture stress	Pa
σ_v	Volume weighted rupture stress	Pa
φ_i	Volume fraction of PMC sample at specified diameter	

Abbreviations

AFM	Atomic force microscopy
APA	Alginate-poly-l-lysine-alginate
ATR-FTIR spectroscopy	Attenuated total reflectance Fourier transform infrared spectroscopy
Beta-C	Beta-carboxyethyl acrylate
CCD	Charge coupled device
CI	Confidence Interval
CMC	Critical micelle concentration
CRT	Cathode Ray Tube
DI	Deionized
DLS	Dynamic Light Scattering
DSC	Differential Scanning Calorimetry
DVB	Divinylbenzene
DVS	Dynamic Vapour Sorption
EDS	Energy-Dispersive X-ray Spectroscopy
ESEM	Environmental Scanning Electron Microscopy
FDCC	Forced Deposition Calibration Curve
FEA	Finite Element Analysis

FEM	Finite Element Modelling
FIB	Focused Ion Beam
FMCG	Fast-Moving Consumer Goods
GC-MS	Gas Chromatography – Mass Spectrometry
HDG	High density granule
HDL	High density liquid
HSP	Hansen solubility parameter
I.D	Inner diameter
ICC	Instrument calibration curve
IFF	International Flavours and Fragrances
INCI	International Nomenclature Cosmetic Ingredient
IPM	Isopropyl Myristate
LFE	Liquid Fabric Enhancer
MF	Melamine formaldehyde
MSD	Mass selective detector
MTM	Mini traction machine
O.D	Outer Diameter
P&G	Procter and Gamble

PAC	Polyacrylate
PALS	Positron Emission Annihilation Lifetime Spectroscopy
PDMS	Polydimethylsiloxane
PLL	Poly-l-lysine
PM546	Pyrromethene 546
PMC	Perfume microcapsule
PMMA	Poly(methyl methacrylate)
PMT	Photomultiplier tube
PPM	Parts per million
PRM	Perfume raw material
PSD	Particle size distribution
PTFE	Polytetrafluoroethylene
RH	Relative humidity
RPM	Revolutions per minute
SAXS	Small Angle X-ray Scattering
SD	Standard deviation
SEM	Scanning Electron Microscopy

SPME	Solid phase microextraction
SRR	Slide to roll ratio
TBAEMA	2-(tert-Butylamino)ethyl methacrylate
TEM	Transmission Electron Microscopy
TGA	Thermogravimetric Analysis
Tof-SIMS	Time of Flight Secondary Ion Mass Spectrometry
UV	Ultraviolet
UV-Vis	Ultraviolet-visible
XPS	X-ray Photoelectron Spectroscopy

Chapter 1. INTRODUCTION

Material encapsulation is readily observed in the natural world in a variety of organisms such as yeast cells, pollen spores, and bacterial spores, which are known to be extremely effective in protecting the precious interior cargo from numerous external stresses such as temperature, extreme pH and the presence of water. Encapsulation acts to keep interior domains or material separate from the external environment either until release is desired, or through holding in a separate environment indefinitely. There has long been an interest in mimicking and commercialising this natural method of material separation in industry. In the 1950's Barrett Green of NCR (National Cash Register Company) successfully synthesised gelatin microcapsules based on the complex coacervation studies of Bungenberg de Jong (National Cash Register Company, 1956). He created a gelatin rich coacervate phase dispersed within an aqueous supernatant. Once oil was added to the mixture the coacervate coated the oil droplets and then, with addition of glutaraldehyde, a crosslinking reaction of the coacervate gel strengthened the coating into a shell, creating a core-shell microcapsule. This breakthrough after a decade of work enabled Green to focus his research on commercialising the method to develop microcapsules for application in carbonless copy paper, where he encapsulated ink on the underside of a copy sheet, which was released through pressure of a pen to form a copy of whatever was being written on the upper sheet. By 1954 the first carbonless paper was released onto the market, and this is seen as the inception of microencapsulation in commercial products.

Since then, industry has been keen to make use of the benefits of encapsulation, whether in the food industry in the masking of tastes and odours (Mourtzinos et al., 2008) and improving stability of ingredients (Rocha et al., 2012, Paini et al., 2015), the pharmaceutical industry in

the controlled release of certain active ingredients in the body through changes in environment such as pH e.g. Salbuatamol (Pradnya et al., 2010) and Propanolol (Vishnu et al., 2011), and in the construction industry where encapsulating actives for road repair (Al-Mansoori et al., 2017) and phase change materials for insulation purposes has been researched (Cao et al., 2017).

The encapsulation of perfume has been a heavily researched application for microcapsules (Ashraf et al., 2015). Perfumes are a carefully selected mixture of compounds with varying volatilities, that aim that the composition draws a pleasant olfactory perception from the consumer. The complex combination of compounds provides a deep complexity to the fragrance that is cherished by the consumer, but this inherent complexity makes them difficult to incorporate into formulated products.

Perfumes are commodity ingredients, and often one of the most expensive components of many commercial formulation products, so maximising impact of perfume, whilst not substantially inflating cost, has long been sought.

The approach of encapsulating perfume has been realised commercially in shower and bath gels, shampoos, and washing up liquids, where the perfume is more stable when separated from the formulation. Through application of mechanical force, the perfume microcapsules (PMCs) rupture to release their fragrant core. Another area in which encapsulation is a commercial technology is in laundry detergent products. More so than in other commercial applications of fragrance encapsulation, in laundry detergents the use of microcapsules has many potential benefits. Impermeable microcapsules keep the fragrance separate from incompatible ingredients in the detergent formulation during production and storage. During the wash process, the microcapsule properties help the process by preventing dilution of perfume in large volumes of water. Microcapsules are retained within fabric fibres and become embedded within

the fabric post-wash. At this stage some free perfume has adhered to the fabric, giving an immediate post-wash bloom. The retention of microcapsules in the fabric means that mechanical interaction with the fabric through wearing and handling the garments causes these microcapsules to rupture, releasing the perfume, and prolonging the desired effect of a successful wash cycle.

Microcapsules are commonly used in fabric softeners (Liquid Fabric Enhancer, LFE). This product is added late in the wash cycle so there is a reduced chance of any loss of perfume through rupture. At this stage, the external environment is much milder on microcapsules, with reduced surfactant levels, and more ambient temperatures.

Not all consumers choose to use LFE in their wash habits, so the ability to incorporate PMCs into the detergent itself, which is added earlier in the wash cycle in a harsher environment, becomes an important alternative. The nature of the market drives the inclusion of microcapsules; fragrance is the key driver for 60 % of consumers in the five biggest markets in Europe, and the cost of including the encapsulation technology in products is offset not only by economic benefit, but also by improved performance (Nielsen, 2016).

There is a real commerical need to improve fragrance delivery to fabrics post-wash, and Procter and Gamble (P&G) identified PMCs as a suitable technology to achieve this. It is currently implemented in some of their product lines, and the design of these PMCs is a challenging task. Taking priority in the design of PMCs is the aim to deposit as many intact capsules as possible on the fabric. They need to be retained throughout the various wash cycles, and then after the wash when the clothing is handled they should rupture. This offers two distinct challenges; how to get the PMCs to deposit on fabric, and how to get them to remain intact until the appropriate moment.

In this project, the adherence of PMCs to fabrics was not the focus of the work. The aim was to study the mechanical response of the commercially developed PMCs delivered through washing detergent, develop techniques to better understand the fate of PMCs in the wash, and to reach insights on how to approach future PMC development. If the manufactured PMCs are too weak, they will rupture during the wash, meaning no post-wash benefit is achieved relative to dosing fragrance to the wash directly. If the PMCs are made too strong, they may embed on the fabric, but they would be unlikely to rupture, meaning no fragrance benefit for the consumer despite the encapsulation efforts. There is a sweet spot in terms of mechanical strength where the PMCs are too strong to break in the wash cycles, but too weak to remain unruptured when mechanical stress is applied post-wash.

Whilst the target is clear, the means of achieving it are certainly more shrouded in uncertainty. Current design of PMCs is largely done through trial and error, with little grasp on how to control mechanical, structural or physicochemical properties to achieve desirable real-world performance within suitable cost constraints.

1.1 Industrial relevance of the project

P&G has already included several generations of different architectures of microcapsules in their detergent products. As a technology it has been found to be sufficiently cost-effective to justify its use, and the benefits seen through their inclusion enable an improvement in consumer perception of the products. There is a wealth of patent literature assigned to P&G which signifies the commitment to the technology, and also the strong position the company is in to protect its technology (Procter & Gamble, 2006, Procter & Gamble, 2014a, Procter & Gamble, 2018).

The primary objective of the project for P&G is to gain a more thorough understanding over the fate and effectiveness of PMCs in the wash, and to be able to have a more predictive, streamlined approach in PMC design, moving away from the “trial and error” approach.

Once predictive measures have been identified, the possibility of tailoring the design of PMCs to suit the market that the detergent is used in becomes feasible. For example, in a market which uses a high agitation wash cycle it would be preferable to have a stronger PMC to survive the strong agitation. There would also be scope for including multiple PMC compositions in the formulation, allowing the PMCs to rupture under different stresses. This would give immediate post wash damp bloom and a more prolonged mechanically triggered dry bloom.

Succeeding in understanding these parameters would give P&G more information about how to reduce production costs without affecting performance, and would enhance product satisfaction in terms of fragrance delivery to increase. A secondary benefit would be that the methods developed to assess PMC performance based on mechanical, structural and physicochemical properties would potentially hold valuable intellectual property to further protect the knowledge base that P&G has over its competitors in encapsulation technology, giving them a competitive edge in the future.

1.2 Aims and objectives of the project

The aim of the project is to further understand and predict burst properties of PMCs to improve the effectiveness of the technology in laundry formulations. It is built from the ground up by looking at the effect of compression and friction on new PMC architectures, and characterising the PMC samples on a capsule by capsule basis, to understand which parameters might be

important in influencing burst properties. Methods will be created to understand how mechanical properties under different stresses can be compared to and applied to scaled up real world wash situations. It will investigate whether insights can be made from quick compression or friction tests that may remove the need to run full scale tests for every single PMC sample, to substantially streamline the PMC development and testing process. All PMC samples are provided by P&G and whilst some sample information is provided by the manufacturer, detailed synthesis parameters are omitted on the grounds of confidentiality.

The outline of the thesis is summarised as follows:

Chapter 2 A literature review of microcapsule shell architectures relevant for encapsulating perfume, and associated synthesis methods is presented. A published review of advanced microcapsule characterisation techniques by the author is revisited and updated to show which properties have been important to study when investigating physicochemical, structural and mechanical properties of PMCs specifically.

Chapter 3 The materials and methods that were used to characterise PMCs mechanically, structurally and physicochemically are presented alongside methods utilised to quantify PMCs from real world wash tests. This includes a succinct theoretical consideration of the techniques and a detailed description of how the methods were applied in the context of this project.

Chapter 4 A variety of PAC PMC samples are introduced and their size distribution, morphology, rupture stress, displacement at rupture, Young's modulus and shell thickness analysed to provide a robust picture of the different samples provided by P&G. The aim was to individually vary one property of the PMCs, meaning links are made between mechanical properties of PMCs and their respective properties. The impact of humidity on mechanical properties is investigated and a novel method of calculating the Young's modulus in core/shell PMCs is presented.

Chapter 5 This chapter presents a detailed story of the development of mass balance protocols for PMCs in the washing machine. This consists of several methods using markers to quantify PMCs in each output stream within the washing machine. Insights are gained into which parameters need to be controlled in real world wash tests to enable a full quantification of deposition and loss to washwater for intact and broken PMCs.

Chapter 6 Results from mass balance experiments are presented. This consists of comparing the different PAC PMCs samples from P&G and relating the results to previously acquired characterisation to create predictive markers for the levels of deposition and breakage observed in real wash situations for any future samples. The chapter will also apply the methods to investigate PMC deposition and breakage in different wash conditions specific to different markets.

Chapter 7 Novel methods for studying the effect of friction on PMC breakage are presented. This is related to bulk breakage under compression and friction to help understand the forces at play in a washing machine and the relative impact of different force types.

Chapter 8 The overall conclusions for the work are presented, and suggestions for future work are made.

Chapter 2. LITERATURE REVIEW

In this chapter the characteristics that make microcapsules so desirable in numerous applications are outlined. Synthesis methods and processing conditions are extremely important in determining final microcapsule properties and the method of delivery of the encapsulated active ingredient is investigated for certain applications. Specifically, interest in this project falls on encapsulation of perfumes in formulations for laundry applications and hence a background is provided into such products. Consideration is taken into why it is so important that perfume is encapsulated during the formulation, storage and laundry processes. Of specific interest in this project is the ability to complete a thorough characterisation to evaluate performance differences between microcapsule samples. Extra detail will also be applied to literature that uses experimentation and modelling to elicit intrinsic capsule properties such as the Young's modulus.

To truly understand the fundamentals behind microcapsule mechanical behaviour it is also necessary to investigate physicochemical and structural properties that are important for encapsulating perfume and the techniques in literature that enable this are outlined. Friction is seldom discussed in relation to mechanical characterisation of microcapsules, however with fabrics in a washing machine, friction becomes an important consideration, and as such, literature on friction measurements of fabric is presented in relation to this project. Finally, transitioning from characterisation on an individual microcapsule scale to full scale in a washing machine, performance analysis techniques in the literature are reviewed to highlight methods to benchmark microcapsule performance.

2.1 Microcapsules

2.1.1 Microcapsule structure and variations

Encapsulation of important internal structures and components as a means of protection to control interaction with an external environment occurs with staggering frequency in single cells in the natural world, including plant cells, yeast cells, red blood cells and. It is on the same principle that the field of artificial microencapsulation originated. A microcapsule has a core/shell structure on the order of 1 – 1000 μm where a core, in any physical state, is surrounded by a membrane or shell, of polymeric material for example. Within this shell is an active ingredient. Protection and delivery of this ingredient are the primary focus of the encapsulation process and when considering performance this dictates, along with the external environment, the compositional recipe for the microcapsules. Whilst a simple single shell, single core structure is most common for applications, it is also possible to create multi shell and multi core structures as well as dispersing the core material within an internal polymeric matrix (Bakry et al., 2016).

2.1.2 Historical development of microcapsules and industrial applications

2.1.2.1 Origins of commercial microencapsulation

Starting in the late 1930's Barrett Green, through studying coacervation processes of Bungenberg de Jong, successfully created gelatin microcapsules with a view of encapsulating ink for use in carbonless copy paper. Force applied when writing would rupture capsules in the lower sheet, exposing the ink to an acidic clay and leaving a print of the original text from the upper sheet (Bungenberg, 1939, National Cash Register Company, 1956). Nine years after originally embarking on the work, the commercial product was ready.

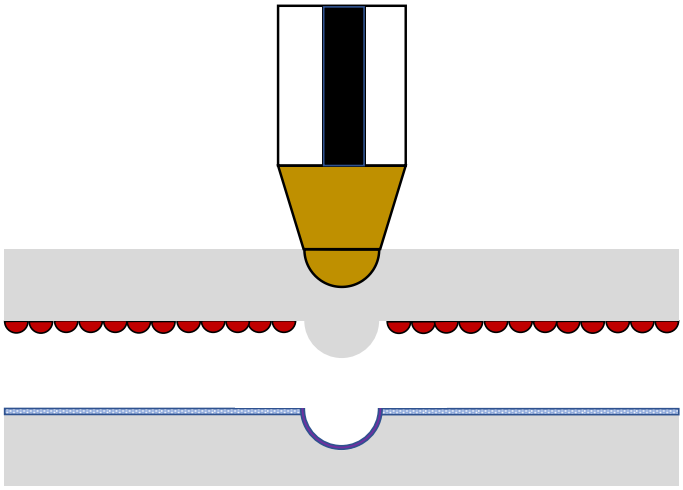

Figure 2.1: Schematic diagram on modern day carbonless copy paper. Microcapsules are filled with a colourless colour-producing substance, which is released through mechanical force of the pen. This material reacts with the substance on the surface of the second layer to produce a copy

This sparked considerable interest and speculation into other wild potential products such as gasoline bricks, dry Martini capsules, and water cooled cigarettes (Fanger, 1974), all with microcapsule technology at their core. Whilst these products seem farfetched now, the benefits of the technology were clear and the field expanded, and continues to expand to this day.

2.1.2.2 Applications of microcapsules

Research into microencapsulation largely falls into two distinct categories: formulation of novel microcapsules and characterisation of microcapsule properties. Ultimately what underpins advancement in the field is the drive to open up new routes of synthesis, refinement of existing routes, and the creation of novel microcapsule formulations for use in industry (Andrade et al., 2015).

An important industrial use of microencapsulation is in pharmaceutical products. There have been numerous works highlighting the benefits of microcapsules as drug delivery agents, e.g. salbutamol (Pradnya et al., 2010), captopril, verapamil (Mukherjee et al., 2005), and propranolol (Vishnu et al., 2011), which have all been encapsulated in polymer shells for clinical use.

In agriculture, microcapsules have been used extensively for protecting pesticides from microorganisms and sunlight, with over 150 microcapsule preparations registered in China as of 2016 (Zhang et al., 2016a, Jia et al., 2014, Li et al., 2016). Further examples of applications of microcapsules in pharmaceuticals and agriculture are outlined in the review on microcapsule industrial applications from the Rochefort Group at Université de Montréal (Zhang and Rochefort, 2012).

Cosmetic products contain biologically active ingredients that are sensitive to pH, temperature and light. Encapsulation can offer a means of protecting these valuable ingredients (Casanova and Santos, 2016). Cosmetic companies such a L'Oréal, Maybelline and Unilever have all filed patents incorporating microcapsules into their products (L'Oréal SA, 1998, Unilever Plc, 2009, Maybelline Intermediate Corp., 1998).

2.1.2.3 Microcapsule release mechanisms

Depending on characteristics such as the strength and porosity of the shell material and response to external stimuli, different release mechanisms of active core materials can be achieved, ultimately grouped into either sustained or instantaneous core release. The pharmaceutical industry often draws upon the ability to control a sustained release of active material by

permeation through the microcapsule shell, dependent on the diffusion coefficient of the active, and its solubility in the barrier (Andersson Trojer et al., 2013b). By utilising microcapsules it is possible to prolong the efficacy of the drug for the patient, relative to an instantaneous release, meaning less frequent administration and better medication compliance (Lee et al., 2014, Tang et al., 2007, Naha et al., 2008).

It has also been possible to synthesise hydrogel membrane microcapsules with reversibly tunable permeation, meaning permeability can be changed by altering pH due to a change in swelling of the membrane (Werner et al., 2018). Another novel release mechanism has taken inspiration from a human heartbeat by encapsulating core materials in composite microcapsules with Fe_3O_4 particles embedded in a polymer shell. Upon application of a magnetic field paramagnetic Fe_3O_4 microcapsules align with this field, causing microcapsule deformation to release core material as inner osmotic pressure rises. This method therefore bridges the gap between sustained release and instantaneous release without rupturing microcapsules by controlling the frequency of the compression-relaxation cycles of the microcapsule (Long et al., 2015).

If an instantaneous release mechanism is sought, the microcapsule must show rapid response to an external stimulus. This could be in the form of a change in temperature, as with the release of bioactive compounds in natural Witepsol microcapsules (Vöpel et al., 2015), or through the creation of photo-responsive perfume microcapsules for visible light-triggered release (Pirone et al., 2019). Particular relevance to perfume microcapsules is instantaneous release through mechanical rupture; by applying a mechanical stress to the microcapsule causing the shell to crack or yield. Pore size needs to be kept to a minimum, to prevent escape of the volatile perfume from the microcapsule, and a dense shell can significantly aid this.

2.1.2.4 Application of perfume microcapsules in laundry products

Delivering perfume to clothing in a washing machine from a detergent is a challenging prospect. The perfume is composed of a combination of volatile ingredients with a variety of molecular polarities. Traditionally, perfume has been added neat to laundry product formulations, meaning it is in-situ with other ingredients and added directly to the wash process without any protection. This exposes the compounds to multiple dilution mechanisms. Whilst energy concerns and laundry formulation design is trending towards lower temperature wash cycles, with 30°C being commonplace, higher temperature cycles and tumble drying fabrics cause evaporation of the volatile compounds in the perfume, starting with the top notes of the fragrance. This can have an undesirable effect on the nature of the fragrance and change the scent that has been carefully designed. Secondly, there is loss of perfume through multiple rinse cycles and draining of washwater liquor. If the perfume has failed to deposit onto the fabric, there is a greater chance that it will be lost to the drain. Unfortunately, this is not aided by the other ingredients in the wash.

Naturally, many compounds in fragrance are oily in nature. This makes them similar to the type of compounds that are desirable to remove from the clothes. This uses the action of surfactants which, being amphiphilic in nature, effectively drag soil compounds from clothes into the aqueous washwater liquor and ultimately down the drain, leaving the garments clean. This highlights why fragrance is typically delivered through fabric conditioners and not detergents. When fabric conditioners are added to the wash, multiple rinse cycles have removed large quantities of the surfactant from the machine, leaving the fragrance less susceptible to dilution.

Fewer rinse cycles remain at the fabric conditioner stage of addition, also a reason why PMCs are used in fabric conditioner.

Not every consumer feels the need to use fabric conditioner to deliver fragrance, and may rely on the detergent to deliver this benefit, meaning PMCs are also required in detergent formulations. Encapsulating the fragrance in a protective shell and forming a population of PMCs is one way that academia and industry has moved to improve the performance and cost-effectiveness of perfume in a formulation. Within this shell, the fragrance is ideally protected from evaporation at high temperatures and a combination of the protection from detergent by the shell and adhesion to clothing fibres, preventing the fragrance from being easily lost to washwater liquor in the rinse and drain cycles.

The trade off in additional expenditure to incorporate encapsulation technology into the formulations must be offset by cost savings from a lower loading of perfume in commercial products, with respect to adding perfume neat in the formulation. An aim of controlled release through mechanical force offers a performance benefit from using PMCs, as tailoring the sample to have a distribution of mechanical strengths can mean a controlled release at different time points; during the wash for wet bloom, and after the wash whenever the garments are handled, meaning the longevity of any fragrance on the clothes can be significantly increased.

Microencapsulation of perfumes for laundry applications is a unique challenge and as suggested by Bruyninckx and Dusselier (2019), it poses possibly some of the most difficult requirements and environments for microcapsules in any industrial application. In the food industry, flavours are not required to be designed for controlled release as the mechanical force of chewing tends to be sufficient. In the pharmaceutical industry, controlled release is required and

biocompatibility is also heavily scrutinised. However, the application of microcapsules in the laundry industry requires both of these properties and more.

The PMCs must be strong enough to withstand the hydrodynamic forces in the washing machine and they must be of the correct size and surface charge to successfully deposit and remain on the fibres of clothing. Biocompatibility is a strong concern, which has seen the gradual removal of incompatible shell materials from the market (Zheng et al., 2014).

Excellent controlled release profiles are required, where delivery of the fragrance is sought through rupture of the microcapsules as a response to mechanical stress. What differentiates perfume from other core materials and applications is the complexity of the core material and the formulations in which the microcapsules are added. The perfume oil contains many volatile compounds, all of which are necessary to give the perfume its desired olfactory profile, but preventing loss through evaporation is a challenge. Not only does the correct synthesis route need to be selected to prevent high temperatures causing evaporation before a shell is formed, but the shell itself also has to have low permeability to prevent loss of the perfume oil after the microcapsules have been synthesised. The low permeability of the shell material is also of importance when considering the deterging laundry formulations in which PMCs are added. The shell material must prevent the extractive nature of the surfactant in the detergent, and this must be the case for up to 18 months in which the product could be stored before use (McCoy, 2018).

Taking all these requirements into account, it is extremely important to understand how a chosen method of synthesis and shell material can affect typical PMC structural, mechanical and physicochemical properties. It is also vital to consider how the final PMC will behave in

formulations in terms of stability of fragrance oil and compatibility with other ingredients, and also to understand the affinity of a PMC for typical fabrics in a wash cycle.

2.1.2.5 Perfume oil

2.1.2.5.1 Commercialisation of fragrance

The emotive response that someone might feel from smelling a rose in bloom is nothing new. It was curiosity into the source of these scents that led to the extraction and distillation of natural compounds to be used as perfumes thousands of years ago in ancient Egypt and Greece (Herrmann, 2007). Applications remained scarce until around the 13th century when pharmacies prepared remedy oils to understand their physiological effects on people. Around the time of the industrial revolution the perfume industry had its own industrial flourish, mostly in Germany and Great Britain, with the industrial synthesis of Vanillin in 1874, and Coumarin in 1878 by the company Haarman & Reimer (now Symrise) (Turin and Sanchez, 2010). At this point in time, due to limitations with techniques, only major components of natural compounds were extracted, which then allowed for identification and separate synthesis. Scale up of this synthesis and commercialisation then allowed for reduced costs and prices (Rowe, 2009). As technology improved with developments in chromatographic and spectroscopic techniques, the ability for analysis to elucidate trace compounds in natural products became possible.

2.1.2.5.2 Source of perfume ingredients

Perfume ingredients can either be naturally derived, that is, they are extracted from plants, trees and animals, or synthetic, where the compounds are created in a laboratory. For naturally

derived perfumes, production can be carried out through expression, where odorants are forced out of the natural source by physical pressure. It can also be achieved through dry distillation or steam distillation which separates essential oils. Finally, solvent extraction can be used to obtain a concrete or resinoid, which can then be extracted with ethanol to give an absolute oil, or further distilled to obtain an essential oil (Pybus and Sell, 2007).

Synthetic fragrances on the other hand are created in the laboratory. The ability to turn to synthetic ingredients can increase the longevity of a fragrance, as synthetics can have the fixative that naturals lack. They can also add depth to fragrances that naturals alone cannot achieve, for example, the addition of aldehydes to lighten heavy scents with a lemon zing (Bomgardner, 2019).

There is a delicate balance when studying what consumers seek from ingredients in their products. Alongside diversifying the palette, synthetic fragrances come at a lower cost. There is a growing consumer desire in fine fragrance to seek natural ingredients in their fragrance. This is largely due to the negative attention surrounding synthetics and the potential harm to humans and the environment, with emphasis on ingredients such as parabens, phthalates and synthetic musks (Juliano and Magrini, 2017). Natural fragrance molecules though are not necessarily a safer route. Limonene, citral, cinnamyl, geraniol and eugenol are all known to be allergens that are required to be present on the International Nomenclature of Cosmetic Ingredients (INCI) list (Bråred Christensson et al., 2016). Additionally, use of naturals can place added strain on the environment through the sourcing of the material. The desire for Indian sandalwood is much greater than the supply, meaning there is heavy deforestation of evergreen trees, whereas synthetic sandalwood can have higher olfactory power, without tree-felling and shipping materials (Bomgardner, 2019).

The creators of a laundry detergent need to decide how the source of the fragrance conforms to the ethos of the company. Decisions include whether it aims to be sustainable in its sourcing of ingredients, if it fits with the intended branding of the product, and whether it aimed at an all-natural segment, or aimed at a more general space.

2.1.2.5.3 LogP_{ow}

The partition coefficient, P_{ow}, describes the relative propensity of a compound to partition between immiscible oil and water phases. In most cases, octanol and water are used as the two phases. Solutes that are hydrophilic will dissolve in the water phase, and those that are hydrophobic will dissolve in the oil phase. As perfume is composed of a complex combination of many compounds with different volatilities, there will also be a range of log*P* values within the composition. This then becomes relevant when considering application on fabrics. The perfume is required to move from an aqueous detergent source to a more hydrophobic fabric, although hydrophobicities of fabrics can vary, with wool cotton and linen being more hydrophobic than artificial polyester or acrylic. The log*P* parameter then strongly correlates with deposition onto the fabric substrate as those molecules with a high log*P* are more likely to deposit on hydrophobic fabrics. For perfume added to fabric conditioners, this is quite a simple process, however with the high surfactant concentration in detergents, the partitioning of the perfume becomes more complex.

Perfume deposition on fabrics during a wash cycle has been modelled by Normand et al. (2008). Without surfactant, after the wash cycle, molecules with low log*P* are not likely to be retained on the fabrics as they are extremely soluble in water, whilst nearly all molecules of high log*P* are deposited on fabrics. With more rinse stages, and fresh water, any loss from the fabrics is

greater for lower log*P* molecules. When surfactant is added to the wash, micelles form above the critical micelle concentration (CMC). Molecules of higher log*P* have a greater chance of being consumed by the micelles and lost to the drain. This means after the first wash stage it is molecules with mid log*P* values that are deposited the most on fabrics, with low log*P* molecules still lost with drain water. This trend continues until the concentration of the surfactant drops below the critical micelle concentration, at which point the perfume molecules trapped within are released and the high log*P* values deposited on the fabrics. This additional process of micellization changes the profile of deposition, as seen in Figure 2.2, such that high log*P* values are of intermediate deposition, and intermediate log*P* values, that were not consumed by micelles, have the highest deposition at the end of the cycles.

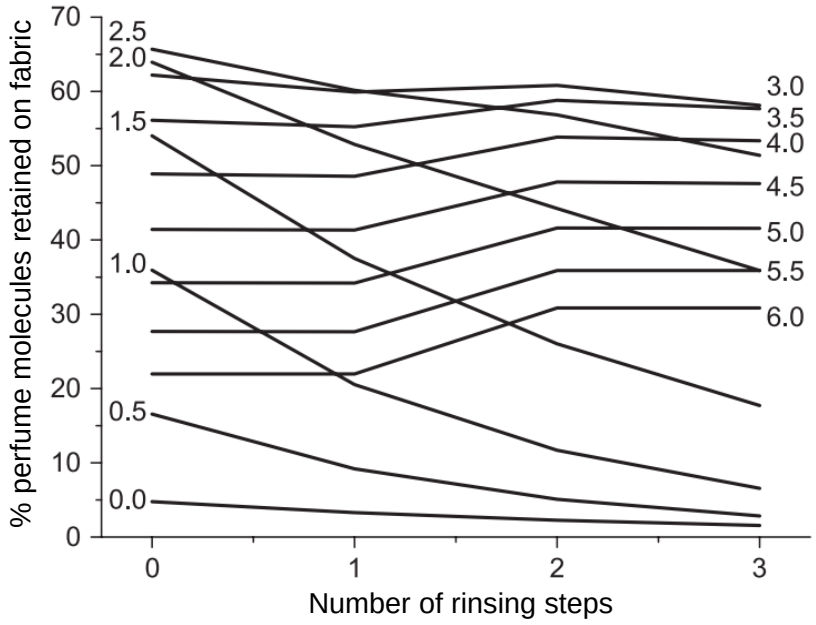

Figure 2.2: The effect of the number of rinsing steps on the % deposition on fabric of molecules with different log*P* values, in the presence of surfactant. Reprinted from Normand et al. (2008)

This process represents the difficulty of designing a perfume. What might have been a carefully designed composition of molecules can completely change character based upon the application in which it is used, and if perfume is to be added neat to the wash cycle these factors need to be understood.

2.1.2.5.4 Perfumes for cosmetics, toiletries and household products

In fine perfumery the fragrance is often only bottled with the solvent, meaning few considerations are required, apart from olfactive resistance to oxidation and UV degradation. In household products on the other hand there are additional considerations to take into account that affect the perception of the product. When considering product appearance, care needs to be taken to ensure the complex perfume design does not cause any product discolouration in storage, which would lead to consumer dissatisfaction.

Another contradiction to fine perfumery for household products is the expectation of performance of the perfume in spite of economic constraints on the product. In fine perfumery the consumer is often willing to spend money for the purpose of wearing an alluring scent, with an additional requirement of longevity of fragrance. In household products, the formulation is expected to offer positive fragrance, alongside a variety of other key performance indicators, including cleaning ability for laundry detergents. Laundry detergents are fast moving consumer goods with a price-point aimed at repeated, regular purchasing. This low price point makes delivering an attractive fragrance from the product even more challenging as the perfume oil is often one of the most expensive ingredients in the formulation (McCoy, 2014). Within the laundry industry, this has led to the application of technologies that aim to extract the most

value from perfume in formulations by reducing waste and degradation of the material and minimising perfume loading in the formulation.

Examples of trying to deliver more fragrance to clothes in laundry products can be as simple as overdosing with perfume oil. Whilst this achieves a stronger olfactive response, it also increases the amount of perfume lost to the drain, which companies try to avoid due to strong competition in costs. This higher loading can also change the hedonics of the composition; whether the consumer perceives the perfume favourably or not.

Another technique to try to maximise the efficiency of adding perfume to laundry products has been the use of pro-fragrances (Herrmann, 2007). This is a chemical release mechanism where precursor fragrance molecules are covalently attached to a substrate, which can be a macromolecule or nanoparticle for example. When covalently grafted to a substrate, the fragrance molecules are odourless and non-volatile, so can be present in the washing machine without being lost through evaporation. To release the fragrance molecule and activate the scent, the covalent bond is broken through an external stimulus such as light, heat or a change in pH, which only requires relatively mild conditions for organic chemistry facilitating use in consumer products. The technology requires good pre-cursor stability, particularly if it is to be added neat to detergent formulations. This means that extra steps are needed in commercial applications to enable inclusion, such as storing in opaque packaging if the precursor is light-activated, incorporating in fabric softeners rather than detergents for a milder environment, and potentially redesigning packaging to have the detergent as a two-component system. As well as the expense to form the precursor, the extra cost of ensuring stability is a disadvantage of the technology. For pro-fragrances, the value comes if they can increase deposition with respect to adding neat to a formulation, or by delivering a more desirable release rate. Fragrances with a

high logP_{ow} are generally more readily deposited on fabrics than hydrophilic ones (Stora et al., 2001, Normand et al., 2008). Pro-fragrances can effectively reduce the hydrophilicity of perfume molecules, potentially increasing deposition on fabrics (Herrmann, 2007).

2.1.3 Variations in microcapsule shell materials

The choice of a shell material for any microcapsule for industrial applications is one of the most important decisions made in the design process. Considerations need to be made on how the core material is released, as outlined in Section 2.1.2.3. It is also of interest to ensure that it is possible to achieve the desired encapsulation efficiency, that is the level of material encapsulated in the shell, for the applications needed. Decisions need to be made to understand whether the method of encapsulation for a chosen shell material can be easily performed and scaled up for any potential industrial application. Compatibility between the core material and microcapsule shell needs to be carefully controlled. The shell material should show good thermal, UV, and oxidative degradation resistance to allow the microcapsules and encapsulated fragrance to be stable over the lifetime of any product (He et al., 2018). All of these considerations are focused solely on how the shell material will influence performance of the microcapsule as a technology, but when contact with the human body is expected, there are a variety of other properties to note such as biocompatibility and toxicity that make the choice of shell material an even more challenging task (Casanova and Santos, 2016).

Historically, in homecare and personal care applications, microcapsule shells have been formed from polymeric materials for the following reasons:

- Material viscoelasticity
- High mechanical strength
- Ease of synthesis
- Triggered release via changes in pH (Wagdare et al., 2011b), osmotic pressure (Zhang et al., 2017), or light (Dispinar et al., 2013)

Owing to many of these properties, melamine formaldehyde (MF) polymer was one of the most commonly used encapsulation shell materials for homecare and personal care applications (Bône et al., 2011) and the shell material of choice for many of the industrial giants in encapsulation: IFF (International Flavors and Fragrances Inc., 2005), Givaudan (Givaudan SA, 2009) and P&G (Procter & Gamble, 2014c). The shell material was commonly prepared by polymerisation of melamine and formaldehyde under acidic conditions, but industrial interest for alternative shell materials has increased in recent years due to potential concerns about formaldehyde. Work has been done to attempt to replace formaldehyde in melamine-based microcapsules with glyoxal, the smallest dialdehyde, which is used instead in combination with melamine to successfully encapsulate fragrances, allowing for core release through mechanical compression (León et al., 2017).

Alternative common polymeric shell materials are polyamide, polyurea and polyurethane. In consideration of the application of microcapsules in laundry products, polyamide microcapsules are too fragile for application in a washing machine, and a double shell is needed to increase robustness, which would substantially increase the cost of an already expensive technology (Rosa et al., 2015, Caruso et al., 2010). They are, however, industrially available as perfume microcapsules for impregnation in leather goods (Kleban et al., 2004). Polyurea and polyurethane microcapsules have been used in industry to encapsulate perfume by Firmenich

and IFF (Firmenich SA, 2015, International Flavours and Fragrances INC., 2017). Alongside polymeric materials, there has been a surge in interest in successfully creating inorganic microcapsules for industrial application, largely driven by uncertainty over the possible restrictions on use of polymeric non-biodegradable material in personal care and home care products that could enter the environment (Bintein, 2017). Silica and calcium carbonate as shell materials are known to form microcapsules, but they exhibit greater porosity than their organic material counterparts due to the poor film forming properties of inorganic materials, leading to defects (Long et al., 2010, Latnikova and Jobmann, 2017, Yu et al., 2014). This significantly limits applicability as carriers for valuable core material, when a triggered release is sought, which is the case when the core material is as volatile as perfume oil. Similar results have been observed in microcapsules made from natural polymer shells due to a highly porous hydrogel-type microstructure (Dardelle et al., 2017).

Polyacrylate (PAC), a polymeric material, was chosen by P&G to be the new shell material for their laundry detergent microcapsule applications, moving away from melamine formaldehyde. One possible reason for the choice of polyacrylate could be from studying the Hansen solubility parameters (HSP) to understand how soluble the core material is within the shell material. Polymers with low affinity in the core results in a well-defined core-shell morphology, with a thin, dense shell, which is preferable if low permeability is desired. This was highlighted in a paper by Hofmeister et al. (2015). Here the encapsulation efficiency of different volatile perfume oils in polyacrylate nanocapsules was compared as a function of their Hansen solubility parameter δ_p for dipolar intermolecular forces, and δ_h for hydrogen bonds, as determined by swelling tests, the results of which are seen in Figure 2.3.

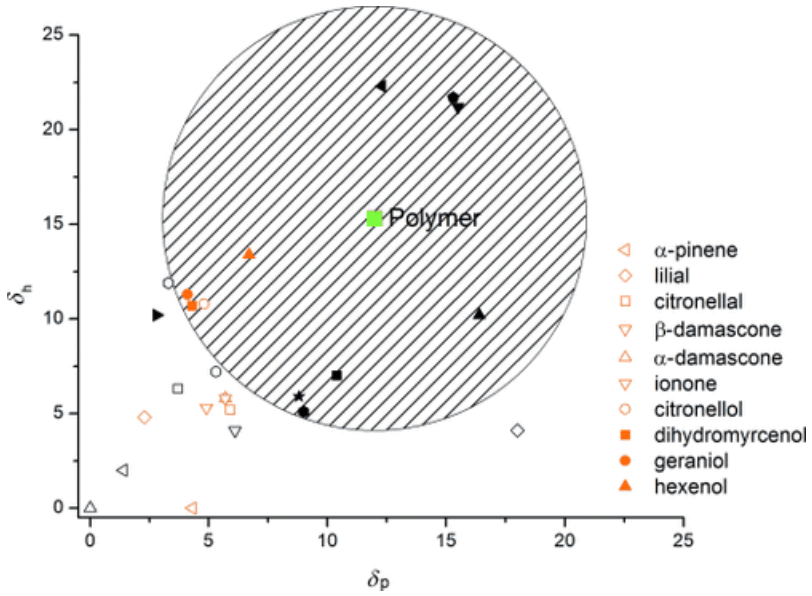

Figure 2.3: Solubility sphere for acrylate is based on swelling experiments, plotting the Hansen solubility parameter for dipolar intermolecular reactions, δ_p, against δ_h, that of hydrogen bonds. Reprinted from Hofmeister et al. (2015)

The perfume oils that were found to be outside the solubility sphere of the polymer were found to have the highest encapsulation efficiency, confirming that if durable encapsulation is required, the polymer and solute need to be incompatible, causing precipitation of the growing polymer in the polymerisation process, and ultimately forming a non-porous shell. Polyacrylate as a polymer is also hydrophilic. This has a specific advantage in a washing machine, as it allows the microcapsules to disperse in the water throughout the wash. This leads to greater homogenisation of microcapsules on the fabrics at the end of the wash, as opposed to a spotty deposition of microcapsules in certain areas of fabric.

2.1.4 Methods of encapsulation

2.1.4.1 Physico-chemical methods of encapsulation

2.1.4.1.1 Coacervation

Coacervation is a term used to describe a partial desolvation of a polymer rich phase (the coacervate) and a polymer-poor phase (the coacervation medium). The partial precipitation, triggered by a thermodynamic change of state, such as a change in pH or temperature causes deposition of the coacervate phase around droplets of the active ingredient of interest. The term was coined by Bungenberg de Jong in 1929 and the potential for encapsulation of droplets was first noted by the same author (Bungenberg de Jong, 1949). Ultimately, it was the first industrial process used for the production of microcapsules by Barrett Green and the National Cash Register Company in the late 1950's, in the development of carbonless copy paper (National Cash Register Company, 1956).

Coacervation as a process can be divided into two classifications: simple and complex coacervation. In simple coacervation, only one polymer is used, and polymer phase separation is achieved by introducing a non-solvent for the polymer to the aqueous solution, or by adding an inorganic salt. Simple coacervation has been overlooked with respect to complex coacervation in industry, because reaching the coacervation zone using salt has a small window, and additional processes are required to completely remove salt from the encapsulated product.

Complex coacervation on the other hand, uses oppositely charged polymers that interact to form the coacervate, a classic example of which is the protein-polysaccharide complex of gelatin and gum Arabic (Leclercq et al., 2009). At a pH of 7-9 there is no coacervate formed. This is because this is the iso-electric point for gelatin, so the material holds no charge. At this pH the gum Arabic is negatively charged. As the pH is decreased the gelatin becomes positively charged

and it is at this point the coacervate between the gelatin and gum Arabic forms and separates the aqueous phase into two distinct phases – coacervate and coacervate medium. The coacervate coats the oil droplets to be encapsulated and then permanent microcapsules can be formed by lowering the temperature of the system (Mishra, 2015). Glycerol or formaldehyde can be used as cross-linking agents to improve the encapsulation ability of the formed microcapsules (Huang et al., 2007).

Coacervation offers the ability to encapsulate at low temperature, which is particularly relevant for encapsulation of volatiles. The technique uses a non-toxic solvent and it can reach a high loading capacity of microcapsules (up to 99%). Additional procedures, however, are needed to isolate the microcapsules and crosslinking agents are required to increase their mechanical strength and to decrease core leakage of compounds such as formaldehyde and glutaraldehyde which bring potential physiological and biological toxicity. This limits the range of applications in formulated products (Jain et al., 2016, Ozkan et al., 2019). There is limited literature detailing encapsulation efficiency of perfume encapsulation and most work is detailed around pharmaceutical encapsulation. Commercial uptake in the process is largely limited by the aforementioned sensitivity to narrow pH range and the delicate influence of salt that can reverse the association of coacervates (Timilsena et al., 2019).

2.1.4.2 Chemical methods of encapsulation

2.1.4.2.1 *In-Situ* polymerisation

When forming microcapsules with an oil core, *in-situ* polymerisation can be used by polymerising in the aqueous continuous phase, migration of the formed polymer to the interface with the dispersed phase, and deposition on the oil surface. The process of depositing the

polymer is controlled by changing the pH, temperature or solvent quality (He et al., 2018). Under acidic conditions for example, the water-soluble amino resin pre-polymer becomes more hydrophobic due to etherification and methylene bridge formation. This drives migration to the hydrophobic droplet and the formation of a primary polymer film on the surface of the droplet. Further cross-linking thickens the shell and results in the final microcapsule structure (Mishra, 2015, Nguon et al., 2018).

The most common shell materials associated with *in-situ* polymerisation are urea formaldehyde and melamine formaldehyde, which are amino resins produced by the reaction of an aldehyde with an amino containing compound, and there are many examples of successful encapsulation of fragrance oil by this method (Lee et al., 2002, Fei et al., 2015, de la Paz Miguel and Vallo, 2019, Zhao et al., 2019).

In-situ polymerisation has been a popular technique for producing microcapsules due to simple scale-up, low cost, fast reaction times in relation to the process, a highly cross-linked impermeable shell, high encapsulation efficiency and excellent thermal and mechanical properties. This makes them ideally suited for applications as fragrance microcapsules (de la Paz Miguel and Vallo, 2019).

Melamine formaldehyde microcapsules made by this process were the previous benchmark for microencapsulation, however, the fast reaction times that facilitate cross linking of shells in-situ also means that formaldehyde can remain unreacted.

2.1.4.2.2 Interfacial polymerisation

Interfacial polymerisation differs from *in-situ* polymerisation as each monomer required for formation of the polymer microcapsule shell is in a separate phase; one hydrophilic monomer, in the continuous aqueous phase, and a hydrophobic monomer situated in the dispersed phase within the oil droplets. Whilst the detailed mechanism is not completely understood, the principles involve an instantaneous reaction between the monomers at the interface, producing a primary membrane (Yow and Routh, 2006). The reaction rate then becomes diffusion controlled as movement of aqueous monomer across the membrane becomes more difficult; the thicker and denser the membrane becomes, the slower the reaction. The aqueous monomer, a diamine in the case of polyamide and polyurea synthesis, and a diol in the case of polyurethane synthesis, diffuses across the membrane and polymer growth then occurs within the oil phase. Once the polymer reaches a certain molecular weight it precipitates out of solution and migrates to the interface to thicken the polymer shell from inside the microcapsule (Perignon et al., 2015). Partial solubility of some fragrance ingredients in water can destabilise the interfacial polymerisation reaction, and it has been established that some of the perfume ingredients can react with monomers, leading to modification of the fragrance (Rodrigues et al., 2008). If interfacial polymerisation is used as the synthesis method for PMCs, extra care has to be taken to reduce the impact of these interactions.

2.1.4.2.3 Suspension polymerisation

In suspension polymerisation, all materials needed to create the microcapsule are held within droplets of the oil core. This includes any monomers, initiators and transfer agents. The oil phase is generally suspended within an aqueous phase with a water-soluble polymer or

inorganic powder present as a stabiliser to prevent agglomeration of oil droplets in the suspensions, and to promote the formation of microcapsules. The success of the stabiliser in preventing agglomeration is largely dependent on its ability of it to form a protective film around the droplet, lowering the interfacial tension between the droplets and water to promote droplet formation, rather than coalescence. Another part of the process that prevents aggregation is utilising substantial agitation within the reactor, which also has a direct effect on the final size distribution of microcapsules, details of which are discussed further in Chapter 4.

Generally, as all the reagents are contained within each oil droplet, providing there is adequate homogenisation through agitation, each droplet can be thought of as a separate batch reactor, as the polymerisation takes place within these droplets. This means the kinetics of initiation, propagation and termination of bulk polymerisation hold true. Generally, water is used as the continuous phase, meaning that the heat transfer medium is economical and provides environmental benefits over solvents used in other encapsulation methods. The final encapsulated product can simply be washed and filtered, meaning low separation costs with respect to emulsion polymerisation (Vivaldo-Lima et al., 1997).

As a process, it is extremely versatile and nearly all common thermoplastics can be made via suspension polymerisation. It has been industrially relevant in the manufacture of many microcapsules of different shell materials such as poly(vinyl chloride), poly(methyl methacrylate), and expandable polystyrene (Brooks, 2010), and used specifically to encapsulate fragrance in polyacrylate/paraffin microcapsules by Zhang et al. (2016b).

2.1.4.3 Physico-mechanical methods of encapsulation

2.1.4.3.1 Spray drying

In this method of encapsulation, an emulsion is created in which a core material is dispersed within a solution containing the shell material. This is then atomised and sprayed through a rotating disc into the heater of a spray dryer. The heat causes rapid evaporation of water, causing the shell material to solidify around the droplets of core material. Spray drying is a popular encapsulation technique for the production of microcapsules with natural polymer shells. Chitosan, a natural polysaccharide of glucosamine and N-acetylglucosamine has widely been used in the pharmaceutical industry as a shell material for encapsulation and it is finding applications in other industries, due to its non-toxicity biocompatibility and biodegradation properties (Li et al., 2013).

The process is easily scalable and it is quite fast so it is well-suited to industrial manufacture of microcapsules. The disadvantage of the technique, specifically when encapsulating volatiles such as fragrance, is that the chamber needs to be hot to evaporate the water, and indirectly also evaporates some of the fragrance. This often results in poor encapsulation efficiency. Literature detailing spray dried encapsulation of fragrance requiring controlled release is also scarce (Bruyninckx and Dusselier, 2019).

2.2 Characterisation of microcapsules

Research into microencapsulation broadly falls into two categories: formation of new microcapsules through techniques highlighted previously, or the characterisation of microcapsule properties and performance. It is necessary to determine the physicochemical,

structural and mechanical properties of microcapsules to completely understand the capabilities of them in relation to their specific applications. The relative importance of properties will vary depending on the desired application and result.

It is important to note the intra-relationships amongst microcapsule properties. The mechanical strength of a certain composition of microcapsules depends greatly on shell composition, structure, thickness and particle size. There are many techniques available to researchers for mechanical, structural and physico-chemical characterisation of microcapsules, each with their own capabilities and limitations.

The choice of technique will depend on the type of information and accuracy required. In the next sections, methods are outlined from literature that have been used for the characterisation of microcapsules. The work has been taken from a publication by the author and developed to also include literature focusing on perfume microcapsules (Gray et al., 2016).

2.2.1 Physicochemical characterisation

2.2.1.1 Microcapsule size and size distribution

Depending on the type of application under consideration, different size distributions of microcapsules might be desirable. However, controlling size distribution at different scales is another question entirely. If a narrow size distribution is required, microfluidics can provide such size, but the rate of production is extremely low, so it cannot be used to produce at industrial scale for fast moving goods (FMCG) applications (Lee et al., 2016). To produce at industrial scale a stirred vessel or homogeniser is often used, though care needs to be taken to control the final size distribution. Microcapsule size distribution is important and can affect

deposition properties of the microcapsules, for example how successfully the microcapsules embed in fabric yarns, and how inhibited they are in flow in the washing machine. The size is also inextricably linked to the mechanical properties of the microcapsules, where increasing diameter but keeping shell thickness constant has a negative correlation with rupture stress (Xue and Zhang, 2009).

Methods for characterising microcapsule size and size distribution can largely be divided into two areas: laser diffraction and microscopy. Considerations need to be taken to decide whether quantitative data is required for individual or bulk microcapsules, and whether visualisation of a smaller number of microcapsules is desired, before choosing the appropriate technique.

Dynamic light scattering (DLS) is a technique for the size analysis of sub-micron particles (1 nm to 1 μm) (Cao et al., 2012, Chen and Zhou, 2015). The technique measures the fluctutation of the intensity of scattered light through a fast photon detector due to interference presented by microcapsules moving under Brownian motion as a function of time. The smaller the size of microcapsules, the faster the fluctuations in light intensity. As an ensemble method, the intensity fluctuations are measured on the whole particle sample, so size distribution data is an output from this technique (Myhra and Rivière, 2012).

As size of the particle increases, potentially from nanocapsules to microcapsules, and if ensemble methods are still sought, laser diffraction opens up as a technique for studying perfume microcapsules (Pirone et al., 2019, Sharkawy et al., 2017). Variations in scattered light intensity passing through a microcapsule suspension as a function of scattering angle can be used to measure average microcapsule size and size distribution from 10 nm to 3 mm. A limitation of laser diffraction is that knowledge of the refractive index of the shell material is required for measurement.

If a true image of the microcapsule is required, rather than bulk analysis from light scattering, microscopy is the other common technique used for size characterisation. This can often be beneficial when studying the morphology of microcapsules, as a result of the synthesis techniques. Ultimately microscopy is a much more time-consuming process, especially if size distribution data is sought, through capturing enough images for statistically robust results from image analysis. Microscopy is seldom used for size distribution analysis, and when focusing on analysis of size specifically, it is often a beneficiary of other techniques which characterise other properties but require the specific microcapsule size to be recorded. An example of this is in atomic force microscopy (AFM) or micromanipulation where mechanical characterisation of individual microcapsules relies on accurate measurement of size during the measurements (Pretzl et al., 2012, Pan et al., 2013b).

Optical microscopy is the simplest type of microscopy in terms of ease of operation and cost of sample preparation, and for those reasons it is a valuable aid in quick analysis of microcapsule size. A limitation is the inherent properties of visible light, with a resolution maximum of 400 nm; the smallest wavelength of visible light. Another drawback of the technique is that out of plane structures can scatter incident light to distort the image. In order to overcome these limitations within the field of microscopy it is necessary to move to scanning electron microscopy (SEM). This technique uses a high energy beam of electrons (20-30 keV) instead of light photons, to generate an image of much higher magnifications (x10,000) and resolution (> 10 nm) than optical microscopy. It is often used in the field to achieve a more precise characterisation of the size of microcapsules (Tekin et al., 2013, Zhao et al., 2016). Whilst achieving higher resolution and less optical distortion than optical microscopy, SEM is conducted under vacuum to prevent collisions with artefacts, so imaging microcapsules in their

natural state, in a dispersion for example, is not possible. To overcome this restriction, environmental SEM (ESEM) can be used to image samples in their native state or in a low vacuum (Bogdanowicz et al., 2013, Teixeira et al., 2012).

2.2.1.2 Microcapsule surface roughness and morphology

Depending on the type of synthesis method chosen, and the relative loading of reactant ingredients, the surface roughness and surface morphology of microcapsules can vary widely. This can have a profound impact on how microcapsules perform. A rough surface can promote agglomeration and decrease dispersion of microcapsules, whereas a smooth surface might decrease ability to deposit in certain applications.

Optical microscopy and SEM have regularly been used to visually inspect the microcapsule roughness and morphology, but this only offers qualitative observations (Miró Specos et al., 2010, Chowdhury et al., 2015). If quantitative analysis of surface roughness is required, AFM and white light interferometry are techniques that can help.

AFM in contact mode can offer surface roughness resolution down to fractions of a nanometer. In this mode, a sharp tip probe is attached to the end of a cantilever and brought into contact with the surface. Remaining in contact with the surface at all times, the tip scans across the surface, and the deflection of the cantilever is monitored by a photodiode detector. Alongside excellent resolution, the absence for the need of an ultra-high vacuum makes the technique extremely attractive for characterisation of surface morphology, and as such it is currently the most widely used technique for quantitative analysis (Choi et al., 2013, Dorati et al., 2006, Lekka et al., 2004, Wang et al., 2009, Xu et al., 1998, Ali et al., 2019, Chatterjee et al., 2014a).

White-light interferometry is a non-contact technique, unlike AFM and is a form of profilometry. A source of light is spilt by a beam splitter; one beam travels to the interferometer and the other travels to the sample. Both beams reflect back to the beam splitter and are combined into interference fringes, which are captured by a charge-coupled device (CCD) camera, creating an interference pattern from which the roughness pattern can be developed. The technique has a resolution of 0.2 nm and spatial resolution of 150 nm in the horizontal plane (Haas et al., 2001). Without any additional preparation it can be used to survey a horizontal plane of up to 10,000 μm, meaning large numbers of particles could be analysed at once (Adi et al., 2008).

Traditionally, the technique has been used to study surface roughness in microparticles and pharmaceutical excipients (Bashaiwoldu et al., 2004, Narayan and Hancock, 2005), however the principles are the same for microcapsules and some examples in literature have been observed (Zheng et al., 2012, Zheng et al., 2014).

2.2.1.3 Microcapsule shell chemical composition

Three methods are widely used to provide information on the chemical compositions of microcapsule shells as a function of depth. These are attenuated total reflectance Fourier-transform infrared (ATR-FTIR) spectroscopy, X-ray photoelectron spectroscopy (XPS), and time-of-flight secondary-ion mass spectrometry (ToF-SIMS; (Rokstad et al., 2014, Tam et al., 2005). Each of these techniques can be used to analyse the surface to different depths, therefore complementary sets of information are obtained.

ATR-FTIR enables samples to be analysed with little sample preparation, which significantly increases the speed of analysis. In terms of microcapsule shell thickness, ATR-FTIR can work at penetration depths in the micrometre range, and is generally used to provide information on the functional groups that characterise the bulk chemistry of the microcapsule shell (Levin and Bhargava, 2005, Zhao et al., 2019, Zheng and Pilla, 2018).

XPS was the first technique used for microcapsule shell composition analysis. X-rays are fired at the surface to eject electrons (de Vos et al., 2003, Chatterjee et al., 2014b). The number of electrons and their kinetic energies are measured and the information enables the elemental origins of the electrons to be determined, giving qualitative information on surface chemical groups to a depth of 100 nm.

In ToF-SIMS, a primary beam of ions sputters the surface of the target material, ejecting secondary ions; the masses of these ions are identified using a mass spectrometer, and used to characterise the compounds in the microcapsule shell. This technique is used for the outermost region of the microcapsule shell, with a depth of penetration of 1–2 nm. Although ToF-SIMS is useful for qualitative analysis, quantification of the individual elemental compositions is difficult as the intensity of the detected secondary ions is heavily influenced by the chemical composition of the surrounding matrix. Other techniques such as energy-dispersive X-ray spectroscopy (EDS) must be used if this is required (Tam et al., 2005).

An interesting comparison and collation of these methods was made by Tam et al. (2005) for modelling the shell structure of alginate-poly-l-lysine-alginate (APA) microcapsules, which are used in the immuno-isolation of secretory cells. Poly-l-lysine (PLL) is used to form the semi-permeable cell membrane, and if PLL is exposed at the surface of the microcapsule membrane, it can generate an unwanted immune response. ATR-FTIR analysis confirmed that PLL was

present in the outermost 3 μm of the microcapsule shell, but this is insufficient to confirm the presence of PLL on the surface, where it is most likely to generate an immune response. XPS was used to determine the surface composition of the outermost 100 Å; the carbon content showed that there were high levels of PLL in this region. Finally, ToF-SIMS was used to study the outermost one to two monolayers of the structure, and it was found that PLL was exposed in these layers. A change in the ToF-SIMS peaks also showed the presence of alginate–PLL complexes on the outermost surface, although this may not be consistent throughout the surface and any free PLL has the potential to cause complications, by generating an immune response.

A combination of EDS and SEM can be used for elemental analysis of the microcapsule surface or across the microcapsule shell. This is because the unique atomic structure of an element results in a unique set of peaks in its X-ray emission spectrum, which can be used to identify an element qualitatively and quantitatively (Han et al., 2011).

2.2.1.4 Surface charge and zeta potential

Stability issues are of paramount importance in consumer products such as detergents. It is an unforgiving industry where good stability of products often goes unnoticed. When instability prevails, the consumer is quick to notice and product confidence, which is hard to build, can be depleted immediately. Instability in microcapsules, if included in a liquid detergent, could potentially be caused by a density mismatch between the suspending medium and the microcapsules and this colloidal instability ultimately leads to product instability. It can also be triggered through microcapsule aggregation due to inadequate control of the zeta potential. The zeta potential is the charge that develops at the interface between a solid particle, such as a microcapsule, and a surrounding medium. Control over the zeta potential can be gained by

altering surface charge of microcapsules and the ionic strength and pH of the suspending medium. The isoelectric point is the pH of the medium where the microcapsules have a zeta potential of zero, carrying no net charge, and therefore any repulsion between particles is screened, causing aggregation. In formulations it is often sought to maximise positive or negative zeta potentials away from the isoelectric point to reduce aggregation.

It is worth noting that due to the complex nature of product formulations, considerations must be made to optimise the surrounding medium, since one type of particle might negatively impact other ingredients in the formulation, in terms of stability. Two methods in particular have been highlighted for calculation of zeta potential in microcapsule dispersions; streaming potential and electrophoresis.

Streaming potential as a technique places samples of microcapsules in a stationary state on a measuring cell and forces electrolyte (the dispersion medium) through the cell. This introduction of electrolyte disrupts surface charges on the microcapsules, causing a measurable potential difference; the streaming potential (Xie et al., 2010).

In electrophoresis the charged microcapsules are moved in the electrolyte by an electric field and the zeta potential can be calculated by measuring the electrophoretic mobility of the microcapsules in the liquid under this electric field (Chatterjee et al., 2014b, Mirabedini et al., 2012, He et al., 2014). The size of microcapsules often governs which technique is used to find the zeta potential, as electrophoresis has an upper limit of around 30 μm due to sedimentation issues. Streaming potential can be used for all sizes of microcapsules.

2.2.2 Structural characterisation of microcapsules

2.2.2.1 Shell thickness of microcapsules

Microscopy has dominated determination of shell thickness of microcapsules, due to clear visualisation of the sample, and electron microscopy specifically has the resolution required to determine shell thickness on a nanometer scale.

SEM, also used to assess microcapsule size and size distribution, can be utilised to study shell thickness (O'Sullivan et al., 2009, Polenz et al., 2015). As with all electron microscopy studies, sample preparation is challenging. The sample needs to be placed under vacuum, which requires it to be dehydrated and fixed to a substrate prior to imaging. This potentially introduces artefacts and may cause shrinkage (Goldstein et al., 2003). To avoid shrinkage, samples can be cryo-fixed and then coated with gold or platinum to increase conductivity. This process is called cold stage SEM (cryo-SEM), and whilst usually reserved for biological samples (Allan-Wojtas et al., 2008, Lensen et al., 2011), it has found applications in microcapsule characterisation (Pirone et al., 2019).

A drawback to conventional SEM for characterising microcapsule shell thickness is the inability to observe the true shell thickness. Slicing a microcapsule using a microtome exposes a cross section, but unless this is at the equator of the microcapsule, this does not represent the true shell thickness and requires statistical correction if studying a collection of microcapsules (Mercadé-Prieto et al., 2011). One possible way to gain better control over creating a microcapsule cross section for imaging is to use focused ion beam (FIB) imaging. This method accelerates heavy metal ions (gold, gallium or iridium), and rasters them across a sample of interest, causing sputtering with surface ions. The momentum of the incident ions is transferred to the surface material, and sputtering occurs if the kinetic energy transferred overcomes the

binding energy for atoms on the surface (Wirth, 2009). It is possible to combine this technique with the capabilities of SEM to create a dual beam instrument. This was first introduced by Sudraud (1988), when a gallium FIB column was added to an SEM. Application and development of the configuration has been reviewed over the years (Groeber et al., 2006, Mobus and Inkson, 2007, Uchic et al., 2007). The dual beam setup enables in-situ monitoring of the milling of the microcapsule, so it is easier to assess the potential success of finding the cross section without laborious prior sample preparation. Examples related to determination of microcapsule shell thickness have been observed in food-grade zein–lime shell–core microcapsules (Wang et al., 2013) and poly(methyl methacrylate) (PMMA) microcapsules enclosing biocides (Andersson Trojer et al., 2013a).

A further development on the dual beam SEM-FIB configuration is the addition of chemical analysis of the shell using Energy Dispersive Spectroscopy (EDS) (Lasagni et al., 2006, Lasagni et al., 2007). As the FIB sputters away the surface, EDS can assess the chemical fingerprint as a function of depth. As each measurement with depth can be thought of as another slice, after which FIB sputtering is required, the technique is time-consuming and requires automation (Schaffer et al., 2007).

Transmission Electron Microscopy (TEM) uses a higher energy beam of electrons; 100-300 keV compared to 20-30 keV for SEM. This enables the electrons to be transmitted through the surface of the sample, rather than reflected off the surface. When the surface is extremely thin, this facilitates identification of internal structures, such as internal shell wall, enabling determination of shell thickness (Long et al., 2010, Polenz et al., 2015). There are particular advantages and disadvantages associated with TEM for shell thickness determination in microcapsules. The extremely high resolution (0.2 nm) and magnification (x10,000,000) are

both an order of magnitude higher than SEM, meaning precise determination of shell thickness is possible. Sample preparation to aid exposure to vacuum conditions is challenging and costly. Generally, samples are fixed in an acrylic resin for imaging, prior to being cross-sectioned by a microtome (Kumar, 2013). The chemical composition of the shell and how this might be affected by treatment to fix in resin must be considered. For example, solvents can potentially dissolve microcapsule shells, such as with PMMA as a shell material (Pan et al., 2013c).

If the shell material is unsuitable for preparation of the sample by electron microscopy, confocal laser scanning microscopy (CLSM) offers a potential alternative. Primarily developed for biological samples, it has also been used for imaging microcapsules (Kaufman et al., 2017, Pan et al., 2013b, Tavera et al., 2009, Lefebvre et al., 2008). It is a non-destructive technique that uses fluorescent light to excite fluorescent markers, which can be incorporated into the microcapsule shells. Compared to the wide-field optical epi-fluorescence microscopy, CLSM only marginally improves resolution to 0.2 µm laterally and 0.5 µm vertically, but the advantage comes through the ability of the confocal pinhole to reject out of focus fluorescent light, providing an image of greater clarity (Schermelleh et al., 2010). Requirements for incorporation of fluorescent dye in the shell decreases the simplicity of the application. A lower resolution with respect to TEM means that CLSM should only be considered if the embedding medium in TEM causes shell degradation, or if alongside shell thickness determination, dynamic in-situ process involving the microcapsule need to be understood, which CLSM can observe.

Moving away from determining the microcapsule shell thickness using optical techniques and image visualization, small-angle X-ray scattering (SAXS) is a non-destructive light-scattering method. It can resolve structures of sizes <1 to 200 nm based on the scattering patterns from X-rays that penetrate the material of interest. X-rays interact with electrons in the structure of the

material and inhomogeneities in the electron density cause changes in the diffraction pattern. SAXS can be used to provide information on the structure and shape of an object (Lifshin, 1999). SAXS can thus be used to analyse microcapsules in a liquid, which is not possible using SEM or TEM, because of the need for a vacuum in the sample chamber. A limitation is that data is related to the average properties rather than individual measurements (Lifshin, 1999). The size restrictions of SAXS mean that analysis has largely focused on nanocapsules (Gutsche et al., 2014, Utama et al., 2015). However, ultra-small-angle X-ray scattering can spatially resolve structures up to 10 μm, making it of interest in microcapsule analysis, although no results have yet been published.

2.2.2.2 Pore size of microcapsule shells

Materials and synthesis methods of microcapsules can affect the number of pores and diameter of pores in the shell. This can have a profound effect on the permeability of the shell, and subsequently impact how microcapsules perform in their desired application. PMCs aim to be non-porous and retain perfume within the core until rupture is triggered. SEM, a technique previously highlighted for characterising microcapsule size and shell thickness, can also be used to assess pore size and total number. However, the failure to assess depth of pore limits quantitative assessment of pore size and size distribution.

The size and total number of pores in the microcapsule shell can be measured using X-ray micro-computed tomography. X-rays are fired at the microcapsule and a planar X-ray detector collects magnified projection images. The microcapsule is then rotated and the process is repeated, collecting hundreds of images. This allows a cross section of the surface structure to be constructed. By summing cross sections at different depths using computer software, it is

possible to create a three-dimensional projection of the microcapsule, enabling visualisation of any pores in the structure. Advantages of the technique are that it is non-destructive to the microcapsule population and offers visualisation of the whole microcapsule. A limitation, certainly for PMCs, is that the resolution of any image captured has a maximum of 1-10 µm, so the total diameter of the microcapsule needs to be on the order of hundreds of micrometers, such as an example which studied pore size distribution in calcium alginate microcapsules, of average size of 300 - 400 µm (Lengyel et al., 2018). The majority of other examples in literature mostly focus on pore size of microcapsules with diameters outside the micro scale, such as with calcium-shellac beads of average diameter 1.35 mm (Law and Zhang, 2007).

AFM was previously described as having use in characterising microcapsule roughness, and it will also be highlighted for applications in characterising mechanical strength. It can be used in tapping mode to investigate the porosity of the shell, highlighting the versatility of the technique for characterising microcapsules (Li et al., 2018, Wagdare et al., 2011a, Naumenko et al., 2012). Tapping mode of AFM is a gentler motion compared to contact mode for measuring surface roughness. The tip is oscillated at a resonance frequency, with the topography of the sample provided through a feedback loop on Z piezo motion.

Positron Emission Annihilation Lifetime Spectroscopy (PALS) has gained attention in investigating porous systems, mainly polymers (Engbrecht et al., 2013, Zaleski et al., 2015), and films (Fukuzumi et al., 2011, He et al., 2013). This technique has been used to investigate free volumes of diameters between Angstroms to tens of nanometres in porous solids, to determine the pore size and pore size distribution up to 30 nm (Gidley et al., 2006). Positrons, the antimatter particle of the electron, are emitted via a radioactive source (^{22}Na), releasing gamma rays. Positronium pseudo-atoms (the bound state of a positron and electron) are formed

randomly in the sample and can occur anywhere. A positron is an unstable species and it can either annihilate intrinsically (125 ps) with its electron or via a pick-off process with an electron in the surrounding material. The lifetime of the ortho-positronium in a solid with a free electron will be 1–4 ns, because of the large number of electrons. However, in a void or pore within a sample, the lifetime will be shorter than that in a vacuum (142 ns), because of annihilation with electrons in the wall (He et al., 2013). On annihilation, more gamma radiation is emitted and the time between the initial radiation and the annihilation radiation is directly related to the pore size.

As well as being used for identifying pores and defects on an atomic scale, PALS can be used to identify closed pores. Measurements can be performed *in situ*, therefore pore size changes over time can be examined (Sun et al., 2002).

2.2.2.3 Monitoring the release of core material from a microcapsule

Understanding the rate of release of core material from the microcapsule is especially important when considering encapsulating perfume. The aim is to make the microcapsule completely impermeable to maximise delivery. Monitoring leakage can be achieved by dispersing a sample of microcapsules in water, or a suitable solvent for the core material, and monitoring change in solute concentration over time. If required, this allows for quantification of the rate of diffusion, $\frac{d_c}{d_t}$, and diffusion coefficient, *D*, providing surface area, *A*, the partition coefficient between core and solvent, H, the shell thickness, h, and the internal and external concentrations of marker C_{int} and C_{ext} are known (Hitchcock et al., 2015) :

$$\frac{d_c}{d_t} = AHD(C_{int} - C_{ext})/h \qquad 2\text{-}1$$

When using PMCs for laundry applications the ideal scenario would be to monitor leakage in water. However, often with volatile and/or organic species, an organic solvent is used to accelerate the leakage. Long et al. (2010) studied the release kinetics of a perfume blend core from melamine formaldehyde-$CaCO_3$ double shell composite microcapsules by dispersing in water and then introducing hexane as a solvent to extract the perfume. Samples from the hexane were taken at intermittent times to monitor increasing concentrations of perfume by analysing with gas chromatography. Similarly Hitchcock et al. (2015) created metallic microcapsules encapsulating volatile species, dispersed in water. They measured leakage via gas chromatography after adding ethanol to increase the solubility of the volatiles in the solute.

Care needs to be taken, however, when choosing a co-solvent along with water. Analysis of leakage of hexyl salicylate from melamine formaldehyde microcapsules using various alcohol co-solvents showed they could potentially damage the shell material (Mercadé-Prieto et al., 2012a). Quantification in this case was done using a UV spectrophotometer to measure UV absorbance as a function of hexyl salicylate concentration.

2.2.3 Mechanical properties of microcapsules

Microcapsules prepared for perfume encapsulation in laundry detergents must be mechanically stable during processing and storage, and must have mechanical strength optimised such that rupture is triggered through mechanical stress either during the wash, or post-wash, depending on what is desired.

The choice of method for characterising mechanical properties depends on speed and ease of data acquisition, and also what type of mechanical properties are sought. If averaged population mechanical properties are of interest, and quick data acquisition is desired, bulk methods of mechanical characterisation are better suited. If size-dependent properties are sought, and more delicate manipulation required, then individual microcapsule mechanical measurements should be utilised. With these methods, data collection is more time-consuming, especially when looking at size-dependency. However, the depth of information achievable is much greater.

2.2.3.1 Bulk methods of mechanical characterisation

The majority of work concerning bulk characterisation of microcapsule mechanical properties has focused around the application of "shear" to the sample, either through manually shaking the samples (Chen et al., 1995, Uludag et al., 2000, Wang, 2000), studying bubble columns (Lu et al., 1992, Martins dos Santos et al., 1997), or through studying breakage in turbine reactors (Poncelet and Neufeld, 1989). These methods have disadvantages such that the breakage of microcapsules is linked to hydrodynamics inherent to the processing equipment used. For PMCs, which are synthesised under high shear conditions, these techniques cannot generally cause rupture, so if analysis from bulk methods is desired, techniques that use compressive forces must be used. Ohtsubo et al. (1991) compressed samples of polyurethane microcapsules between two glass parallel plates and collected data on the required pressure to break 50 % of the microcapsule population. The principles behind this method have since been updated and standardised for industrial applications by use of a texture analyser to automate the compressive force application. However, the smallest diameter of microcapsule studied usually

ranges around a few hundred micrometers. At this size, it is possible to study individual microcapsule mechanical strength (Rosiñski et al., 2002).

2.2.3.2 Individual microcapsule mechanical characterisation

There are many techniques that can be used to characterise the mechanical properties of single microcapsules, and as seen in Figure 2.4, each has a typical force range within which characterisation is possible. The more sensitive techniques are often restricted to biological samples, where picoNewton (pN) force resolution is required to monitor microcapsule deformations.

The most sensitive technique, which has an upper force limit of 50 pN is optical or magnetic tweezers. Photons from a laser are directed at a dielectric object, causing a change in momentum, pushing the object towards the path of the laser. For example, if two glass beads are attached to opposite ends of the microcapsule, or red blood cells in the works by Suresh (2006), the glass beads' position can be manipulated to cause an extension to the capsule of interest, allowing for the measurement of elastic properties (Hénon et al., 1999).

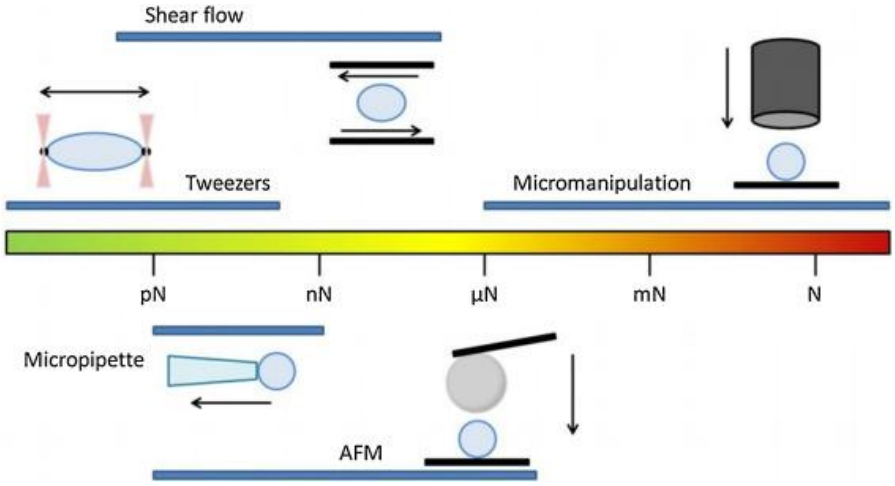

Figure 2.4: Schematic representation of single-capsule measurement techniques, each with typical available force range. Arrows indicate directions in which forces act (Neubauer et al., 2014)

Similarly, red blood cells, other biological capsules and microcapsules with natural shell materials can be deformed using the micropipette technique, capable of reaching slightly higher forces than optical tweezers (nanoNewtons, nN). The microcapsule is sucked under a carefully controlled pressure through a micropipette of known diameter and after analysis of the deformation after studying by optical microscopy, elastic properties can be calculated, such as stretching elastic constants (Fery and Weinkamer, 2007, Kleinberger et al., 2013).

For the microcapsules with synthetic shells, applicable for encapsulating perfume due to mechanical robustness, techniques that can deform microcapsules under greater forces are required. AFM is one of the most popular techniques used to characterise microcapsules with synthetic shells, and unlike previous techniques mentioned, it utilises compression of the microcapsules to determine mechanical properties. AFM as a technique for compressing microcapsules can be divided into two categories; compression using a colloidal probe, and compression using a sharp tip to indent. The colloidal probe technique was first introduced by

Butt (1991) and Ducker et al. (1991), and uses a probe that is larger in diameter than the microcapsule. The geometry of the compression between the probe and microcapsule is well-defined, simplifying mechanical characterisation, and the larger geometry of the probe ensures that no unintentional damage is done to the microcapsule. It has been used frequently in the literature to characterise perfume microcapsules (Pretzl et al., 2012, Charlon et al., 2015, Pan et al., 2013c). Characterisation using AFM in indentation mode can add further compressive stress to the microcapsule, not only complicating analysis, but also causing unintentional damage to the shell, so care has to be taken to elastically deform and not crush the capsule non-elastically. There are contact models, however, to take into account the geometry of the tip and as such the technique is readily used for characterising mechanical properties of microcapsules (Sarrazin et al., 2016, de Loubens et al., 2014).

2.2.3.2.1 Micromanipulation

Micromanipulation is another popular technique to characterise the mechanical properties of microcapsules, particularly when forces greater than microNewtons (μN) are required. The technique was first introduced by Zhang et al. (1991) to study the bursting force of single mammalian cells. Since then, it has been widely used to characterise microcapsules of many shell materials, including synthetic perfume microcapsules (He et al., 2014, Pan et al., 2013a). Microcapsules rest on glass slides (dry measurements) or in a chamber (wet measurements) and are compressed by a normal force under a flat surface, usually a cylindrical probe of diameter larger than the microcapsule. The change in voltage, recorded by the force transducer attached to the probe as the microcapsule is compressed, enables creation of force-displacement curves, from which mechanical properties are extracted. Micromanipulation is particularly useful when

compression to rupture is required, as it can reach forces in the scale of Newtons. Additionally, given the wide magnitude of forces the method is sensitive to small deformations on the scale of μN can be investigated, making the technique extremely versatile. Another benefit of the technique is that it is extremely simple to prepare samples and operate the equipment, and acquisition of data from multiple microcapsules is fast.

It is possible to extract information on the rupture force, deformation at rupture, nominal rupture stress, and nominal wall tension from the force–displacement curves (Liu, 2010). These properties depend on the shell composition, microcapsule size, and shell thickness. As well as compression to rupture, loading and unloading experiments at small deformations are performed to determine the intrinsic material properties of microcapsules, such as the Young's modulus, which are determined using theoretical models and the obtained force verses displacement data.

2.2.3.2.2 Determination of intrinsic properties of microcapsules

For laundry applications it is desirable for microcapsules to be quite elastic, rupturing at large fractional deformations. For microcapsules that rupture at high fractional deformations, it is not always purely elastic behaviour that dominates (Mercadé-Prieto et al., 2012b). Perfume microcapsules for laundry applications, with melamine formaldehyde shells as a benchmark, are known to exhibit elastic-perfectly plastic behaviour, and large rupture strains of 0.6-0.7 fractional deformation (Hu et al., 2009, Zhang, 2001). That means the microcapsule initially deforms elastically and can return to its original state if the deformation is reversed. At a certain point the stress remains constant despite increasing deformation, known as the yield stress. This is followed by a further increase in stress in a plastic strain hardening region, before rupture

occurs at the rupture stress. This means that the rupture stress required to break the microcapsule, as well as the deformation required to achieve this rupture is significantly heightened if the microcapsule exhibits this elastic-perfectly plastic behaviour.

This type of large deformation could only be achieved using micromanipulation, yet it is still possible to extract small deformation information using the same technique from compressing between parallel plates. The simplicity of this technique has also lent itself to modelling deformations for impermeable microcapsules, like those highlighted for perfume microcapsules. (Liu, 2006). Most models, however, have been restricted to membrane models where stretching and no bending of the shell is considered, meaning they can only be applied to thin shell studies at small deformations. Any microcapsules where the shell thickness is not <1 % of the radius see the model fail. It is possible, however, to neglect bending if the microcapsule is elastic up to large deformations, though this is not the case for most synthetic polymer-shelled microcapsules. This means that the region where the profile is elastic, where models could be used to predict the force profile is exactly the region where bending effects are important, rendering the models void. Alongside incorporating bending into any model for describing the theoretical force profile, wrinkling that presents under the compression planes further complicates the scenario.

Finite element modelling, FEM, has been used to overcome the complications of including bending, considering wrinkling, and not assuming the deformed shape of the microcapsule (Mercadé-Prieto et al., 2011, Nguyen et al., 2009). Theoretical force curves from FEM have shown that upon changing the shell thickness to radius (h/r) ratio, different dimensionless force profiles are observed, meaning that matching a force-displacement curve of a known microcapsule of radius, r, can yield the shell thickness of the microcapsule. Consequently,

matching the correct theoretical force curve to the *h/r* value, the Young's modulus can be estimated (Mercadé-Prieto et al., 2011).

2.3 Thermal stability of microcapsules

Characterising the thermal stability of microcapsules does not specifically sit solely within physicochemical or mechanical characterisation. Depending on the focus of investigation, thermal analysis can be used in multiple applications. Microcapsules are widely researched in literature as vehicles for encapsulating phase change materials (PCMs) (Al Shannaq and Farid, 2015, Ng et al., 2017). These materials have high heat values of fusion and solidification, so can absorb and release large amounts of latent heat energy during a phase transition, meaning they show potential as energy storage materials (Liu et al., 2019).

As the heat flux of the phase change material within the microcapsule core is desired, data specifically related to crystallization enthalpy and melting enthalpy, differential scanning calorimetry (DSC) is a powerful tool for PCM thermal analysis. Moving away from PCMs as core materials, DSC can also give yield information on encapsulation efficiency of the microcapsules, the percentage of core material included in the synthesis that was encapsulated, by comparing enthalpies of crystallization and melting of pure core material to the microcapsules (Liu et al., 2019).

When focusing on how thermal analysis can provide information on the mechanical strength of microcapsules, thermogravimetric analysis (TGA) is a technique that can provide a variety of information on the microcapsules. TGA monitors the change in mass of a microcapsule sample as temperature is increased. The first mass loss is often associated with the evaporation of the

core material, especially when the core is volatile fragrance oil. When encapsulated, this onset of evaporation is often delayed with respect to the TGA profile of solely the fragrance oil, due to thermal protection by the shell. The onset of the mass loss for the capsule is triggered by the microcapsule rupturing due to expansion of the core material, and the extent to which this onset is delayed reflects differences in the mechanical properties of the shell material. As temperature is increased, and the fragrance oil completely evaporates, the remaining mass loss is caused by the degradation of the shell material, of which the temperature of onset is also a function of the mechanical strength of a shell, and often the extent of crosslinking. This full profile of mass loss was observed in fragrance microcapsules by Zhao et al. (2016)

2.4 Performance assessment of microcapsules in laundry applications

2.4.1 Techniques for quantifying microcapsules in fabrics

2.4.1.1 UV Vis spectroscopy

One way to evaluate the deposition of microcapsules on fabrics is to evaluate the amount of oil released from the microcapsules. In this technique, fabrics are generally soaked in a solvent for the oil for which UV-visible spectroscopy is used to determine the mass loading of the oil on the fabrics. Zhao et al. (2016) evaluated the durability of fragrance microcapsules on textile substrates using this technique, however, it must be noted that multiple solvents are needed to accurately determine the deposited intact microcapsules. One solvent must solubilise the oil from broken microcapsules whilst leaving the shell unperturbed, whilst another solvent must break down the shell and solubilise all of the oil. The sample results must then be compared with calibration standards for accurate quantification.

2.4.1.2 Microscopy

Fluorescence microscopy was used by Mercadé-Prieto et al. (2012c) to quantify microcapsules deposited on fabric. In this method a fluorescent dye was either contained within the core of the microcapsules, or the microcapsules were stained with a fluorescent dye *a posteriori*. Adding the dye to the core of the microcapsule limits application for industrial scale microcapsule manufacture due to the cost, which is where staining the microcapsules with a lipophilic partially water-soluble dye after synthesis could be used for larger scale syntheses. The issue with staining after synthesis is a lower efficiency of using the dye, often an extremely expensive material, and the intensity of the fluorescence was found to be substantially lower for this method.

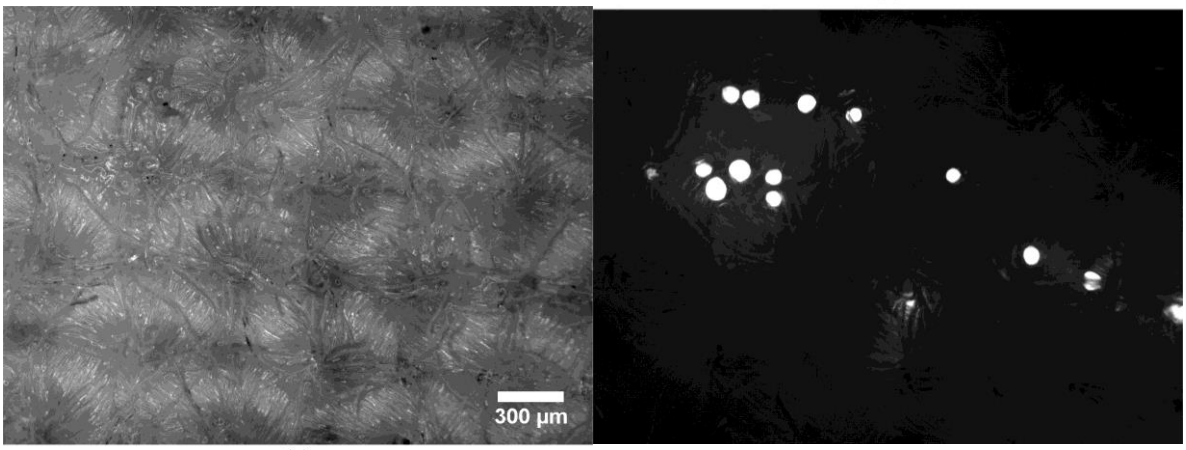

Figure 2.5: Micrographs of fluorescent MF microcapsules deposited in cotton fabric under brightlight (left) and fluorescent light (right). Reprinted from Mercade-Prieto et al. (2012c).

The advantages of microscopy are that by using image analysis software, it is possible to assess the size distribution of microcapsules deposited, potentially yielding information on future

formulation strategy for preferential deposition. Fluorescence microscopy in particular has advantages over SEM, which is also used to identify microcapsules deposited on fabric (Hu et al., 2011, Rodrigues et al., 2008, Dirlik-Uysal et al., 2017) as it is much cheaper in terms of sample preparation and operation. It can be utilised when fabrics are damp or dry, and can be used in combination with other apparatus to assess rupture (Mercadé-Prieto et al., 2012c). Fluorescence microscopy using an epifluorescence microscope does have its drawbacks in quantifying microcapsules; there is an inability to focus at different depths, meaning accurate quantification of microcapsules deposited is difficult when only viewing a single focal plane. Confocal microscopy can be used to negate this limitation and provide quantification with depth (Kouisni and Rochefort, 2009).

With all microscopy techniques there are opposing drivers about which magnification to use; too high a magnification can mean a huge number of micrographs are required to gain statistical significance over the findings, and too low a magnification can mean resolution of microcapsules is poor, especially with the fabric complicating the image. If quantification of deposition on a more simple substrate is desired it is possible to obtain a smaller number of micrographs at a lower magnification, giving fluorescence microscopy a real advantage as an analytical method.

2.4.1.3 Headspace GC-MS

When quantification of microcapsules deposited on fabrics is done by using the perfume as a marker, headspace GC-MS (gas chromatography-mass spectroscopy) is the method of choice for analysis. This is due to the apolar nature and high volatility of the perfumes which need a technique capable of analysing in gaseous form. Samples of fabric can be added to vials either

neat, or with a solvent to solubilise the perfume. Equilibration with the headspace then occurs before sample injection into the GC-MS system. The technique can be used to identify individual compounds in the perfume to understand how they have been affected. It can also be used to quantify total perfume in the system of interest, analogous to total microcapsules when encapsulation efficiency is known. As with UV-Vis spectroscopy, in order to differentiate between broken and intact microcapsules on fabric, the perfume from broken microcapsules can be dissolved in the solvent. The total perfume from intact and broken microcapsules, allowing for calculation of intact microcapsules can be found by rupturing all remaining microcapsules on the fabric prior to headspace GC-MS analysis, noting that the quantification is bulk, and not based on individual identification. For a high number of samples, where good accuracy is required headspace GC-MS analysis is the most appropriate choice when using perfume as the marker for quantification and it has been used on several occasions in literature (Zhao et al., 2019, Teixeira, 2010, Shin et al., 2017).

2.4.2 Quantifying breakage of microcapsules through friction application

As outlined in Sections 2.2.3.1 and 2.2.3.2, the majority of mechanical characterisation for microcapsules rupture originates from compression against the microcapsules under a normal load, either on a bulk sample or individual microcapsules. To the author's knowledge there has been little research on separating out the relative importance of compression and friction on the rupture of microcapsules. One such study from Mercadé-Prieto et al. (2012c) used a custom built rig to abrade fabrics against either a fabric or steel material and assessed the rupture of microcapsules using fluorescence microscopy, showing that the size distribution of the sample is shifted to lower average size and number of microcapsules decreases with each pass. It does

not however provide accurate description of the forces that microcapsules are subjected to under this abrasion, which would be valuable information.

Chapter 3. MATERIALS AND METHODS

3.1 Introduction

This chapter presents the materials and conventional experimental techniques that have been used in the project. The materials section details the specifics of each PMC sample used and other components that aid tests on individual particles and in full scale wash conditions. The methods section is divided into techniques that characterise mechanical, structural and physicochemical properties of the PMCs, and also methods that were used to quantify PMCs, either individually, or by bulk.

To evaluate individual mechanical properties of PMCs, micromanipulation was chosen as a method to diametrically compress particles. This technique is capable of force resolution of microNewtons, it is relatively simple to operate, and yields a wide variety of mechanical information of the PMCs. Experiments were conducted in dry and humid conditions using an environmental chamber to assess the impact on mechanical properties of PMCs. To justify any mechanical differences in different PMC samples further characterisation was provided via TEM to measure shell thickness, dynamic light scattering to study the size distribution and thermal analysis of PMCs using thermogravimetric analysis.

Performance analysis of the PMCs in real-world wash situations was made possible by tracking perfume and a fluorescent dye tracer as markers. For the perfume, headspace GC-MS allowed for quantification of PMCs, and for the fluorescent dye, this was made possible by the use of fluorescence spectrophotometry.

To study rupture on an ensemble scale a texture analyser and a MTM2 tribometer were used to apply consistent stress to PMC populations in order to draw conclusions on the impact of different force situations.

3.2 Materials

The predominant materials used in the experiments were polyacrylate (PAC) perfume microcapsule (PMC) samples, each with slightly different physicochemical properties or structural properties. Care was taken just to adjust one particular property in each sample with a view to create a landscape analysis of what is possible under current economic and technical formulation conditions.

3.2.1 Polyacrylate microcapsules

PAC PMCs were supplied in a slurry with water by P&G (Belgium). Though details were scarce on the specifics of the synthesis procedure due to confidentiality issues, there were readily available patents from the company that gave information on methods of formulation .(Procter & Gamble, 2017a, Procter & Gamble, 2017b, Procter & Gamble, 2014a). The PMCs were filled with a perfume oil core, for which the specific composition was known to the author, but cannot be shared as the information is proprietary to P&G. The core of the PMCs also contained a fluorescent dye, Pyrromethene 546 (PM546) (Merck KGaA, Germany) which was added to the core at 500 ppm.

Samples were supplied by the company with certain physicochemical characteristics provided, as summarised in Table 3.1:

Table 3.1: Structural and physicochemical characteristics of PAC PMC samples for landscape analysis. The presented ratio or wt % values are based on analysis from the supplier

Sample name	**Median particle size / µm**	**Core/shell ratio**	**Total perfume oil / wt %**	**% solids**	**Total Isopropyl Myristate (IPM) / %**	**Other information**
Reference	18.9	90/10	22.00	45.52	45	N/A
20% IPM	25.8	90/10	30.48	43.60	20	N/A
Lower median size	12.2	90/10	21.09	43.89	45	N/A
95/5 core/shell ratio	19.3	95/5	21.00	41.66	45	N/A
Lower median size and 95/5 core/shell ratio	12.8	95/5	21.18	42.02	45	N/A
75°C curing only	19.8	90/10	21.44	44.61	45	75°C curing only
Cationic PMC	21.2	90/10	20.83	43.39	45	3 x TBAEMA cationic polymer
X1	30.0	90/10	26.96	39.66	20	SR368 / 3x TBAEMA with $Al_2(SO_4)_2$

3.2.2 Detergent

For the PMC mass balance and olfactive experiments, detergent was used in the final finished product form with nil perfume added to allow for addition of PMCs. This was in the form of a heavy-duty liquid (HDL), or a heavy-duty granule (HDG) depending on the wash conditions

and the preferences of the target consumer. The specific reasons for the individual conditions such as a regional preference were confidential to P&G.

The dosage conditions and form of detergent for the washes conducted are shown in Table 3.2:

Table 3.2: Detergent load and level of perfume added for different wash scenarios

Type of washing machine	Mass and form of detergent	Level of perfume added in dosage (wt %)
Front load	65.6 g HDL	0.56 %
Front load	65.6 g HDG	0.13 %
Top load semi-auto	106 g HDG	0.12 %
Hand wash	10.8 g HDG	0.12 %

3.2.3 Fabrics

All fabrics were sourced from Warwick Equest, UK. All procured fabrics were prewashed and boil washed to remove any external waxes and post-processing impurities. A mixed ballast load for a wash cycle consisted of polyester, flat cotton, knitted cotton and terry cotton. Specific surface area of flat cotton was 12.4 $m^2.kg^{-1}$, 6.6 $m^2.kg^{-1}$ for knitted cotton, and 3.9 $m^2.kg^{-1}$ for terry cotton.

3.2.4 Jesmonite Resin

Jesmonite resin (Jesmonite LTD, United Kingdom) is a water-based solvent-free acrylic resin largely used in the arts and crafts industry due to its strength, optical properties and non-toxicity. It was used in this project as a means of immobilising PMCs on a surface for friction studies. Immobilisation was achieved mainly through physical entrapment, though the possibility of bonding to the PAC PMCs was also possible, but not thought to be the main method of immobilisation. The resin was mixed in a 2.5:1 ratio of gypsum:acrylic liquid by weight in

accordance with instructions from the manufacture. The two-part resin was then stirred for 5 minutes by hand to create a homogenous workable mixture. This was then poured into silicone moulds in a disk shape for use on the mini traction machine tribometer in later work. The resin was allowed to initially cure in the mould for 30 minutes. It was then removed, turned over, and allowed to cure for another 60 minutes. At this point PMCs diluted in deionised (DI) water were added to the surface that was previously the lower surface against the silicone mould. Concentrations of PMCs solutions are listed in Chapter 7. This timing ensured that the PMCs did not become buried in the Jesmonite resin, but encouraged the PMCs to become entrapped by the resin above the surface. The resin disks and PMCs were left to cure for a further 24 hours to reach the final strength.

3.3 Methods

3.3.1 Washing machine programmes for full scale experiments

Under ideal conditions, the mass balance of PMCs in a wash cycle would be conducted on small scale laboratory equipment such as a tergotometer; simulating the action of a domestic washing machine in a bench-top instrument. This would allow for smaller quantities of test materials (fabric and detergent) and water. It would potentially yield greater accuracy due to the well-defined test parameters and also reduce test times. The drawback in this small scale tergotometer is that the force history of a washing machine cycle can not be fully matched. The force in the tergotometer largely comes from rotation of impellers and hence a lot of the impact of fabric dropping in the washing machine drum and fabric-fabric friction is not observed, and modelling the cleaning and PMC breakage to full scale conditions has not been successful thus far in industry. The decision was made to focus on full scale front load and top load semi-

automatic machines to gain a greater understanding of the true performance of different PMC batches under different key conditions.

3.3.1.1 Front load Electrolux FOM71 CLS machines

The front load machines that were used were not standard 'off the shelf' commercial washing machines. The cycles were completely programmable using the Electrolux FOM71 CLS front load machine (Electrolux AB, Sweden), with precise speed control, excellent bath temperature and water-filling accuracy, and a built-in load cell. The cycles created for the mass balance development is seen in Table 3.3:

Table 3.3: Front load wash cycle programmes for mass balance development

	High Energy Cycle	**Low Energy Cycle**
Main Wash	Add 16 L of water	Add 16 L of water
	Heat to 30°C	Heat to 30°C
	60 minutes at 40 rpm, on for 9 seconds, off for 1 second	30 minutes at 59 rpm, on for 2 seconds, off for 8 seconds
	Drain	Drain
Rinse 1	Spin for 2½ minutes at 1000 rpm	Spin for 2½ minutes at 1000 rpm
	Rinse with 16 L of water for 8 minutes at 40 rpm, on for 9 seconds, off for 1 second	Rinse with 16 L of water for 8 minutes at 40 rpm, on for 9 seconds, off for 1 second
	Drain	Drain
Rinse 2	Spin for 1 minute at 1000 rpm	Spin for 1 minute at 1000 rpm
	Rinse with 16 L of water for 7½ minutes 59 rpm, on for 8 seconds, off for 2 seconds	Rinse with 16 L of water for 7½ minutes 59 rpm, on for 8 seconds, off for 2 seconds
	Drain	Drain
Final Spin	Spin for 3 minutes at 1100 rpm	Spin for 3 minutes at 1100 rpm

The detergent and PMCs were added along with water to dry fabrics at the start of the wash. Prior to each drain, swatches of fabric could be removed to assess deposition and breakage of PMCs, and all water was collected from the drain and the mass removed was recorded before sampling was done for quantification of intact and broken PMCs in washwater.

3.3.1.2 Top load semi-automatic machines

Top load semi-automatic machines have separate drums; one for the wash and rinse cycle, and one for the spin cycle. The semi-automatic notation is due to the need to manually transfer the fabrics from the wash drum to the spin drum once drained. In addition to the differences that top load semi-automatic machines have compared to front load machines as shown in Table 3.4, the detergent and PMCs were added to the water prior to the fabrics being added to the machine.

The machine used was a Panasonic NAW600X Soakmatic (Panasonic Corporation, Japan) and the protocol for the machine is shown in Table 3.4:

Table 3.4: Wash cycle for top load semi-automatic machine

	Top load semi-auto
Main Wash	Add 48 L of water
	16 minutes wash cycle
	Drain
	Transfer to spin drum and spin for 2 minutes
Rinse	Add 48 L of water
	5 minutes rinse cycle
	Drain
	Transfer to spin drum and spin for 2 minutes

3.3.2 Optical Microscopy

An optical microscope (Leica DM1000, Leica Microsystems, Germany) was used to study the morphology of PMCs by either suspending them in water and placing a suspension droplet on a microscope slide and imaging, or imaging after water had evaporated.

To observe the PMCs deposited in fabrics or in any surface where they were likely to be buried, it was necessary to image via fluorescent light to create a contrast against the fabric fibres. A Laser light source was fitted to the microscope (Leica SFL4000, Leica Microsystems, Germany) and the samples were illuminated with light with a filter set to 470 nm, which allowed the fluorescent emission from the PM546 dye to be captured.

Alongside directly imaging the PMCs with the microscope, the microscope was also used in other means such as measuring micromanipulation probe diameters.

3.3.3 Transmission Electron Microscopy

Microcapsules have extremely thin shells and this rendered optical microscopy unsuitable for characterising the shell thickness, as the technique is limited by the size of the wavelength of natural light itself. For this reason, TEM was instead used to study cross sections of subjects of interest when a nanometer scale was required. The PMCs were embedded in a resin in accordance to the following procedure in order to create a dispersion of capsules with sufficient numbers to measure a wide variety of PMC diameters:

- 2 mL of PMC slurry was placed in an Eppendorf tube and centrifuged at 2000 rpm under centrifugal force for 1 minute. The supernatant was removed and 1.5 mL of 2.5% glutaraldehyde in phosphate buffer solution was added to retain shell integrity during resin preparation.

- The solution was kept in the fridge for 1 hour at 4°C before centrifugation at 2000 rpm for 1 minute was repeated to remove excess glutaraldehyde solution.
- Usually ethanol dehydration steps are then used to remove the water as this is immiscible with the resin. Ethanol was thought break down the PMC shell, so this step in TEM sample preparation was removed as the purpose was to observe the natural shell in any image.
- The PMCs were added to hydrophilic LR White acrylic resin (London resin Company Ltd., UK) and placed in a rotator (R2, Agar Scientific, UK) at 4 rpm for 2 days to ensure the capsules were well embedded.
- One drop of this resin/PMC mixture was added into a commercially available gelatin capsule (0.37 mL, 6 mm diameter, Agar Scientific, UK) along with pure LR white resin to provide a good template block for sectioning. The sealed gelatin capsule was then placed in an oven at 60°C for 12 hours to polymerise the resin.
- The gelatin capsule was removed leaving the polymerised resin block with capsules embedded. An ultramicrotome (Ultracut E, Reichert-Jung, Austria) was used to trim and section the resin block into ultrathin sections approximately 80 nm in thickness.

Following preparation of the PMC-embedded resins the ultrathin sections were imaged using a Jeol 1200EX Transmission Electron Microscope (Jeol UK Ltd, UK) at an acceleration voltage of 80 keV. For each sample 50 images were taken in order to get a good representation of the average shell thickness for the sample.

Once an image had been captured it was analysed in ImageJ (National Institute of Health, USA). Each PMC was divided into 8 equal segments and the shell thickness at each of these 8

intersections was measured to calculate the average shell thickness of a single PMC. This was necessary as although the outer wall was smooth, there was some fluctuation in the smoothness of the inner wall, causing some change in shell thickness.

Intuitively it is the case that PMCs embedded in the resin can be sliced into a cross section at any point from the equator to the edge. If sliced at the equator along radius, *r*, it is the actual shell thickness that is measured, but at any point either side the shell thickness is overestimated. Smith et al. (2000) were the first to try to model this to obtain the real thickness, but assumed equal probability of slicing at any angle between 0° and 90°.

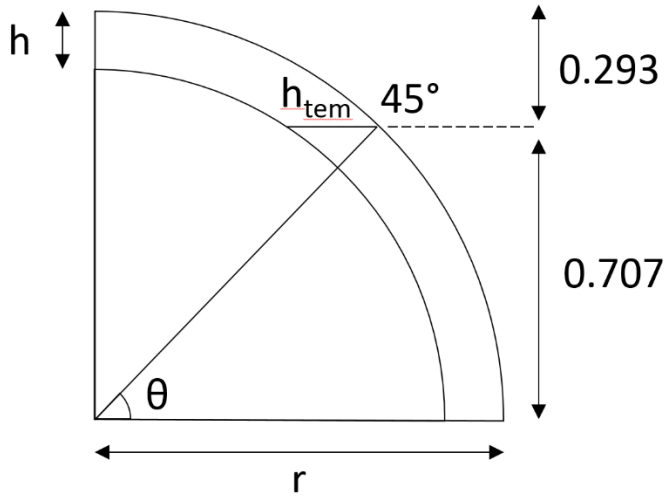

Figure 3.1: Visualisation of how the probability of slicing the PMC between 0°- 45° is much greater than 45°- 90° and how this will affect TEM measurement of real shell thickness

It can be seen in Figure 3.1 from choosing an angle of 45° from the equator of the capsule the projection length as a ratio of the radius is 0.707 for angles 0°- 45° and 0.293 for angles 45°- 90°, meaning the length over which a horizontal slice can be made is much greater for angles 0°- 45°. Mercadé-Prieto et al. (2011) considered slices at all positions, omitting those between 85-100% away from the equator as they were deemed unlikely and determined an average

correction factor of 0.86 to account for random cuts between 0 and 85% of the microcapsule radius.

3.3.4 Mastersizer

A Mastersizer 2000 (Malvern Instruments, UK) uses laser diffraction to measure the size of particles by passing a laser through a colloidal dispersion and measuring the intensity of the light that is scattered off the particles. It was used as a means of analysing the size distribution of a sample; understanding the average sizes as well as the breadth of the distribution. To do this the PMC slurry was diluted in DI water and then added to the sample dispersion unit to such an extent as to satisfy the obscurity levels and deliver the particles to the laser unit at the correct concentration.

3.3.5 Micromanipulation

Micromanipulation is a technique that was developed in the 1990's in the University of Birmingham (Zhang et al., 1991, Zhang et al., 1999). The benefits behind the machine are that it offers the capability of compressing single particles between parallel plates to elicit mechanical properties from well-defined force-displacement relationships. A schematic of the setup is displayed in Figure 3.2. It shows the microcapsule dried onto a glass plate and a cylindrical glass probe directly above the microcapsule. This intricate setup is relayed through a lens to a camera on a cathode ray technology (CRT) screen for clear visualisation. The glass plate is placed on a stage that can be moved in XY directions to move from capsule to capsule. The probe height is controlled by a stepper motor and can be manually adjusted or programmed

to travel a set distance at a set speed, compressing a capsule under parallel compression until rupture.

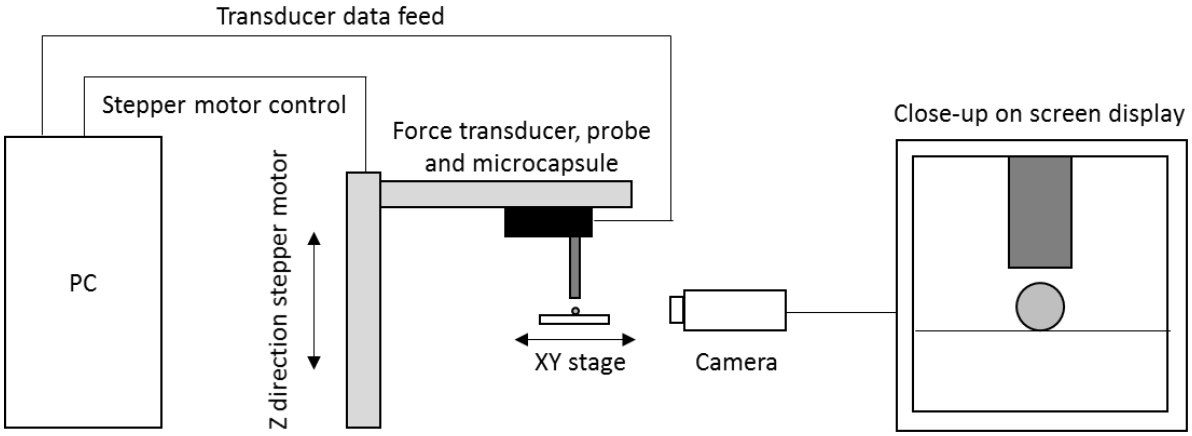

Figure 3.2: Schematic representation of the micromanipulation setup

A droplet of PMCs in slurry was placed onto a piece of glass and allowed to dry to leave PMCs resting on its surface. A force transducer with 5 mN sensitivity (403A, Aurora Scientific Inc., Canada) was fitted with cylindrical glass probe. The probe was positioned above the PMC and compressed at a set speed. Previous experiments reported in literature found that changing the speeds from 0.5 – 6 $\mu m.s^{-1}$ did not affect the mechanical response of the microcapsules, signalling the importance of elastic rather than viscous effects (Zhang, 2001). As the probe comes into contact with the PMC, the voltage change, recorded by the force transducer was converted to a force by using the inherent sensitivity of that particular transducer ($mN.V^{-1}$). From knowing the distance that the probe travels over time it was possible to calculate the speed and thus create a force vs displacement relationship. This was then used to investigate such mechanical properties as the nominal rupture stress and the deformation at rupture as well as intrinsic material properties of the PMCs such as the Young's modulus.

3.3.5.1 Preparation of flat probe for compression

A borosilicate glass capillary tube (1 mm outer diameter, 0.58 mm inner diameter, GC100-15, Harvard Apparatus Ltd, UK) was suspended vertically in a MicroForge MF-900 (Narishige, Japan) and heated at its midpoint whilst a weight was attached to the lower half. This caused the tube to break into two pieces, with sharp spikes that sealed new ends of now two tubes.

A piece of this glass tube was then secured vertically in an EG-40 micropipette grinder (Narishige, Japan) with the spike pointing down towards a sandpaper surface. It was then gradually lowered onto the rapidly rotating sandpaper to polish into a flat surface. The further the tube was lowered, the larger the diameter of the flat probe as more glass was polished. The probe could be removed at any point and viewed under a microscope to achieve the desired diameter of probe.

Glass probes were then attached to transducers vertically using the minimum amount of Araldite rapid epoxy resin (Huntsman Advanced Materials, Switzerland) on the glass tube which is itself attached perpendicular to the transducer cantilever within the casing.

3.3.5.2 Calibration of transducer sensitivity

The transducer manufacturer provides a number of different types of transducers with different levels of sensitivity. This is related to the strength of the cantilever beam within the transducer case that is attached to the probe. In this work the 5 mN transducer provided the greatest degree of sensitivity without risking damage to the transducer. The degree of deflection of the cantilever beam was directly related to the change in voltage. To relate the voltage change to the force, the sensitivity of the transducer was required ($mN.V^{-1}$). The manufacturer provides an estimate of the sensitivity, but an accurate calibration was required to ensure that the forces

calculated were precise. After removal of the outer casing of the transducer there was an output tube attached to the cantilever beam which provided a contact for attaching the glass probe. When calibrating the sensitivity of this tube, it was left exposed and small pieces of paper were added to an inverted transducer with an increasing mass of Blu-tack (Bostik, USA). The paper and Blu-Tack is weighed using a balance accurate to ± 0.001 g. To calculate the force applied to the transducer at each weight, F, the mass of the paper, m, was multiplied by the acceleration due to gravity, a (9.81 $m.s^{-2}$). When the force at each of the data points was plotted against the voltage, V, the gradient of the regression was the transducer sensitivity, K_s, according equation 3-1.

$$F = K_s V \qquad 3\text{-}1$$

3.3.5.3 Calibration of transducer compliance

The cantilever beam shows some degree of bending when a compressive force is applied through the beam. This can mean the true travelling distance of the probe may be slightly different to the recorded distance. This was corrected by calibrating the compliance of the transducer beam.

A glass cylindrical probe was fixed to the output tube as outline in Section 3.3.5.1, and the probe was moved down towards the glass plate. If there was no deflection in the cantilever beam the force would immediately reach maximum levels, however bending in the beam meant a linear relationship was observed for voltage vs sampling points, which corresponds to sampling time since the sample frequency had been set. The specifications for the transducer as reported by the manufacturer was 1 $\mu m.mN^{-1}$, but that figure was reported without the

compressive probe attached. The calibration of the compliance to account for this was carried out using the following equation:

$$C_{com} = \frac{v_s t_a}{\bar{m} K_s} \qquad 3\text{-}2$$

where C_{com} was the compliance of the transducer, v_s was the velocity of the probe movement, t_a was the sampling time from the onset of compression, $\bar{m}$ was the gradient of a positive straight line on a curve of voltage vs sampling time, as seen in Figure 3.3.

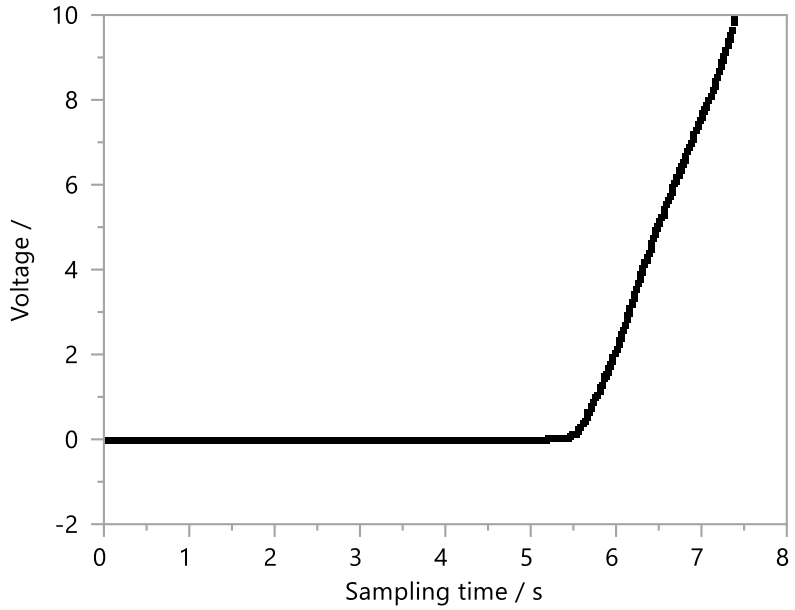

Figure 3.3: Voltage vs sampling time, plotted to find the gradient to calculate the compliance of a transducer and probe.

3.3.5.4 Calibration of probe speed

The speed of movement of the probe was calibrated using a micrometer that was placed alongside the probe and viewed through the camera attached to the microscope. The time taken to move a set distance at 2 µm.s^{-1} was recorded and it was found that at 10, 20, 40, 60 and 100 µm the speed matched the 2 µm.s^{-1} speed requirements.

3.3.5.5 Compression of PMCs in an environmental chamber

It was of interest to study how the exterior environment around the PMCs affected the mechanical properties; rupture and elastic. A custom environmental chamber was commissioned by Longshore Engineering (UK), in order to pre-condition PMCs in a set temperature and humidity environment.

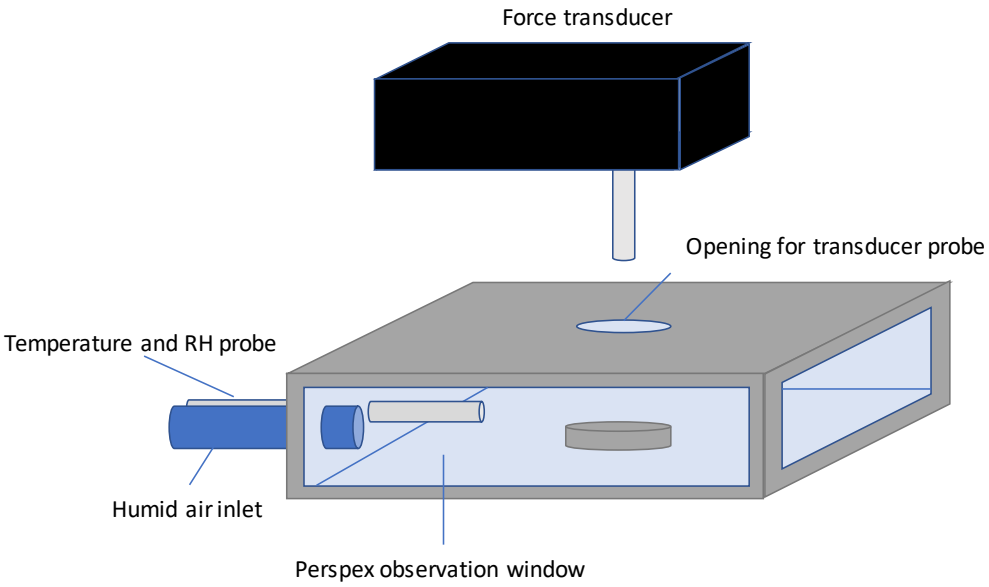

Figure 3.4: Schematic of the environmental chamber for the micromanipulation rig

The chamber fitted around the existing micromanipulation setup, allowing normal experimental procedures to be completed. The chamber consisted of a steel rectangular frame with a stage for the PMC samples in the centre. Perspex windows allowed for observation of the samples during compression and a small spherical orifice above the stage allowed for entry of the probe into the chamber without compromising the environmental conditions. A temperature and humidity probe (Hygropalm 21, Omni Instruments, UK) was inserted into the chamber to provide accurate measurement and control. A gas vapour humidity generator splits air through a water reservoir and a dry flow at different ratios to reach the desired humidity. The time

needed to equilibrate under a set atmospheric environment was found from dynamic vapour sorption experiments as outlined in Chapter 4.

3.3.6 Thermogravimetric analysis

The thermal stability of the PMC shell can be attributed to the degree of crosslinking in the polymeric material and this in turn potentially has the ability to change the mechanical properties of the microcapsules (McFarland and Pojman, 2015).

Thermogravimetric analysis (TGA) measures the mass loss as a sample is exposed to increasing temperatures. A microbalance is situated in a furnace and itself is thermally isolated with an inert atmosphere of nitrogen in this case. The mass loss occurs due to materials within the sample approaching and exceeding temperatures of combustion or evaporation. By plotting the differential of the TGA signal it was also possible to assess the rate of change of mass in the sample. In this project, microcapsule slurries were analysed via TGA to identify the inherent thermal properties of each component and to distinguish any thermal differences between samples.

By looking at the sequential mass loss as the temperature was increased it was possible to identify the individual components of the sample through a combination of this temperature and the percentage mass of this component in the whole sample. Three PMC samples that showed markedly different mechanical properties were chosen for TGA analysis. The machine used was a TA Instruments Discovery (TA Instruments, USA). Aluminium pans were used and the sample was equilibrated at 25°C and kept at isothermal conditions for two minutes. The sample was then heated to 500°C at a heating rate of 5°C min^{-1}.

3.3.7 Spectrofluorometry

In the synthesis of the PMCs the fluorescent dye Pyrromethene 546 (Exciton, US) was added to the core oil at 500 ppm prior to shell polymerisation. This fluorescent dye then acted as a potential marker to quantify PMCs visually through fluorescence microscopy or by measuring the fluorescence intensity coming from a solution containing the dye, allowing for potential bulk quantification of free dye in solution. In this work spectrofluorometry was used to measure fluorescence intensity in two solvents, used in the dye extraction techniques mentioned in Chapter 5, measuring fluorescence intensity in ethanol, and fluorescent intensity in hexane via a spectrofluorometer.

The principle of spectrofluorometry is to use the characteristics of the fluorophore to quantify the marker in solution. Each fluorophore is excited at a specific wavelength, absorbing photons to change the electronic state of the fluorophore. The fluorophore then undergoes an electronic state change and light emitted is of a longer wavelength and this transition is known as the Stoke's Shift, most commonly observed in fluorescent materials.

In literature, the maximum absorbance wavelength of PM546 in methanol has been reported as 493.5 nm and the respective maximum fluorescence wavelength is 505 nm (Chung et al., 2016). The Stoke's Shift of 11.5 nm is a relatively small gap for a fluorophore, so a wavelength cut-off filter helps to reduce the interference of the excited light on the detection of the emitted light.

The spectrofluorimeter used was a Spectramax M2e microplate reader (Molecular Devices, USA), which is primarily used in biochemical studies. The benefits for these experiments were that the spectrofluorimeter had separate tuneable monochromators so could scan the excitation and emission wavelength separately. The equipment also had a cut-off filter included. The light

source was a high-powered Xenon flash lamp and experiments were conducted to find the fluorescence endpoint maximum.

Taking into consideration the small Stokes shift in methanol, full excitation and emission scan experiments were conducted with PM546 in ethanol and hexane to tailor the instrument parameters to the fluorophore to maximise the fluorescence signal.

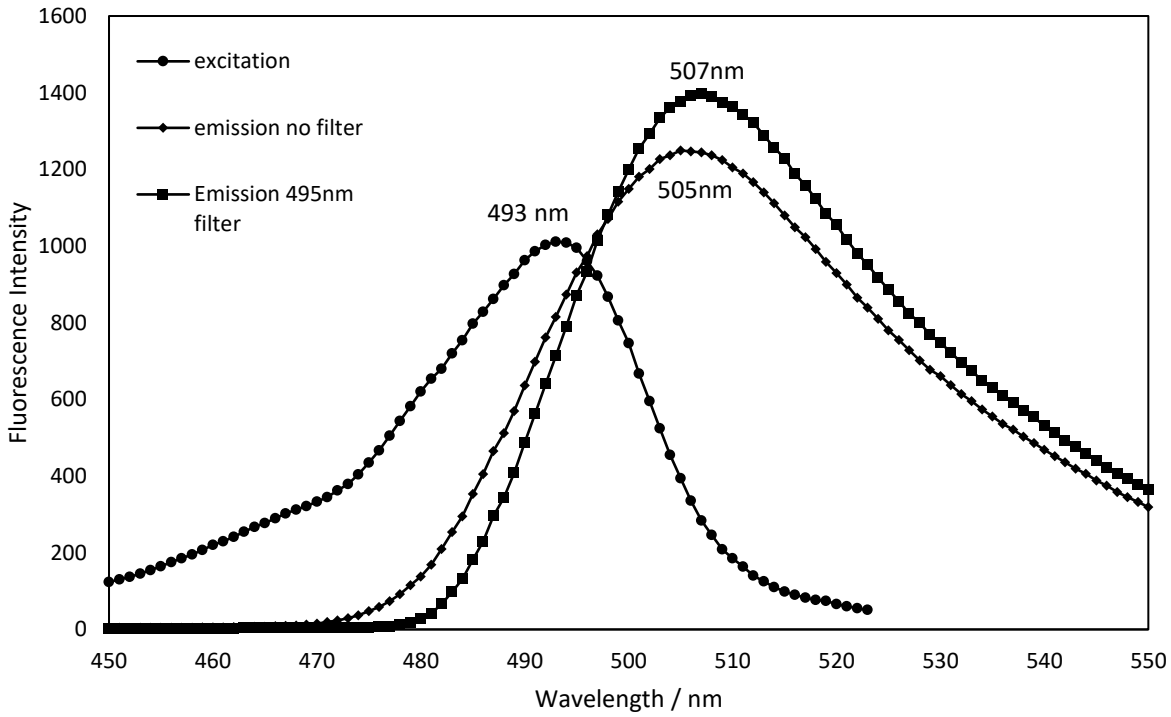

Figure 3.5: Fluorescence spectra of PM546 in ethanol - full excitation scan, emission scan and emission scan with a 495 nm filter

The full excitation scan in ethanol, displayed in Figure 3.5 showed that the maximum absorbance occurred at 493 nm. The full emission scan with no filter showed the maximum fluorescence signal at 505 nm. The gap in these wavelengths allowed for the inclusion of a cut-off filter at 495 nm. This subsequently increased the fluorescence intensity and slightly shifted the maximum wavelength to 507 nm, which more accurately determined the wavelength of

fluorescence emission maximum. Wavelengths of 493 nm and 507 nm generated the maximum intensity responses, however for the experiments, an excitation scan wavelength of 488 nm was chosen as the optimum excitation wavelength, as this minimised the overlap of the excitation and emission spectra whilst still maintaining good absorbance and fluorescence signals.

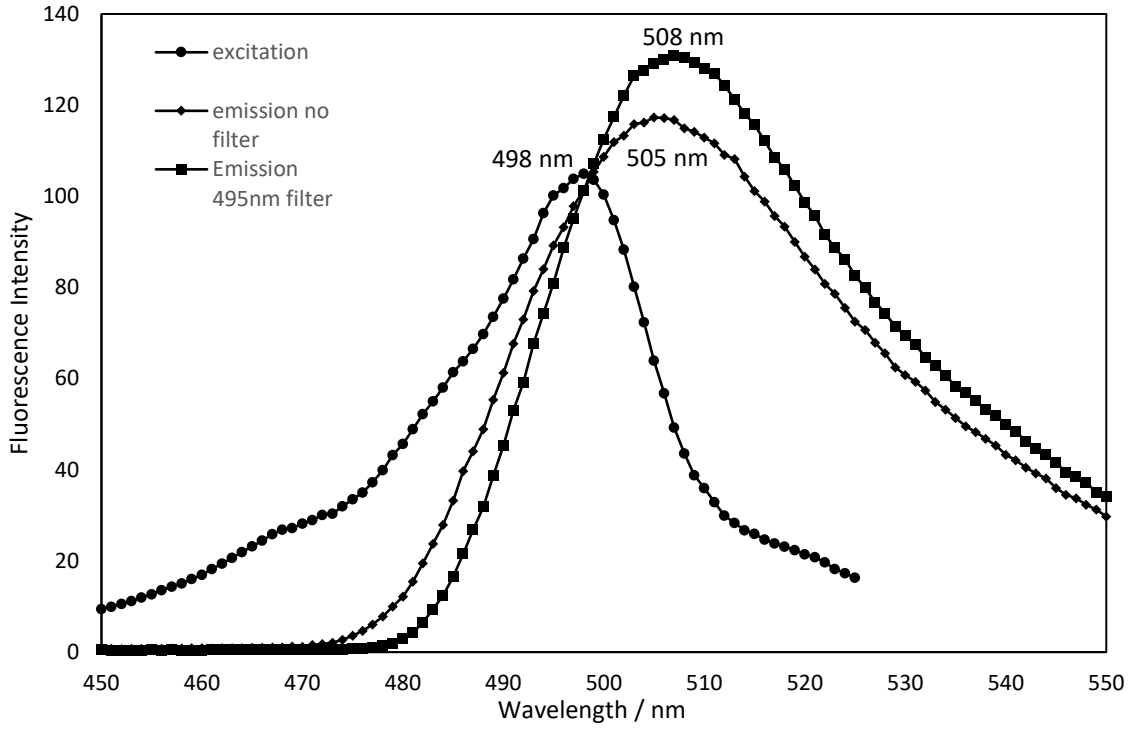

Figure 3.6: Fluorescence spectra of PM546 in hexane - full excitation scan, emission scan and emission scan with a 495 nm filter

The same protocol was undertaken for hexane as the solvent in place of ethanol, as seen in Figure 3.6. In this case the maximum excitation signal occurred at 498 nm, the maximum fluorescence intensity in the emission scan with no filter occurred at 505 nm and when a 495 nm filter was applied the maximum fluorescence intensity occurred at 508 nm. To optimise the wavelength pairs by minimising interference between excitation and emission scans and

enabling the use of a filter the excitation wavelength was chosen to be 493 nm and the emission wavelength 508 nm and a wavelength filter at 495 nm.

3.3.8 Headspace GC-MS Analysis

Alongside PM546 as a potential marker for PMC quantification, the inherent perfume in PMCs provided a consistent chemical fingerprint that could be identified and quantified using headspace gas chromatography-mass spectrometry (GC-MS) analysis.

In the case of perfume, normal GC injection will contain the perfume itself, along with water, alcohol and other ingredients. The chromatogram produced will contain many unwanted peaks, and has the potential to mask the peaks of interest. In headspace GC-MS, when a vial of sealed sample is heated, the more volatile molecules start to partition in the gas phase, until an equilibrium is reached with the liquid phase. The less volatile compounds that are not of interest remain in solution. A solid-phase microextraction (SPME) fiber is inserted into the sealed vial via a septum. The fiber is often coated with a polymeric film such as polydimethylsiloxane (PDMS) to promote adsorption of analytes from the gas phase, or additionally, adsorbent particles such as divinylbenzene (DVB) or carboxen are bound to the surface with PDMS. When adsorbent particles are used the adsorption is more efficient, meaning suitability to lower concentrations.

Figure 3.7 shows an example of sample in a headspace vial. In a sealed environment, volatile components diffuse into the gas phase until an equilibrium is reached with the liquid phase and it is the partition coefficient, K, that governs the concentration of an analyte in the gas phase and the relationship is highlighted Equation 3-3:

$$K = \frac{C_s}{C_g} \quad 3\text{-}3$$

where C_s is the concentration of analyte in the sample phase, and C_g is the concentration of the analyte in the gas phase. Lower values of K are observed in more volatile compounds and this is desirable in headspace analysis when separating them out from non-volatile unwanted contaminants.

In SPME analysis, the coated fiber becomes a third phase in the system in Equation 3-4:

$$C_0V_s = C_fV_f + C_hV_h + C_sV_s \quad 3\text{-}4$$

Where C_0 is the initial concentration of analyte in sample, C_f,C_h, and C_s are the concentrations of the analyte on the fiber, in the headspace and in the sample respectively and V_f , V_h and V_s are the volumes of the fiber, headspace and sample respectively (Parkinson et al., 2016). In a SMPE headspace extraction the fiber/headspace partition coefficient is $K_{fh} = C_f/C_h$ and the gas/sample partition coefficient is $K_{hs} = C_h/C_s$, the mass of analytes adsorbed by the coating at the surface in moles, n, is shown in Equation 3-5:

$$n = \frac{K_{fh}K_{hs}V_fC_0V_s}{K_{fh}K_{hs}V_f + K_{hs}V_h + V_s} \quad 3\text{-}5$$

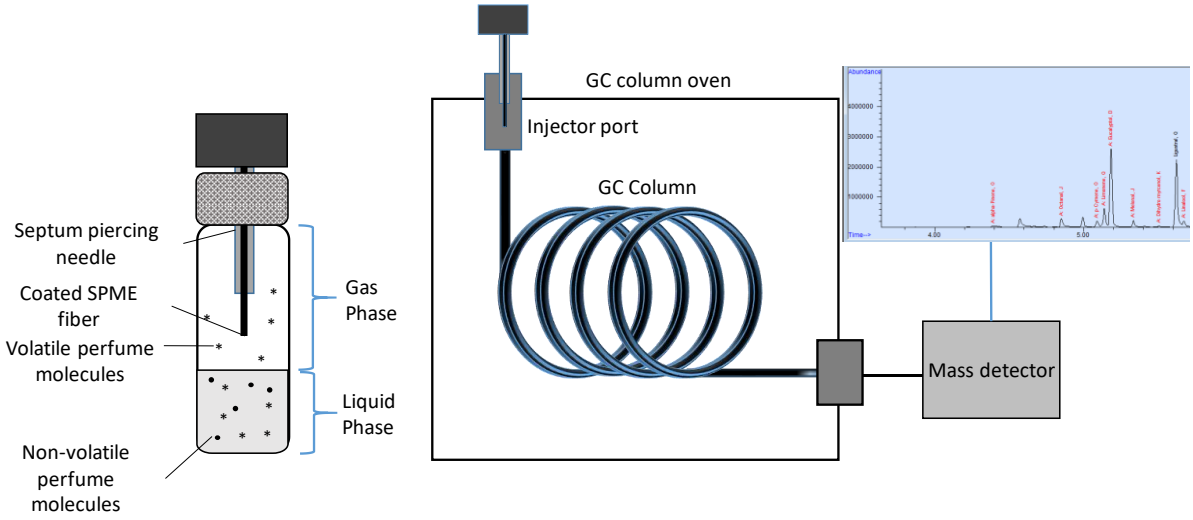

Figure 3.7: Schematic of SPME fiber equilibration in sample headspace vial and of the headspace GC-MS system

P&G have developed a 'fast headspace' setup at the Newcastle Innovation Centre whereby the software identifies and labels the individual perfume raw materials (PRMs) based on the elucidation time as temperature is increased. Two specific programmes were used; one for quantification of free perfume oil on the surface of the fabric, i.e. from broken PMCs (setup 1), and another for quantifying the perfume oil present in washwater samples from broken PMCs (setup 2), details of which are shown in Table 3.3.

Each sample was prepared in 20 mL glass headspace vials with magnetic screw caps, with 18 mm thread with PTFE/ silicone septum (Supelco, USA). The GC system was an Agilent HP 6890 (Agilent, USA) with a splitless injection system. An Agilent 5973 MSD mass selective detector (Agilent, USA) was attached to complete the GC-MS system. A Gerstel multipurpose sampler (Gerstel, USA) with solid phase microextraction (SPME) and agitator was also attached to automate sampling for up to 100 vials.

Table 3.3: Setup parameters for headspace GC-MS analysis for quantifying perfume oil

Sample volume	1 mL
Vial volume	20 mL
SPME fiber	100 µm PDMS (Setup 2) or 50/30 µm DVB/Carboxen/ PDMS coating (Setup 1)
Extraction temperature and time	40°C for 5 minutes (Setup 2), 65°C for 5 minutes (Setup 1)
Desorption temperature and time	270°C for 3 minutes
Fiber cleaning	Heated inlet, 270°C, 5 minutes between samples, 30 minutes pre-run bakeout
GC Column	J&W 122-5532 DB-5ms (30 m x 250 µm i.d x 0.25 µm film thickness)
Carrier gas	Helium (14.5 psi), 44.4 $mL.min^{-1}$ (inlet), 1.8 $mL.min^{-1}$ (GC column)
Injector	T = 270°C, splitless
Oven programme	40°C initial Heat 17°C per minute to 270°C
MS conditions	Range *m/z* 35-300

The extraction time was chosen to be 5 minutes, which, on the advice of technicians was known to have equilibrated sample liquid and headspace for the samples of interest under the volumes chosen. A volume of 1 mL of sample was selected for each headspace vial, because, at this volume, there was an adequate headspace response above the noise levels of the apparatus, the availability of sample was plentiful and also there was sufficient headspace volume for the SPME fiber above the solution in the 20 mL vials.

3.3.9 Dynamic Vapour Sorption

Moisture sorption isotherms of the PMCs were measured by Dynamic Vapour Sorption (DVS) (Q5000, TA Instruments, USA). The purpose of this work was to understand the kinetics behind moisture sorption that could be applied to the experimental setup for micromanipulation under temperature and humidity control, to ensure that under compression the PMCs had equilibrated within their environment. In this technique dry nitrogen was used as the carrier gas. A portion

of this gas is passed over a water reservoir, saturating the nitrogen with water vapour. By controlling the mass flow of a combination of dry nitrogen gas and nitrogen saturated with water vapour it is possible to control the relative humidity of the flow of gas into the sample chambers. The technique uses gravimetric analysis to measure the moisture content change in the sample. Two ultra-sensitive microbalances are used; one containing the sample of interest, and one as a reference balance. 0.17 mg of reference PMC slurry was added to the sample microbalance and allowed to equilibrate at 20% relative humidity (RH). Once equilibrated at a baseline the RH was cycled between a 20% baseline and 70%, 80% and 90%, measuring the sorption isotherm after a change is made. In each case the RH remained constant until the change in mass of the sample was less than 5 µg over a 10 minute period, which signalled that moisture sorption equilibrium had been reached, and the RH then continued to cycle.

3.3.9.1 Friction studies using Mini traction machine tribometer

The mini traction machine 2 (PCS Instruments, United Kingdom) is a commercially available tribometer, predominantly used in assessing the performance of lubricants such as engine oils. It can also assess the frictional properties of non-lubricated contact between surfaces. A ball (3/4 inches diameter) is fixed to an upper holder and a disk (46 mm diameter). The ball is descended and brought into contact with the disk at which point several sensors can monitor the normal load applied to the disk by the ball and the friction force as relative movement between the ball and the disk is introduced. This can come from simultaneous concurrent rotations to initiate rolling (slide to roll ratio (SRR) 0%), or it can result from the disk rotating, but the ball remaining angularly stationary, creating a sliding motion (SRR 200%). Additional

functionality allows a bath to be filled with water or lubricant for alternative setups and additional sensors can measure the electrical contact resistance and the wear between the substrates.

The normal load, F_n, is related to the dynamic frictional force, F_k, in equation 3-6:

$$F_k = \mu_k F_n \qquad 3\text{-}6$$

where μ_k represents the coefficient of kinetic friction. In theory the equation is independent of the speed of movement in contact. There is also the case of static friction, denoted by F_{max}, which is the force that is needed to be overcome to get relative motion between the substrates to occur.

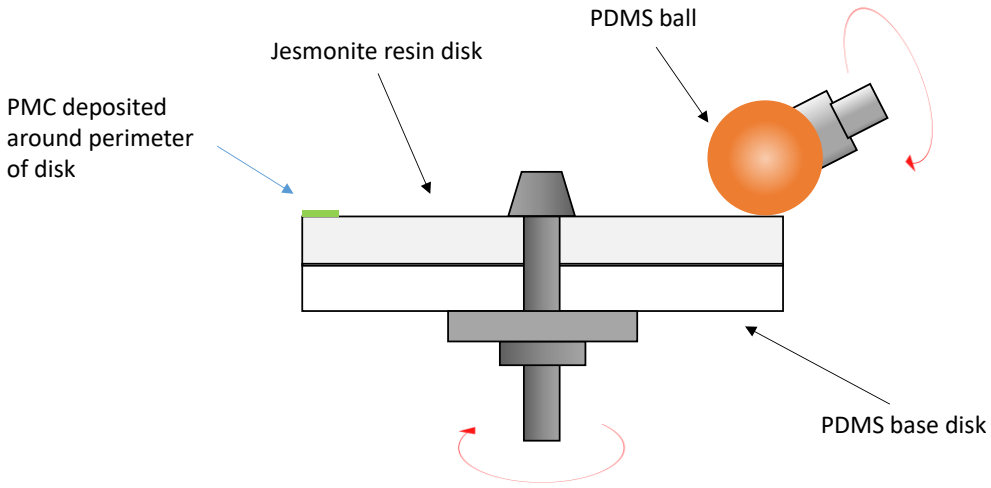

Figure 3.8: Schematic of the MTM2 tribometer with Jesmonite disk and PDMS ball

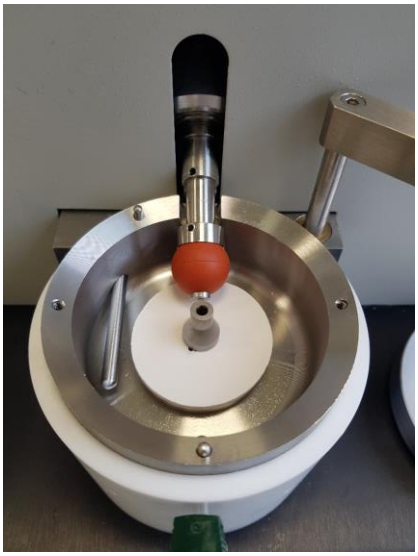

Figure 3.9: Image of setup surrounded by a bath capable of performing tribological measurements in solution

There are other methods to assess the frictional properties of two surfaces in contact such as reciprocating tribometers and texture analysers with friction attachments. These were trialled as a means of studying the impact of friction on the rupture properties of PMCs, but uncertainty and variation in localised contact stresses triggered the need to use the MTM2 as a technique for addressing this problem.

The main benefit of the MTM2 with respect to other techniques for this work was the well-defined contact region between sphere and surface. The spherical geometry on an elastic half space meant that for compression at least, the Hertz contact theory is applicable. The theory takes into consideration the slight deformation of two elastic surfaces in contact and relates the contact stress to the normal load, radii of curvature of the surfaces and modulus of elasticity for the surfaces.

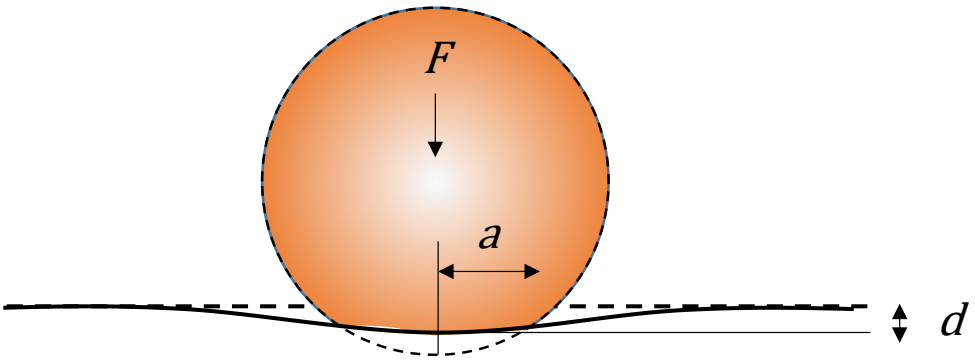

Figure 3.10: Schematic of Hertzian contact between a sphere and elastic half space. F is the normal load applied, a is the radius of the contact area and d is the displacement of the flat surface

Hertz introduced a theory of contact between elastic bodies in 1882 (Hertz, 1882). To find the deformation of the surface, the contact area and the resultant contact pressure that results from applying a normal load, the combined Young's modulus of the two surfaces, E^* is needed:

$$\frac{1}{E^*} = \frac{1-{\nu_1}^2}{E_1} + \frac{1-{\nu_2}^2}{E_2} \qquad 3\text{-}7$$

Where E_1 and E_2 are the Young's modulus of each surface, and ν is the Poisson's ratio of that surface. Using this equation it is then possible to calculate the deformation of the surface from Equation 3-8:

$$F_n = \frac{4}{3} E^* R^{\frac{1}{2}} d^{\frac{3}{2}} \qquad 3\text{-}8$$

where F_n is the normal load applied, R is the radius of the elastic sphere, and d is the displacement of the surface. Geometrically this displacement is related to the contact area radius, a, through equation 3-9:

$$a = \sqrt{Rd} \tag{3-9}$$

The maximum contact pressure, p_0, at the centre of the spherical contact with the flat surface is given by Equation 3-10:

$$p_0 = \frac{3FR}{4E^*} \tag{3-10}$$

And the distribution of the contact pressure, $p(r)$, as a function of the radial distance from the centre of contact is given by Equation 3-11:

$$p(r) = p_0\left(1 - \frac{R^2}{a^2}\right)^{1/2} \tag{3-11}$$

The assumptions in Hertzian theory of non-adhesive elastic contact are that the strains are small and within the elastic limit, that each body can be considered an elastic half-space, the surfaces are continuous and non-conforming, and the bodies are in frictionless contact. Once the disk on the MTM starts to rotate, the Hertzian contact stress relationship falls down.

The parameters for the friction experiments on the MTM2 were that a PDMS ball was fixed with no rotation (SRR 200%) in order to focus on static and dynamic friction rather than rolling friction, considering the likely modes of friction of entrapped PMCs in the wash. The normal load applied to the disk ranged from 1 N to 5 N, depending on test conditions, and the rotational speed of the disk was 1 – 2 $\mu m.s^{-1}$, depending on test conditions. In certain instances, water was added to the chamber and samples allowed to equilibrate for 10 minutes prior to running a sample. Taking into consideration the circumference of the sample the protocols either ran for

30 seconds for one complete rotation, or multiples of 30 to increase the number of complete rotations.

3.3.10 Texture analyser

The MTM2 tribometer does not have the ability to apply a normal load without applying lateral movement without removing safety features of the machine. The texture analyser is a versatile material tester with numerous physical attachments to characterise a variety of properties such as hardness and tensile strength, and it is commonly used in the food and pharmaceutical industries. In the standard vertical configuration it can compress a material at speeds up to 40 $mm.s^{-1}$. The apparatus was used to apply a normal load on Jesmonite resin to compare levels of PMC breakage under a combination of friction and normal load as tested by the MTM2. The PDMS spherical ball was retained from the MTM experiments. The texture analyser was fitted with a 500 N load cell, capable of sensitivity on ± 0.1 N.

Chapter 4. INVESTIGATION OF THE MECHANICAL PROPERTIES OF POLYACRYLATE PMCs BY DIAMETRIC COMPRESSION

In this chapter PMC samples were characterised to understand how each sample provided by P&G behaved differently when studied under diametric compression. To study the morphology of the structures, SEM and optical microscopy were used, the latter in both light field and fluorescence modes. TEM was used to identify the average shell thickness of the samples and laser diffraction was used to determine the size distribution of PMCs in each sample. The data, along with some fundamental sample information provided by the manufacturer showed the effect that changing certain processing conditions had on the structural and physico-chemical properties of the PMCs. Micromanipulation was performed on the samples, compressing single PMCs until rupture. Force-displacement curves yielded data on the rupture force, nominal rupture stress, nominal wall tension, deformation at rupture, and elastic limits of the PMCs. An application of an existing method to calculate the Young's modulus of the shell material of the PMCs was modified for the PAC PMCs. Micromanipulation experiments were also performed in alternate humidity conditions to understand the environmental influence on mechanical properties; something which is extremely important for where there is such variety between the humidity in the washing machine to that when the PMCs are embedded in dry fabrics.

4.1 Processing conditions of PMC sample and rudimentary information from P&G

Whilst information regarding the specific details of the synthesis conditions of the PMCs was withheld from the researcher, public information for the microcapsules is disclosed in multiple patents (Appivon Inc, 2014, Procter & Gamble, 2017a) where it is stated that the PMCs were likely formed through suspension polymerisation, judging by the list of ingredients and synthesis methods.

Fragrance oil and isopropyl myristate (IPM) were added with azo initiators to a 35°C temperature-controlled steel jacketed reactor and mixed at 100 rpm under a nitrogen blanket (100 $mL.min^{-1}$). Over 45 minutes the temperature was heated to 75°C, held at 75°C for 45 minutes and then lowered to 60°C for 75 minutes. The monomers were then added, and in the example in the patents these were tertiarybutylaminoethyl methacrylate, 2-carboxyethyl acrylate, and Sartomer CN975 along with more fragrance oil. Water and colloid 351, a droplet stabiliser, were then added as the continuous phase. Mixing was started at 2500 rpm for 60 minutes to effectively emulsify the oil droplets in water, at which point mixing was continued at 350 rpm at 60°C for 45 minutes before the temperature was raised to 75°C for 4 hours to activate the initiators and begin the polymerisation of monomers. The system was then heated to 90°C and held there for 8 hours to complete the reaction before cooling to room temperature.

4.2 Morphology of Polyacrylate PMCs

The morphology of the PMC samples was observed using an optical microscope in light field mode. The PAC PMC shell is hydrophilic, so once the slurry was added to water it was

immediately dispersed and individual PMCs did not aggregate. This was the case in aqueous solution, however, when allowed to dry on a glass slide the microcapsules did show some aggregation.

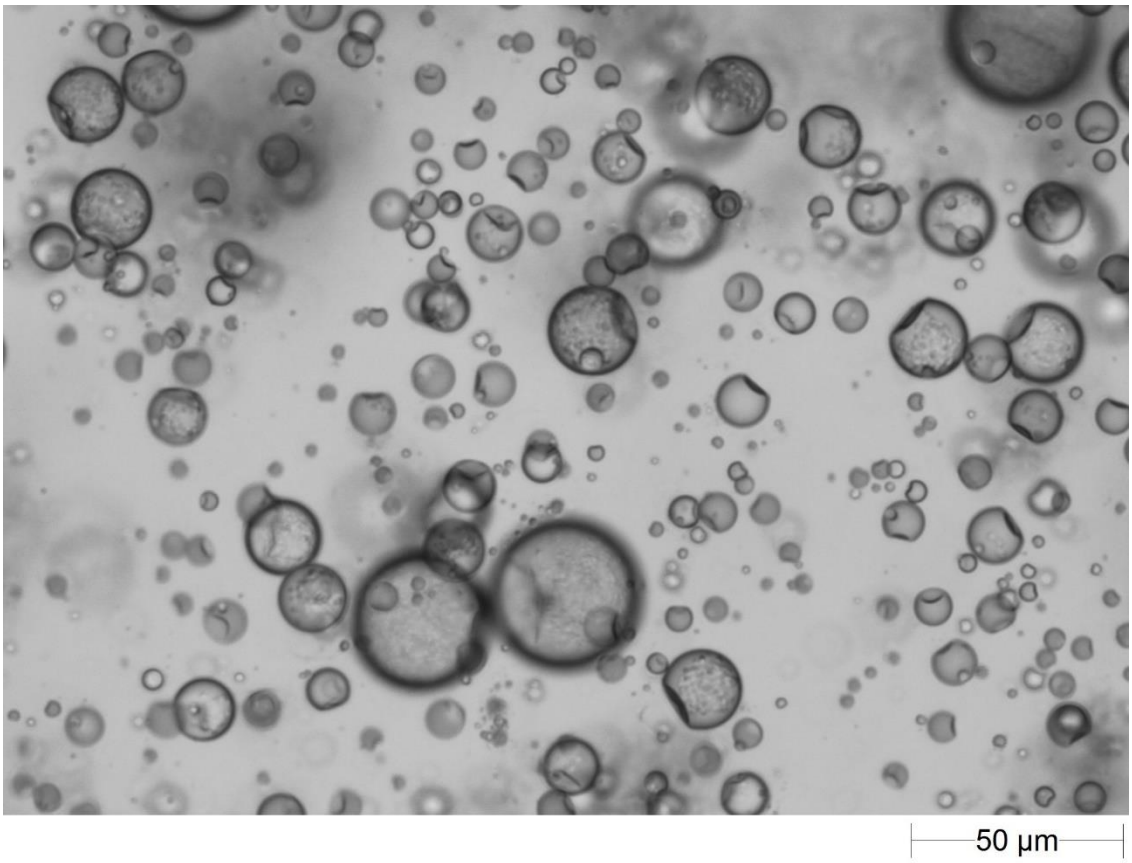

Figure 4.1: Optical Microscopy image of Polyacrylate PMC morphology in the reference sample

As is seen in Figure 4.1, the PMCs were generally spherical, however a ‘Soft spot’ or crater in the capsule sphere was often seen in capsules of all sizes.

4.2.1 Formation of the ‘soft spot’ in the PMC morphology

The PMCs in this project were formed from suspension polymerisation, a summary of which is seen in patents from P&G (Appivon Inc, 2014, Procter & Gamble, 2017a). In this technique, droplets of monomers, initiators, perfume and IPM are created and stabilizers are used to sterically stabilize them within an aqueous solution. Once the droplets have been formed the vessel is heated, causing the droplets to expand in volume. At a certain temperature the initiators will begin the polymerisation of the monomer molecules which will eventually precipitate out and form a shell at the droplet interface. This occurs at a larger surface area than if the solution had not been heated. Once the polymerisation has run to completion, the solution containing the now encapsulated organic material is cooled, creating free volume in the interior of the PMC. The free volume within the PMC creates a hydrostatic pressure mismatch between the capsule interior and exterior continuous phase and at the critical pressure this can cause the shell to collapse on itself. If, however, the critical pressure is not reached and if the shell is impermeable to osmotic effects, as is the case with these polyacrylate PMCs, the capsule remains intact with a finite indentation as the incompressible fluid core prevents any further buckling into a sickle cell shape. (Knoche and Kierfeld, 2014). This process causes a ‘soft spot’ in the PMC shell. This circular inhomogeneity in the shell material can cause a ‘snap through’ of the shell material in this region as hydrostatic pressure relative to the core is increased (Paulose and Nelson, 2013). In literature this has been seen in the synthesis of microcapsules with a methylmethacrylate-based copolymer shell where the lower contraction coefficient of the shell causes a dimple to form, though the appearance of the dimple was abated in more crosslinked samples (Qiu et al., 2012).

4.3 Size Distribution of PMC samples

The size distribution for each sample was recorded using a Malvern 2000 laser diffraction particle size analyser. The specific details on how the sample size distributions were controlled during PMC synthesis was proprietary information to the supplier for P&G and therefore not available to the researcher, however in the literature, as highlighted herein, there are many ways in which to gain control over size distribution by changing the chemistry of the polymerisation reaction and by controlling the physical processing conditions of the microcapsule synthesis.

Table 4.1: Size distribution of all PMC samples received from P&G

Sample Information (highlighting differences from reference)	D_{10} / µm	D_{50} / µm	D_{90} / µm	Span
Reference	6.90	18.22	30.42	1.28
95/5 core/shell ratio	7.57	19.32	28.46	1.08
95/5 core/shell ratio and lower median size	6.12	12.79	20.06	1.09
20% IPM	10.48	25.76	37.00	1.03
Lower median size	5.82	12.17	20.06	1.17
Cationic PMCs	9.56	20.21	31.04	1.06
Lower curing temperature (75°C)	8.01	19.83	28.26	1.02

In large vessels, like those used to produce the PMCs for this project, the suspensions are often exposed to turbulent conditions. When this turbulence is isotropic and the liquid droplets exceed the Kolmogorov length, break up of droplets will occur. The diameter of the droplets can be calculated by the following equation:

$$\frac{d_{32}}{L} = a(1 + b\emptyset)We^{-0.6} \qquad 4\text{-}1$$

where d_{32} is the Sauter mean droplet diameter, $\emptyset$ is the volume fraction of the dispersed phase, L is the impeller diameter and a and b are constants (Shinnar, 1961). The Weber number, We, describes the ratio between deforming inertial forces and the stabilising cohesive forces, so

therefore provides insight into the likelihood of droplet breakup. It is described by the following equation:

$$We = \frac{\rho u^2 L}{\sigma} \qquad 4\text{-}2$$

where ρ is the density of the dispersed phase, u is the linear speed of the impeller and σ is the interfacial tension between the dispersed and continuous phases. The droplet size results from balance between turbulent kinetic energy acting on the surface of droplets trying to break them up, and interfacial tension and internal viscosity trying to promote coalescence. If the dynamic turbulent forces exceed the interfacial tension forces the droplets will break up, whereas droplets will coalesce if the opposite is observed.

The relevance of the equations was apparent in the sample where a lower median size was achieved with no chemical alterations. In this case a change in the energy supplied to the system was the most likely cause of change in size distribution. As seen in Equations 4-1 and 4-2, increasing the impeller speed would decrease the droplet size, leading to the formation of smaller PMCs up to a critical stirring rate, giving an asymptotic look to the relationship, where at a certain point. any further increase in turbulence kinetic energy is unable to break up and droplets due to the presence of attractive forces immediately causing coalescence (Alexandridou and Kiparissides, 1994). To obtain a lower median size PAC PMC sample, an increase in impeller speed was thought to be the root cause. Similar results have also been observed in various studies of suspension polymerisation of microcapsules (Gonçalves et al., 2011, Cordoví et al., 1997).

It was seen that the sample with a core containing 20% isopropyl myristate compared to 45% in all other samples the average size of PMCs in the sample increased. IPM has a viscosity of

4.8 cP at 25°C, whereas the majority of all perfume ingredients have a viscosity close to 1 cP at 25°C. A higher internal phase viscosity, with a greater loading of IPM in the core should have given the droplets a greater resistance to breakage, meaning the formation of larger droplets, but the opposite was observed. Alternatively, a higher loading of IPM may have had the effect of increasing the interfacial tension, promoting droplet coalescence and increasing average size of the droplets. If neither of these explanations suffice then it may have been possible that processing parameters for the two samples might not have been consistent (Alexandridou and Kiparissides, 1994).

Because of a combination of chemical and physical factors in the remaining samples, it was difficult to assess why the size distribution changed as it did, but the characterisation of such a parameter was useful to understand the importance of subsequent mechanical analysis over the whole sample.

4.4 Shell Thickness of PMC Samples

The shell thickness was measured by looking at cross sections of ultrathin sections of PMCs, prepared in accordance to the method described in Chapter 3. In each sample 50 random PMC cross sections within the resin were imaged. For each PMC the image was divided into 8 segments from the centre anchor point of the microcapsules and the shell thickness at the intersection of each segment was measured, giving 8 results per PMC image. The average of these 8 segments and the subsequent average over the 50 PMC population was taken. A correction factor of 0.86, calculated from work done by Mercadé-Prieto et al. (2011), was applied to account for the probability of not slicing each microcapsule through its equator to give the actual mean shell thickness for that particular PMC sample.

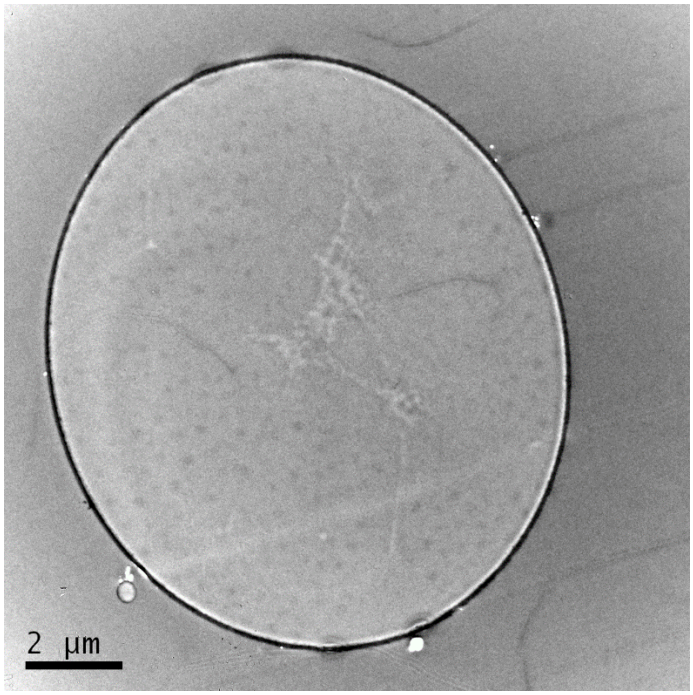

Figure 4.2: TEM image of a PMC, shell thickness 89 ± 5 nm and capsule diameter 11.4 µm

It was rare to observe a completely spherical PMC in the TEM images. As such, instead of taking the diameter of the PMC from an arbitrary angle in the image, the area of the PMC was found using image analysis and from reforming the area as a perfect circle, the diameter was found from this information. The purpose of finding out the diameter of each PMC was to investigate whether there was any variation in shell thickness with PMC size within the same sample. If there was not any variation in this, then the mean thickness for the whole sample stands true, without showing any weighting for diameter. The results of the PMC thickness analysis are seen for all samples in Table 4.2:

Table 4.2: Summary of mean shell thicknesses for each of the PMC samples. The standard error of the mean is shown from 50 PMC measurements

Sample Information	Mean Shell Thickness / nm
Reference	104 ± 1
95/5 Core/Shell Ratio	84 ± 1
95/5 Core/Shell Ratio and Lower Median Size	94 ± 1
20% IPM	134 ± 2
Lower Median Size	86 ± 1
Lower curing temperature	108 ± 1

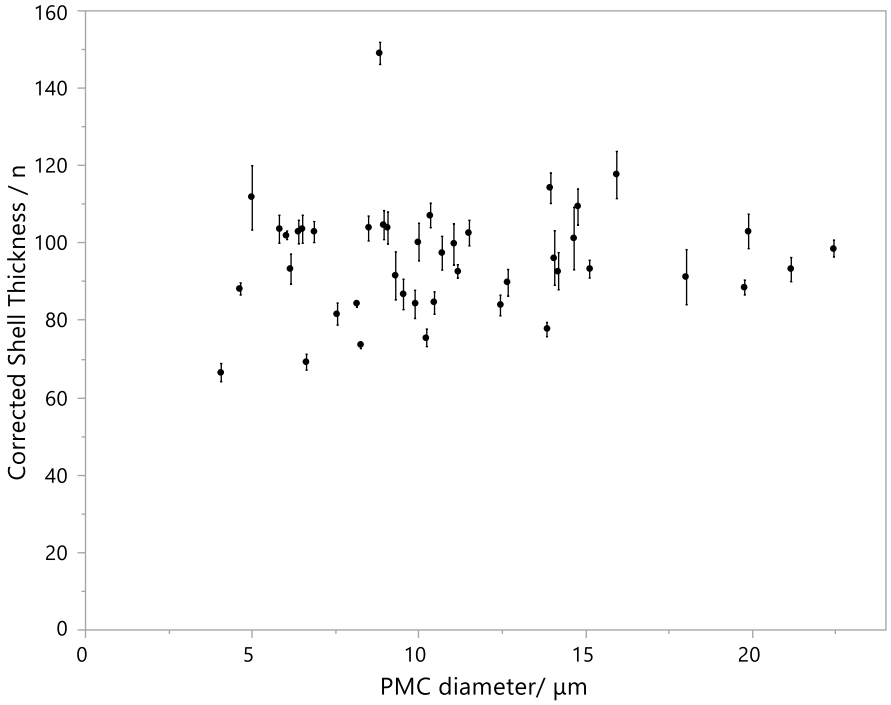

Figure 4.3: Relationship between corrected shell thickness and diameter of PMCs for the 95/5 core/shell ratio with lower median size sample. Error bars are standard error of the mean from 8 shell thickness measurements on each PMC

A similar trend of constant shell thickness with microcapsule diameter was observed in the work of Jiao et al. in forming microspheres of polymerized methyl methacrylate and methyl acrylate (Jiao et al., 2018).

The samples with 95/5 core shell ratio compared to the 90/10 standard core/shell ratio showed lower average shell thickness. In these samples there was a lower concentration of reactive shell forming monomers. This reduced the amount of shell forming material present in the oil phase, leading to a thinner shell.

The largest influence on the shell thickness was caused by changing the IPM inclusion level from 45% to 20%, which had the effect of increasing the mean shell thickness from 104 ± 1 µm to 134 ± 2 µm. IPM is included as a partitioning modifier to improve the solubility of the perfume in the PMC core. Ethanol is usually used as a solvent for the perfume, but it has the effect of destroying the PMC shell, as seen in Section 5.2.4. In suspension polymerisation, the organic solvent for the monomers can affect their solubility, the solubility of any formed oligomers, and the precipitation conditions and partition coefficient of the monomers, which can ultimately change the morphology and thickness of the shell (Percebom et al., 2018).

4.5 Mechanical Properties of single PMCs

Micromanipulation was used to measure the mechanical response of single PMCs to diametric compression. Figure 4.4 shows a typical force displacement curve for a PAC PMC. The raw data are collected as voltage change against time. The speed of the probe compression was measured at 2 µm.s^{-1} allowing conversion of the time axis to displacement.

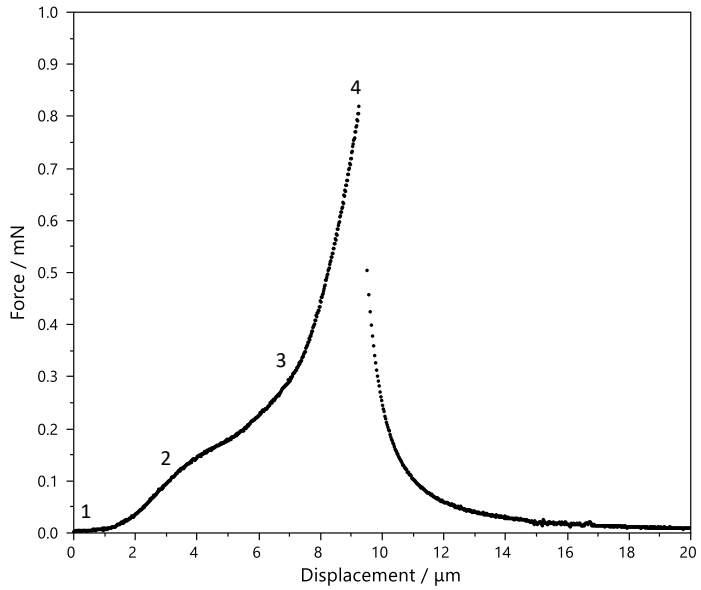

Figure 4.4: Force-displacement curve for a 19 µm polyacrylate PMC from the reference sample

At point 1 on the curve the glass probe touches the top of the PMC and begins to register a force response. In the case of PAC PMCs there is then an elastic response of the microcapsules, where returning removing the probe would see the force drop to zero under the same curve and the PMC return to its original shape. At the displacement at point 2 on the curve the elastic limit is reached, indicated by an inflexion point in the curve. Beyond this point if the probe were to be removed the force would follow a different profile and would drop to zero prematurely, indicating permanent deformation of the shell due to plastic deformation. With further compression after the onset of plastic deformation, between approximately points 3 and 4 on the curve strain hardening occurs. At this point the deformation induces stresses that were caused by increased orientation of chains. The higher the deformation the more oriented the polymer chains are, and the fewer conformations there are in which to orient. This acts to prevent deformation and as such very high stresses are needed to force further deformation.

Finally, at point 4 on the curve the stresses hit a maximum level and the PMC shell ruptures, causing the force to sharply decrease.

The force does not immediately drop to zero as the PMC residue is still compressed. Eventually the probe would hit the glass plate and the force would sharply rise again, but this was avoided to prevent any force transducer damage.

From the force-displacement curve it is possible to obtain a variety of mechanical properties that are useful as fundamental properties of the PMCs, but also provide information about how the PMC samples might perform in real world conditions. The list of properties that have been measured in this work are as follows:

- Rupture force
- % Deformation at rupture
- Nominal rupture stress
- Elastic limit
- Nominal wall tension
- Young's modulus

The rupture force is simply the force at point 4 in Figure 4.4, where the shell ruptures due to the stress under compression. At this point it is also possible to calculate the % deformation at rupture. After 9.2 μm displacement from the original contact point the PMC ruptures, which represents 48 % deformation at rupture for the 19 μm PMC.

The rupture stress of the PMC is related to the force under which the capsule ruptures, and the contact area at this point of rupture. To accurately measure this required using a vertical microscope to view the contact area during the compression. This was not possible under the

equipment set up, and would have required applying a theoretical model, e.g. Lardner and Pujara's model (Lardner and Pujara, 1980), FEA in combination with compression data (Mercadé-Prieto et al., 2012b), or direct measurement through nanomanipulation and electron microscopy (Ren et al., 2007). In this instance the nominal rupture stress was chosen for simplicity, which takes into consideration the force at rupture, F_R and the original PMC diameter, D_m

$$Nominal\ rupture\ stress = \frac{F_R}{\pi\left(\frac{D_m}{2}\right)^2} \quad 4\text{-}3$$

As mentioned previously, point 2 in Figure 4.4 represents the elastic limit of the PMCs. Graphically, this is shown by an inflexion point and a deviation from the elastic fit. It is possible to calculate the Young's modulus by studying the force-displacement relationship below this point, as seen in Section 4.5.9.

The nominal wall tension, T_R, was defined as the ratio of the rupture force to the PMC circumference as outlined in Equation 4-4:

$$T_R = \frac{F_R}{\pi D_m} \quad 4\text{-}4$$

The nominal wall tension is based on the assumption that the PMCs have a uniform shell thickness. Its origins were outlined suggesting that a dimensionless force curve of a microcapsule was independent of the overall size (Wang et al., 2004).

4.5.1 Polyacrylate PMC reference sample

50 PMCs were randomly chosen and compressed to rupture. The rupture force and nominal rupture stress was plotted against microcapsule diameter. As can be seen in Figure 4.6, as the diameter of the microcapsules increased, the nominal rupture stress decreased through a power law decay which suggested that larger microcapsules break more prematurely than the smaller microcapsules in consumer applications when a normal load is applied. The sample was also repeated to examine whether the technique was reproducible for separate measurements on different days.

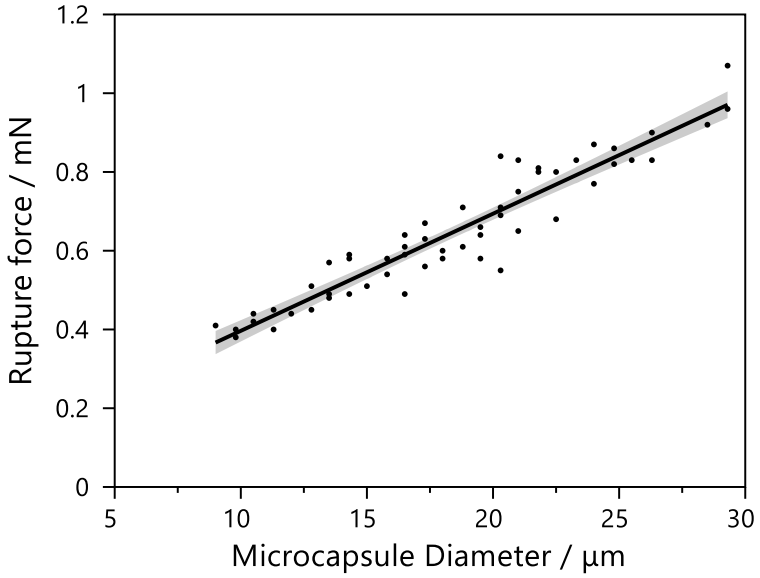

Figure 4.5: Relationship between rupture force and microcapsule diameter for PAC reference sample. Shaded region = 95% CI from linear regression fit

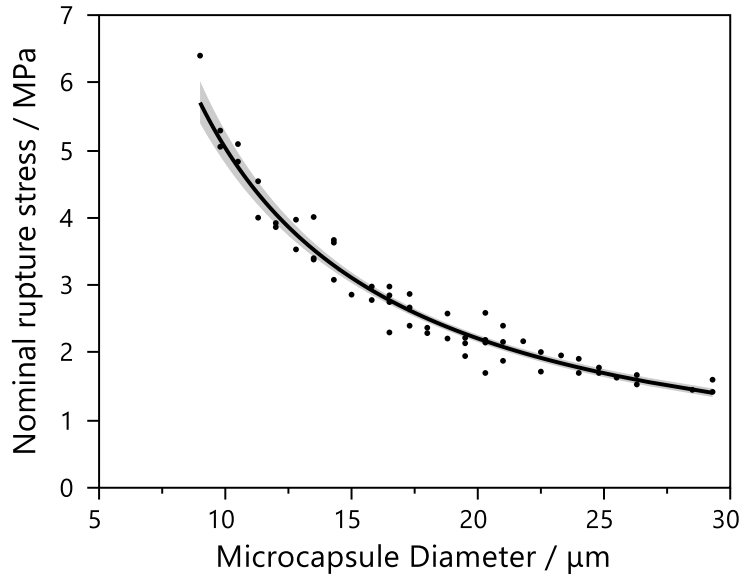

Figure 4.6: Nominal rupture stress vs microcapsule diameter for the PAC reference sample. Shaded region = 95% CI from power law fit

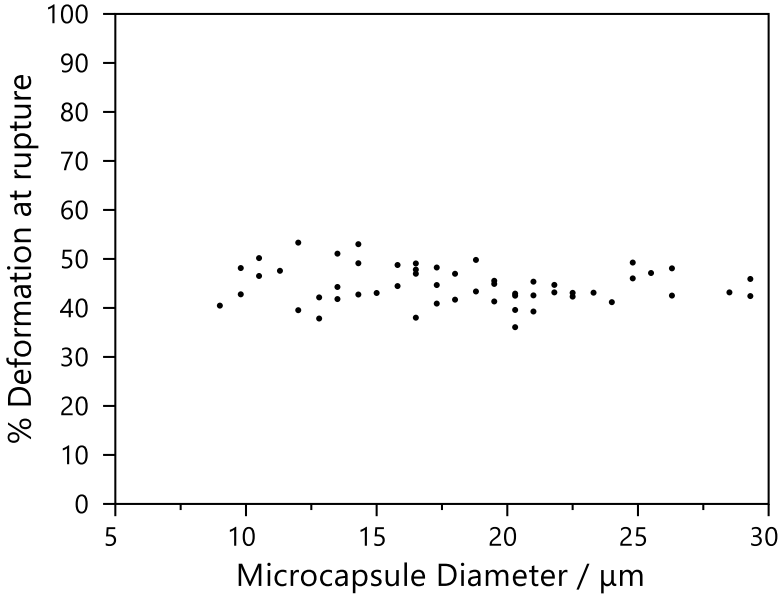

Figure 4.7: % Deformation of rupture vs. microcapsule diameter for PAC reference sample

From the same force-displacement data, the % deformation at rupture was plotted against PMC diameter, as seen in Figure 4.7. It was clear that as the diameter of the PMCs was increased, the % deformation at rupture was constant, and this was known to be consistently the case for

microcapsules (Mercadé-Prieto and Zhang, 2012). This suggested that the PMCs supplied were robust, and were not prone to rupture by crack propagation, as this would be more random both in terms of rupture stress and rupture deformation.

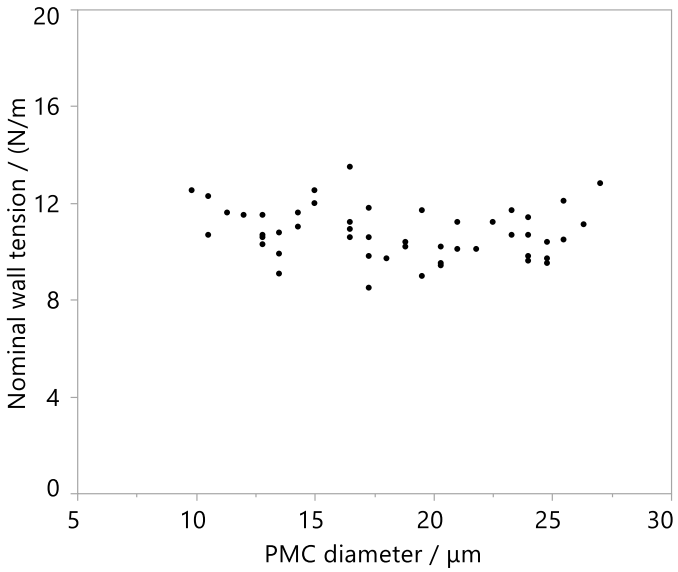

Figure 4.8: Nominal wall tension vs PMC diameter for the reference sample

As seen in Figure 4.8, the nominal wall tension was relatively independent of PMC diameter for all measured PMCs. Alongside comparing the graphs of nominal rupture stress vs PMC diameter, the nominal wall tension of the PMC sample could be used as a measure to compare the relative strengths of samples with different mean diameters.

Alongside size distribution data, used to support mechanical data from micromanipulation, thermal analysis using TGA can yield information about the material properties of the PMC, and how these might relate to mechanical properties. Figure 4.9 shows the TGA curve for the reference PMC slurry. The sample was presented at room temperature and at this point was represented by a weight of 100%. Temperature was increased and the mass loss in the sample

was recorded. The initial weight loss event represented the loss of water (49.79 wt %) through evaporation from the slurry, leaving only the PMCs themselves behind. The intact nature of the shell prevented core ingredients from evaporating. At 183.3°C the second mass loss event began to occur. This represented the rupture of PMCs and the release and subsequent evaporation of core material (41.58%). If only one molecular constituent was present in the oil this would have been a significant mass loss over a very small temperature range. In this case the temperature range for the mass loss was broad, which could have been caused by the extremely varied composition of the perfume and solvents in the core. All that remained at this point after the second weight loss incident was the shell material and any remaining polymeric emulsifier.

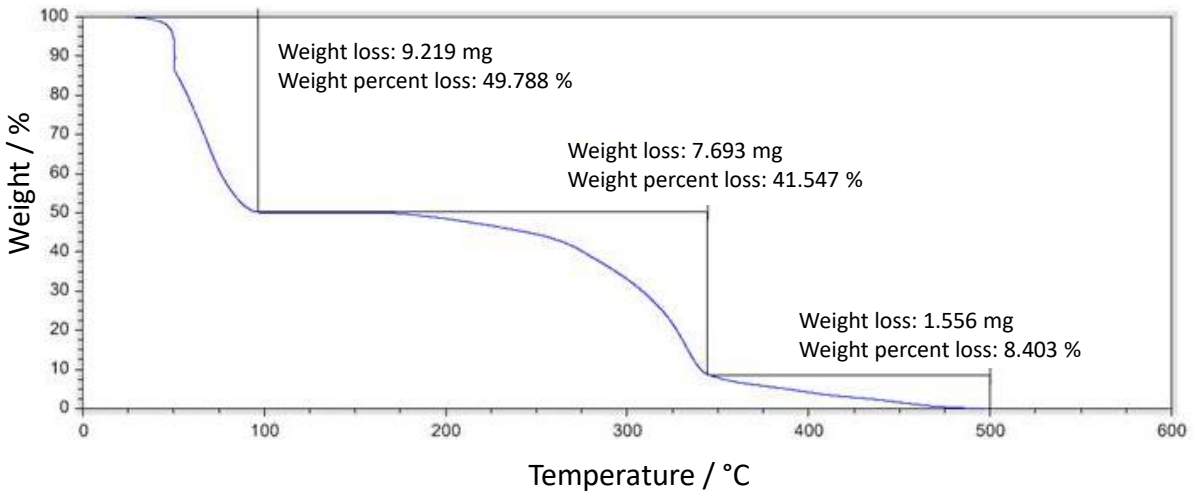

Figure 4.9: TGA curve of the slurry of the reference PAC PMC sample

The temperature at which these mass loss events occur when looking at different PMC samples can offer information about material differences between the samples.

4.5.2 95/5 core/shell ratio polyacrylate PMC sample

Compared to the reference sample, which had a core/shell ratio of 90/10, a sample was produced where the core/shell ratio was altered to be 95/5, so less shell material was available for polymerisation. All processing conditions and chemical composition were aimed to be kept constant, see Table 3.1.

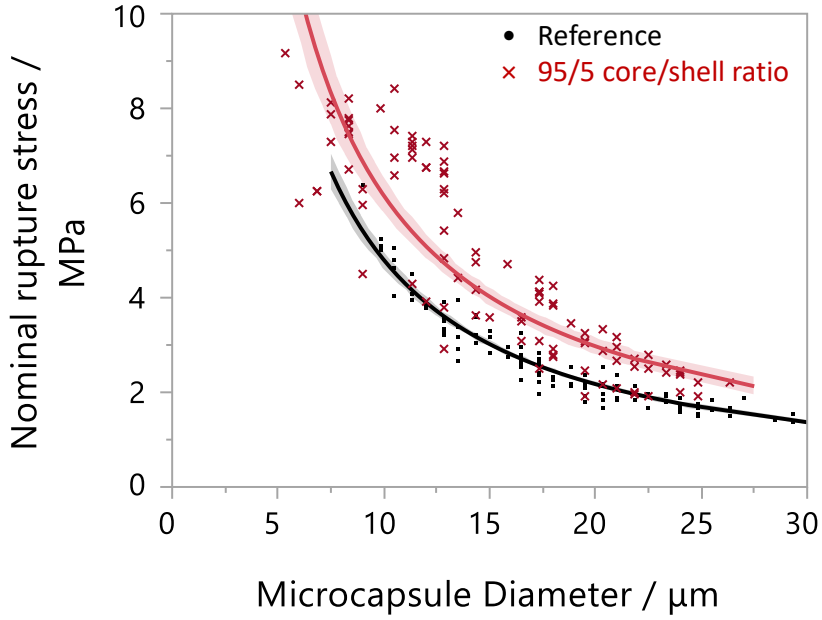

Figure 4.10: Nominal rupture stress vs diameter for the reference and 95/5 core/shell ratio PMC samples. Shaded region is the 95% CI of the fitted line

As seen in Figure 4.10, the 95/5 core/shell ratio PMCs showed a higher nominal rupture stress at all diameters with respect to the reference sample. Similarly, the average % deformation at rupture and nominal wall tension were significantly greater than the reference sample, as seen in Table 4.3.

Table 4.3 Comparison of mechanical properties between reference sample and 95/5 core/shell ratio. The figures after ± represent the standard error of the mean

Sample name	**Average Deformation at rupture / %**	**Average nominal wall tension / $N.m^{-1}$**
Reference	43.0 ± 0.5	11.1 ± 0.2
95/5 core/shell ratio	47.3 ± 0.5	15.5 ± 0.1

As seen earlier in the chapter, the mean shell thickness of the 95/5 core/shell ratio sample was 84 ± 1 µm compared to 104 ± 1 µm for the reference sample, which was in line with the expectation that less shell material would lead to a thinner shell. It was somewhat counterintuitive that the nominal rupture stress, deformation at rupture and nominal wall tension would increase despite a lower shell thickness. One possibility might lie in the minimum shell thickness of the respective PMC samples. Despite having a greater average PMC shell thickness, the higher loading of shell material might have caused a more heterogeneous shell thickness in the reference sample, with a smaller minimum shell thickness leading to a decreased mechanical strength (Vian and Amstad, 2019).

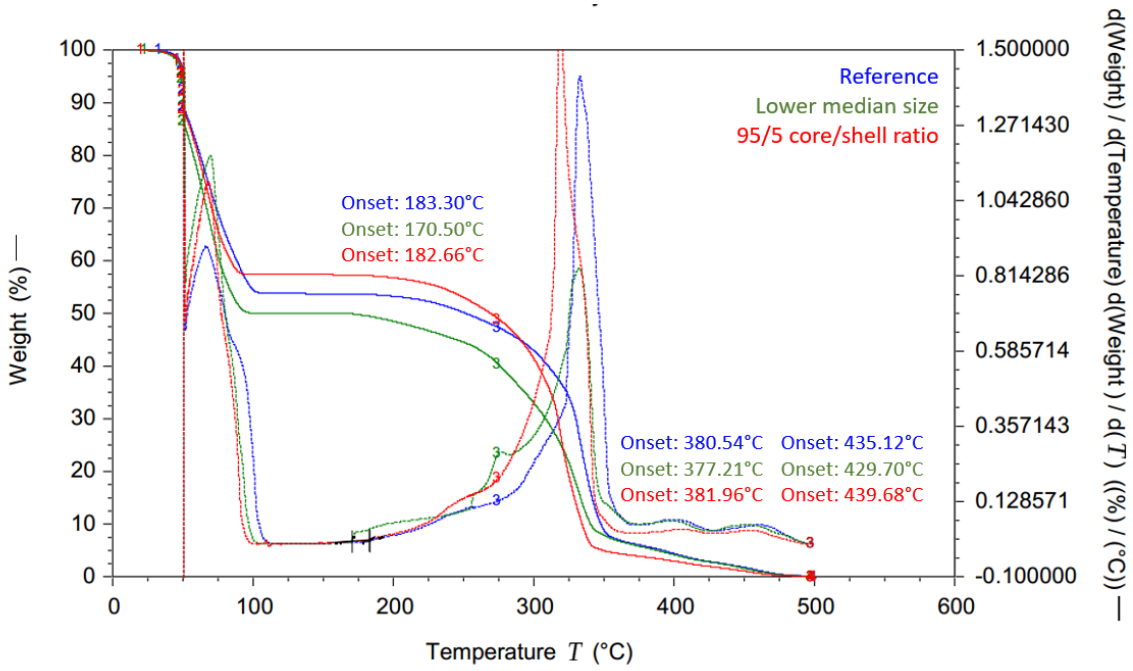

Figure 4.11: TGA curve of the reference PMC sample, the 95/5 core/shell ratio PMC sample, and the lower median size PMC sample

Another possibility for the increased nominal rupture stress of the 95/5 core/shell ratio sample despite having a thinner shell than the reference could lie in the degree of crosslinking of the PAC shell material. From studying the TGA curves in Figure 4.11, the onset of mass loss due to rupturing of the PMC shell was very similar between the reference sample and 95/5 core/shell ratio sample at 183.3°C and 182.7°C respectively. At this temperature the rupture was possibility caused by an internal pressure increase resulting from expansion of the core materials due to the high temperatures. When temperature was increased further, the mass loss was more likely caused by decomposition of shell material, both mass loss events occurred at a slightly higher temperature for the 95/5 core/shell ratio samples, which potentially indicated that the shell was more resistant to decomposition, something that increased crosslinking would provide.

4.5.3 Lower median size polyacrylate PMC sample

In terms of chemical composition, there was nothing different between the reference sample and lower median size sample, however increased energy in the reaction system, caused by a higher impeller speed in the emulsification step was the likely cause of lowering of the PSD, as seen in Table 4.1. Unfortunately due to confidentiality issues there was no specific change in impeller speed mentioned, however patent US 9,221,028 B2 (Procter & Gamble, 2015) suggested this was the method of choice to decrease PMC size.

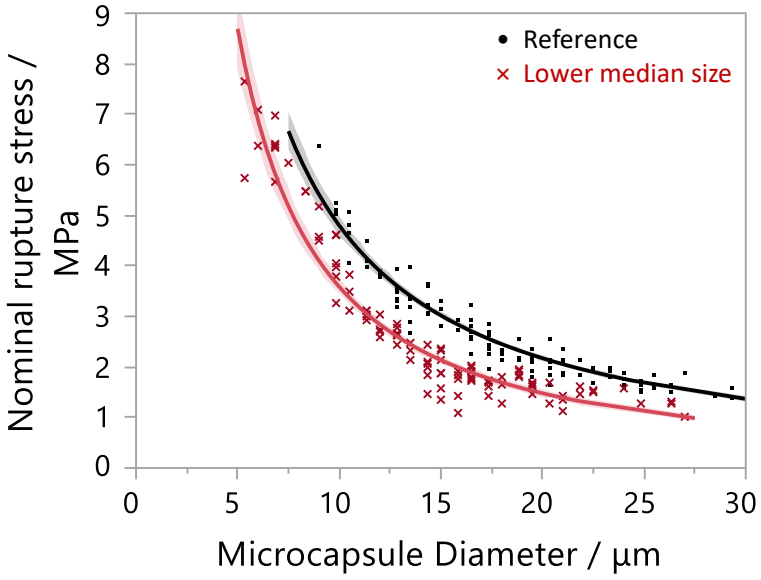

Figure 4.12: Nominal rupture stress vs diameter for the reference and lower median size PMC samples. Shaded region is the 95% CI of the fitted line

Table 4.4: Comparison of mechanical properties between reference and lower median size PMC samples. The figures after ± represent the standard error of the mean

Sample name	**Mean deformation at rupture / %**	**Mean nominal wall tension / N.m^{-1}**
Reference	43.0 ± 0.5	11.1 ± 0.1
Lower median size	45.8 ± 0.6	8.3 ± 0.1

As seen in Figure 4.12, the lower median size sample had a significantly lower nominal rupture stress at all diameters measured. This was also reflected in the significantly lower mean nominal wall tension. Thermal analysis of the lower median size PMC sample using TGA, highlighted in Figure 4.11, showed that compared to the reference the lower median size sample exhibited an onset temperature related to loss of core material due to PMCs rupturing at 170.5°C compared to 183.3°C for the reference PMC sample. This agreed with the micromanipulation data that the lower median size sample was easier to rupture than the reference sample. At a higher temperature where decomposition of shell material occurred, in two mass loss events the lower median size sample showed lower onset temperatures than the reference sample, indicating that the shell material itself was less resistant to decomposition, potentially due to less crosslinking.

4.5.4 Combination of lower median size and 95/5 core/shell ratio PMC sample

Whilst efforts were made to only change one specific physicochemical or structural parameter in each sample, there was a sample provided that combined lower size and 95/5 core/shell ratio. In Section 4.5.2 it was seen that changing the core/shell ratio to 95/5 from 90/10 increased the PMC strength at each diameter. Conversely, as seen in Section 4.5.3, lowering the median size of the sample decreased the PMC strength at each diameter. As observed in the data from Figure 4.13 and Table 4.5, the combination of both of these properties mitigated the respective changes in the mechanical strength and moved the mechanical properties close to the reference sample, although the reference sample has a slightly lower rupture stress at each PMC diameter and was less resistant to rupture in terms of nominal wall tension and deformation at rupture.

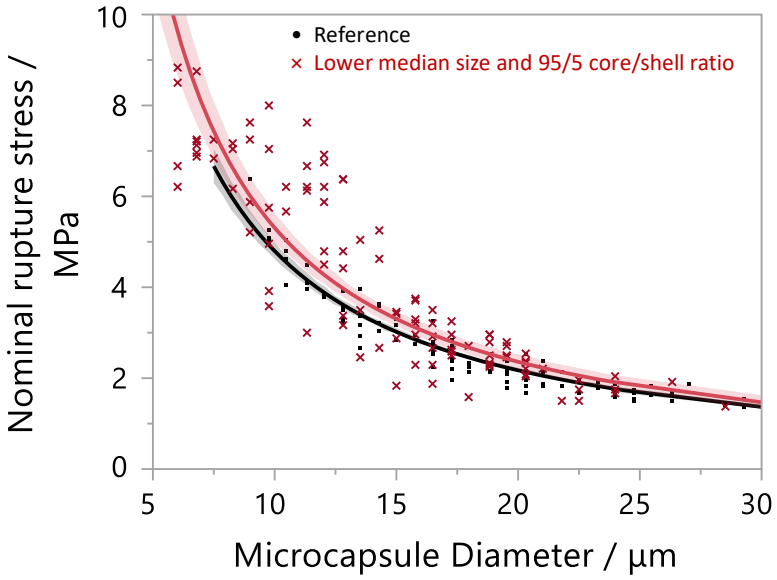

Figure 4.13: Nominal rupture stress vs diameter for the reference PMC sample and PMC sample with lower median size and 95/5 core/shell ratio. Shaded region is the 95% CI of the fitted line

Table 4.5: Comparison of mechanical properties between reference PMC sample and PMC sample with lower median size and 95/5 core/shell ratio. The figures after ± represent the standard error of the mean

Sample name	**Mean deformation at rupture / %**	**Mean nominal wall tension / N.m^{-1}**
Reference	43.0 ± 0.5	11.1 ± 0.1
Lower median size and 95/5 core/shell ratio	47.0 ± 0.9	12.9 ± 0.6

4.5.5 Cationic PMC sample

In the oil phase of the PMC synthesis, for the reference sample and the majority of other samples, 2-(tert-Butylamino)ethyl methacrylate (TBAEMA) was combined with Beta-carboxyethyl acrylate (Beta-C) to pre-form part of the shell material, in the presence of radical initiators. TBAEMA is a chemical that can be polymerised and the pKa means that in water it can become positively charged. This makes it anti-microbial as the polymer is then similar to

polymyxin, a polycationic amphiphilic antibiotic that binds strongly to lipopolysaccharides in gram-negative bacteria through replacing divalent cations at binding sites of the bacteria causing disruption of outer membrane (Lenoir et al., 2006). From this point of view the cationic properties can be useful in laundry applications. Natural fibres are inherently negatively charged and therefore introducing a PMC with more positive charge may help adherence to the fabric and increase deposition. In these PMCs Beta-C, unable to become positively charged in water, was left out of the oil phase pre polymer mixture, and replaced by 3x TBAEMA to try to increase the inherent positive charge on the PMCs.

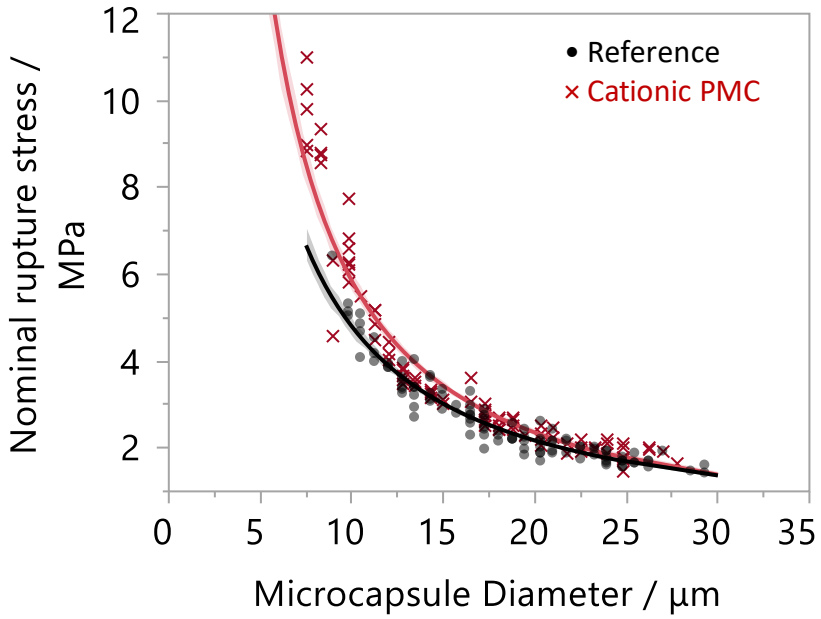

Figure 4.14: Nominal rupture stress vs diameter for the reference and cationic PMC sample. Shaded region is the 95% CI of the fitted line

Table 4.6: Comparison of mechanical properties between reference and cationic PMC samples. The figures after ± represent the standard error of the mean

Sample name	Mean deformation at rupture / %	Mean nominal wall tension / $N.m^{-1}$
Reference	43.0 ± 0.5	11.1 ± 0.1
Cationic PMC	44.8 ± 0.6	12.9 ± 0.2

The results of the nominal rupture stress in Figure 4.14 show that the cationic PMC sample recorded a slightly higher nominal rupture stress at all PMC diameters measured. Similarly, as shown in Table 4.6, the mean deformation at rupture and nominal wall stress were also higher for the cationic PMC sample. Unfortunately, it wasn't possible to measure the shell thickness of the cationic PMC, but as a significant change happened to the nature of the polymer in the shell this could have been the result of a multitude of structural and physicochemical changes, not to mention processing changes.

4.5.6 PMC sample with 20% IPM in the core material

When the PAC PMC composition was changed from a core inclusion of 45% IPM to 20% IPM, the nominal rupture stress did not significantly change for all diameters measured, as seen in Figure 4.15. Interestingly though, as shown in Table 4.7, the mean deformation at rupture and nominal wall tension for the sample with 20% IPM was greater than the reference sample. TEM analysis showed that the mean shell thickness of the 20% IPM sample was 134 nm, compared to 104 nm for the reference. Providing that the processing conditions were kept the same, it was likely this change shell thickness that caused the heightened deformation at rupture and nominal wall tension for the 20% IPM sample. This was despite the sample showing no increase in nominal rupture stress.

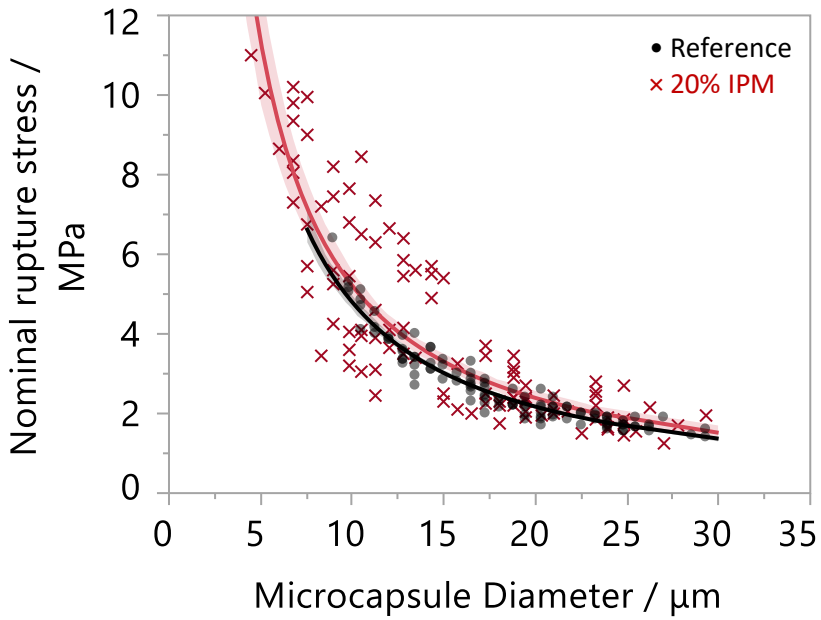

Figure 4.15: Nominal rupture stress vs diameter for the reference and 20% IPM PMC samples. Shaded region is the 95% CI of the fitted line

Table 4.7: Comparison of mechanical properties between reference and 20% IPM PMC samples. The figures after ± represent the standard error of the mean

Sample name	Mean deformation at rupture / %	Mean nominal wall tension / $N.m^{-1}$
Reference	43.0 ± 0.5	11.1 ± 0.1
20% IPM	50.8 ± 0.7	13.0 ± 0.4

4.5.7 PMC sample formed at a lower curing temperature

Information from patents suggested that the polymerisation temperature to create the final PMC shell was 90°C (Procter & Gamble, 2014b). A sample was received where this temperature was lowered to 75°C in order to understand the effect on the mechanical properties. Lowering the temperature of polymerisation has the effect of changing the solubility of the polymer formed and lowering the rate of radical formation, which in turn should have resulted in an increase in PMC average size.

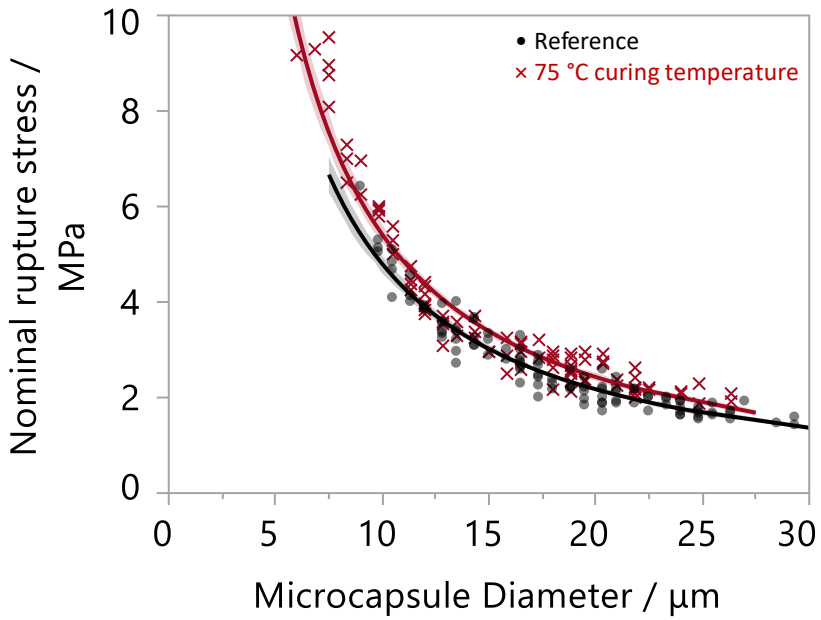

Figure 4.16: Nominal rupture stress vs diameter for the reference sample and sample with 75°C polymerisation temperature. Shaded region is the 95% CI of the fitted line

The nominal rupture stress for the reference sample and sample polymerized at 75°C are shown in Figure 4.16. At all measured PMC diameters, the rupture stress of the sample produced under a lower polymerisation temperature was slightly stronger than the reference sample. This could be rationalised by considering the molecular weights of the final polymer. A higher rate of free radical formation from the initiator molecules increases the probability of chain termination by the initiators (Ober and Hair, 1987). This has the effect of decreasing the molecular weight, M_w, of the polymers that precipitate to form the PMC shell, in turn giving the polymer shell a lower tensile strength and lower impact resistance which leads to the lower rupture stress of the PMCs produced at a lower polymerisation temperature. The lower temperature polymerisation also resulted in a mean deformation at rupture of 47.4 ± 0.5 % compared to 43.0 ± 0.5 % for

the reference and an increased mean nominal wall tension of 12.8 ± 0.2 $N.m^{-1}$ compared to 11.1 ± 0.1 $N.m^{-1}$ for the reference sample.

Table 4.8: Comparison of mechanical properties between reference sample and sample with 75°C curing temperature. The figures after ± represent the standard error of the mean

Sample name	**Mean deformation at rupture / %**	**Mean nominal wall tension / $N.m^{-1}$**
Reference	43.0 ± 0.5	11.1 ± 0.1
75°C curing temperature	47.4 ± 0.5	12.8 ± 0.2

4.5.8 Young's modulus calculations of the samples

To calculate the Young's modulus of the whole PMC the Hertz model was used with reference to force vs displacement data collected from micromanipulation. When PMCs are elastic, the plot of force, F against $(\delta)^{3/2}$, in equation *4-5*, where δ is the probe displacement, is linear. This was the case for all samples tested up to a fractional deformation of at least 0.10, an example of which is seen in Figure 4.17, where there was good fitting of the data to the Hertz model. It must be noted that the 'soft spot' of the force-displacement graphs, if it occurred in the compressions, was removed from the Hertz model calculation plot. The calculations for how this soft compression was omitted and the elastic limit, beneath which the PMCs display elastic behaviour is seen in Section 4.5.9.

Using this linear plot, the Young's modulus, E, can be found from the gradient of the line, as outline in Equation 4-5, where v is the Poisson's ratio, and r is the PMC radius:

$$F = \frac{4}{3}\frac{E}{(1-v^2)}r(\delta)^{3/2} \qquad 4\text{-}5$$

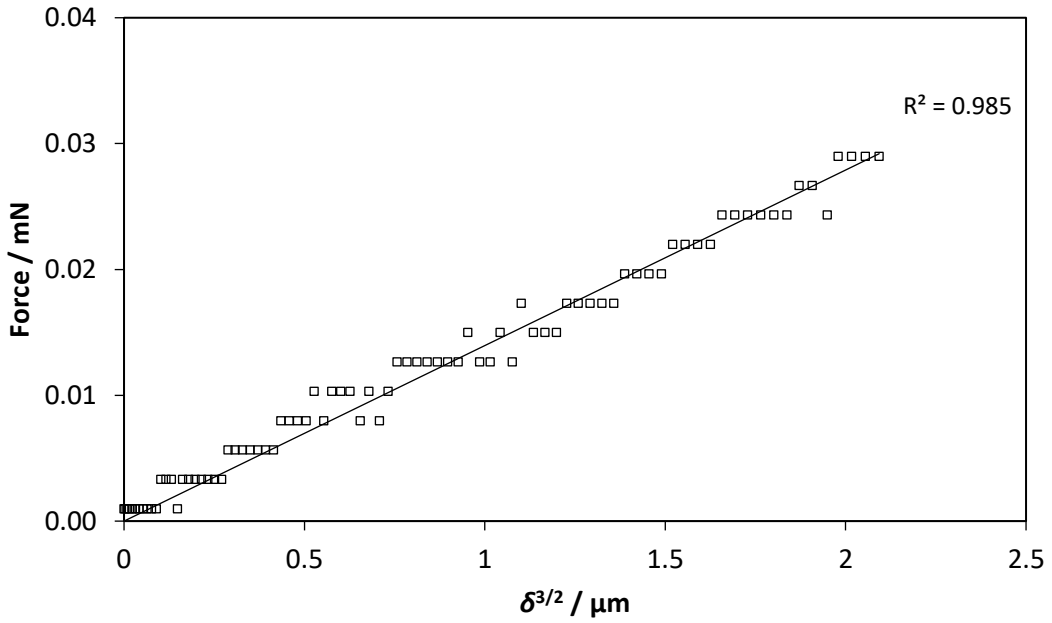

Figure 4.17: Linear fit of the hertz model to the compression data of a 16.5 µm PMC up to 10% fractional deformation

Table 4.9: Results of the calculations of the Young's modulus for each of the PMC samples using the Hertz model. 50 PMCs were compressed for each sample. The figures after ± represent the standard error of the mean. Results are also shown for a Tukey-Kramer test for comparing all mean pairs. Levels not connected by the same letter are significantly different α=0.05

Samples Name	Mean Young's modulus / MPa	Tukey Kramer
Reference	5.89 ± 0.51	AB
95/5 Core/shell Ratio	5.33 ± 0.18	AB
95/5 Core/shell Ratio and Lower Median Size	4.58 ± 0.16	AB
20% IPM	3.41 ± 0.14	A
Lower Median Size	4.29 ± 0.21	AB
Cationic PMCs	6.61 ± 0.28	B
75°C curing temperature	6.16 ± 0.41	AB

The Tukey Kramer test is used after a one-way anova and the minimum significant difference between two sample means is calculated. If the observe difference between the two samples is

greater than the pair of means are significantly different. This is highlighted by levels not being connected by the same symbol in the analysis. As can be seen in Table 4.9, the Young's modulus of the samples, when calculated using the Hertz model were extremely similar, with only the samples significantly different to each other being the 20% IPM sample and the cationic PMC sample.

4.5.9 Investigating the Young's modulus of the PMC shell

Determination of the elastic properties of PMC shell required comparison to a theoretical dimensionless force profile. From FEM simulations it was found that changing the shell thickness to radius ratio, also known as the h/r ratio, changed each force profile and subsequently the elastic properties of the shell. It was difficult to observe the *h/r* value for the specific PMC tested as the micromanipulation technique was destructive. Average values can be found for the population of the sample as seen earlier in this chapter, but the technique outlined by Mercadé-Prieto et al. (2011) offered a method to estimate *h/r* values based on comparing to theoretical force values at different h/r values.

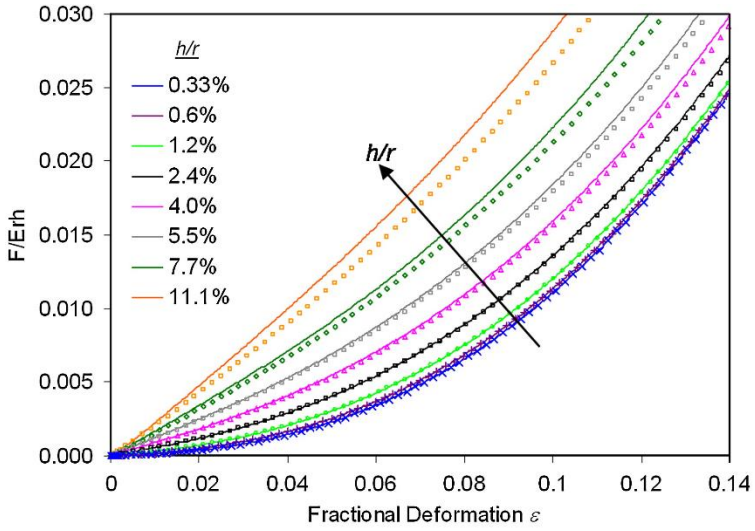

Figure 4.18: Visualisation of dimensionless force profiles for different shell thickness ratios. Reprinted from *Mercadé-Prieto et al. (2011)*

Using the FEM analysis from Mercadé-Prieto, six fractional deformations, ε, at 0.03, 0.04, 0.05, 0.06, 0.07 and 0.08 were chosen from which to determine the average *h/r* value for the force profile. At each ε the force/capsule diameter was normalised against that at $\varepsilon = 0.1$. Plotting this ratio yielded the *h/r* ratio for each deformation.

Once the average *h/r* ratio was calculated, the 2nd order dimensionless force profile was required in order to calculate the elastic modulus. The equation for the dimensionless force profile was formed as follows:

$$\frac{F}{Erh} = a\varepsilon^2 + b\varepsilon + c, 0.03 < \varepsilon < 0.1 \qquad 4\text{-}6$$

The coefficients, a, b and c have been correlated to individual *h/r* values and equations for the high order polynomials for each coefficient, as they enable estimation of each coefficient based upon calculated *h/r* values.

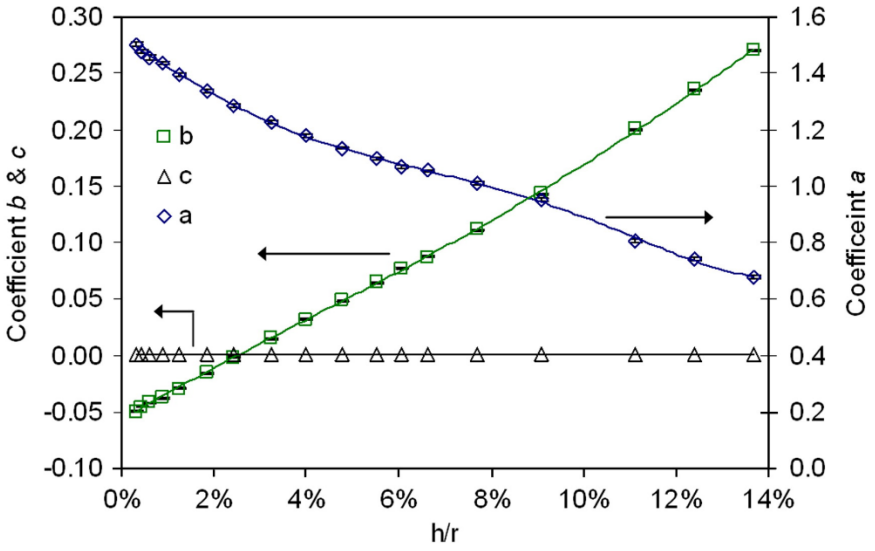

Figure 4.19: Second order coefficients from Equation 4-7 at different simulated *h/r* values. Reprinted from Mercadé-Prieto et al. (2011)

Once the equation for the polynomial at a certain average *h/r* was found it was possible to calculate *Eh* by comparing the experimental force profile with the calculated profile:

$$Eh_{\varepsilon} = \frac{F_{\varepsilon}/r}{a\varepsilon^2 + b\varepsilon + c} \qquad 4\text{-}7$$

The average Eh from the seven fractional deformations was calculated and knowing the average shell thickness from the average h/r value, the shell thickness can be calculated without the need for microscopy of samples. Further details of the methodology are described in Appendix A.

Table 4.10: The mean shell thickness and mean Young's modulus as calculated from the FEM methodology. The numbers after ± are the standard error of the mean. Results are also shown for a Tukey-Kramer test for comparing all mean pairs. Levels not connected by the same letter are significantly different α=0.05

Sample name	Mean shell thickness / nm	Tukey Kramer	Mean Young's modulus / GPa	Tukey Kramer
Reference	127 ± 6	B	2.85 ± 0.18	A
20% IPM	153 ± 8	AB	1.27 ± 0 .07	C
Lower median size	151 ± 8	AB	1.58 ± 0.09	C
95/5 core/shell ratio	184 ± 13	A	1.37 ± 0.09	C
Lower median size and 95/5 core/shell ratio	174 ± 8	A	1.56 ± 0.09	BC
75°C curing only	171 ± 13	AB	2.41 ± 0.25	AB
Cationic PMC	158 ± 9	AB	2.67 ± 0.17	A

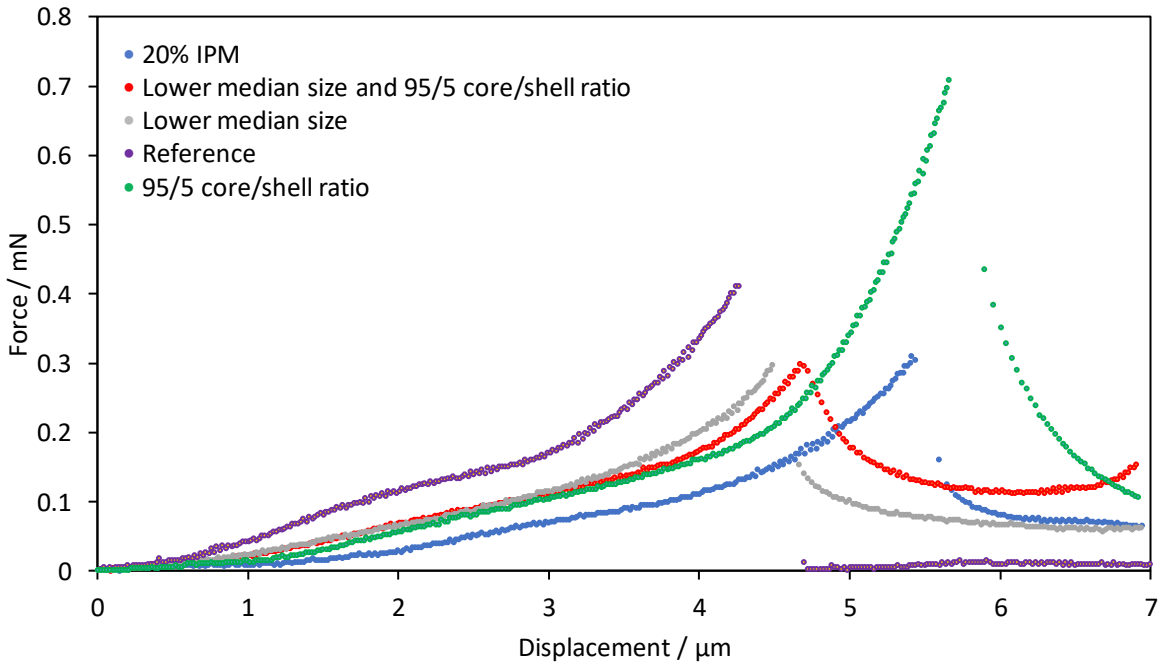

Figure 4.20: Force displacement curves for an 11 µm PMC of different samples showing the variation of initial elastic compression and strain hardening regions

A visualisation of force-displacement curves of an 11 μm PMC for some of the samples is shown in Figure 4.20. The magnitude of the Young's modulus influences the elastic compression at the start of the displacement, before plastic deformation occurs. The samples in the graph show agreement with the results from the FEM methodology results in Table 4.10 as the reference sample displays the highest Young's modulus, where the same displacement causes a significantly larger force response. The lower median size and lower median size with 95/5 core/shell ratio samples show a very similar initial compression profile both in the visual representation and in the FEM methodology. The 20% IPM PMC sample showed the lowest Young's modulus both when calculated by the FEM methodology and when displayed graphically. An interesting observation was that the 95/5 core/shell ratio despite having the largest rupture force did not have the largest Young's modulus. The reason this PMC sample had a large rupture force was the slight increase in deformation at rupture, combined with significant strain hardening up to this point.

Compared to the Young's moduli calculated by the Hertz model, the Young's moduli as calculated by FEM methodology were on the order of GPa rather than MPa. This was because rather than studying the elastic response of the whole PMC under compression in the Hertz model, the Young's modulus from the FEM methodology focused only on the shell material. The order of magnitude of the Young's modulus of the shell was the same the findings from Keller and Sottos (2006) where an analytical model was used for fluid-filled shells, neglecting the bending resistance of the capsule shell wall (Lardner and Pujara, 1980, Feng and Yang, 1973).

4.5.10 Mechanical properties of the reference PMC sample at different humidities

Until this point all micromanipulation experiments had been conducted at ambient relative humidity (RH) in the lab. Evidently, when PMCs are present in a washing machine cycle the relative humidity is much greater than in an open lab environment and therefore it was important to understand how this affected the mechanical properties. As outlined in the materials and methods section, an environmental chamber was constructed where it was possible to control the humidity in a closed vessel, in which micromanipulation of single PMCs was possible. In ambient lab conditions the PMC sample was applied to the slide and the water carrying the PMCs evaporated, leaving them resting on the glass surface, for ease in micromanipulation. The PAC shell material is quite hydrophilic and can absorb water. To get accurate representations on the effect of humidity on the PMC mechanical properties it was necessary to reach an equilibrium in the water retained in the shell structure at a given RH.

Dynamic vapour sorption (DVS) was used as a method to show the kinetics of water absorption to help understand the time needed for equilibration. A sample of the reference PMC sample was placed in the aluminium pan at 20% RH and once at equilibrium, less than 0.005% mass change over a 10 minute period, RH was changed to 70%. Once equilibrium mass was reached at the RH it was reduced back to 20% RH and the process was repeated to 80% and 90% RH. Results show the time taken to reach equilibrium following each step change, seen in Figure 4.21.

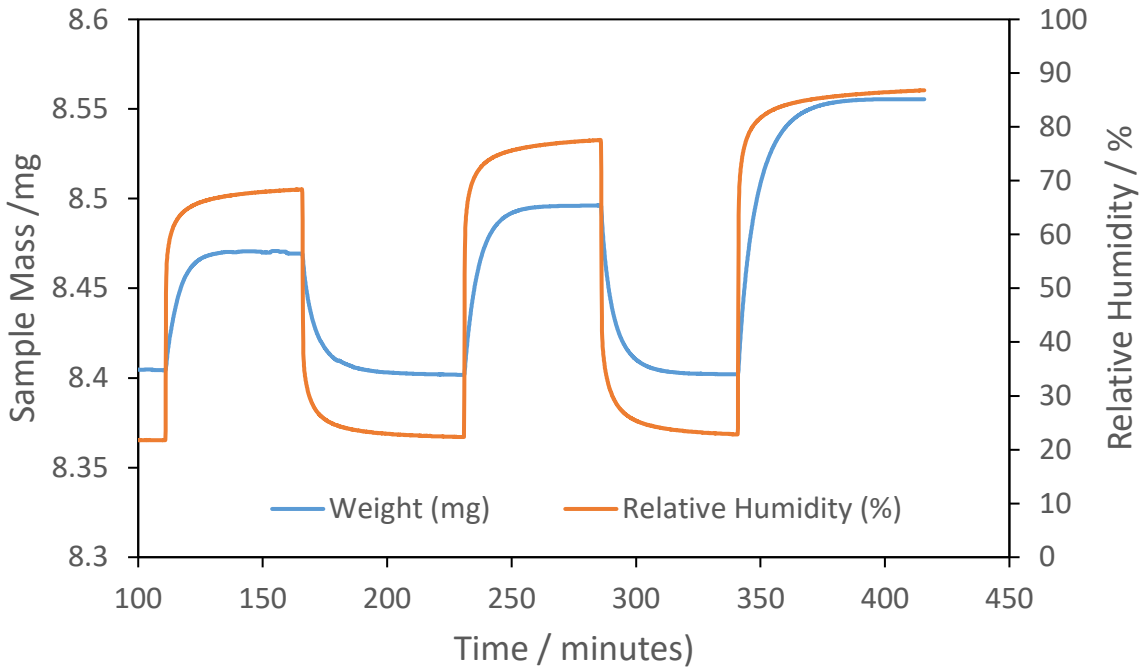

Figure 4.21: Response of reference PMC sample mass as the atmospheric relative humidity is cycled over time

Table 4.11: Time taken for the reference PMC sample to equilibrate at different RH where the change in mass < 0.005 % over 10 minutes

	70% RH	**80% RH**	**90% RH**
Time to equilibrate at specific RH / minutes	55.8	55.0	75.00

As the relative humidity was increased the mass of water taken on by the PMCs increased. The sensitivity was set so any mass change < ±0.005% over a 10 minutes period was thought to be equilibrated. The time taken to equilibrate after the RH had been changed from 20% to 70%, 80% and 90% are shown in Table 4.11. The lowest time to equilibration at a raised RH was 55.0 minutes. The sample was added directly from the slurry. Once the water in the slurry had evaporated it would leave an agglomerate of PMCs in the pan. This was in contrast with PMC

on a glass plate dried from diluted aqueous solution for micromanipulation where they dry individually resting on the plate. Time to reach water content equilibrium would be much shorter in the case of single PMCs rather than agglomerates and therefore the 60 minutes mark for equilibration in humidity chamber micromanipulation was a conservative estimate, but would guarantee that any PMCs compressed would be in their equilibrium conditions within the set atmospheric conditions.

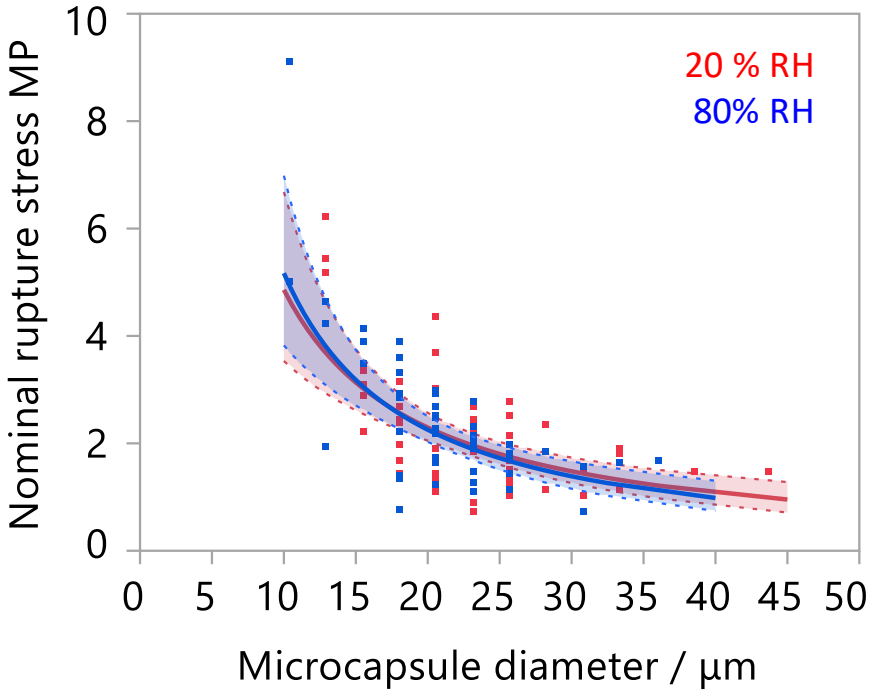

Figure 4.22: Nominal rupture stress vs diameter for the reference PMC sample at 80% and 20% RH. 95% CI limits shown on the graph

Figure 4.22 shows the results from compression of the reference PMC sample under 20% RH and 80% RH conditions. These were set as the extremes of the environmental chamber setup. Under the diameters measured there was no significant difference between the two samples in terms of nominal rupture stress, indicating that whether they were dry, deposited on a surface or when wet, in the washing machine, the PMCs would still burst under the same stress.

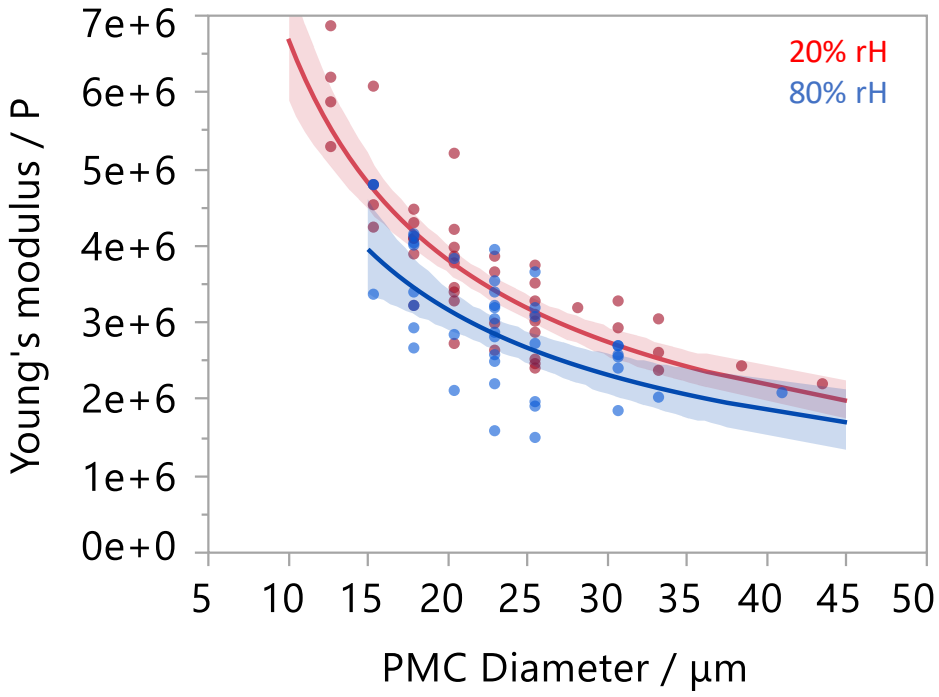

Figure 4.23: Comparison of how the Young's modulus, as calculated by the Hertz model, varies with PMC diameter at 20% and 80% relative humidity. 95% CI limits shown on the graph

It was also important to study the Young's modulus of the samples. In a more hydrated state there is increased shell volume and greater mobility for the chain segments, which lowered the stiffness of the shell, shown by a lower Young's modulus at all measured diameters in Figure 4.23. Lower humidity means less water in polymeric chains, decreasing free volume of the material, meaning the chains are closer together. This was of particular relevance in laundry applications as the PMCs were not being stressed in dry conditions, but rather in water, so understanding that they become more flexible in water is an important piece of information.

4.6 Conclusions

PAC PMC samples were provided by P&G with a view to providing a better understanding of the influence of certain structural, physicochemical parameters on the mechanical properties of PMCs, which would ultimately lead to differences in how the PMCs would perform in application. Care was taken to try to only vary one parameter at a time, such as median PMC size, core/shell ratio, curing temperature and IPM content. PMC samples were also provided with a more cationic shell, and a sample which combined 95/5 core/shell ratio with a lower median size.

Each sample was diametrically compressed using the micromanipulation rig, yielding information on mechanical properties of each sample such as rupture force, nominal rupture stress, percentage deformation at rupture and nominal wall tension. PMCs were also characterised using TEM to measure the average shell thickness of each sample. It was found that relative to the reference sample, only two samples showed significant deviation in terms of nominal rupture stress. The 95/5 core/shell ratio sample ruptured at a significantly higher nominal stress than the reference, whilst the lower median size sample ruptured at significantly lower nominal rupture stress.

Whilst it was possible to postulate reasons for mechanical differences in the samples from studying shell thickness, size distribution and thermal degradation profile, without being given the full processing conditions this is largely speculation. For example, increasing initiator concentration in a suspension polymerisation reaction would decrease average chain length of the polymer, potentially altering the mechanical properties. Without the confidential processing information it was unreasonable to make conclusive remarks on reasoning behind mechanical differences, aside from reporting them and hypothesising. In the future if a real detailed

understanding is warranted, I would suggest full disclosure of processing conditions, and would open up the opportunity to either create a design of experiments based either on structural or physicochemical characteristics of PMCs as factors, or more realistically, processing conditions used as factors.

An environmental chamber enabled the diametric compression of the PAC PMC reference sample under 20% and 80% RH conditions. It was observed that compression under each condition did not show any significant difference in the nominal rupture stress, however the Young's modulus, as calculated by the Hertz model, showed that PMCs compressed under 80% RH showed a lower Young's modulus, suggesting the PMCs became more flexible in higher humidity, something which would be advantageous in surviving a wash cycle with multiple collisions.

The Young's modulus of all of the samples was calculated, firstly using the Hertz model, relating to the whole PMC, which had been verified in the literature, and secondly, using a method based on FEM modelling and adapted to take into account the 'soft spot' during compression and calculating the Young's modulus of the shell. Only the 20% IPM sample, which was significantly weaker, and the cationic PMC sample, which was significantly stronger, showed any difference in Young's modulus from the other samples when using the Hertz model. Using the FEM methodology the results were more widespread, but generally the same trends were observed, albeit on the scale of GPa compared to MPa for the Hertz model.

Chapter 5. METHOD DEVELOPMENT FOR THE CREATION OF THE MASS BALANCE OF PMCs IN A WASHING MACHINE

Quantifying the distribution of PMCs in a washing machine is a complex problem to approach. Within the closed system of the washing machine drum, during the cycles, the PMCs are confined and can segregate into different phases; dispersed in solution, or embedded on different fabric substrates. Despite considerable attention on the mechanical characterisation of microcapsules, the work is seldom translated to assessing the performance of PMCs in real world applications in literature, where an understanding of the process is important to determine how many PMCs break, where they break, and when they break. In the washing machine the location of PMCs at any point in the cycle can be explained by a distinct output stream that contributes to the mass balance: PMCs intact and embedded in fabric, PMCs broken and embedded in fabric, having released the contents to the fabric strands, PMCs intact and present in the washwater, and finally PMCs that have broken and released their contents to the washwater. In this chapter, several novel methods are presented that each individually contribute to a component of the mass balance, with a detailed method development outlined for each, clarifying why steps were taken to design in such a way. To assess the deposition of PMCs on fabric, a method is presented that uses specific solvent extractions of an encapsulated fluorescent dye marker, Pyrromethene 546 (PM546), to separately quantify the intact and broken PMCs using spectrofluorometry. Using the same apparatus, the intact PMCs in the

washwater are quantified by a combination of filtration and solvent extraction. Finally, to complete the mass balance the broken PMCs are quantified using the perfume within the PMC core as the marker and headspace GC-MS as the analytical technique capable of measuring this marker.

5.1 Identification of markers to quantify PMCs in the washing machine

5.1.1 Perfume

The perfume within the PMCs was a mixture of over 20 different components, comprising of aldehydes, ketones and terpenes amongst other compounds. The compounds spanned a range of volatilities so that the highly volatile compounds offered the top notes of the fragrance, and over time the fragrance developed to leave only the less volatile base notes. The specific formulation was proprietary to P&G, however the individual perfume raw materials (PRMs) were known and all formed part of quantification. The perfume was an excellent marker for quantifying the PMCs for two reasons:

- It was ultimately the active ingredient sought to deliver to fabrics, so quantifying this gave a clear indication of what this meant in terms of performance of the PMCs.
- The perfume was composed of defined raw material compounds. Detection of these compounds was an excellent indication of the perfume levels held within the PMC core.

There was one specific drawback, however, with using perfume as a marker in that the perfume degraded when exposed to the detergent chemistry and washwater environment. Whilst encapsulating in PMCs prevented this degradation, once the PMCs ruptured, the perfume was exposed to the washwater liquor containing reactive ingredients in the detergent as well water

itself and a potentially changeable pH. Aldehydes within the formulation were good reducing agents due to the reactive hydrogen on the α-carbon of the carbonyl. They could be oxidised to carboxylic acids. This was just one type of reaction that could occur, along with reactions with other acids and addition reactions. For the detergent to work effectively, it was formulated to change the washwater environment to alkaline conditions. This could have a substantial impact on the rate of degradation of certain compounds in the perfume formulation. The combination of these effects meant that if perfume was to be used as a marker, the analysis of the fabric or washwater must be conducted extremely quickly, prior to the onset of any degradation. The characteristic scent of the perfume, immediately noticeable in washwater after the wash, was barely recognisable a few days later, suggesting a change in character and therefore composition of the perfume which would therefore influence any subsequent quantification if delays in analysis occurred.

5.1.2 Pyrromethene 546 fluorescent dye

Pyrromethene 546 is a fluorescent dye. Pyrromethenes rival rhodamines as tuneable lasers in the visible regime as they may have higher lasing efficiencies, as well as a fluorescence quantum yield close to 1. The Pyrromethenes also have a high photostability, meaning the lifetime of the dye under fluorescence is large. This was important to simplify the visualisation of PMCs under image analysis as a photobleaching was less prevalent, meaning less fading of the specimen.

How PM546 behaved in solvents was extremely important in considering it as a marker for the mass balance. It was soluble in apolar, polar and protic organic solvents, but insoluble in water and in water /ethanol mixtures with >5% vol water (López Arbeloa et al., 1999).

5.1.3 Choice of markers for each output stream of the mass balance

In each PMC sample the fluorescent dye was added to the core material of the capsules at 500 ppm prior to encapsulation. This meant that all of the PMC was observable under fluorescence microscopy.

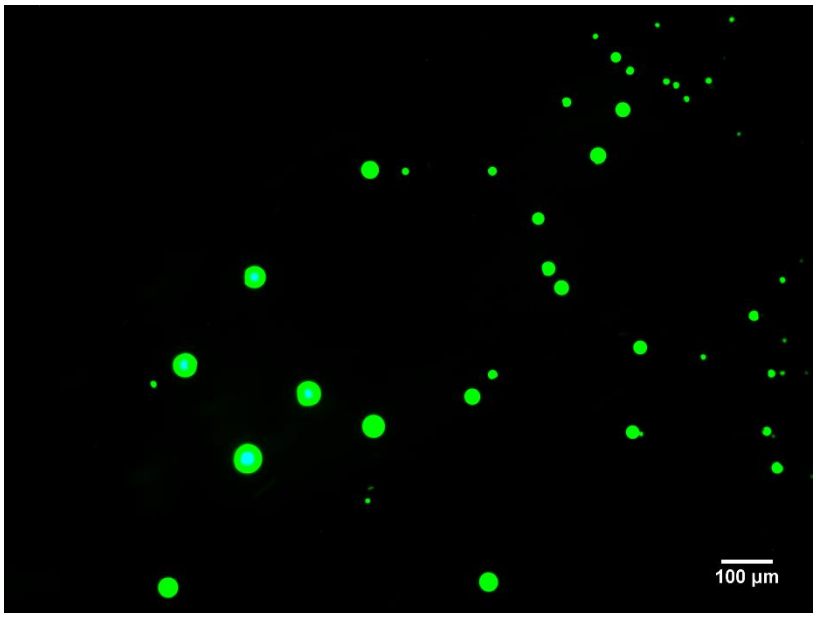

Figure 5.1: Example fluorescence microscopy image of PMCs on a glass slide

In ideal circumstances the perfume would always be used as the marker for quantification. The perfume was the active ingredient of interest and analysis of this would mean quantification could be done on ready-for market PMC formulations without fluorescent dye addition. The issues with this ideology were two-fold:

- In washwater the perfume experienced degradation through reactions such as hydrolysis with water as previously mentioned.

- On fabrics as soon as the swatches were removed from the washing machine evaporation began and the overall quantification of perfume from broken PMCs decreased over time, which would lead to inaccurate quantification.

The combination of these effects meant that time was extremely important in analysing perfume as a marker, but the analysis itself was quite time consuming. The fluorescent dye on the other hand was extremely stable to evaporation. The melting point was 259-261°C, but no literature data on boiling point, and therefore the analysis was somewhat time independent in terms of evaporation.

A decision was made to combine the two markers for the analysis. Perfume as a marker was to be used to quantify broken PMCs in the washwater, whilst PM546 fluorescent dye was used for deposition analysis of broken and intact PMCs on fabric, eliminating the issue of evaporation of marker. The dye was also used in the quantification of intact PMCs in the washwater. Either marker in this case could have been chosen as they were both confined in a closed environment until the PMCs were broken at point of analysis. The fluorescent dye was therefore chosen as a marker as it removed the strict time dependency on analysis.

For all method development the reference PMC sample was used for experiments.

5.2 Quantifying the number of PMCs deposited on fabric – intact and broken

5.2.1 Fluorescence microscopy to quantify intact PMCs

Initial efforts to quantify deposition of PMCs on fabric was concentrated on identifying the number of deposited PMCs through fluorescence microscopy, using the dye as a marker. These

preliminary experiments were conducted on melamine formaldehyde microcapsules before the focus was switched to polyacrylate architecture. 100 images were taken at random for each swatch in the washing machine and then the number of microcapsules in total in the images was quantified using ImageJ. A scale up factor to cover the total ballast surface area was applied to get the total number of PMCs deposited on fabric. This was repeated for swatches removed from the wash at the end of each different cycle, and also between high energy and low energy cycle programmes. The number of PMCs quantified post-cycle was compared to the theoretical total number of PMCs based upon the volume distribution of the different sized PMCs in solution and the volume of PMC slurry added.

The calculations for the total theoretical number of PMCs and the number of deposited PMCs in the wash are shown in Appendix C.

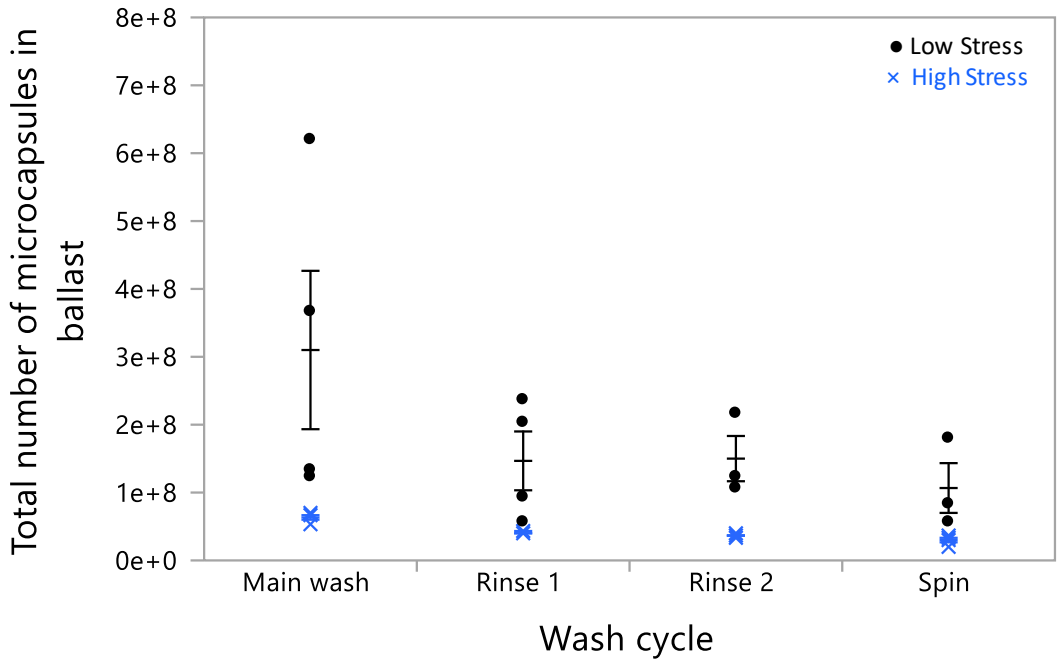

Figure 5.2: Deposition of PMCs in fabric at the end of each wash stage for high stress and low stress cycles as quantified by fluorescence microscopy. Error bars represent the standard error of the mean from 4 measurements.

Figure 5.2 shows the total number of PMCs recovered in each wash stage in the programmable cycles for high stress and low stress conditions, details of which are were outlined in section 3.3.1. As seen in these results, there were significantly more intact PMCs remaining on fabric under low stress conditions than in high stress conditions. This was largely due to a shorter cycle time, hence less chance for breakage of PMCs after deposition, and a lower energy agitation exposing the PMCs to lower hydrodynamic forces in the wash. More important to the mass balance formation though was the total number of PMCs recorded. The highest quantity of PMCs recorded in this method represented only around 1.3% of the theoretical total deposition, based on total input.

Table 5.2: Calculation of the % deposition on fabric from analysis of fluorescence microscopy of fabrics and theoretical total PMC input

Number of PMCs quantified in ballast	Total number of PMCs input into wash	Deposition / %
6.19×10^{8}	4.61×10^{10}	1.3

It was expected that the overall deposition would be much greater than 1.3% and hence doubts were cast into the accuracy of this method. PMCs could become buried within the fabric structure, meaning they may not be quantified. In addition, the method was extremely time consuming. The technique also failed to quantify broken PMCs, and this would need to be quantified in a separate method, adding to the time constraints for the total mass balance. The combination of these issues meant analysis of the quantity of PMCs deposited on fabric by fluorescence microscopy was not taken forward as one of the mass balance methodologies, and focus turned to bulk quantification of dye release.

5.2.2 Solvent extraction of encapsulated dye and analysis via spectrofluorometry

As mentioned previously the chosen dye was soluble in polar, apolar and protic organic solvents, so there were a variety of solvents that might be suitable to extract the dye from the microcapsules. Ideally one solvent had the ability to extract any core oil that had deposited on fabric from broken PMCs, and one solvent had the ability to extract the core oil from intact capsules, either from rupturing the shell or causing the dye to migrate from the core to the solvent environment. After this extraction samples would be analysed via spectrofluorometry against calibration samples to quantify the dye,

5.2.3 Hexane as solvent for extracting dye from broken deposited PMCs

To be a useful solvent for broken PMCs it must leave the intact PMCs unaffected during any extraction process. In Figure 5.3 it was seen that adding PMCs into hexane showed an increase in fluorescence intensity over time when sampled for spectrofluorometry. On the face of it this suggested that hexane does indeed extract dye from the core of PMCs, meaning the hexane may have been suitable for extraction of dye from broken PMCs.

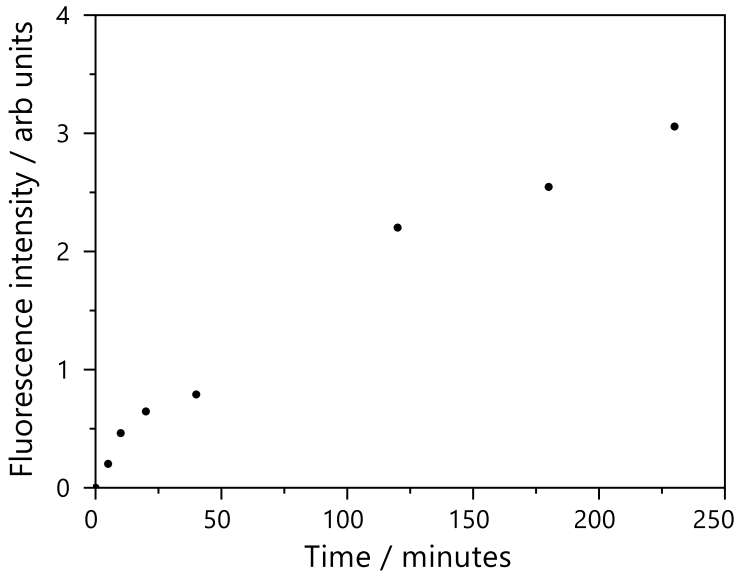

Figure 5.3: Extraction of the fluorescent dye from PMCs using hexane from PMCs over time

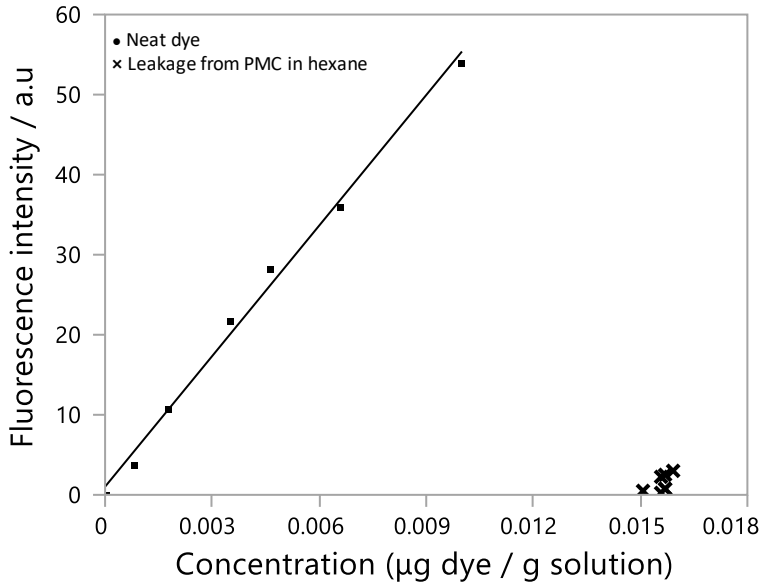

Figure 5.4: Comparison between extraction in hexane of neat dye and leakage of dye from PMCs in hexane

In Figure 5.4 the fluorescence response at different concentrations was plotted in a calibration curve. These concentrations reflected 0-100% theoretical deposition of PMCs on fabric. The

fluorescence response from concentrations of dye added in the time dependent extraction experiment in Figure 5.3 were also plotted in Figure 5.4. This showed that the fluorescence intensities were insignificant with respect to total input of dye in the system. After 40 minutes only ~1.7% of the dye had been extracted and after 230 minutes of extraction ~6.6% of the dye had been extracted. Hexane was chosen as an acceptable solvent providing the balance was found between complete extraction of dye from broken PMCs and unwanted extraction of dye from intact PMCs.

5.2.4 Ethanol as a solvent for extracting encapsulated dye from broken PMCs

Another complicated scenario was with intact PMCs. As seen in water and hexane the PMCs had extremely low permeability, so most solvents left them unaffected. In addition to this, the large hydrodynamic forces during production suggested PMCs were resistant to breakage through this type of force, so this could not be employed in rupturing PMCs in a select solvent. When fixed using an epoxy adhesive and submerged in ethanol it was clear that the intensity of the fluorescent dye in the PMCs decreased, as seen in Figure 5.5, so extraction was possible. When the experiment was repeated at 60°C for 30 minutes any fluorescent dye seen within PMCs at the start was completely lost.

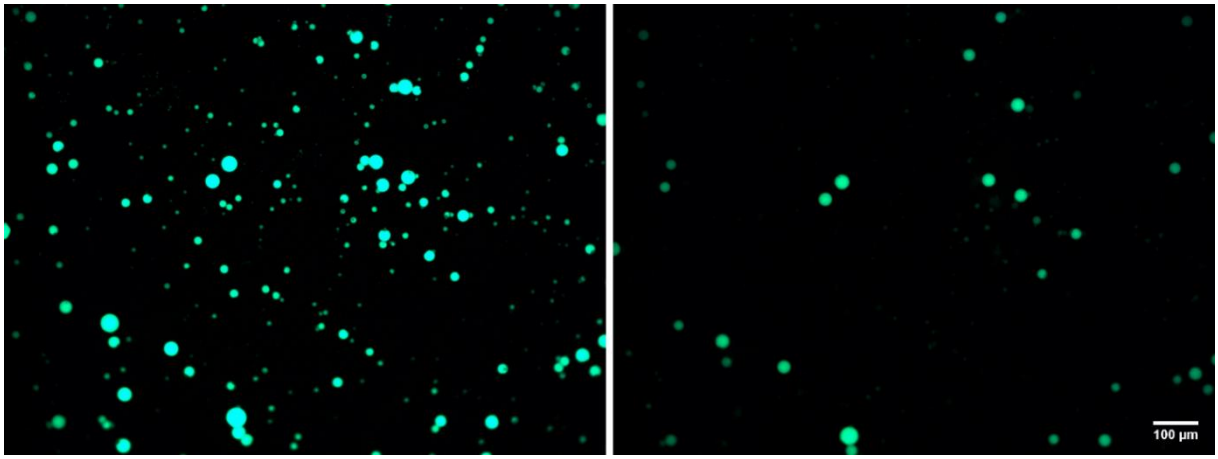

Figure 5.5: PMCs viewed under a fluorescent microscope at t = 0 seconds and after ethanol addition and heat at 270 seconds

In this case though the dye from the intact PMCs was solubilised along with the dye from broken PMCs, so any fluorescence intensity recorded in spectrofluorometry was a combination of both intact and broken PMCs. To identify solely intact PMCs it was necessary to perform the hexane extraction for broken PMCs in tandem and subtract the percentage from the total quantification.

5.2.5 Formation of calibration curves for fabric dye extraction using ethanol and hexane

Absolute quantification of PMC deposited on the fabric was sought. In order to use solvent extraction of dye from fabrics effectively it was necessary to replicate the process using known amounts of dye, with enough concentration points to reduce the prediction limits associated with the calibration curve. These curves were termed forced deposition calibration curves (FDCC). There was also a need to form an instrument calibration curve (ICC) using extraction of the neat dye to understand the detection limits of the spectrofluorometer and also to test the recovery capabilities of the dye from fabrics compared to dye directly dissolved in solvent.

Table 5.1: Input parameters for initial wash tests and resultant calibration curves

Dosage of detergent	65.6 g Heavy duty liquid (HDL)
Perfume Loading	0.56% wt %
Mass and type of ballast	3 kg mixed ballast
Mass and number of swatches	Eight 30x30 cm terry towel swatches

As seen in Figure 5.6, the line of fit via the least squared regression through the calibration concentrations showed the data had good agreement with the fitted line, as confirmed by the high R^2 value. The prediction intervals were also plotted on the calibration curve to show the areas of 95% confidence if a new point randomly chosen was plotted onto the curve. In this case the prediction intervals were quite broad, for example, if the fluorescence intensity of the ethanol wash corresponded to 30% deposition from the regression fit, the error associated with this is around ±12%. To tighten the prediction intervals seven calibration points were subsequently used to form the curve rather than six. It was also clear that there was no deviation from linearity of the calibration curve in the deposition fractions of interest, indicating that experiments were within the maximum fluorescence limits for the spectrofluorometer.

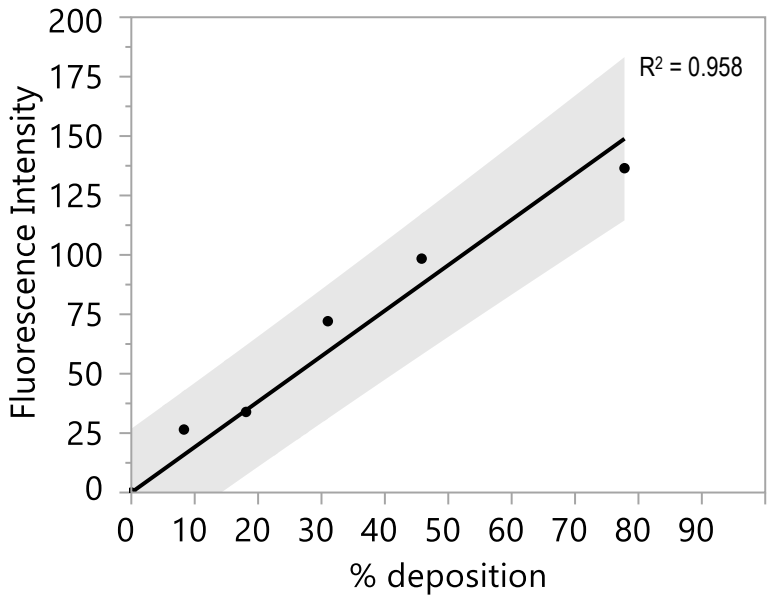

Figure 5.6: Example of initial forced deposition calibration curve from reference sample ethanol extraction

The ICC was formed when the dye was dissolved directly into ethanol. It was created primarily to assess the limits of detection of the spectrofluorometer, to assess the lowest concentration of dye was that the machine could detect. As seen in Figure 5.7 the ICC was plotted along with the line of regression and prediction intervals. At nil concentration of dye, using inverse prediction with the prediction intervals, the concentration limit was found to be 0.00046 µg dye.g^{-1} sol, as indicated by the edge of the prediction intervals at zero fluorescence intensity.

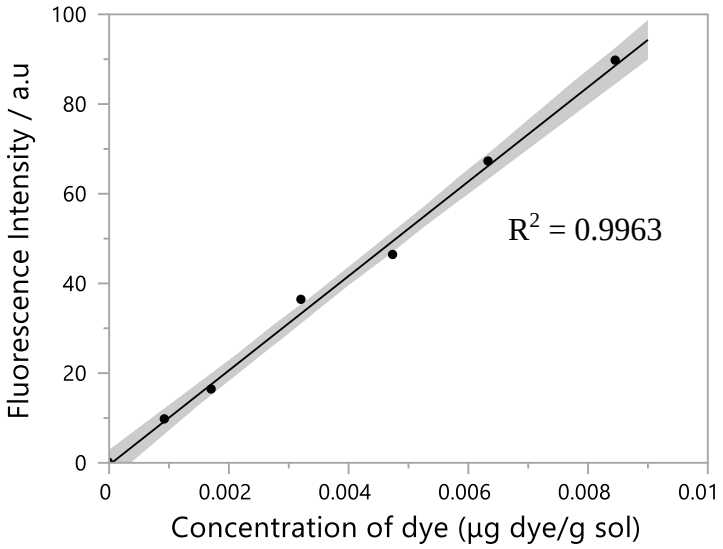

Figure 5.7: Instrument calibration curve for PM546 dye in ethanol

Another result from the ICC was to compare the fluorescence intensity recorded with neat dye dissolved in ethanol with the same amount of dye in ethanol, but this time in encapsulated form in a PMC and needing extraction with the ethanol. From the relative gradients of the regression of each calibration line it was possible to calculate the extraction efficiency. As seen in Figure 5.8, the gradient of the FDCC was lower than the ICC. Had the gradients been the same this would indicate equal extraction efficiency. The extraction efficiency of the forced deposition protocol was 84%, as highlighted in Table 5.2, and calculated from the ratio of the gradients of the FDCC and ICC. The encapsulated dye could migrate into the shell structure as seen by residue images in Figure 5.9, and even after extraction had finished there was still some residual dye in the shell material, which could be the source of the incomplete extraction efficiency.

This, however, was not an issue for quantification of PMCs in wash as the fabric would be treated in the same way as FDCC fabrics, so the extraction efficiency was the same.

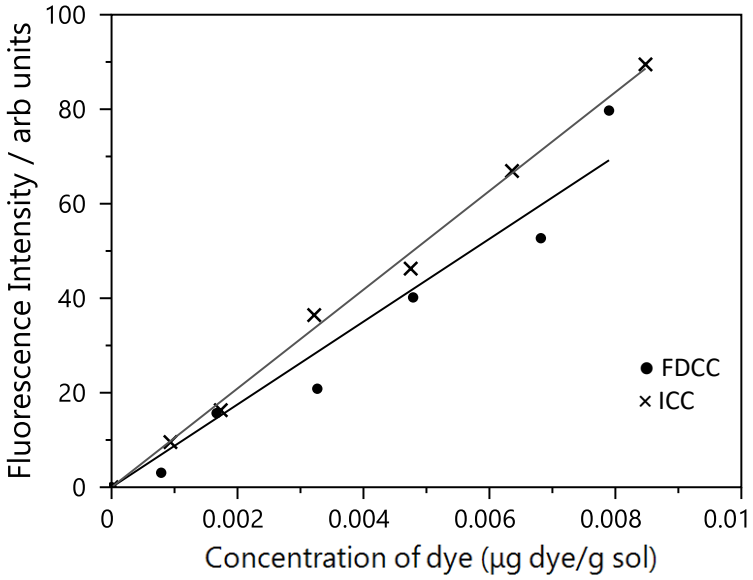

Figure 5.8: Comparison between extraction efficiencies of instrument calibration curves (ICC) and forced deposition calibration curve (FDCC)

Table 5.2: Comparison of gradients of ICC and FDCC for ethanol extraction and the resultant extraction efficiency

Gradient of ICC	Gradient of FDCC	Extraction efficiency
10452	8761	84 %

For the hexane calibration curve the known amounts of PMCs deposited on the fabrics needed to be ruptured prior to extraction so that the all the dye was released and ready to be quantified as with the broken PMCs on the wash fabrics. The images analysed show no intact PMCs remained after compression under the pneumatic press.

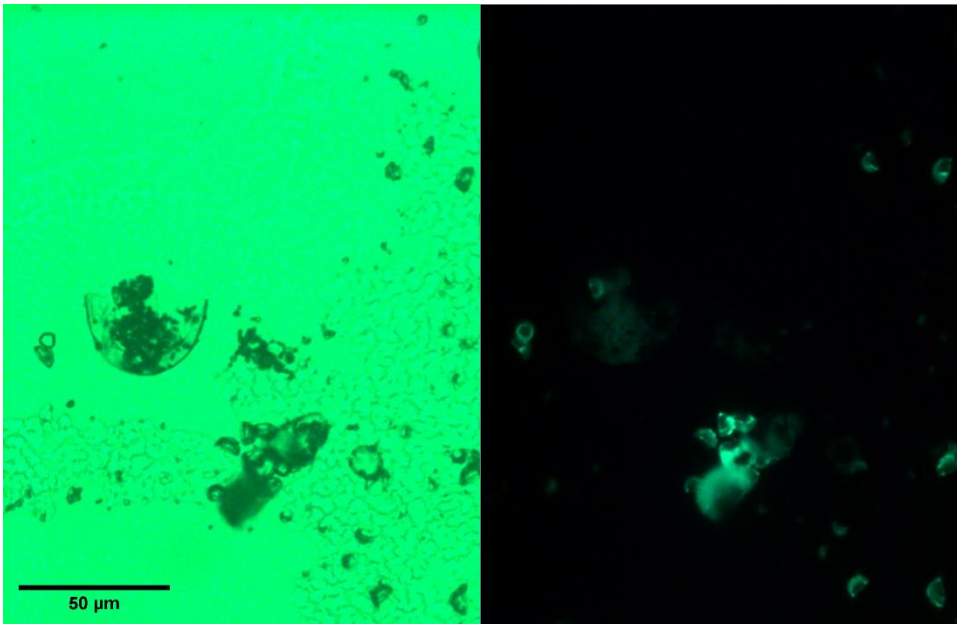

Figure 5.9: Residue of fluorescent dye after extraction seen under bright light to show shell residue, and under fluorescent light

5.2.5.1 Extraction conditions and times

The extraction of the dye into ethanol and hexane solvent phases needed to be identical for both fabrics used to obtain the calibration curve and the wash test results. Extracting the dye from PMCs using ethanol was much more efficient at 60°C, without damaging the dye. The dye was extremely soluble in hexane and there was no need to extract from the core of the PMC, so extraction was chosen to occur at room temperature.

The fluorescence intensity over time was recorded from extractions with hexane and ethanol on fabrics recovered from washes using the standard PMC and heavy-duty liquid detergent conditions and removing aliquots over time for spectrofluorometry analysis. As can be seen in Figure 5.10 after around 60 minutes the extraction process was largely complete and the remaining extract was likely from the shell of the PMCs or the dye trapped deep within the fabric yarns. The extraction could have continued for a longer period of time to ensure

completion, but 60 minutes was chosen as the extraction time to take forward when also considering full experimental time and organisation. The same experiment was run with hexane as a solvent, as seen in Figure 5.11, and it was clear that 60 minutes was needed to ensure excellent extraction of the dye from the fabric. After that there was little change, hence 60 minutes was chosen as the extraction time for both hexane and ethanol.

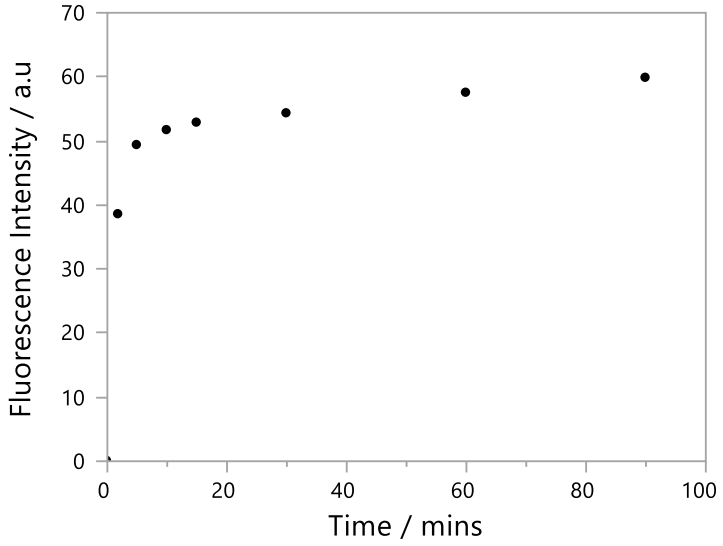

Figure 5.10: Relationship between fluorescence intensity and extraction time for ethanol extraction

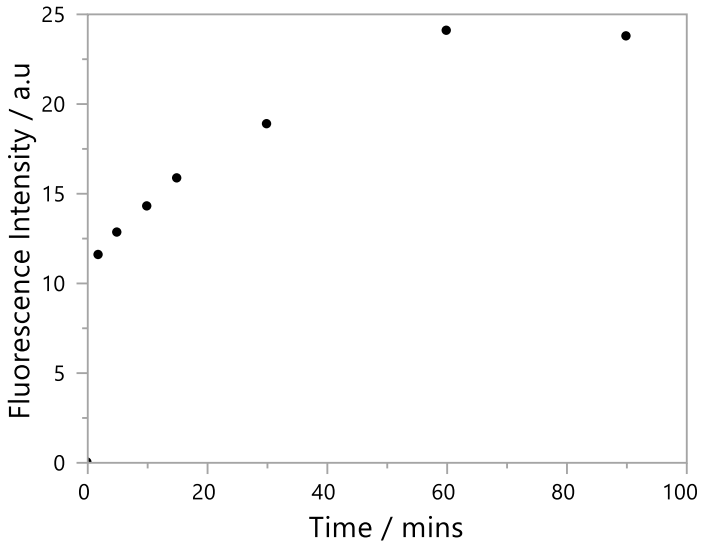

Figure 5.11: Relationship between fluorescence intensity and extraction time for hexane extraction

5.2.5.2 Forced deposition calibration curve (FDCC) for ethanol

Calibration curves for ethanol extraction of the reference sample run under a high energy washing cycle with mixed ballast were formed, to obtain the quantity of PMCs deposited at each stage of the wash, and a percentage for how many remained at the end of the wash. As seen in Figure 5.12: Results for deposition of PMC throughout the wash in a mixed ballast with terry towel swatches. Error bars represent the standard error of the mean. The overall total deposition started above 150 % after the main wash, which was impossible, so the extraction overpredicted the amount of PMCs present.

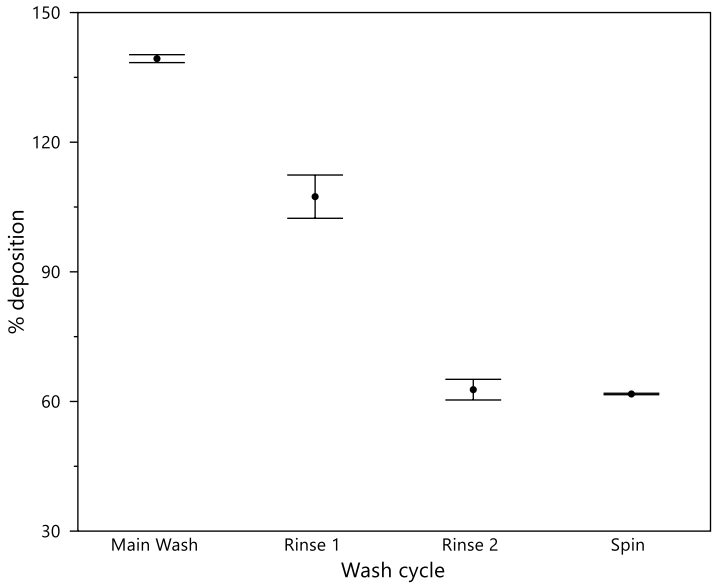

Figure 5.12: Results for deposition of PMC throughout the wash in a mixed ballast with terry towel swatches. Error bars represent the standard error of the mean.

Firstly, the influence of HDL detergent was tested to understand if there was any residual fluorescence in certain materials in the formulation that contributed to the overall fluorescence signal recorded in the deposition extraction. As seen in Figure 5.13, running the extraction with no HDL or PMC yielded the same fluorescence intensity, indicating that the HDL contributed no residual fluorescence to the results. Once the extraction was performed with PMC present within the detergent formulation, there was a significant increase in the fluorescence signal. This confirmed that it was only the PMC that contributed to any fluorescence signal observed in the extraction process under the stated input parameters.

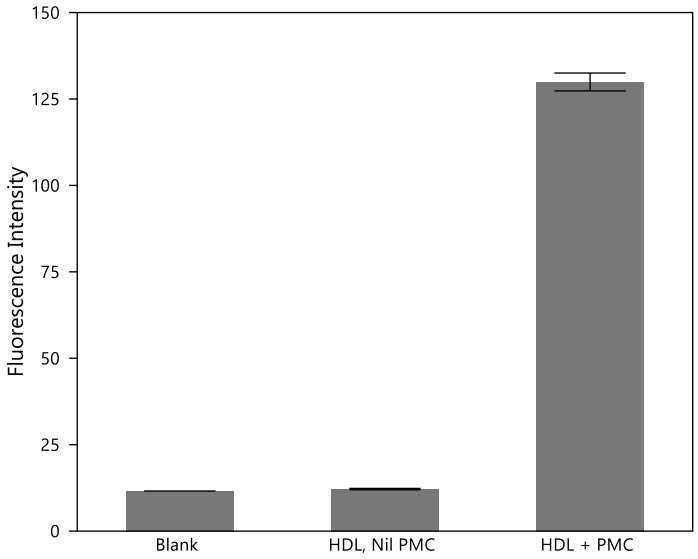

Figure 5.13: Fluorescence response from blank, HDL only, and HDL with dosage of PMC added. Error bars represent the standard error of the mean for 4 experiments.

Another aspect of the forced deposition method that was potentially contributing to the overestimation in fluorescence was the impact of the ballast. The mixed ballast load was composed of terry cotton, knitted cotton and polyester. Each type of fabric has an associated maximum water absorbency. Terry cotton for example absorbed up to 4.5 kg of water per kg of fabric, knitted cotton absorbed 3 kg of water per kg of fabrics. As the terry cotton held more water. and the PMCs were dispersed in the water, this meant that more PMCs could become embedded in the fabrics for higher absorbency types. If the swatches were made from terry cotton a disproportionate number of PMCs would deposit here rather than on the other swatches, meaning the effective loading of PMCs to terry cotton would exceed 100%, accounting for the overestimation in deposition throughout the wash cycles in a mixed ballast wash scenario. Tests were run with 3 kg of knitted cotton ballast and knitted cotton swatches to remove the impact of mixed ballast affecting homogenous PMC deposition. Knitted cotton was

chosen over terry cotton as the structure was able to retain its water absorbency capabilities after many washes, unlike terry cotton which loses its absorbency.

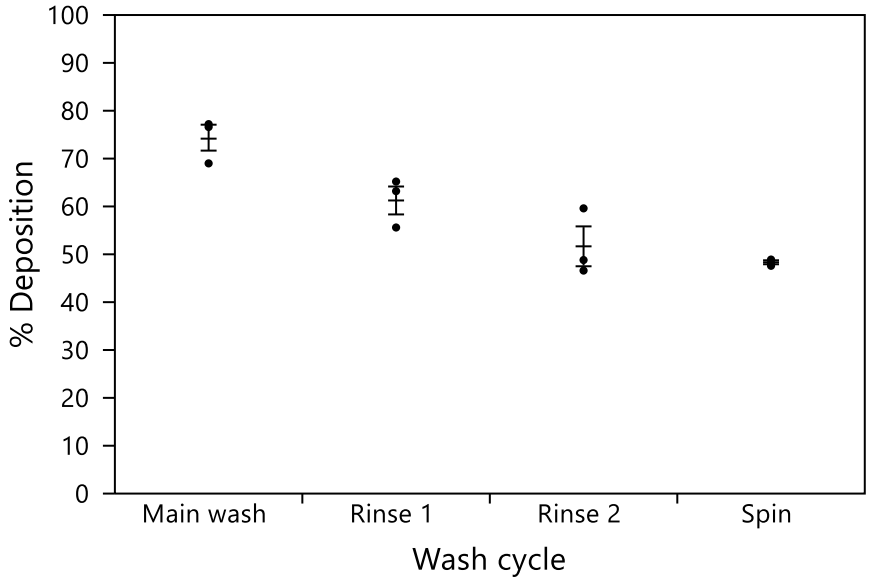

Figure 5.14: Results for deposition of PMC throughout the wash in a knitted cotton only ballast. Error bars represent the standard error of the mean.

As seen in Figure 5.14, the total deposition never exceeded 100%, so changing to a single fabric ballast removed the overestimation of the total deposition on fabric at the end of each wash stage.

5.2.6 Effect of sampling from different swatches / different areas on the same swatch

Investigating how the deposition of PMCs on fabrics differed on the same swatch and between swatches was important in understanding how many samples needed to be taken for each wash cycle to get a result that was representative of the whole ballast load. If there was “spotty” deposition on the fabrics it meant that certain areas contained disproportionately higher numbers of PMCs than others. For example, the surface area at the edges of the fabric was

slightly increased compared to the centre due to the presence of the additional edge, but then this might have been less proficient in acting as a filter for PMCs. Experiments were conducted where six fabrics samples were cut from each swatch, and within the swatch the fabric was cut from the edge, the centre, and one in between, two samples for each. The sample was repeated for another swatch and the two sample t-test showed no significant difference between replicate 1 (mean = 46.9, SD = 1.8) and replicate 2 (mean = 48.1, SD = 4.8) t=0.385, p=0.05.

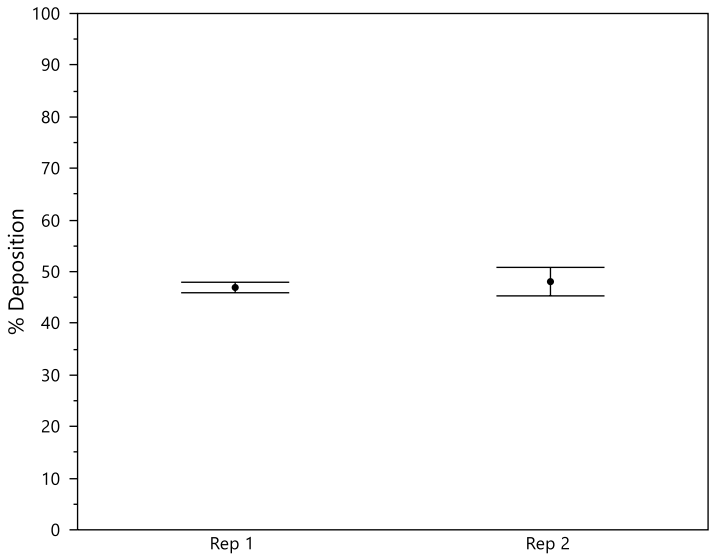

Figure 5.15: Results showing variation in deposition of PMC on the same swatch and between different swatches. Error bars represent the standard error of the mean.

5.3 Quantifying intact PMCs in washwater

5.3.1 Filtering the washwater samples and applying ethanol extraction method

A simple setup was created to quantify the number of intact PMCs present in washwater. With all samples tested, < 1.5 vol. % of the PMCs were < 2.5 µm in diameter. A filter paper with a 2.5 µm pore size was chosen and a vacuum filtration setup was used to filter washwater solutions through, whilst trapping the PMCs on the surface. Known quantities of PMCs were

also filtered to form a calibration curve, and an extraction of PM546 fluorescent dye in ethanol was conducted, similar to the deposition method for total PMCs deposited in fabric.

Prior to the extraction the filtrate was washed with hexane. This ensured that any dye from broken PMCs that resided on the filter paper was washed away, leaving just the intact PMCs.

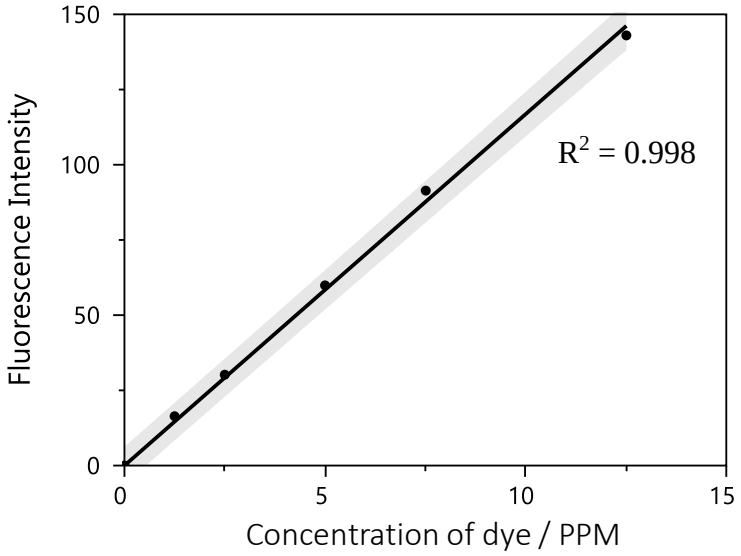

Figure 5.16: Example ethanol forced deposition calibration curve for filtration of PMCs, used to quantify intact PMCs in washwater

5.4 Quantifying broken PMCs in washwater

As mentioned earlier in the chapter, perfume was used as the marker for quantification of broken PMCs in washwater. Perfume, however, is insoluble in water – part of the reason why it is not used as a solvent in the fragrance industry, alongside reactivity of water with some ingredients. In washwater, however, there were surfactants from the detergent present which aided emulsification of the perfume in water, making a much more homogenous solution and opening up the possibility to quantify. As in all other previously introduced methods, the unknown volumes of perfume in the washwater were quantified by comparing cumulative peak

areas from all individual constituents in the perfume with the total peak area measured from forming a calibration curve with known amounts of perfume, and the reasoning behind this is explained in Section 5.4.1.

In contrast to the deposition method, the perfume for the calibration curves was added directly to the solutions, and not extracted from intact PMCs, hence the variation in points was expected to be much lower.

To fully form the mass balance, it was necessary to collect all wash water to account for all capsules from the multiple wash stages.

5.4.1 How to use peak areas of individual perfume raw materials from GC-MS to quantify overall breakage

Given the complexity of the perfume there were several approaches that could be taken in order to calculate an overall number of PMCs broken in washwater. It was possible to assess the peak areas of individual perfume raw materials (PRMs), or by taking all PRMs into consideration and cumulatively assessing peak area.

The issue with assessing individual PRMs was that several factors can affect the accuracy of any formed calibration curve for the PRM such as the volatility of the compound, related vapour pressure, the partition coefficient of the compound in each phase, related to the relative solubility, and also the relative quantities of each compound, where the sensitivity of the GC-MS could limit accuracy.

Taking this into consideration it was decided that the total peak area for each PRM was to be summated to get a cumulative peak area, which simplified analysis and removed any bias towards specific PRMs.

5.4.2 Washwater liquor as background baseline signal

Each drained sample of washwater from the washing machine exhibited a different chemistry. For example, the liquor drained from the main wash contained most of the detergent chemistry. The first rinse contained some chemistry rinsed off the clothes and the final rinse contained less of this chemistry. The impact this had on headspace GC-MS analysis was related to changing the partition coefficient. Perfume dissolved in a specific environment showed a specific tendency to partition into the headspace from the solution phase, altering the cumulative peak areas between what should be identical calibration samples. This hypothesis was tested by spiking washwater samples with known amounts of perfume. Headspace GC-MS analysis was conducted on the washwater samples and the spiked washwater samples. The headspace response of the washwater was then subtracted from the spiked washwater samples to give solely the headspace response of the perfume. Variation in this value, as seen in Figure 5.17, showed that the water in each wash cycle drain impacted the overall peak area measured for the neat perfume, and as such, for each wash cycle (main wash, rinse 1, rinse 2) an individual calibration curve was formed to remove this influence. It was seen that despite spiking washwater with identical amounts of perfume, the headspace peak area response for the neat perfume in each sample was different. This was evident through the difference in gradient, meaning that the same concentration of perfume gave a different peak area. The main wash showed a much lower peak area response, meaning an overestimation of PPM of perfume in an unknown washwater sample, and hence an overestimation in the number of broken PMCs in the washwater compared to using water from the two rinse stages.

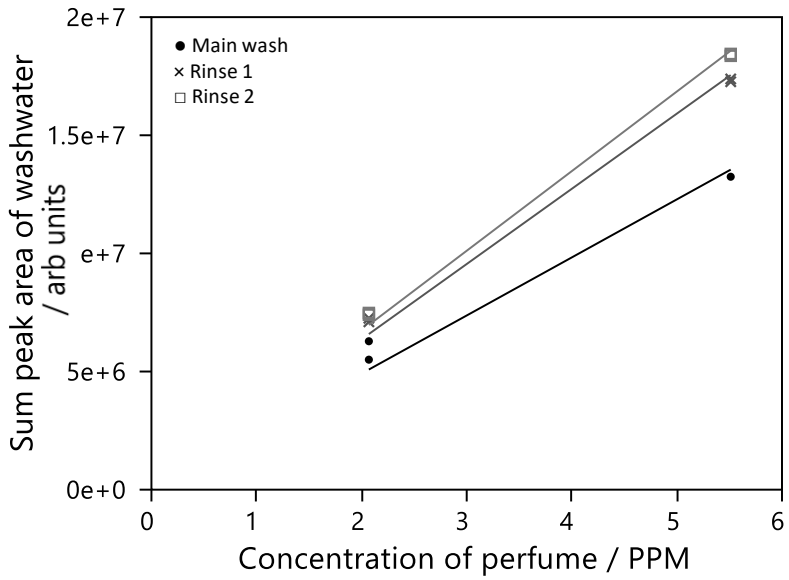

Figure 5.17: Comparison of calibration curves for washwater from different wash cycles spiked with known quantities of perfume

5.5 Example of completed mass balance

Once each of the methods was finalised it was possible to tie them all together to complete the mass balance. The conditions used were 65.6 g of perfumeless HDL with 0.56% perfume added via PMCs. 3 kg of knitted cotton ballast was used along with 30 x 30 cm knitted cotton swatches. The programme was the high energy wash scenario as detailed in Chapter 3.

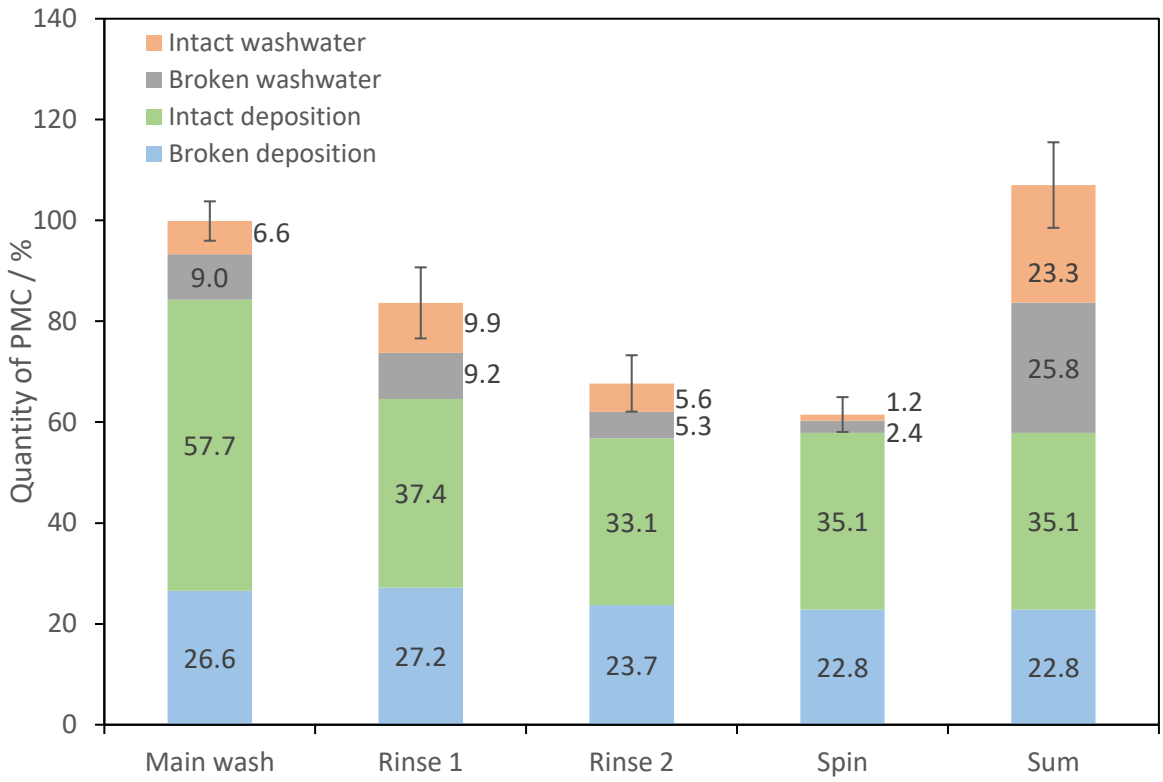

Figure 5.18: Results of how the PMC mass balance varied throughout the wash cycle and the total mass balance. Errors bars represent 95% CI for of all output streams for each wash stage

The experiment was split up to identify PMC quantification after each wash cycle. The mass balance after the main wash stage, where all PMCs were still present within the closed system of the drum closed out at 99.9 ± 3.9%. Prior to rinse 1, PMCs in the washwater were lost to the drain. Theoretically the PMCs in the system were then confined to those deposited on the fabric. As the cycles progressed the overall mass balance should be the sum of broken and intact deposition should not exceed that of the previous cycle.

It was observed that once deposited on fabric after the main wash, further breakage occurs during the first rinse as intact deposition drops from 57.7% to 37.4%. After this stage the intact

deposition only fell to 35.1%, potentially indicating that once deposited and embedded deep in the fabric breakage did not occur significantly.

To obtain the total overall mass balance in the machine it was necessary to include the final deposition quantities and the sum of all the PMCs lost to washwater throughout the wash. This totalled 107 ± 8.5%. The calculations for converting concentrations to PMC input percentages, along with error calculations associated with combining mass balance methodologies are detailed in Appendix B. As such, the mass balance needed to be treated as a good approximation of overall PMC numbers, which could be uniquely used to identify counterbalances in output streams under different conditions and a good comparison of the same output streams under different conditions. This approximation was taken into consideration when drawing conclusions on absolute values, as outlined in Chapter 6.

5.6 Conclusions

To identify the quantities and locations of intact and broken PMCs after a wash cycle, the system was divided into four output streams; intact and broken in fabrics and intact and broken in washwater. An analytical technique was devised for each output stream to accurately quantify PMCs.

For intact PMCs in fabric fluorescence microscopy was initially used, however this severely underestimated the number of intact PMCs. Instead, a method based on extracting fluorescent dye from the PMC core using ethanol was used which quantified the total PMCs on fabric. Steps were taken to ensure the correct extraction conditions in terms of solvent choice, time and temperature were chosen, and work was carried out to prove that the calibration curves were

accurately quantifying unknown numbers of PMCs. This involved ensuring a single ballast load was chosen to remove influence of the absorbency of fabrics and linked affinities of PMCs on the quantification. In a similar vein the number of broken PMCs was found by using a similar extraction method, this time with hexane as the solvent. This ensured any intact PMCs remained intact and were not quantified. Steps were taken to choose the correct extraction times and temperatures, and by subtracting the quantity of broken PMCs from the total quantity of PMCs in fabric as found by ethanol extraction, it was possible to estimate the number of intact PMCs.

To quantify the number of intact PMCs in washwater a similar extraction method using ethanol was introduced, with an added filtration step. This built on the previous learnings to accurately quantify PMCs.

Finally, a method was developed to quantify broken PMCs in washwater by analysing the quantity of perfume present against known quantities using calibration curves. It was found that individual calibration curves were needed for quantification of each wash cycle due to changeable partition coefficients of the washwater liquor. By combining quantities from wash cycles it was possible to accurately quantify the unknown number of broken PMCs in each stage. The cumulative peak area for all the perfume components from GC-MS was used as this reduced the influence of volatility on quantification.

By running each of the quantification techniques for the output streams it was possible to collate data for a complete mass balance either after each cycle of the wash, or at the end of the wash. Using the reference sample under a high stress wash scenario it was possible to understand how the quantities of PMCs in each output stream changed as the wash progressed. The overall mass balance closed out at 107%; a good approximation considering the complexity of the mass balance. The value in the technique was in comparing the mass balance between different PMC

samples or different wash conditions to understand how to improve deposition and reduce unwanted breakage and this was investigated in the following chapter.

Chapter 6. APPLICATION OF MASS BALANCE, OLFACTIVE AND HEADSPACE GC-MS PROTOCOLS TO ASSESS PMC PERFORMANCE

6.1 Introduction

In the work presented in Chapter 5 it was demonstrated that through the combination of several methodologies, it was possible to quantify the PMCs in a front load washing machine, whether they were intact or broken, and at any time during the cycle. These techniques open up the possibility of assessing PMC performance in full scale washing situations. Supplementary techniques presented in this chapter such as fabric headspace GC-MS and olfactive evaluation backup the mass balance by showing relative tangible performance differentials that translate absolute quantity differences between samples into meaningful, perceivable results for end user application. The ability to provide both absolute quantification of each output stream and the relative performance differentials can allow for refinement of wash conditions, it can influence PMC design to optimise the capsules, and provide clarity on the correct dosage of PMCs in the finished product, which not only impacts performance, but can drive cost-effectiveness.

Firstly, samples that showed strong variation in mechanical strength assessed through micromanipulation measurements of single PMCs in Chapter 4 were selected for full mass balance experiments in front load machines to investigate whether the difference in mechanical strength impacted performance through changing the distributions of PMCs in the output streams in a full scale wash scenario. Olfactive evaluations and relative headspace GC-MS analysis were also conducted on these samples.

The mass balance quantification protocols not only offer insights into how different samples and wash conditions affect the distribution of PMCs into each output stream, but they also offer the opportunity to build mechanistic understanding of what drives breakage in the wash. Wash cycles were run without ballast to understand the importance of fabric and hydrodynamic forces on PMC breakage. The effect of frequency of rotations of the drum was tested in a front load wash scenario. In these experiments a low energy cycle, akin to a 'delicates' wash was run alongside a high energy standard short wash to assess how this impacted deposition and breakage of PMCs.

After reflection on data from initial samples chosen from nominal rupture stress resulting from micromanipulation, additional samples with more extreme mechanical properties were requested and worked through the quantification protocols. Combining all results together allowed for the identification of a new set of tests for predicting PMC sample performance in a wash before conducting full scale experiments.

Business needs dictate that work to understand PMC performance was also conducted on alternative wash scenarios. This involved reapplying the protocols on a top load semi-automatic washing machine to complement the work already done in front load machines.

As discussed in Chapter 5, wash cycles were conducted using single fabric ballasts to increase accuracy in quantification. For the mass balance experiments the aim was to provide as closely as possible an absolute quantification of PMCs in each output stream based on volume of core material present, but to be realistic since completing the true mass balance was an extremely challenging task. Due to there being multiple wash cycles and 4 potential output streams there was propagation of many errors and therefore it was important to display the degree of error

associated with each estimation to show the degree of confidence under which results can be cross compared.

6.2 Completing the distribution of PMCs for the reference PMC sample and knitted cotton ballast using the mass balance quantification protocols

Figure 6.1 focuses firstly on the deposition of PMCs, both intact and broken from a high energy wash cycle on the reference PMC sample with a knitted cotton ballast. It was seen that the total deposition plateaued at the end of the main wash cycle at 84.3 ± 3.8%. This suggested that the PMCs overall had a strong affinity for the fabric, either through chemical attraction to the fibres or by physical entrapment in the fabric yarn structure.

The largest decrease in deposition was seen during the first rinse, either through PMCs becoming dislodged due to not being strongly held enough by the fabrics, or through breakage. As the wash progressed to rinse 2 and the final spin, the total deposition did not change significantly. Additionally, once rinse 1 had started the quantity of broken and intact deposition of PMCs did not show significant difference in any stage. For the deposited broken PMCs it was not possible to decipher solely from deposition data whether this was due to the dye remaining on the fabrics, or some dye being washed away and replenished with dye from newly ruptured PMCs. Whatever remained deposited on the fabric at the end of the spin was used as the deposition data for the mass balance. When focusing on the intact PMCs, however, an interesting insight was that whatever was deposited after rinse 1 largely remained on the fabric.

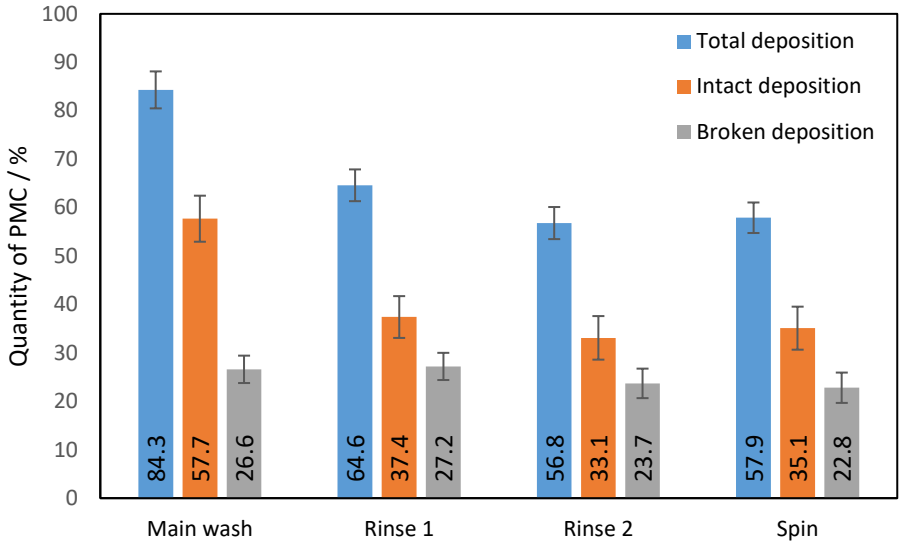

Figure 6.1: Variation in the deposition of intact and broken PMCs on fabric over the course of a wash for the reference sample with a knitted cotton ballast. Error bars = 95% CI

The mechanisms of reducing intact and broken deposition of PMCs could be approached in a number of ways. Firstly, the PMCs could rupture, decreasing the deposition on fabrics. Secondly, PMCs that were not sufficiently well embedded within the pores of the yarns in the fabrics could become dislodged upon the movement of the drum and fabric.

Within this dislodging there hides a third mechanism of removal through diffusophoresis via the "stagnant core problem" (Shin et al., 2018). The tiny pores in fabrics do not allow significant fluid flow inside them and therefore any PMCs that enter these inner pores would find it extremely difficult to vacate them. It was seen, however, in the study that particles in fabric pores left on much faster timescales than expected. This only happened for particles deep within the pore when the surfactant rich fabric was exposed to fresh rinse water and not when the water was surfactant rich. The surfactant gradient causes diffusiophoresis; a directed motion of surfactant molecules down a chemical gradient that also removes entrained particulate matter,

such as dirt or PMCs with it. The observations in this test would agree with this theory, where the largest chemical gradient was observed after the main wash as the fresh water for rinse was introduced. This cycle saw the greatest reduction of intact PMCs, followed by a smaller reduction in rinse 2, as the chemical gradient decreased less severely. By the final spin the surfactant had largely been removed, and hence there was no change in intact deposition. As mentioned earlier however, the deposition and removal of intact PMCs was likely a combination of breakage, dislodgement due to poor entrapment, and dislodgement through diffusiophoresis.

The error bars in Figure 6.1 were displayed as the 95% confidence intervals of the mean values. The equation for this can be seen in Appendix B and takes into consideration the errors in the measurement of the unknown measured y values from samples, and the errors associated with the calibration curve. The error for total deposition and broken deposition were determined directly, however the error for intact deposition was a propagation of the total and broken deposition.

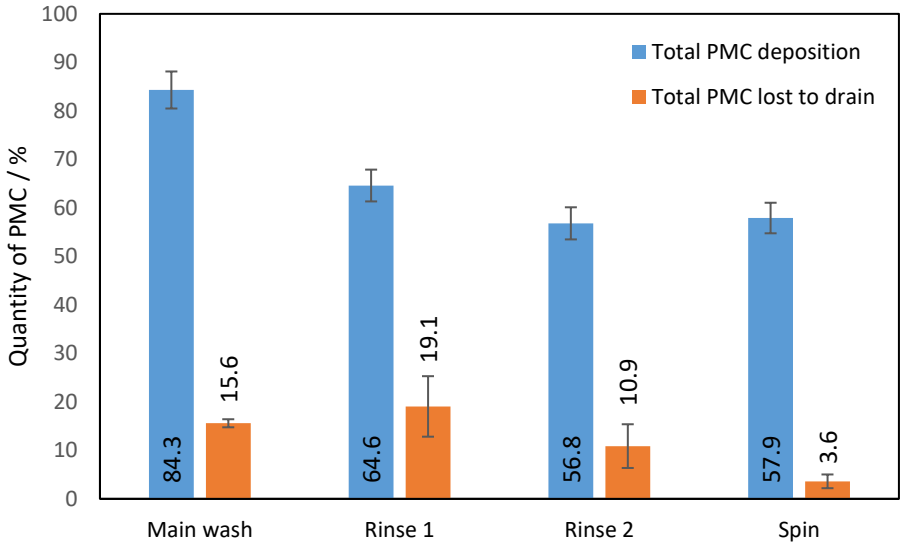

Figure 6.2: The development of the quantity of total PMCs deposited in fabric over the wash cycles and the counterbalanced loss of intact and broken PMCs to the drain via the washwater. Error bars = 95% CI

As seen in Figure 6.2, and as highlighted previously, the total deposition (intact and broken) of PMCs on fabric at the end of the main wash was high and subsequently reduced to 57.9 ± 4.5% by the end of the wash. The ability for the mass balance to capture the location of PMCs was highlighted when taking the PMCs lost to the drain into consideration. At the end of the main wash 84.3 ± 3.8% of the PMCs input in the wash (intact and broken) were deposited on fabric. To counterbalance this, the washwater liquor analysis captured 15.6 ± 0.8% of PMCs (intact and broken) in the washwater liquor, and the combination of the two was an excellent estimate for total PMC input. For the rinse 1 cycle the total input of PMCs was a carry-over from the quantity of PMCs deposited on the fabric at the end of the main wash, as the remaining PMCs in washwater at this stage were now lost to the drain. Again, the combination of total deposited PMCs in rinse 1, 64.6 ± 6.0% and the total quantity of PMCs lost to the drain, 19.1 ± 6.2% was

an excellent estimate of the new total input for that wash stage (84.3 ± 3.8 %). This trend was continued for rinse 2 and the spin.

6.3 Investigating the distribution of PMCs for lower median size and 95/5 core/shell ratio samples using the mass balance quantification protocols

As seen in Chapter 4, the two samples that most altered the nominal rupture stress of the sample at each PMC diameter compared to the reference sample were the lower median size sample, which significantly lowered rupture stress, and the 95/5 core/shell ratio which significantly increased the nominal rupture stress at all diameters measured. These samples were then subjected to the same wash conditions as the reference sample, and mass balance protocols for each of the output streams were completed to investigate how this impacted the distribution of PMCs. The results of these experiments can be seen in Figure 6.3.

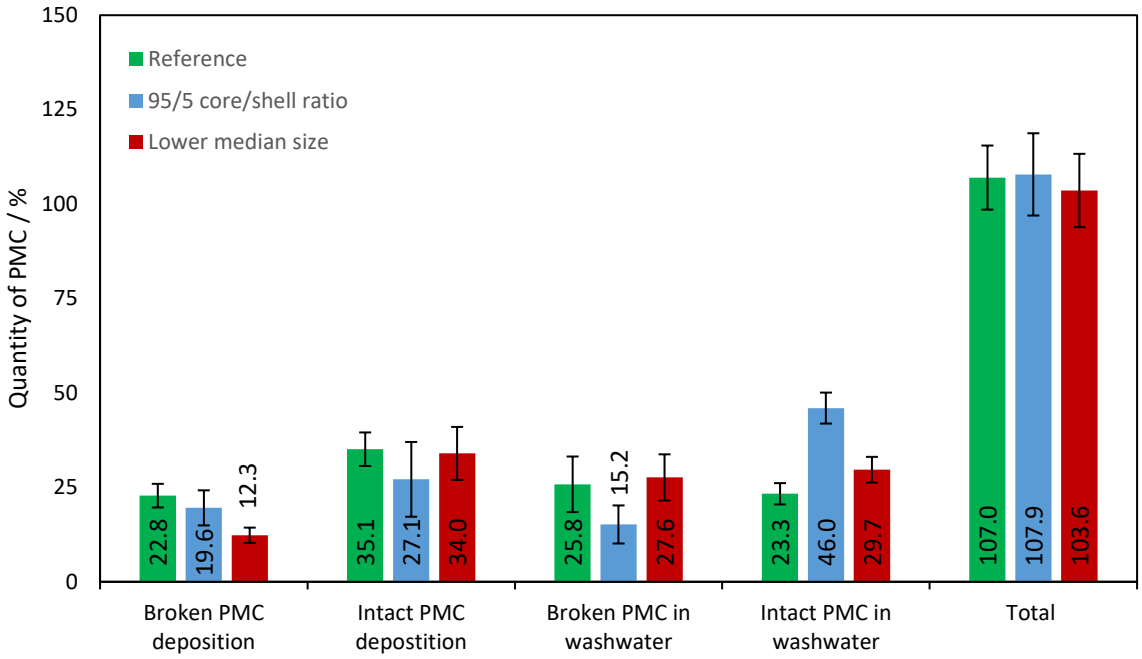

Figure 6.3: The mass balance of PMCs of the reference sample compared to lower median size and 95/5 core/shell ratio samples, broken down into the different output streams. Error bars = 95% CI

The number of intact PMCs quantified in washwater was significantly greater for 95/5 core/shell ratio sample at 46.0 ± 4.1% compared to 23.3 ± 2.8% for the reference sample. This agreed with the mechanical strength data as indicated by the nominal rupture stress where the 95/5 core/shell ratio sample was significantly stronger than the reference. As expected, the trend in broken PMCs in washwater was the reverse of this, where fewer broken PMCs were quantified due to this increase in size. Surprisingly the lower median size sample did not follow this trend. It was weaker as measured by nominal rupture stress compared to the reference as seen in section 4.5.3, but there was no significant difference in intact PMC numbers in washwater and broken PMC numbers in washwater between the two samples.

The deposition data showed no significant difference in the samples in terms of intact deposition and in broken deposition on fabric, and only the lower median size sample showed a significant

decrease in deposition with respect to the reference and 95/5 core/shell ratio samples, which would not have been expected given the weaker nature of the sample. Other than the weaker mechanical strength of the sample the median size is also much lower with a d_{50} of 12.2 µm compared to 18.2 µm in the reference sample. Despite this there seemed to be no significant effect on the ability of these PMCs to deposit intact on the fabrics and stay deposited.

6.4 Understanding the influence of fabric on the rupture of PMCs

PMCs are synthesised under extremely high shear conditions, which accounts for the small size of the microcapsules. The hydrodynamic forces in the washing machine were expected to be significantly lower than those experienced in synthesis. It was therefore hypothesised that breakage observed in washing machines could not be caused by hydrodynamic forces in the water, but rather through interaction between the PMCs and fabric. These forces could be applied through compression, or through friction against the fibres; a subject which will be investigated in Chapter 7. To study this, a wash was conducted under high energy conditions but in the absence of fabric ballast. With no ballast present, the quantification protocols for fabric deposition were redundant, and only the protocol for broken PMCs in washwater was studied.

Table 6.1: Quantity of PMCs broken in each wash cycle in a high energy wash in the absence of fabric ballast

Wash Cycle	Broken PMC in washwater / % of input
Main wash	0.7
Rinse 1	0.1
Rinse 2	0.7
Spin	0.0

As shown in Table 6.1, the number of PMCs broken in each wash cycle was extremely small, totalling under 2% of overall input. The source of this 2% might also have been from residual perfume that has diffused out of the PMCs in storage and hence a conclusion was drawn that it was predominantly the fabric that caused rupture of PMCs in a wash cycle and not the rotation of the drum and resultant hydrodynamic forces.

6.5 Understanding the effect of the frequency of rotations in wash cycles on the overall mass balance and the distribution of PMCs

Energy is put into a washing machine predominantly from two different sources; the heating of the water to a wash temperature and keeping it at that temperature, and the energy required to rotate the drum. Most of the work was needed to get the drum in motion and once moving the energy requirement was reduced. As outlined in the materials and methods section, two wash cycles were created to mimic what would be a high and low energy wash in a more controlled way than if it were a pre-set cycle. The difference between the two cycles was in the rotational frequency of the drum. The low energy cycle, akin to a 'delicates cycle' rotated the drum at 60 rpm, and the high energy cycle, akin to a standard fast wash, rotated the drum at 45 rpm. Had these cycles been run without ballast, the energy of the cycle would be correlated with the rotation of the drum, with more rotations using more energy. When ballast was added to the washing machine this reversed the energy impact on the drums. At 60 rpm the ballast moved around the edge of the drum with the aid of the inner drum paddles, never dropping to the base as there was not enough stationary time. This meant that after the drum momentarily stopped rotating, the fabric still largely moved as a unit with the drum, so that when the rotations started again the fabric easily started to rotate with the drum. At 45 rpm, there was increased stationary

time and fabric at the top of the drum in these cycles dropped to the base of the drum prior to the rotations resuming. The impact this had energetically was that more torque was needed on the drum to resume movement, as there was a greater mass of now loose heavy ballast that needed to begin motion. The energy difference between the cycles was an impact of the internal movements of the fabric in the drum rather than the directly correlating with the rotation of the drum. Typical energy usage in the machines at high and low energy as recorded by an in-line power meter are seen in Table 6.2 below:

Table 6.2: Power consumption of the washing machines in high energy and low energy cycles with associated standard deviation from 3 complete cycles

	45 rpm cycle	**60 rpm cycle**
Power used / W	1231 ± 41	1180 ± 32

The impact that this change in motion had was seen in Figure 6.4, where the quantification of the number of PMCs in each output stream was measured.

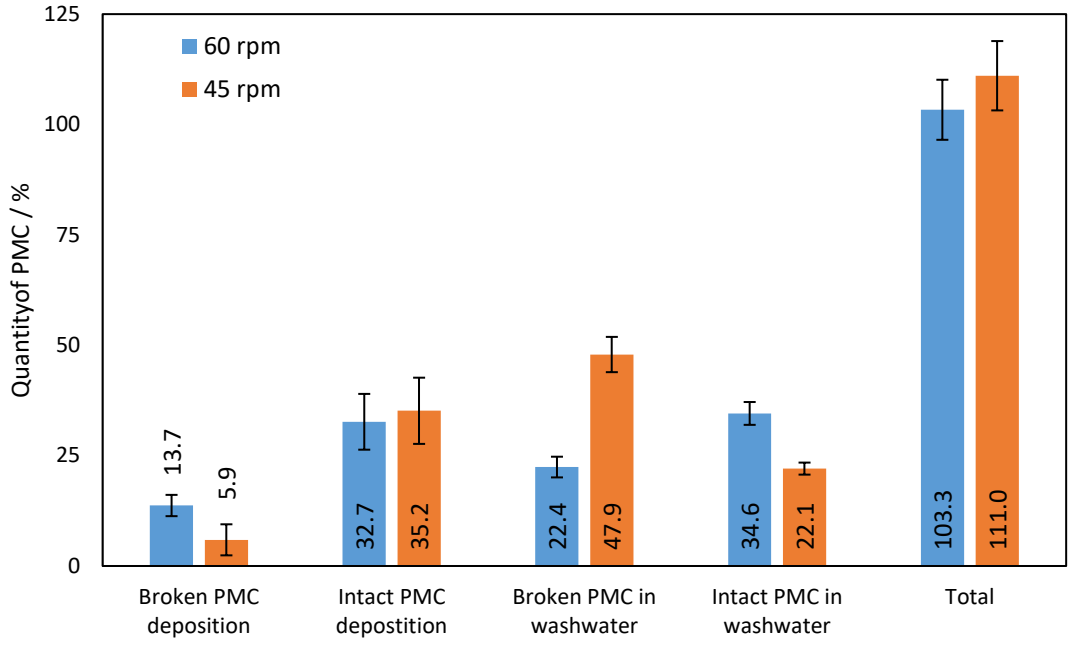

Figure 6.4: Distribution of the quantity of PMCs across each output stream at the end of 45 rpm and 60 rpm wash cycles. Error bars = 95% CI

Firstly, when studying the data there were 22.4 ± 2.3% PMCs broken in washwater in a 60 rpm cycle, compared to a significantly larger 47.9 ± 4.0% broken PMCs in washwater in the 45 rpm cycle. The cause of this was likely due to a combination of an increased compressive force between the PMCs and the fabric as it fell from the roof of the drum upon the drum pausing, and through the increased agitation of the fabric, causing localised areas of compression and friction through folding. Despite the changes in the characteristics of movement of the fabrics within the drum, the quantity of intact PMCs deposited on the fabric was not significantly different, with 32.7 ± 6.3% on fabrics from a 60 rpm wash, and 35.2 ±7.5% on fabrics from a 45 rpm wash. As there was significantly more breakage in washwater for a 45 rpm wash, and parity observed in intact deposition, the counterbalance for PMC totals was found in the broken PMC deposition and the quantity of intact PMCs in washwater, where the values were

significantly larger for the 60 rpm wash cycle. A greater number of intact PMCs in washwater agreed with the notion that the 60 rpm wash cycle subjected the PMCs to lower compressive and friction forces against the ballast, resulting in a greater proportion of intact PMCs in the washwater.

6.6 Understanding the effects of ballast type on the distribution of PMCs using the mass balance quantification protocols

Each fabric type has its own specific density, and fabrics themselves have different water absorbency characteristics depending on the fibre material, as highlighted in the method development of the mass balance protocols in Chapter 5. A study was conducted where the knitted cotton ballast and tracers were replaced by the same mass of terry cotton ballast and tracers. Identical wash conditions were used for each fabric type, and the impact that the change of fabric had on the volume of free water was clear as it was removed from the machine, as seen in Table 6.3. 16 L of water was added in each wash, and at the end of the main wash 7.20 L was removed when the ballast was knitted cotton compared to 5.61 L removed when the ballast was terry cotton. This suggested that more water was retained by the fabric when the ballast was terry cotton. A similar trend was subsequently observed for both rinse cycles, and at the point before the final spin there was more water in the terry cotton fabric (7.46 L) than the knitted cotton (6.48 L) and therefore a greater volume was removed under the final spin.

Table 6.3: Volume of water removed from the drain for each cycle in washes with different ballast and tracer fabric types

	Volume of water removed / L	
	Knitted cotton ballast	**Terry cotton ballast**
Main wash	7.20	5.61
Rinse 1	15.56	13.24
Rinse 2	15.32	14.54
Spin	6.48	7.46

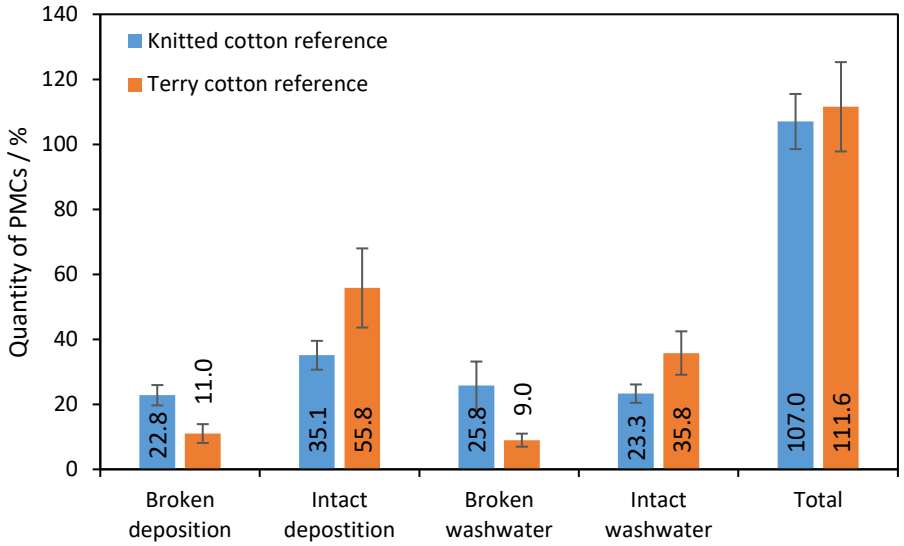

Figure 6.5: Distribution of PMCs across each output stream for knitted cotton only and terry cotton only ballasts in high energy wash cycles. Error bars = 95% CI

The quantification of PMCs in each of the output streams was conducted for each of the ballast loads to understand the influence of fabric type on the distribution of PMCs at the end of the wash, and the overall results are shown in Figure 6.5. Intact deposition in a terry cotton ballast was significantly higher than in a knitted cotton ballast at 55.8 ± 12.2% compared to 35.1 ± 4.0%. This was likely caused by a combination of effects. Firstly, as previously mentioned, the terry cotton can absorb more water per kg of fabric compared to knitted cotton. This meant that more PMCs could be held deep within the fabric yarns, increasing the likelihood that they

became deposited. Secondly, when terry cotton ballast was used it substantially increased the volume of suds observed with the drum during each cycle. The increased volume of suds had the effect of not only abating hydrodynamic forces in the wash, but also decreasing the movement of fabric in the drum and therefore decreasing the fabric-fabric forces. For this reason, the quantity of broken deposited PMCs was significantly lower in terry cotton, at 11.0 ± 2.9% than it was in knitted cotton, 22.8 ± 3.1%. Similar trends were also observed in the PMCs lost to the drain in washwater as significantly more PMCs were broken in knitted cotton than terry cotton and conversely more intact PMCs were lost to the drain in a terry cotton only ballast. It was seen in Section 6.5 that there was hardly any PMC rupture without ballast load, so the presence of fabric was the main factor in breaking PMCs. The more suds present in the drum, the more difficult it was for fabrics to come into close proximity that would cause the forces needed to rupture PMCs.

6.7 Studying the influence of washing machine type on the distribution of PMCs at the end of the cycle

Whilst all work so far has been on understanding the fate of PMCs in a front load washing machine, the methodologies needed to be applicable to other wash scenarios for more industrial relevance. Top load washing machines are drastically different to front load machine in the way that they operate and can either be fully automatic, meaning the spin cycle occurs in the same drum as the wash cycle, or semi-automatic if the clothes must be transferred manually from a wash drum to a spin drum. Because of this, fully automatic machines are more expensive machines and are more prevalent in the North American market. Semi-automatic top load machines are significantly cheaper and are extremely popular in Asian markets. At the time of

this work there was a preference for the study of semi-automatic top load machines. These machines differ quite significantly from the front load machines common in European countries in terms of cycle conditions, with a comparison shown in Table 6.4 below:

Table 6.4: Comparison of wash cycle parameters between front load machine and top load semi-automatic machines used in the experiments

	Front load machine	**Top load semi-automatic**
Volume of water in each cycle / L	16	48
Mass of ballast in each cycle / kg	3	2
Main wash Cycle Duration / minutes	60	15

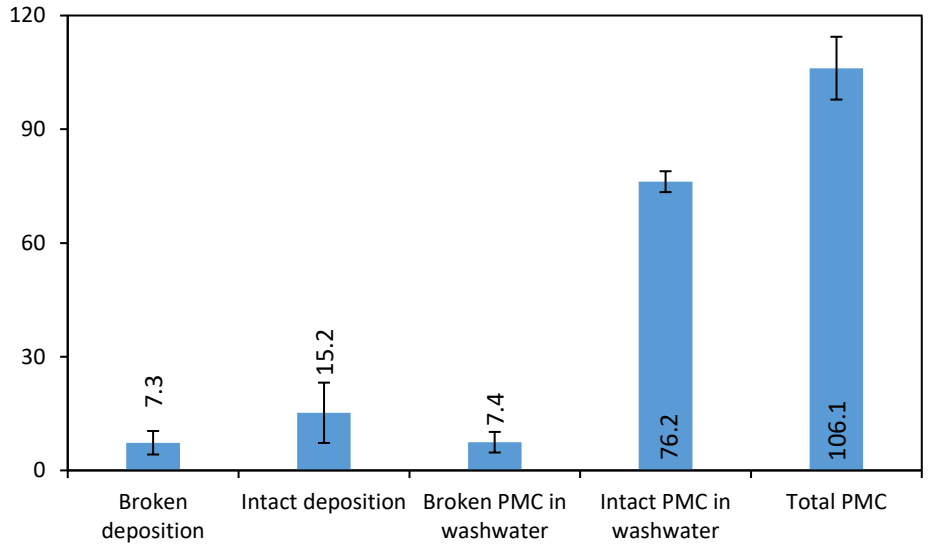

Figure 6.6: Distribution of PMCs in different output streams after a complete wash using a top loading semi-automatic washing machine with knitted cotton ballast. Error bars = 95% CI

The first thing to notice when looking at the distribution of PMCs in a top load semi-automatic washing machine was that the levels of deposition achieved in this machine were extremely low at 7.3 ± 3.1% for broken PMCs and 15.2 ± 7.9% for intact PMCs. This was a dramatic

reduction in deposition compared to the same sample in front load conditions presented in Section 6.2 where 22.8 ± 3.1% of PMCs deposited broken on fabric and 35.1 ± 4.4% of PMCs deposited intact on fabric. The shorter wash cycles in a top-load semi-automatic machine impacted the ability for PMCs to deposit in comparison to a front load machine. In addition to this, the type of agitation that occurred in top-load machines would not be expected to cause deep penetration into the fabric by PMCs. Paddles rotated within a disk at the base of the machine which caused the fabric to rotate with the water at the surface, but this was substantiallyy less agitation than was experienced in a front load wash, and the combined impact of these two effects may have caused the extremely low intact and broken deposition on fabrics in the top load semi-automatic machines.

Because the agitation in the top load washing machines was extremely low and durations of cycles were short, 76.2 ± 2.8% of PMCs remained intact in washwater at the end of the wash, with 7.4 ± 2.7% broken PMCs lost to washwater.

The deposition benefit achieved from encapsulating perfume, and the cost saving associated with a lower perfume inclusion in the formulation should outweigh the extra cost needed to encapsulate the fragrance. The extremely low deposition and large loss of PMCs to the drain will likely hit profitability. With this type of PMC that balance is called into question. An additional consideration is the market in which top load machines are used, especially when considering the cheaper semi-automatic variety. In a study by Nielsen (2016) it was found that in the Asia-Pacific market, 35% of consumers sought a fragrance as a benefit when purchasing a laundry detergent. This was the lowest of all global regions, highlighting the need for the chassis that the detergents are based on to be flexible, as PMCs may not be incorporated in certain markets for reasons described above.

6.8 Predicting PMC performance based on mechanical properties

As seen in Figure 6.3, earlier in the chapter, the quantity of intact and broken deposition did not substantially change between the reference sample, the lower median size sample and the 95/5 core/shell ratio sample.

When considering the nominal rupture stress of each sample as seen in Chapter 4, it was clear that the lower median size sample was significantly weaker at each PMC diameter with respect to the reference, and the 95/5 core/shell ratio sample was significantly stronger at all PMC diameters measured. This suggested that using solely this data there was an apparent disconnect between these mechanical results and what was measured in terms of deposition performance in the mass balance protocols. The nominal rupture stress as a single marker for predicting performance was inadequate when compared with the data collected in the quantification protocols in each output stream. Therefore, more work on assessing performance or quantifying sample strength was needed in order to become more predictive in PMC design.

With this in mind, the three samples were run through the high energy wash cycles with knitted cotton and analysed with the fabric headspace evaluation method in wash conditions as outlined in the materials and methods chapter. It was observed in Figure 6.7 that relative to the reference sample, the weaker lower median size sample showed a higher damp headspace response, indicative of more deposition of broken PMCs on the fabric. Conversely the stronger 95/5 core/shell ratio sample showed a decreased damp headspace response relative to the reference, indicative of lower deposition of broken PMCs. This successfully followed the expected trends given the strength of the PMCs.

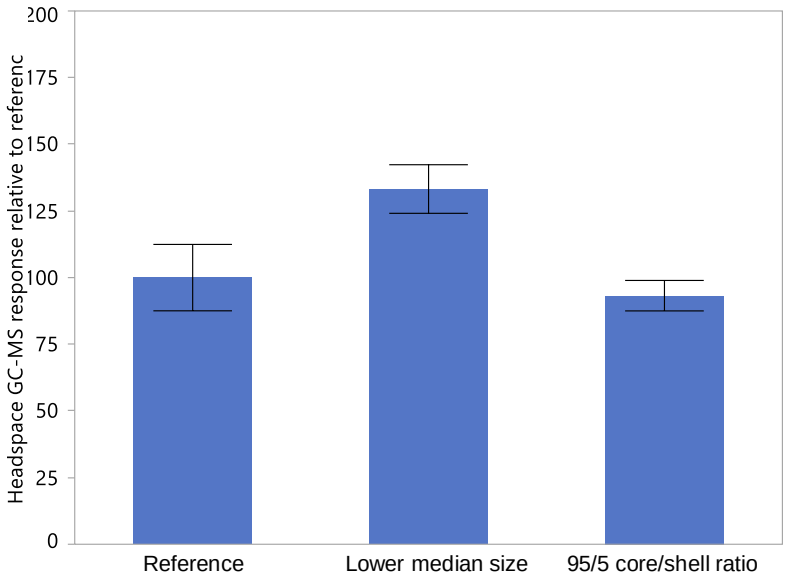

Figure 6.7: Headspace GC-MS analysis for damp fabrics of lower median size and 95/5 core/shell samples against the reference. Error bars = 95% CI

Once samples of the fabric had dried, any intact PMCs deposited were forced to break using the pneumatic press for dry pressed fabric headspace GC-MS analysis. The responses recorded in Figure 6.8 were a function of the total number of intact PMCs remaining on the fabric. Relative to the reference, both samples showed significantly lower headspace GC-MS perfume intensity response, suggesting lower intact deposition. To verify these results the samples were submitted for olfactive evaluation by professionally trained evaluators. As fabrics from the same wash cycles were used, the same general trends were expected. When the fabrics were damp there was no difference in the intensity of the fragrance between the reference and the lower median size sample, with a slight decrease in intensity between the reference and 95/5 core/shell ratio sample as seen in Table 6.5. When the samples were dry rubbed, similar to the dry pressing, where the intensity of perfume response was a function of intact PMCs deposited on fabrics, both the lower median size sample and the 95/5 core/shell ratio showed slight increases in intensity with respect to the reference (+2.5 pts). These results were in contrast to

the results obtained through headspace GC-MS evaluation. An important point to note though was that any relative change in olfactive intensity ≤ 5 pts was deemed too minor for an untrained nose to distinguish and therefore it was quite feasible that the more sensitive headspace GC-MS technique could show contrasting results to the olfactive analysis under these conditions. Whilst there were significant differences in headspace GC-MS of damp and dry pressed fabrics, these differences when translated into tangible consumer performance differentials through olfactive evaluation were not apparent. The differences in mechanical strength appeared to be successful in headspace GC-MS at changing deposition due to the high sensitivity of the technique, but from the mass balance results and the olfactive evaluation there was no such correlation.

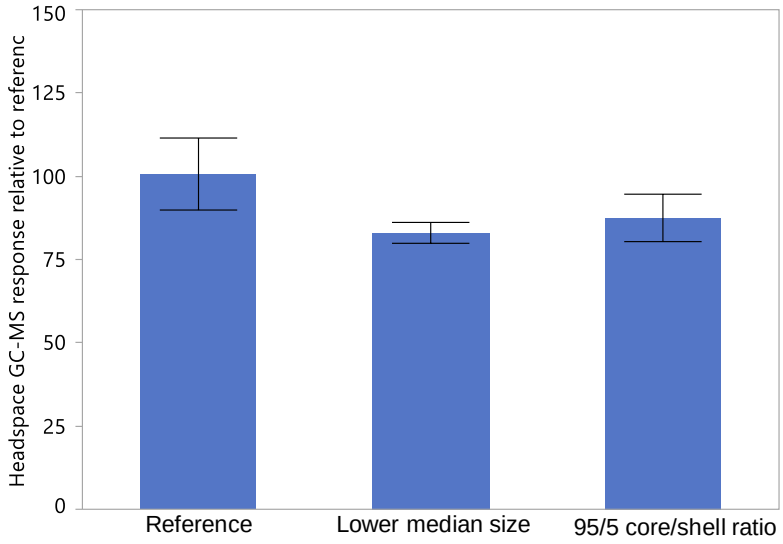

Figure 6.8: Headspace GC-MS analysis for dry pressed knitted cotton fabrics of lower median size and 95/5 core/shell samples against the reference in a high energy wash cycle. Error bars = 95% CI

Table 6.5: Comparison of olfactive evaluation of samples immediately after the wash (damp), once dried to equilibrium in atmospheric conditions (dry) and once rubbed by trained evaluators (dry rubbed)

	Damp	**Dry**	**Dry rubbed**
Reference	45	40	50
Lower median size	45 (+0)	45 (+5)	52.5 (+2.5)
95/5 core/shell ratio	42.5 (-2.5)	42.5 (+2.5)	52.5 (+2.5)

Whilst nominal rupture stress at all measured diameters was significantly different to the reference for both samples, the magnitude of this difference may not have been large enough to force out performance differences, as seen in the olfactive evaluation of the samples from identical wash cycles. As such, new samples were requested from P&G that could potentially cause a larger shift in nominal rupture stress with respect to the reference. These samples were characterised in the materials and methods section but were labelled sample X1 and sample Y1.

The nominal rupture stress vs PMC diameter for both samples was characterised and displayed in Figure 6.9. When compared back to the samples from Chapter 4, the magnitude of difference in nominal rupture stress was much greater, indicating that these samples could potentially be more successful at forcing out any performance differentials.

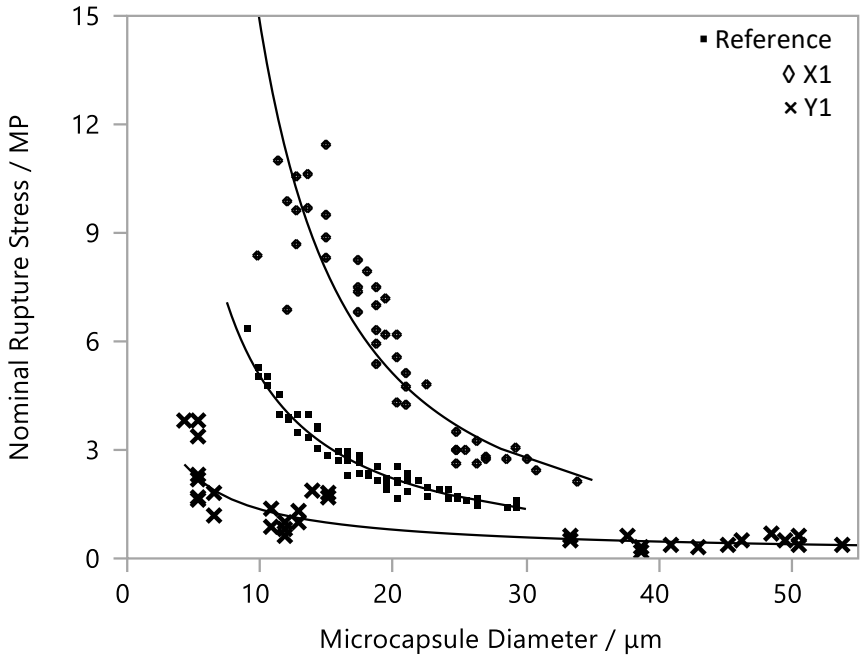

Figure 6.9: Nominal rupture stress vs microcapsule diameter for samples X1 and Y1, with the reference for comparison

Whilst it was possible to gain a deeper understanding of the wash process via completing the quantification techniques for the mass balance, having a quicker screening method for predicting microcapsule performance based on quick techniques would also be beneficial.

When olfactive evaluations and headspace GC-MS analysis were conducted on these new samples there were some interesting trends as shown in Table 6.6 and Figure 6.10. For sample Y1 there was a 5 point intensity increase in olfactive evaluation compared to reference when damp and when dry pressed, indicating that there were more broken and intact PMCs deposited.

In the damp olfactive evaluation, sample X1 had a +12.5 point intensity relative to the reference. This was a performance differential that an untrained person could easily distinguish. Similarly, in headspace analysis as seen in Figure 6.10 the intensity of perfume headspace response was almost double that of the reference. This was a much greater differential compared

to the original samples as seen in Figure 6.7, indicative of a substantial increase in deposition of broken PMCs for the different monomer sample. Conversely, for headspace analysis of dry pressed fabrics, displayed in Figure 6.11, there was a significant reduction in intensity when compared to the reference as seen in Figure 6.8. This was indicative of the number of deposited intact PMCs almost halving with respect to volume of perfume oil.

Table 6.6: Comparison of olfactive evaluation of samples immediately after the wash (damp), once dried to equilibrium in atmospheric conditions (dry) and once rubbed by trained evaluators (dry rubbed)

	Damp	**Dry**	**Dry rubbed**
Reference	45	40	52.5
X1	57.5 (+12.5)	45 (+5)	55 (+2.5)
Y1	50 (+5)	47.5 (+7.5)	57 (+5)

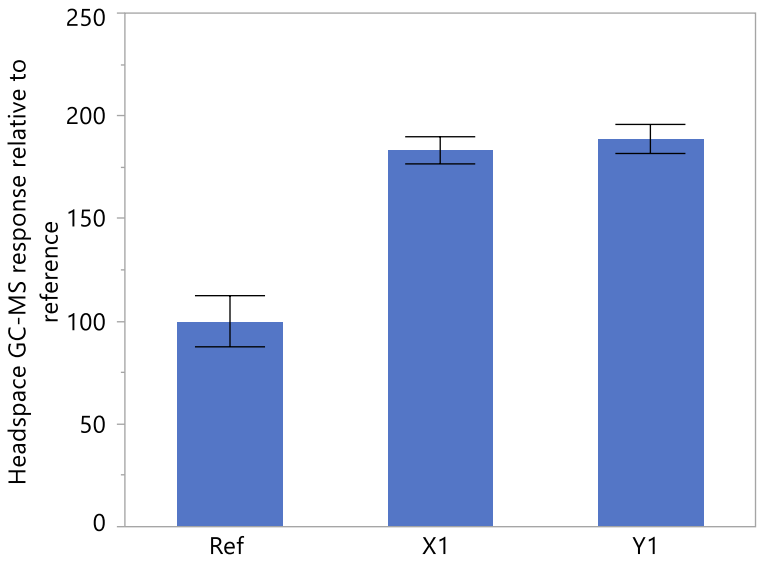

Figure 6.10: Headspace GC-MS analysis for damp fabrics of X1 and Y1 samples against the reference. Error bars = 95% CI

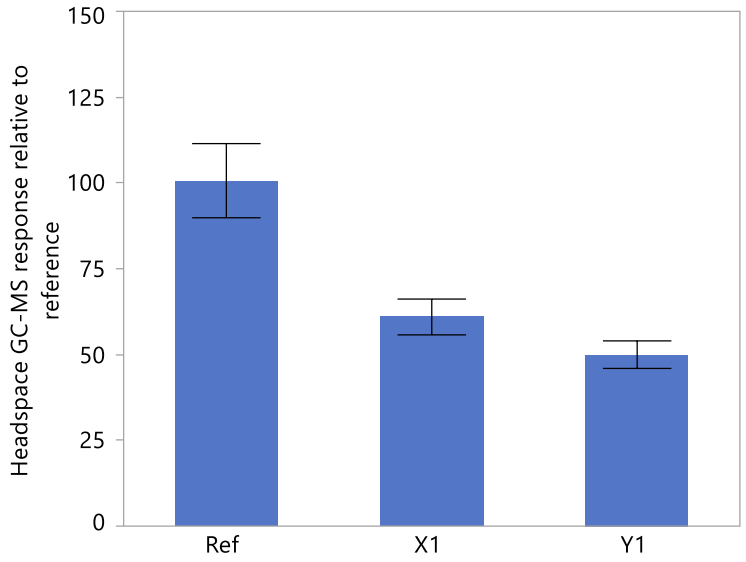

Figure 6.11: Headspace GC-MS analysis for dry pressed fabrics of X1 and Y1 samples against the reference. Error bars = 95% CI

By changing the mechanical strength, it appeared that it was possible to more dramatically shift the deposition numbers of PMCs on fabric that were intact and broken compared to the original samples. The issue, however, was that given how the mechanical strength of the different monomer sample was significantly stronger, it would be expected to give a lower headspace GC-MS and olfactive intensity when damp, and higher when dry pressed, but the opposite was seen. This further highlighted that nominal rupture stress as an individual unit was not adequate in predicting performance in full scale tests.

6.9 Volume weighted rupture stress

Traditionally, the method to compare mechanical strength at rupture was through studying the nominal rupture stress at different size bands, whilst compressing up to 50 PMCs. If comparing PMCs of different samples at identical sizes, this was a good way of understanding the relative strength between the samples at each discrete PMC diameter. However, the performance of the PMCs is related to applying the whole sample population to stresses such as a washing machine cycle, the complete distribution of PMC diameters becomes an important factor, over the whole sample size distribution, and not just on those measured via micromanipulation. Taking this into consideration, the volume weighted rupture stress of each sample was calculated based on the nominal rupture stress with diameter of samples measured, and the volume, and hence size distribution of PMCs, based on laser diffraction data, as seen in Appendix C.

The equation for the volume weighted rupture stress is seen below:

$$\sum(\sigma_R \times \varphi_i) \qquad 6\text{-}1$$

Where the φ_i is the volume fraction of a PMC sample at a certain diameter, and σ_R is the corresponding nominal rupture stress as measured by micromanipulation. Summing over all diameters yields the volume weighted rupture stress. The volume weighted rupture stress for all samples where performance analysis was conducted is seen in Table 6.7 alongside size distribution.

Table 6.7: Volume weighted rupture stress for each PMC sample used in performance analysis

Sample	D_{10} / µm	D_{50} / µm	D_{90} / µm	Volume weighted rupture stress / MPa
Reference	6.90	18.22	30.42	1.68
Lower median size	5.82	12.17	20.06	1.43
95/5 core/shell ratio	7.57	19.32	28.46	2.36
X1	20.29	31.25	72.14	0.57
Y1	16.84	39.88	58.75	0.55

It could be seen that despite sample X1 having a much higher nominal rupture stress at discrete PMC diameters compared to the reference sample, the volume weighted rupture stress was much lower than the reference sample at 0.57 MPa compared to 1.68 MPa, and on par with the sample Y1 at 0.55 MPa, showing the impact that the size distribution of PMCs had on this value.

Once the volume weighted rupture stress for each sample was calculated, it was possible to plot these values against the results from damp and dry headspace GC-MS of fabrics to assess whether a link could be found to suggest that the volume weighted rupture stress, rather than nominal rupture stress, was a good indication of performance.

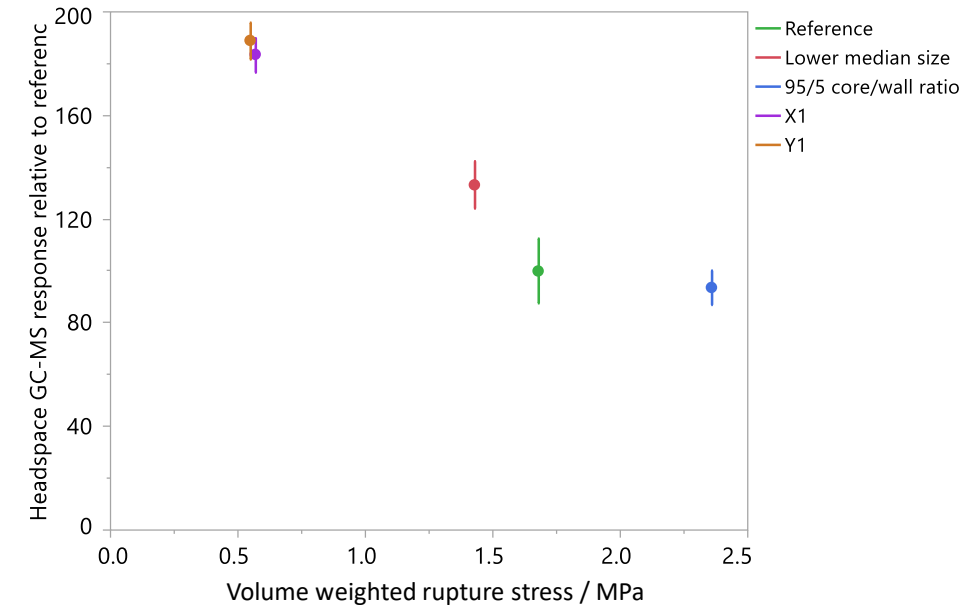

Figure 6.12: Damp headspace GC-MS results for each sample relative to the reference plotted against the volume weighted rupture stress. Error bars are standard error of the mean from 9 measurements

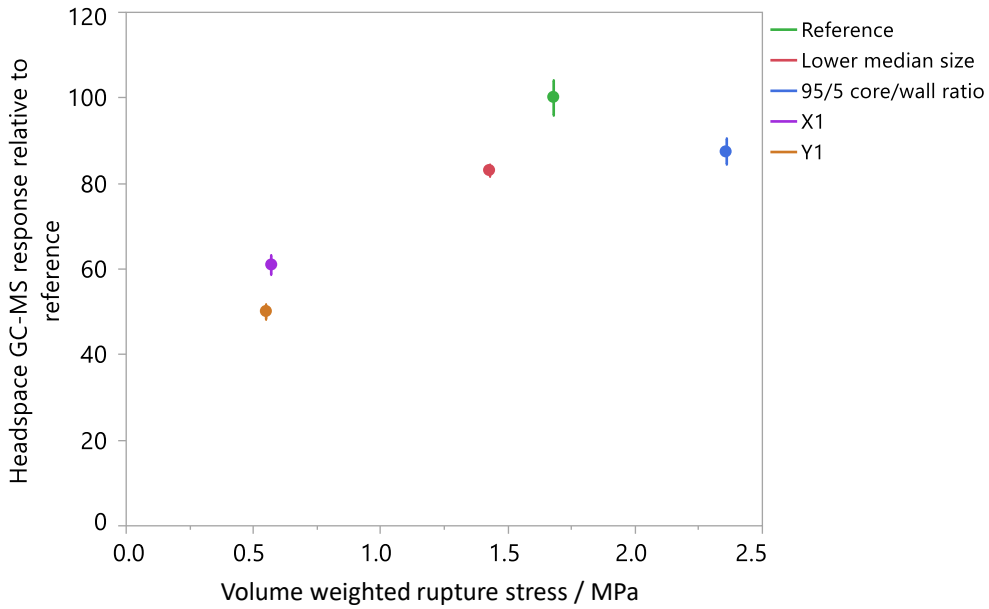

Figure 6.13: Dry pressed headspace GC-MS results from each sample relative to the reference, plotted against the volume weighted rupture stress. Error bars are standard error of the mean from 9 measurements

As can be seen in Figure 6.12, there was a trend that as the volume weighted rupture stress of the samples increased, the damp headspace GC-MS response intensity decreased, indicating that a stronger PMC population, as measured by this parameter, corresponded to less breakage of PMCs that were deposited on the fabric during the whole wash. Conversely, in Figure 6.13, as the volume weighted rupture stress increased, the dry pressed headspace GC-MS response increased, indicating higher deposition of intact PMCs on the fabric.

It is worth highlighting that these methods were relative to the reference samples, as no calibration curve was formed for headspace GC-MS experiments on fabric in order to elucidate absolute quantification. It was therefore desirable to compare the volume weighted rupture stress against the mass balance results displayed earlier in the chapter. Unfortunately, as the new X1 and Y1 samples were requested for analysis beyond their point of production there was no opportunity to include the PM546 fluorescent dye in the core. This meant only the washwater breakage methodology was applicable for comparison to the volume weighted rupture stress, as this technique used the perfume as a marker. The Y1 sample was not included in this analysis as the perfume was a slightly different specification to those previously tested. As it can be seen in Figure 6.14, there was a strong correlation between volume weighted rupture stress and total washwater breakage between each of the samples tested. As the volume weighted rupture stress increased, the number of broken PMCs in washwater decreased which was to be expected.

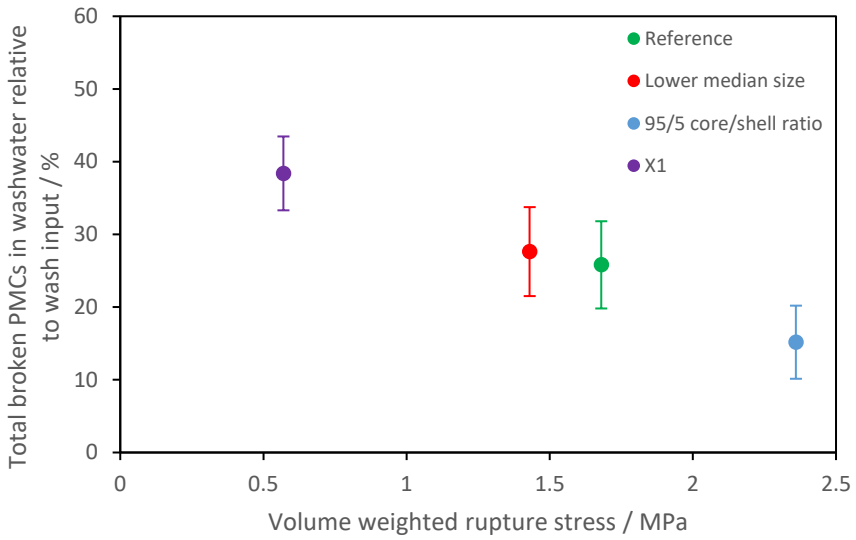

Figure 6.14: Total percentage of broken PMCs in washwater plotted against the volume weighted rupture stress for different samples. Error bars = 95% CI

The significance of these three plots was that they offer the potential to model performance of PMC samples without the need to run extended full cycle tests. By populating the graphs with more samples it would be possible to create a model to predict relative performance of headspace GC-MS of fabrics and absolute performance of headspace GC-MS of washwater solutions. Instead of needing a week to run full scale wash tests and analysis, obtaining the size distribution of the sample and micromanipulation data from 50 compressions would be the only data required to find the volume weighted rupture stress to predict performance from the constructed models and accelerate sample screening.

6.10 Conclusions

This chapter has presented new array of techniques to shed light on what happens to PMCs in the wash cycle. The techniques have quantified PMCs in each output stream in the wash, and when put together they provide a good estimate of the mass balance of the total input of PMCs. The techniques were used to show that deposition did not drastically change when studying the reference sample against lower median size and 95/5 core/shell ratio samples. It was discovered that any breakage in the wash was triggered by the presence of fabric, and that the hydrodynamic forces of water without fabric were not strong enough to cause any significant PMC breakage. The techniques also showed that changing ballast from knitted cotton to terry cotton can significantly increase deposition and reduce PMC rupture. Top load semi-automatic washing machines had very different wash cycle parameters to front load machines, and the lower wash times and agitation meant that the techniques quantified the majority of the PMCs leaving the top load semi-automatic machine intact via the washwater liquor, with extremely low deposition. The number of revolutions of the drum per minute was found to significantly increase the breakage of PMCs when the fabric's movement included them dropping from the top of the drum, but was not found to dramatically impact intact deposition on fabrics.

The nominal rupture stress as a predictive marker for performance failed to correlate with headspace GC-MS and olfactive performance data. However, when combined with volume distributions of sample from light scattering measurements, identification of the volume weighted rupture stress parameter opened up the possibility of predicting how a PMC sample will mechanically behave in the wash. This is a novel approach discovered during the project and it means that P&G can screen new samples much quicker and become more targeted in their approach creating PMCs to achieve a certain level of breakage/deposition based upon what

is desired. The parameter is ready for P&G to secure intellectual property if they desire, any may be especially useful in validating claims in new PMC technology.

Chapter 7. ASSESSING THE EFFECT OF FRICTION ON THE BREAKAGE OF PMCS

Microcapsule populations that break under mechanical stress in consumer applications can rupture under normal compressive force, but other force types may also play a role. If any lateral force is applied to the microcapsule it is likely that it will experience some friction against the application substrate. This seems especially relevant in PMCs for laundry applications as the fabric yarns within which the PMCs are embedded are constantly in frictional contact with each other in the washing machine as they tumble and fold upon each other. To the author's knowledge the influence of friction on the breakage of microcapsules has had limited investigation in literature, with abrasion of fabrics with microcapsules embedded studied by Mercade-Priéto et al. as outlined in Section 2.4.2. In this chapter a method was proposed to deposit fluorescently labelled PAC PMCs on a resin substrate to fix them on a surface, and then using a tribometer, the PMCs were abraded against PDMS spherical probes under carefully controlled force conditions. Populations of PMCs were also compressed under a normal load via a texture analyser for comparison. The degree of breakage was then assessed using fluorescence microscopy and any differences in breakage between compression and friction was observed, along with differences in breakage in water and in dry conditions, and studying breakage from probes of different friction coefficients. Several PMC samples were also abraded to assess whether their damage could be correlated to the breakage observed in micromanipulation experiments in Chapter 4 matched results when looking at a more bulk experimental setup.

Friction can be applied in four distinct scenarios. Two of these types of friction; static and dynamic sliding friction occur on embedded microcapsules in fabrics in a washing machine. Static friction occurs between two objects that are applying forces in opposite directions, without relative movement of the objects. Dynamic sliding friction then follows on from static friction, where relative movement of the substrates starts to take place. Two other types of friction; rolling friction, where an object is slowed as it rolls on a surface, and fluid friction, observed as the force that slows down an object moving in a fluid are less relevant to rupture in a washing machine scenario, and therefore they are omitted in this work, with the focus being on static and dynamic sliding friction.

7.1 Experimental

7.1.1 Fixation of PMCs on a substrate

There was a challenge in fixing the PMCs on the surface of a substrate; on one hand the surface was sought to be as flat as possible to ensure balanced force application to the PMCs, and on the other hand there needed to be some sort of roughness or adhesion so to keep the PMCs fixed in place. On the extreme ends of the scale, even the lowest force application, at 0.2 N by the mini traction machine tribometer (MTM 2, PCS Instruments) completely swept the PMCs off a glass microscope slide. If an adhesive was added to the surface it was possible to fix a highly concentrated area of PMCs to prevent contact between the adhesive and spherical probe, but once PMCs were broken the probe could stick to the surface leading to severe stick-slip phenomena.

Jesmonite AC100 is a two-part acrylate resin; a water based acrylic resin and a gypsum mineral powder. It is often used in the arts and crafts business due to its ease of application, strong mechanical properties, and low cost. A benefit of choosing an acrylic resin is that there is potential to crosslink with the PAC PMCs, further fixing them to the surface.

Procedure:

1. Mix the gypsum powder with the acrylate resin in a 2.5:1 wt % ratio and stir for 2 minutes
2. Pour the resin into silicone moulds in the shape of the disks required for the MTM2
3. Cover the disks for 30 minutes until the resin appears solid
4. Leave the resin disks in the mould, open to air for a further 75 minutes to allow for evaporation of water and significant curing
5. Drop 0.02 mL of PMC slurry in deionised water at $1 g.L^{-1}$ into spots around the edge of the disk and leave overnight. Dropping the solution at this late stage ensured the PMCs sit on the surface, rather than becoming embedded within the resin.

7.1.2 Using the MTM2 and texture analyser to apply force to the resin disks

The MTM2 tribometer was used to apply a normal and lateral force to the PMCs and Jesmonite resin disks. In each experiment a PDMS ball (PCS Instruments) was moved over a rotating resin disk with a slide to roll ratio (SRR) of 200%, meaning the ball was fixed and no rolling occurred. The disk was moved at $2 mm.s^{-1}$ and one full rotation was applied per disk to ensure multiple passes did not occur. A texture analyser (Stable Microsystems, UK) was used to apply normal compression load to the disks, as the MTM2 lacked the functionality to do so without rotation.

7.1.3 Particle tracking using ImageJ to quantify intact PMCs embedded in Jesmonite resin

Examples of the images captured for the PMCs embedded in the Jesmonite resin are shown below in Figure 7.1. The image showed an area containing fluorescent PMCs before compression. The coordinates of the position from the microscope stage were noted and then force was applied, 1 N normal load with lateral rotation of the disk in the case of this image, and Figure 7.2 shows the same area after the force application. It could be seen that the abrasion against the probe caused some rupture of PMCs on the surface, but that the residues of the broken PMCs can still be seen by the microscope, indicating that the PMCs remained stationary as the force was applied, and were not rolled away. The key then to quantify this data was to:

1. Capture enough images to get a true representation of rupture over the whole PMC population.
2. Capture the number of intact and broken PMCs automatically to reduce analytical error and save time.

To ensure enough images were taken, several Jesmonite disks embedded with PMCs were abraded for each sample, and four spots of deposited PMCs around the edge of the disk were imaged to ensure the total number of PMCs ranged in the thousands. The analysis of the images was performed using ImageJ. Tests were completed to refine the parameters by which the software should threshold the image using factors of particle circularity, colour intensity, and minimum/maximum diameter to identify intact PMCs. This also meant that any fluorescent residue remaining from a ruptured PMC would not be included in the analysis. The programme outputs data on the area of the PMCs in order to assign diameters. The procedure for thresholding an image for analysis of intact PMCs is outlined in the Appendix D, and examples

of a completed image analysis are seen in Figure 7.1 and Figure 7.2 which show the outlines of the intact PMCs as identified by the macro.

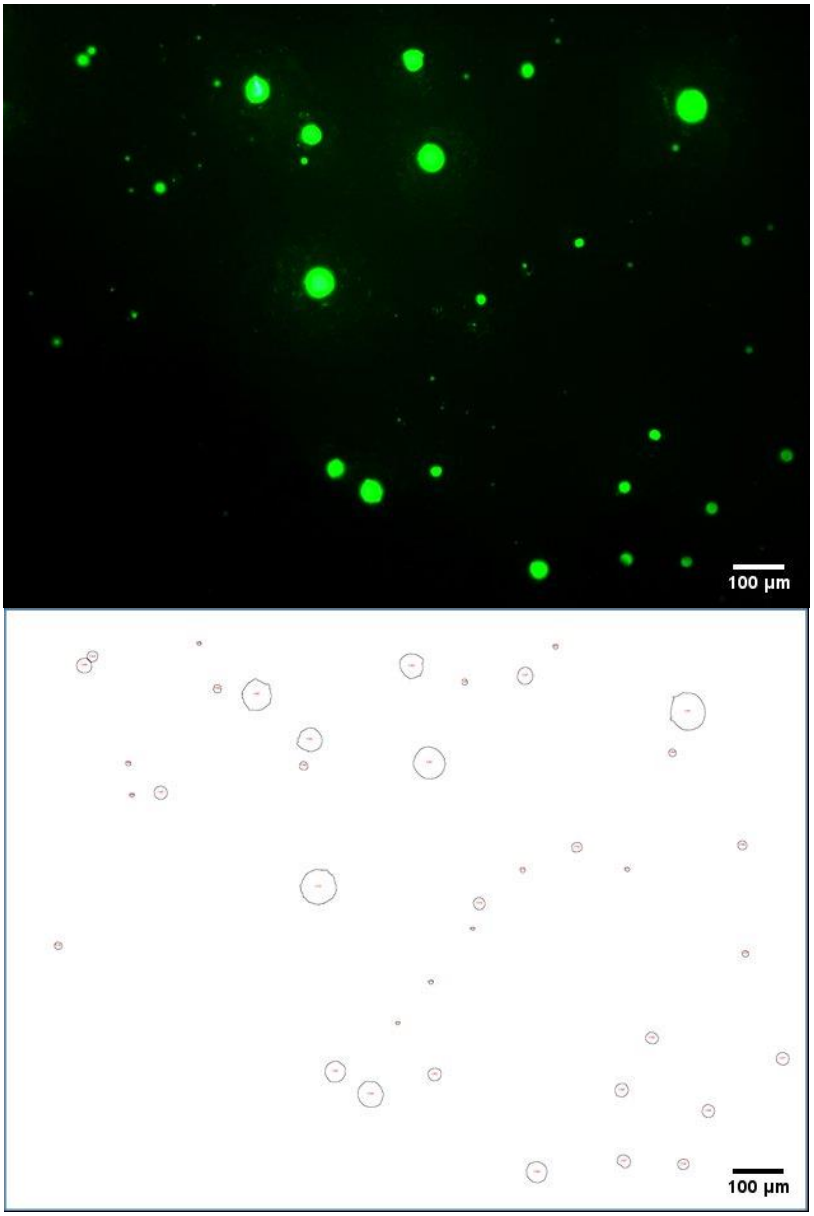

Figure 7.1: Raw image of PMCs before compression and the PMCs identified by the ImageJ protocol

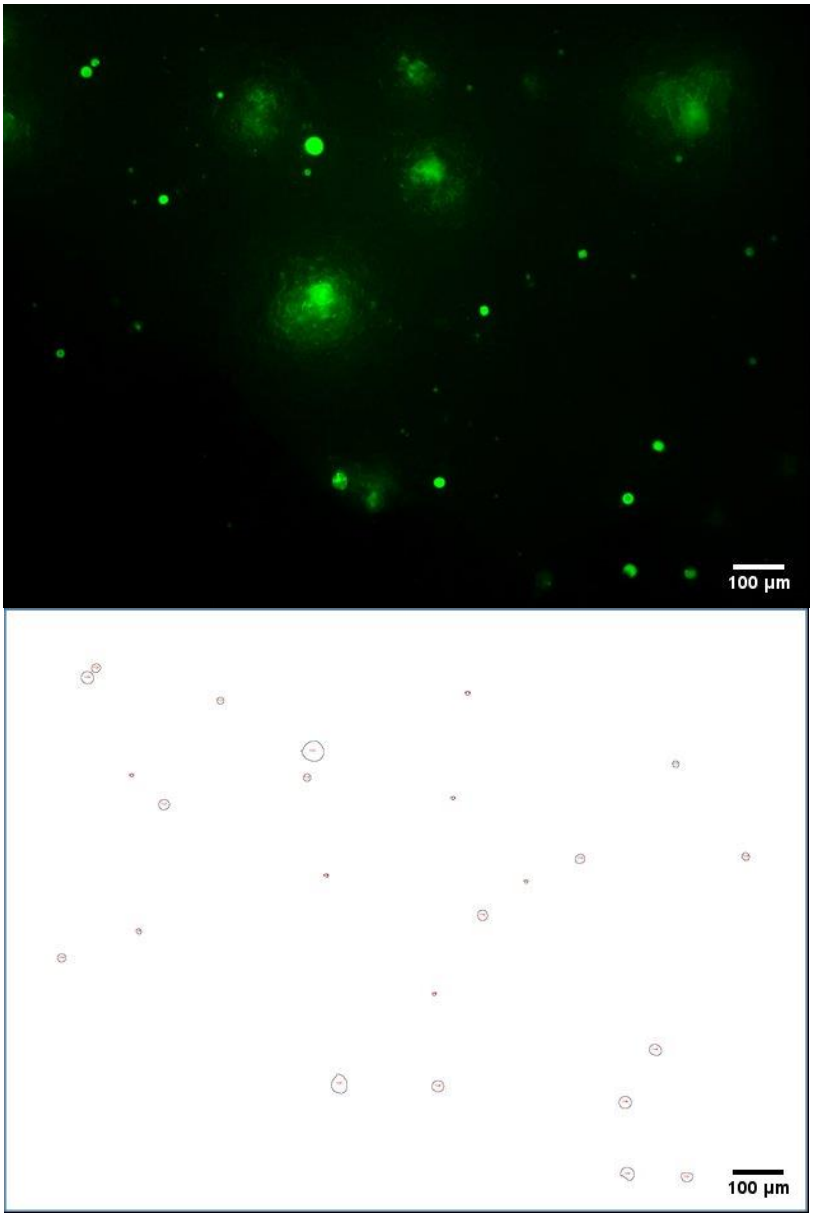

Figure 7.2: Raw image of PMCs after 1 N abrasion by PDMS spherical probe and the PMCs identified by the ImageJ protocol

7.1.4 Young's modulus of spherical probes

The MTM2 applied force through spherical probes, so that a well-defined contact geometry was used. The probes are usually constructed from steel for studying properties of lubricants, which was the main application for the tribometer, however in this case, PDMS spheres were

obtained which served to increase the contact area against the Jesmonite resin with respect to the steel in addition to lowering the contact stress due to a lower Young's modulus.

The material properties of the spherical probe had a substantial impact on the contact mechanics between it and the substrate. This was mainly governed by the Young's modulus of the probe material, as this subsequently affects contact area and applied stress to the surface. Once the Young's modulus was known it was possible to study the contact radius of the probe on the surface through fluorescence microscopy of PMC damage after compression to assess if the Hertz model correctly calculated the stress applied. To delve further into the apparent and effective applied stresses on the surface would require characterisation of the roughness of the material, which was beyond the scope of this work.

The Young's moduli of two different PDMS spherical probes were calculated using the Hertz model, as described in Section 4.5.8 :

$$F = \frac{4E\sqrt{R}}{3(1-v_p)^2}\delta^{\frac{3}{2}} \qquad 7\text{-}1$$

where F is the force applied by the sphere on the rigid surface, E is the Young's modulus, R is the spherical probe radius, v_p is the Poisson ratio of the probe, and δ is the displacement of the probe into the surface.

An example of the force-displacement curve is shown below in Figure 7.3. In this instance the probe was attached to a texture analyser and compressed effectively between two parallel plates at 2 $mm.s^{-1}$. Both PDMS probes show an elastic response throughout the compression. By plotting the force against the $\delta^{3/2}$, as seen in Figure 7.4, a pseudo-linear relationship was

observed and from this gradient it was possible to calculate the Young's modulus of the probe, given the radius and Poisson ratio of the probe.

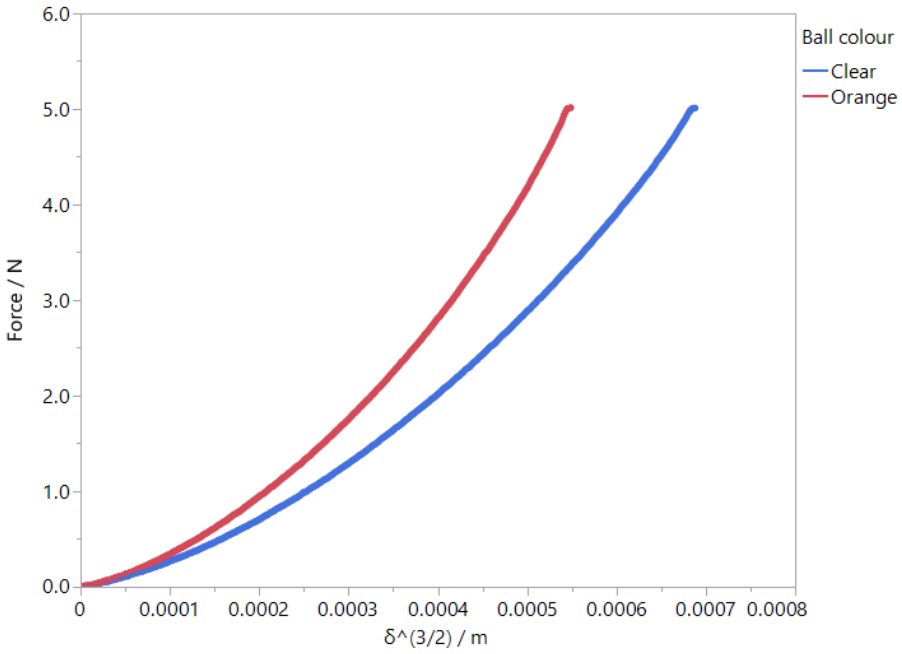

Figure 7.3: Force vs δ curve of each spherical PDMS probe

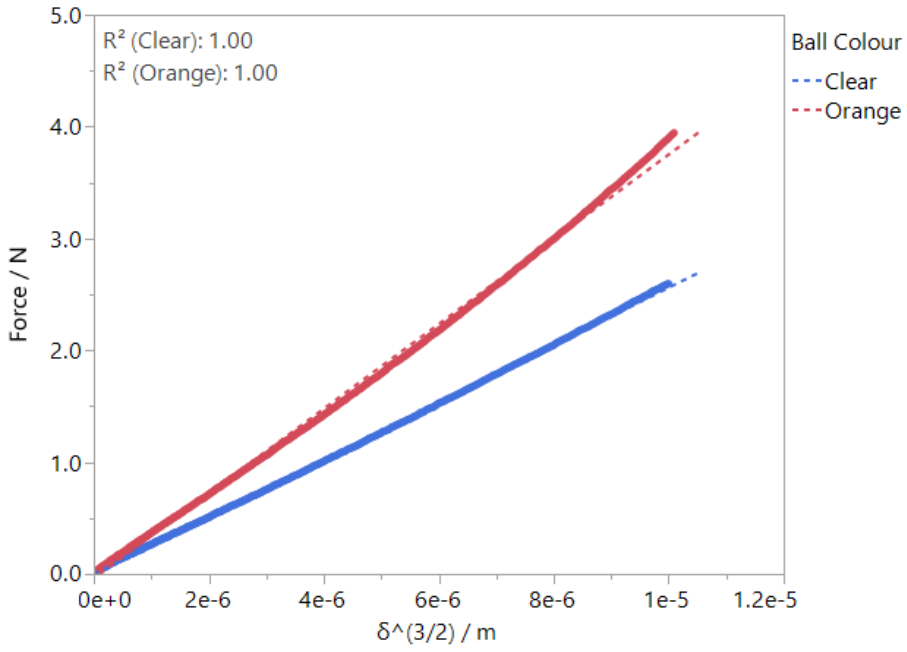

Figure 7.4: Force vs $\delta^{3/2}$ curve for compression of the spherical PDMS probes

Five measurements were recorded for each of the PDMS balls and results for the Young's modulus of each are seen below and were of the same magnitude as those recorded on PDMS balls by Røn and Lee (2014):

Table 7.1: Mean Young's modulus values for two PDMS balls used as probes from five compressions. The values after ± are the standard deviation of the mean values

Clear PDMS ball	Orange PDMS ball
$1.50\times10^{6} \pm 3.61\times10^{4}$ Pa	$2.16\times10^{6} \pm 9.33\times10^{4}$ Pa

7.2 Friction between surfaces with and without PMCs

To understand how the deposition of PMCs on the Jesmonite resin affected the contact between the probe and the surface it was necessary to collect a range of friction coefficients. The PMCs were deposited on the edge of the disk in a dispersion with deionised water at 1 $g.L^{-1}$, and the water was allowed to evaporate to leave the PMCs embedded on the surface.

Table 7.2: Mean friction coefficients between the orange PDMS probe and a dry Jesmonite resin disk, the whole setup submerged in DI water, and the friction coefficient of dry Jesmonite with PMCs deposited on the surface from dispersions at different concentrations. The figures after ± are the standard error of the mean from five measurements

	No PMC	Water	0.001 $g.mL^{-1}$	0.004 $g.mL^{-1}$
Mean friction coefficient	0.79 ± 0.03	0.80 ± 0.04	0.79 ± 0.03	0.75 ± 0.02

As seen in Table 7.2, the friction coefficient did not change when the disk was submerged in water, nor when low concentrations of PMC were deposited on the surface, applicable for observing breakage. This suggested that because the PMCs occupy such a small area fraction of the surface contact, they had no impact on the bulk friction between the spherical probe and the Jesmonite surface. This also showed that under the conditions suitable for the experiments,

leakage of core oil from the PMCs upon rupture also did not serve to lubricate between the contact and decrease the friction coefficient.

7.3 Assessing the impact of speed of force application on the rupture of PMCs

It is known that for polymeric microcapsules, rupture forces, deformation at rupture and pseudo yield points are independent of compression speed when studied by micromanipulation (Zhang, 2001). It was necessary to understand if the same could be said for compression of a population of microcapsules using the texture analyser, to allow for comparison with the force applied through the MTM2 tribometer. Examples of such previous studies of compression of microcapsules using a texture analyser can be seen in Section 2.2.3.1.

Using the orange PDMS probe attached to the texture analyser, Jesmonite resin, embedded with PMCs was compressed at speeds of 0.05 $mm.s^{-1}$ and 0.5 $mm.s^{-1}$ on four spots of embedded PMCs on two disks to assess whether compression speed impacted rupture of PMCs.

Table 7.3: The mean number-based percentage of PMCs remaining intact after a 15 N compression at either 0.05 $mm.s^{-1}$ or 0.5 $mm.s^{-1}$. The numbers after the ± are the standard deviation

	0.05 $mm.s^{-1}$	**0.5 $mm.s^{-1}$**
Mean percentage of intact PMCs	75.9 ± 8.4	77.6 ± 8.1

An independent t-test was run on the results to compare the difference between the 0.05 $mm.s^{-1}$ compression (M =75.9, SD= 8.4) and the 0.5 $mm.s^{-1}$ compression (M=77.6, SD=8.1) conditions $t(14) = 0.803$, $p = 0.05$, so the null hypothesis was accepted and there was no

significant difference at p = 0.05 between the two compression speeds, thus agreeing with the findings from individual PMC compression in micromanipulation.

7.4 Effect of different compression forces on breakage

Before comparing friction and compression it was necessary to understand if changing the compressive force affected rupture as it did with compression on single PMCs through micromanipulation. This would also ensure that the PMCs were indeed sitting on the surface and not buried in the resin structure.

Using the texture analyser, areas of PMCs were compressed by the orange PDMS ball at 0.5 $mm.s^{-1}$ up to a force of 10 N and a force of 40 N. Four replicates of each compression were conducted to get a good understanding of the degree of breakage in the PMC population under the different force values. As a rough guide to assess what the contact stress might be against the PMCs and Jesmonite the equation for the Hertz model was slightly modified to account for the effective Young's modulus, E^* of both bodies, with the relationship shown in equation 7-2, where v_1 and v_2 are the Poisson ratio of the two bodies, and E_1 and E_2 are the Young's moduli of each of the materials in contact :

$$\frac{1}{E^*} = \frac{1 - {v_1}^2}{E_1} + \frac{1 - {v_2}^2}{E_2} \qquad 7\text{-}2$$

With the equation relating the normal force to the Young's modulus altering as follows for contact between a sphere and an elastic half-space in equation 7-3:

$$F_n = \frac{4}{3} E^* R^{1/2} d^{3/2} \qquad 7\text{-}3$$

The Young's modulus for Jesmonite resin at the ratio of ingredients for these experiments was known to be 5.5 MPa, given in information from the supplier (Jesmonite Limited, 2017), allowing for calculation of the effective Young's modulus given that the Young's modulus of the orange and clear spherical probes was calculated in section 7.1.4. The relationship between the radius of the contact area, a, and the normal load, radius of the sphere and effective Young's modulus is shown in equation 7-4:

$$a^3 = \frac{3F_n R}{4E^*} \qquad 7\text{-}4$$

With these equations it was possible to calculate the contact area between the orange PDMS probe and the substrate surface, and subsequently the effective contact stress. This gives an idea of how likely it was that PMCs would rupture under the normal loads:

Table 7.4: The contact area and contacts stress for contact between the orange PDMS probe and the Jesmonite substrate at 10 N and 40 N normal load on the texture analyser

	10 N	**40 N**
Contact area / m^2	7.19×10^{-5}	1.81×10^{-4}
Contact stress / MPa	0.14	0.22

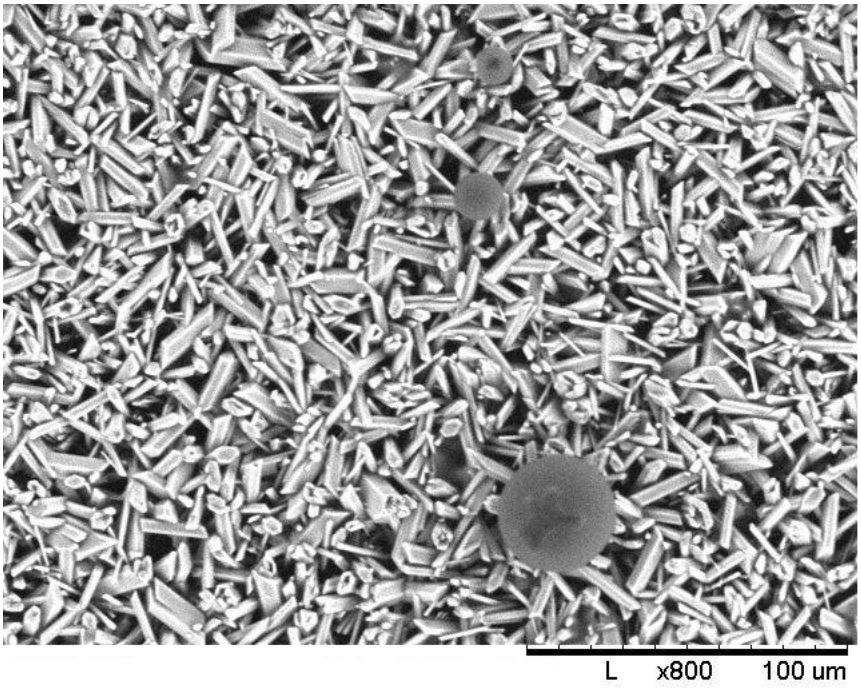

Figure 7.5: SEM image of PMCs on the surface of the Jesmonite resin

When the normal load was increased from 10 N to 40 N this only had a small effect on increasing contact stress, as seen in Table 7.4. As seen in Figure 7.5 the gypsum particles form the majority of the base surface, surrounded by acrylate resin, but it was clear that it would not be completely flat. By studying a collection of SEM images it was decided to have a minimum cut-off of 4 μm PMC diameter for inclusion in any rupture measurements, as below this size it was apparent that if the voids were gaps, rather than filled with acrylate, then the PMCs might sit in the voids, unable to rupture.

Table 7.5:The mean number-based percentage of PMCs remaining intact after a 10 N or 40 N compression using the orange PDMS probe. The numbers after the ± are the standard deviation

	10 N	**40 N**
Mean percentage of intact PMCs	74.5 ± 7.8	66.1 ± 9.7

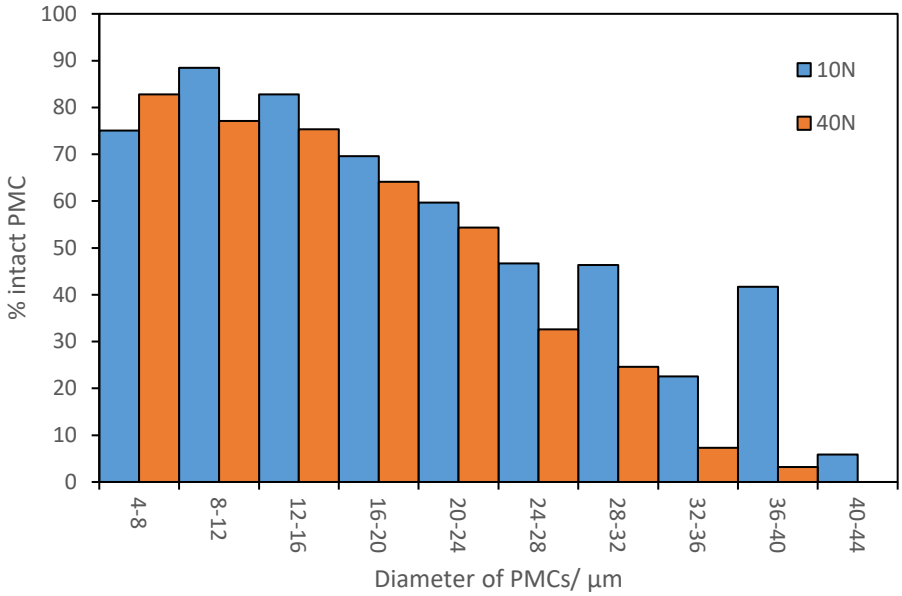

Figure 7.6: Histogram showing the number-based percentage of intact PMCs for the reference sample after a 10 N compression and 40 N compression. Only size bands with more than 10 PMCs total were counted

An independent one tailed t-test was conducted on the results to assess whether the overall percentage of intact PMCs from the 10 N compression (M =74.5, SD=7.8) was greater than the 40 N compression (M=66.1, SD=9.7). Conditions $t(10) = 0.074$, $p = 0.05$, so the null hypothesis was accepted and the 40 N compression did not significantly decrease the percentage of intact PMCs over the whole sample compared to a 10 N compression with the data collected. It was seen however in Figure 7.6 that at all but the lowest diameter of PMCs show a decreased percentage of intact PMCs for a 40 N compression compared to a 10 N compression. The small differences in number of broken PMCs could potentially be justified when considering how little the contact stress would change when moving from 10 N to 40 N compression, but without knowing true contact area, it is difficult to offer a certain judgement.

7.5 Studying the impact of water on the breakage of PMCs through friction

As highlighted in Section 4.5.10, the impact that relative humidity has on the rupture properties of PMCs is especially relevant when considering application in a washing machine and in ambient conditions when clothes have dried. It was seen in that section that when compressing individual PMCs in 20% and 80% humidity, that the nominal rupture stress did not change with changing humidity, but the Young's modulus decreased in the 80% RH equilibrated sample. A similar setup was conceived for the MTM2 where a sample of reference PMCs was abraded using the orange PDMS probe under a 1.5 N load at 2 $mm.s^{-1}$ in dry conditions, and also when the probe and substrate were submerged in water. The samples submerged in water were allowed to equilibrate for 30 minutes prior to force application and two disks were used in each of the conditions.

Table 7.6 shows the results from the experiment and an independent t-test was run on the two sets of data to compare the difference in the mean percentage of intact PMCs in a dry environment (M=35.1, SD=7.8) and when submerged in water (M=33.4, SD=5.3) over the whole sample population. Under conditions $t(12) = 0.7259$ at $p=0.05$ so the null hypothesis that there was no significant difference in the percentage of intact PMCs after abrasion for in both dry and submerged in water conditions was accepted, which agreed with the findings in section 4.5.10 where no significant difference was found in nominal rupture stress at 20% RH and 80% RH at all measured PMC diameters.

Table 7.6: The mean number-based percentage of PMCs from reference sample remaining intact after 1.5 N normal load with lateral rotation in ambient conditions or submerged in water. The numbers after the ± are the standard deviation

	Dry environment	**Submerged in water**
Mean percentage of intact PMCs	35.1 ± 7.8	33.4 ± 5.3

7.6 The relative impact of compression and abrasion on the rupture of PMCs

Experiments were conducted to investigate the relative impact of compression and abrasion on the rupture of PMCs. Abrasion of the PMCs was carried out using the MTM2 tribometer, with the orange PDMS spherical probe attached. The speed of the rotation of the Jesmonite resin disk was set at 2 $mm.s^{-1}$ and the slide to roll ratio (SRR) was set at 200%, meaning there was no rotation of the probe. The normal load applied by the sphere to the surface during abrasion was 1.5 N. Using the same probe, a texture analyser was used to apply a 30 N normal load to PMCs, and then to assess the rupture. Compression alone was not possible using the MTM2 tribometer.

Analysis was conducted on three disks for each run, and within the disks, with four spots of PMCs around the edge of the disk imaged before and after force application. As seen in Table 7.7, PMCs embedded on the disks when subjected to a 30 N compression had a significantly higher survival rate at 77.0 ± 5.2 compared to only 26.3 ± 7.8 % when a 1.5 N normal load with lateral motion, was applied. Despite a much greater force applied by the probe to the resin, the survival rate of the PMCs was higher when only compressed. Once lateral motion of the probe was introduced in a sliding fashion, the PMC survival rate depleted, suggesting that friction could be an important factor in the rupture properties of PMCs. Both intact percentages are shown with relative standard deviations to show the inherent variability in the technique.

Table 7.7: The mean number-based percentage of PMCs intact after either 1.5 N abrasion or 30 N compression for three disks. The figures after ± are the standard deviation

	1.5 N abrasion	**30 N compression**
Percentage of intact PMCs	26.3 ± 7.8	77.0 ± 5.2

Figure 7.7 and Figure 7.8 show the relative distributions of PMCs from the reference sample as recorded by fluorescence microscopy before and after force application for the 30 N compression and 1.5 N abrasion samples. The median size for the reference PMC sample was 18.9 μm as seen in Section 4.3, but this was the volume weighted median size. The size distributions seen below are number weighted, and as such, the most frequently observed PMCs fall into smaller size bands. The shape of the profile of size distributions was typical of large-scale manufacture of PMCs, with limited control over the size distribution. This suggested that the image-capturing and analysis was a robust method for quantifying the PMCs present on the resin. From simply looking at the size distributions it was difficult to understand if the diameter of PMCs impacted the survival rate after a 30 N normal load, or 1.5 N abrasion. However, by plotting the percentage of intact PMCs from both experiments, as seen in Figure 7.9, it was clear that in both cases as the PMC diameter increased, the fraction of intact PMCs after application of force decreased. It is known that as the diameter of microcapsules increases, the nominal rupture stress decreases, as seen in Chapter 4, and this was reflected in this result. In reality, a power law relationship is observed, but it was likely that not enough PMCs were counted at the extreme diameters of the size distribution to replicate this relationship. Nevertheless, the data showed that the technique could capture mechanical performance of the sample as an ensemble.

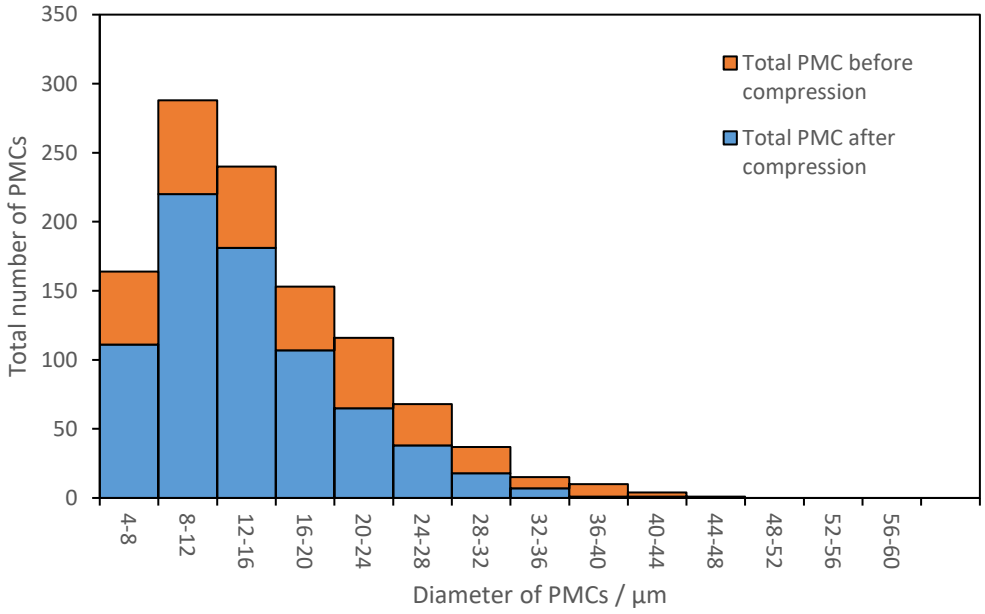

Figure 7.7: A histogram showing the total number of intact PMCs present before and after 30 N compression with the orange PDMS spherical probe

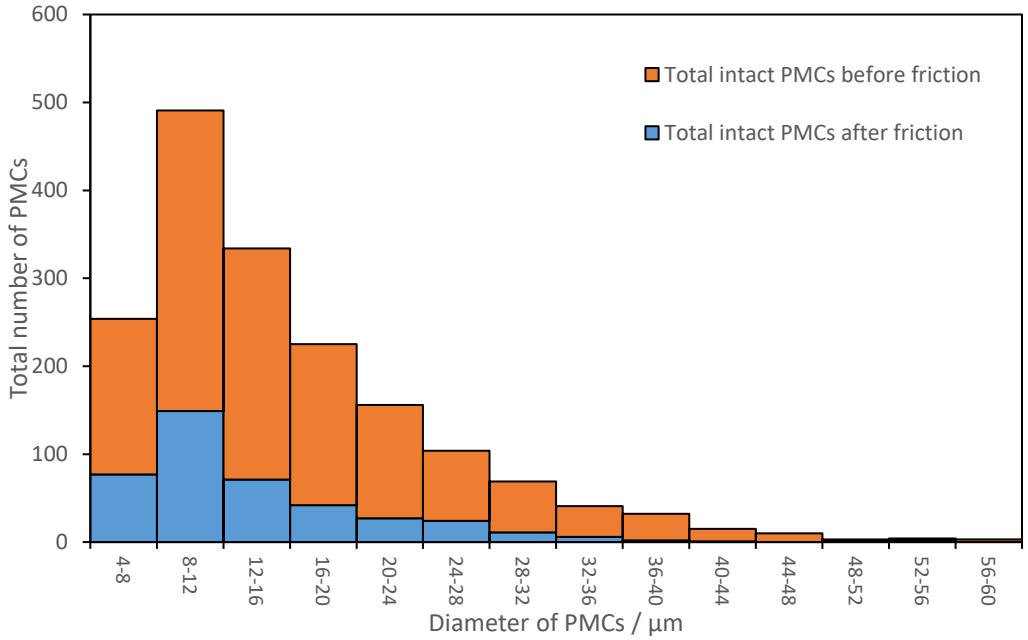

Figure 7.8: A histogram showing the total number of intact PMCs present before and after 1.5 N compression with lateral rotation against the substrate with the orange PDMS spherical probe

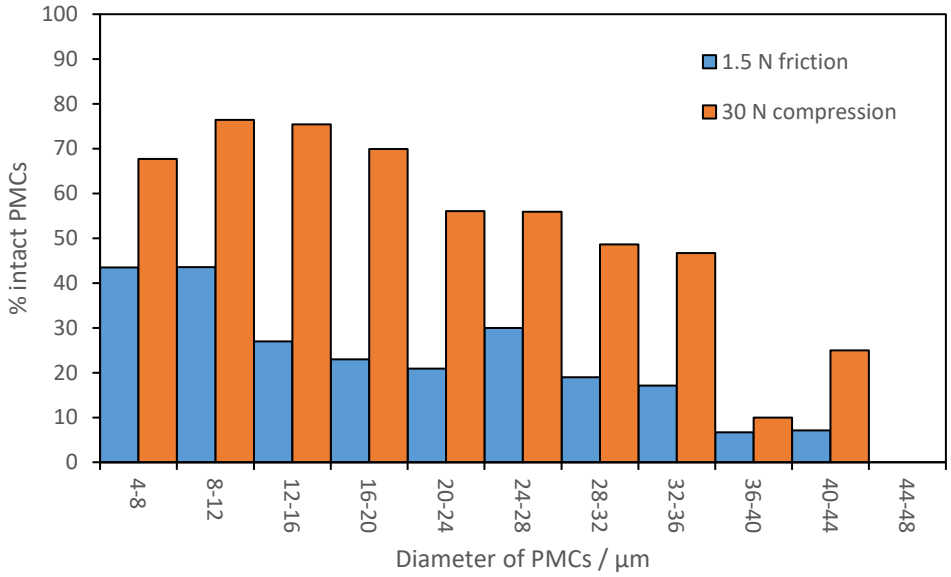

Figure 7.9: A histogram showing the number-based percentage of intact PMCs captured after either 30N compression of 1.5 N compression with lateral rotation

7.7 Comparing the rupture of a population of different PMC samples under abrasion

Alongside the reference sample the lower median size sample showed significantly lower nominal rupture stress at all PMC diameters as measured through micromanipulation in Section 4.5.3. Both samples were deposited onto Jesmonite disks and abraded under a 1 N normal load on the MTM2 at 2 $mm.s^{-1}$ rotation, with the orange PDMS ball used as the probe. As with previous abrasion runs, as seen in Section 7.6, the size distribution followed a similar shape profile to the true size distribution of both samples, as shown in Figure 7.10 and Figure 7.11.

Table 7.8 shows the average percentage of intact PMCs after the 1 N abrasion for both the reference samples and lower median size sample with associated standard deviation from three disks. Despite the reference sample appearing to show reduced breakage with respect to the

lower median size sample as seen in Table 7.8, there was no significant difference in the samples as described through a two-sample t-test for the reference sample (M = 35.7, SD = 5.6) and the lower median size sample (M = 28.2, SD = 7.4) conditions t(6) = 0.1279, p = 0.05. Increasing the number of disks analysed would serve to make it more likely to prove significance in lower median size showing greater percentage rupture compared to the reference sample.

Table 7.8: The mean number-based percentage of PMCs intact for the reference sample and lower median size sample after 1 N abrasion for three disks. The figures after ± are the standard deviation

	Lower median size sample	**Reference sample**
Percentage of intact PMCs	28.2 ± 7.4	35.7 ± 5.6

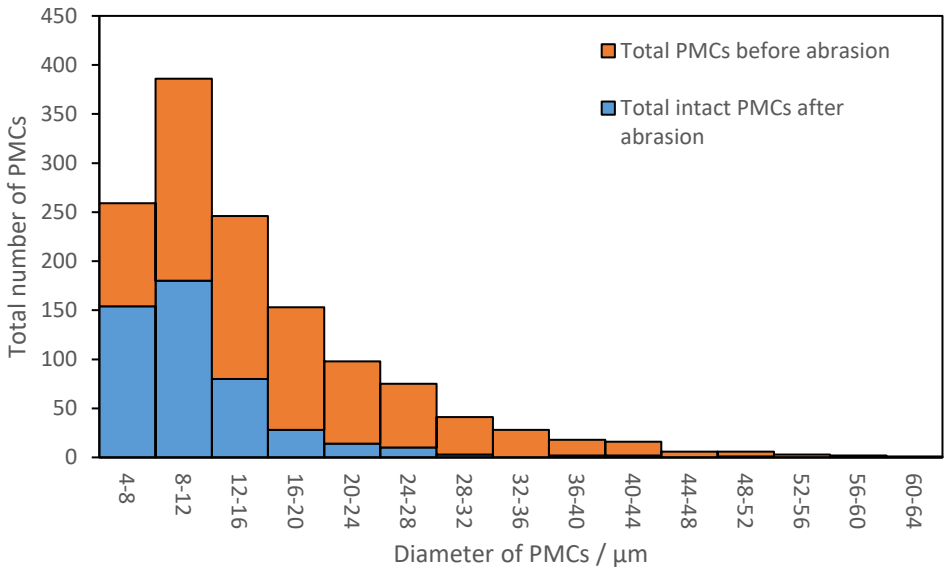

Figure 7.10: Histogram showing the number of intact of PMCs present before and after 1N abrasion with the reference sample

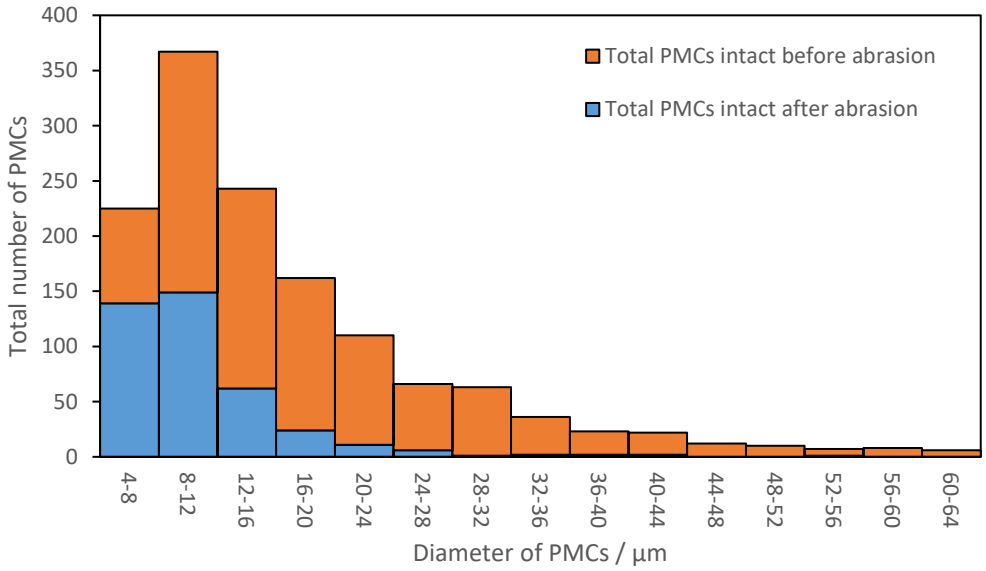

Figure 7.11: Histogram showing the number of intact of PMCs present before and after 1N abrasion with the lower median size sample

Figure 7.12 breaks down the percentage of intact PMCs for both samples into size bands in a histogram. To ensure it was representative of true numbers, only size bands with greater than ten PMCs recorded were included. The figure showed that for almost all of the size bands the lower median size sample showed decreased levels of intact PMCs, which was in line with the sample being more susceptible to rupture at lower stresses at all diameters compared to the reference sample.

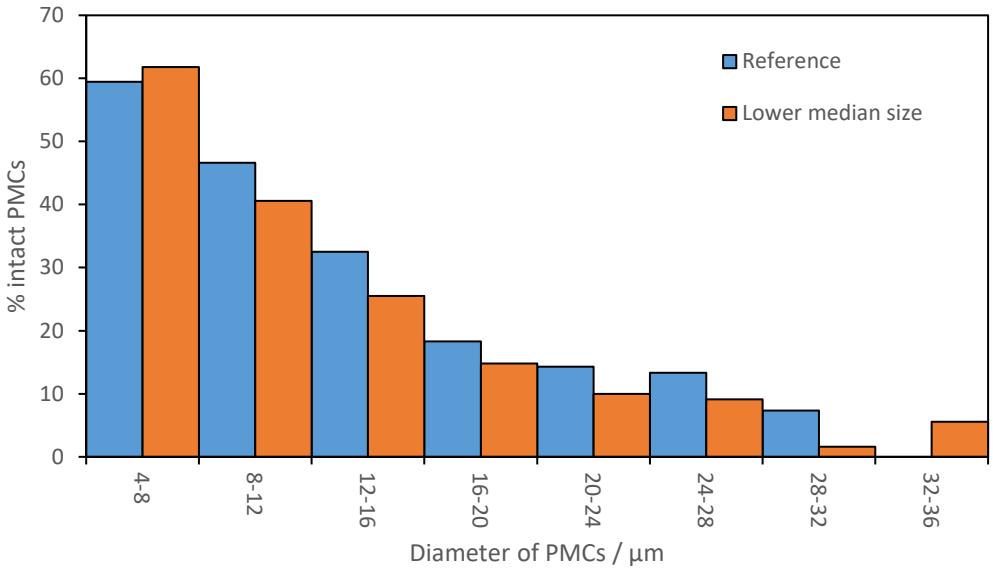

Figure 7.12: Histogram showing the number-based percentage of intact PMCs for the reference and lower median size samples after a 1 N abrasion. Only size bands with more than 10 PMCs total were counted

7.8 Assessing the rupture of PMCs under probes of different friction coefficients

The Young's modulus for the clear and orange balls was measured in section 7.1.4. When these values were applied to the Hertz model, see Equation 7-1, this gave contact areas and apparent contact stresses on Jesmonite resin under a 2.5 N load shown in

Table ***7.9***:

Table 7.9: The contact area and apparent contact stresses of orange and clear PDMS probes from analysis of compression data

	Clear PDMS ball	**Orange PDMS ball**
Contact area / m^2	2.8×10^{-5}	2.2×10^{-5}
Contact stress / MPa	0.089	0.113

In this situation a higher contact stress leads to a higher degree of rupture when solely considering compression, as shown in Section 7.4 . The friction coefficients of each of the probe were then investigated. As seen in Section 7.2, the friction coefficient between Jesmonite resin and the spherical probe did not change when PMCs were applied. Each different PDMS probe was therefore chosen to apply friction to a Jesmonite resin disk without PMCs at a speed of 2 $mm.s^{-1}$ under a load of 2.5 N with five rotations. Four replicates using different resin disks were conducted. The average friction coefficient for each probe was displayed in Table 7.10 below:

Table 7.10: Average friction coefficient for each colour of PDMS probe against the Jesmonite resin disks. The number after ± is the standard deviation

	Clear PDMS ball	**Orange PDMS ball**
Mean friction coefficient	1.06 ± 0.15	0.87 ± 0.05

These results showed that the coefficient of friction between the Jesmonite resin and the probe for the clear PDMS ball was higher than that of the orange PDMS ball. As such, experiments on the MTM studying the levels of breakage using each different probe highlights relative influence of friction. If friction had little impact then the orange PDMS ball, with a slightly higher contact stress may well show negligible change in breakage, but if an increased friction coefficient is important, there would be greater breakage seen in the results from the clear PDMS ball.

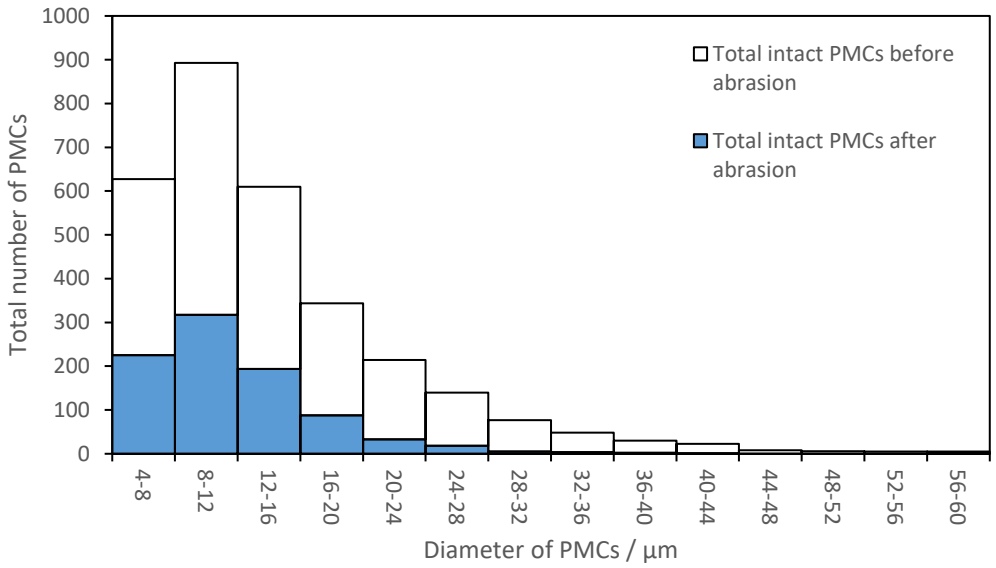

Figure 7.13: Histogram showing the number of intact PMCs present before (clear) and after (blue) a 2.5 N normal load with lateral rotation with the clear PDMS probe

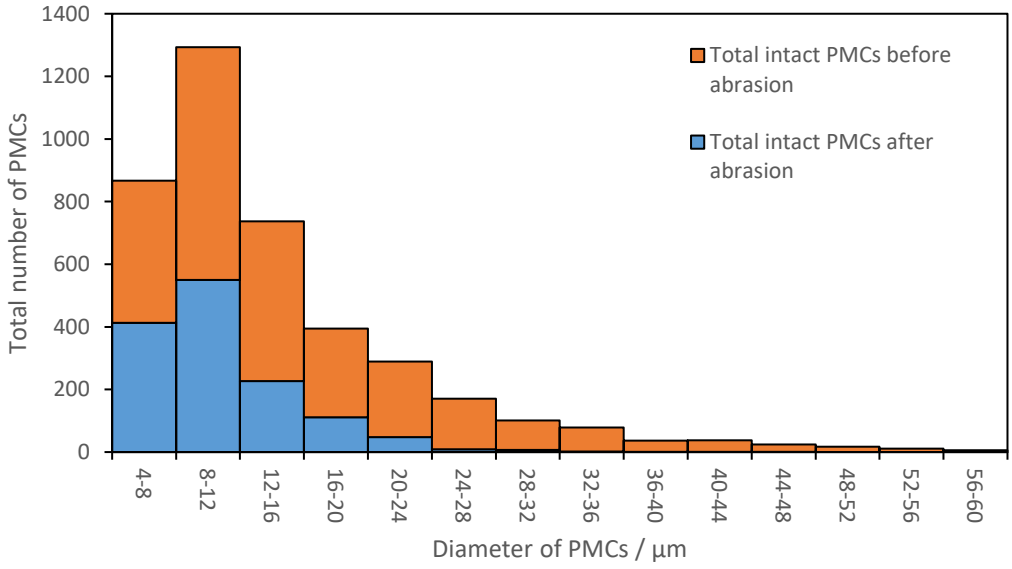

Figure 7.14: Histogram showing the number of intact PMCs present before (orange) and after (blue) 2.5 N normal load with lateral rotation with the orange PDMS probe

Figure 7.15 shows the percentage of intact PMCs at each size bands after abrasion by both probes. It was clear that below 12 µm, substantially more PMCs remain intact after abrasion with the orange PDMS probe; with the lower friction coefficient. Conversely, at higher diameters more PMCs remained intact with the clear probe. As seen by the distribution of total PMCs in Figure 7.13 and Figure 7.14, there were substantially more PMCs at the lower diameters suggesting this was a more robust view of the effect of the probes. Further investigation into this was conducted by looking at the percentage of intact PMCs over the whole sample distribution, and the results of which are displayed in Table 7.11. An independent t-test showed that for the four disks analysed the clear PDMS probe (M= 42.0, SD=7.6) showed significantly greater percentage rupture over the whole sample than the orange PDMS probe (M=32.3, SD=7.1) conditions $t(6) = 0.035$, $p=0.05$.

These results showed that despite applying a lower contact stress than the orange PDMS probe, albeit calculated from the Hertz model, which falters when friction is added, the clear PDMS probe with a greater coefficient of friction showed significantly greater rupture of PMCs under the same experimental conditions. This indicateed that friction as a force to rupture PMCs plays an important role, and certainly warrants more investigation in the future.

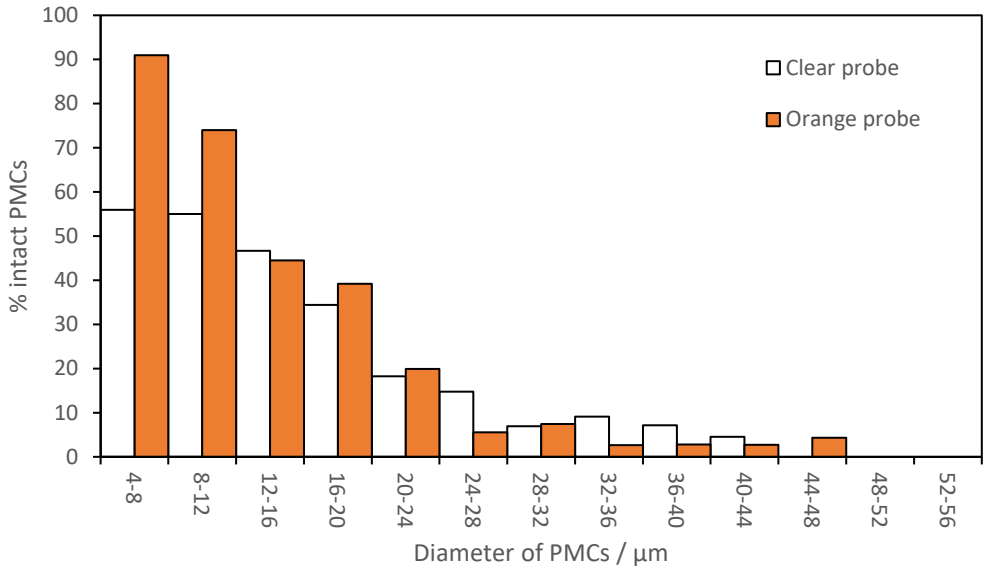

Figure 7.15: A histogram showing the number-based percentage of intact PMCs captured after 2.5 N abrasion for orange and clear PDMS probes

Table 7.11: The mean number-based percentage of PMCs intact for the reference sample with the orange and clear PDMS probe and a 2.5 N abrasion. The figures after ± are the standard deviation

	Orange PDMS probe	**Clear PDMS probe**
Percentage of intact PMCs	52.3 ± 7.1	42.0 ± 7.6

7.9 Conclusions

A new method for fixing PMCs on a substrate and imaging before and after abrasion whilst carefully controlling applied forces was devised. PMCs with a PM546 fluorescent dye in the core were fixed on a Jesmonite resin surface, allowing for imaging via fluorescence microscopy. An MTM2 tribometer, made by PCS instruments, was then used to apply a well-defined normal load through a spherical probe, with rotation of the base substrate containing the PMCs to promote abrasion between a PDMS spherical probe and the PMCs and substrate.

Imaging of the same area was captured before and after abrasion and image analysis thresholded PMCs by size, circularity and brightness was used to identify intact PMCs, allowing for quantification of intact PMCS of different sizes in the sample.

PMCs were compressed using a texture analyser to assess rupture of PMCs in the sample population through a normal force application of either 10 N or 40 N. It was found that despite the large increase in applied force under a 40 N compression, the percentage of PMCs remaining intact was not significantly less than the 10 N compression. Overall after compression there was a high number of intact PMCs for both compression forces. This was likely a result of the overall contact stress of the probe against the substrate which was found to be much lower than the stress required to break an individual PMC as measured in Chapter 4. This, however, was assuming the contact area was as calculated, but in reality it was likely due to asperities in the surface which would conversely increase the contact stress above that necessary to cause PMC rupture.

Friction forces were applied to PMCs fixed on the Jesmonite resin disk in dry conditions and in wet conditions after the setup was submerged in water. It was found that the friction coefficient between the probe and substrate did not change in either environment and the percentage of PMCs intact after friction force application was not significantly different. Individual PMC compression experiments in Chapter 4 confirmed that the rupture stress of the reference PMC sample did not change in 20% or 80% RH conditions. The results of the friction experiments agreed with these findings.

The relative impact of compression and friction was studied by quantifying the percentage of intact PMCs after 1.5 N abrasion and 30 N compression. It was found that the number of PMCs quantified displayed a size distribution profile of similar shape to the true size distribution of

PMCs in the sample. As the diameter of PMCs increased, the percentage of intact PMCs decreased after both 1.5 N abrasion and 30 N compression, and in all other measurements in the chapter. This agreed with the fact that the rupture stress PMCs decreases with increasing diameter, so fewer of the larger PMCs would survive. It was found that the percentage of intact PMCs significantly dropped after 1.5 N abrasion compared to 30 N compression, so despite a much lower normal load, the application of friction increases rupture.

The effect of friction on the percentage of intact PMCs was studied for the reference sample and the sample with lower median size, known from Chapter 4 to have a lower rupture stress at all diameters measured. The results from friction experiments was not able to show statistical difference in the survival of PMCs between the two samples after friction, however it was possible to see that at all PMC diameters there was a slight visible reduction in the number of intact PMCs for the lower median size sample in comparable size bands.

A clear PDMS probe was introduced which had a slightly lower Young's modulus and therefore a larger contact stress than the orange PDMS probe. Conversely, contact between this probe and the substrate had a higher friction coefficient than the orange probe. Analysis of the percentage of intact PMCs in the sample showed that the clear probe caused greater rupture of PMCs, indicating that the friction coefficient was more impactful than the contact stress on causing rupture.

The findings from these experiments, whilst very introductory, show that when there are friction forces acting on PMCs in the application they are intended for, such as when embedded in fabric in the wash, the effect of friction on the rupture of PMCs was potentially greater than anticipated and warrants further, more detailed study.

Chapter 8. OVERALL CONCLUSIONS AND RECOMMENDATIONS FOR FUTURE WORK

8.1 Overall conclusions

PMCs made from a PAC polymeric shell were shown by P&G to be the next generation of microcapsules for use in encapsulating perfume for laundry applications. Whilst a robust synthesis method had been established, deeper understanding of how to control the mechanical properties of the PMCs by utilising changes in structural and physicochemical properties was sought. The project in the first instance positioned to characterise PMC samples to understand which, if any of these parameters could impact mechanical properties, and if so, which of the properties proved to be most impactful in changing mechanical properties. Samples of PMCs were provided by P&G and the aim was that recommendations could be put forward on how to tailor the PMCs in order to meet a required mechanical strength performance profile.

Each sample, prepared by suspension polymerisation to encapsulate a commercial perfume oil, was subject to characterisation in order to determine basic structural properties such as shell thickness via TEM, size distribution via laser diffraction, and importantly mechanical properties via micromanipulation. This included studying the deformation at rupture of PMCs, the rupture force, nominal rupture stress, and intrinsic properties such as the Young's modulus of the shell material.

As expected for a microcapsule shell made from polymeric material, the rupture force for individual PMCs in all samples increased with increasing diameter, and the nominal rupture stress of PMCs decreased with increasing PMC diameter. The fractional deformation at rupture

was independent of PMC diameter for all samples. A reference sample, chosen as the benchmark formulation for P&G was compared against samples made with different structural or physicochemical characteristics. Ideally a design of experiments setup would have been preferred for truly understanding the effects of each factor, but this was overlooked for a variety of reasons such as economic constraints and processing constraints from the supplier. Characterisation was conducted for seven PMC samples in total. It was found that the sample with lower median size had a significantly lower nominal rupture stress than the reference, and a 95/5 core/shell ratio sample had a significantly greater rupture stress than the reference with a 90/10 core/shell ratio. All other samples showed no significant difference to the reference sample in terms of nominal rupture stress at each PMC diameter. Hypotheses for reasons for differences in mechanical strength based on structural and physicochemical differences between samples were put forward, however with the lack of information on the synthesis conditions these were only possibilities, rather than definitive reasons.

Development of a controlled environment chamber for the micromanipulation rig enabled characterisation of the mechanical properties of the PMCs at different humidities. It was found that when the humidity was changed from 20% to 80% RH, the nominal rupture stress did not change, but the Young's modulus as described by the Hertz model dropped significantly, meaning the PMCs became more deformable under the same force application. This was an important finding for application of PMCs in a washing machine given that the washing drum was an extremely humid environment.

A method of calculating the Young's modulus of the shell material, based on previous work and an FEM methodology was put forward, with adaptations made to take into consideration the widespread initial 'soft spot' compression. The results calculated Young's moduli in the

expected magnitude for a polymer shell, although the calculation of the shell thickness as a result of this model did not translate to actual shell thickness measured by TEM.

Once characterisation of individual PMC mechanical properties of the samples was conducted, it was important to understand how these findings translated into real world performance in the washing machine. A methodology was devised to completely quantify PMCs in a wash cycle in each possible output stream, giving an overall mass balance of PMCs. This could have been completed at any point during the wash, giving extremely valuable information about how PMCs were depositing, and if they were surviving. For intact and broken PMCs deposited on fabric a method was created to extract a fluorescent dye from the PMC core using either ethanol or hexane as a solvent and using the dye as a quantitative marker. Absolute quantification of dye was made possible by forming a calibration curve of known PMC quantities using fluorescence spectroscopy as the analytical technique.

For characterisation of intact and broken PMCs in washwater two more techniques were used. In a similar vein to quantifying intact PMCs in fabric, intact PMCs present in the washwater liquor were quantified by extracting the fluorescent dye from the core, but first by filtering the PMCs. Broken PMCs in washwater were quantified using headspace GC-MS analysis of the washwater liquor, using calibration curves of known concentrations of perfume.

Collectively these techniques offer the first incidence of being able to completely understand the fate of the PMC sample throughout the wash cycle. Not only does this enable accurate comparison between samples, but it also allows for identification of in which cycles the PMCs deposit, and which cycles they may rupture.

When the mass balance on the samples of PMCs was studied after washing cycles had run to completion it was observed that the percentage of intact PMCs depositing on the fabrics did not significantly differ between the reference sample, the lower median size sample, and the 95/5 core/shell ratio sample, which showed that the significant mechanical property differences measured through micromanipulation, giving the first indication that mechanical strengths of PMC samples, did not entirely correlate with the deposition from mass balance techniques.

It was found that conducting a wash cycle without fabrics did not cause any PMC rupture, meaning the hydrodynamic forces alone were not high enough, which was to be expected given the high shear processing conditions for forming PMCs. This also suggested that the fabric played a significant role in rupturing PMCs, either through compression, or through friction.

The collection of mass balance techniques was more accurate when a single ballast load was used in the wash. When the ballast type was moved from a knitted cotton ballast to terry cotton the deposition greatly increased, as well as abating PMC rupture. This was likely caused by an increased water absorbency meaning PMCs came into closer contact with fabrics as well as an increased creation of suds that reduced the forces in the machine.

Investigations were conducted to understand how the same PMCs responded to a different washing machine type, used in a different market; specifically the top-load semi-automatic machine. The competed mass balance showed markedly lower intact deposition and a large percentage of intact PMCs lost to the drain. This was caused by a decreased agitation with respect to standard front load machines, and a shorter cycle duration. This finding allows P&G to focus more on formulating PMCs with improved deposition profiles in these markets, rather than toiling over mechanical strength of the PMCs.

As previously highlighted, the nominal rupture stress alone did not provide good correlation with performance in the washing machine. Two more samples, X and Y, had much more extreme nominal rupture stresses than the lower median size sample and 95/5 core/shell ratio samples as a means of attempting to force out performance differences. Performance analysis of all samples was conducted where headspace GC-MS and olfactive analysis of damp and dry fabrics was indicative of PMC deposition and breakage. A new parameter, the volume weighted rupture stress, was devised as a potential marker. This used the power law fit of the nominal rupture stress against PMC diameter, and the size distribution of the sample to calculate a volume weighted average. This was calculated for all samples and showed excellent correlation with the performance analysis. This finding means that along with the mass balance protocols, which offer a more detailed understanding of PMCs in the wash, P&G also has a method to quickly screen new samples based upon the nominal rupture stress from micromanipulation data and the size distribution from light scattering measurements to model how samples would be expected to perform on fabrics. It can potentially take the guesswork out of estimating PMC performance. The principles of these protocols are transferrable, so they also enable the company to utilise for other applications.

A new method was devised for fixing PMCs on a substrate in order to observe rupture via friction, in addition to compression. PMCs were fixed on a Jesmonite resin which was cut into a disk for application on a Mini traction machine tribometer. Intact and broken PMCs were observed before and after force application with a PDMS spherical probe using fluorescence microscopy and image analysis allowed for quantification of PMCs and accurate determination of diameters.

Bulk compression of the PMCs on the resin was conducted using a texture analyser and a PDMS probe, as previously used in the field. It was found that increasing the compressive force from 10 N to 40 N increased the percentage of ruptured PMCs, but fell significantly short of causing complete rupture.

When friction was applied to the PMC sample by the tribometer in dry conditions, and in wet conditions when the sample was submerged, there was a decrease in the Young's modulus in the wet sample, but no significant difference in the percentage of rupture PMCs, which agreed with the findings of compression of single PMCs via micromanipulation under different humidities.

The relative effects of compression and friction were studied by compressing with a 30 N normal load, and applying friction under a 1.5 N normal load. Significantly more PMCs were ruptured due to friction than compression, even when a much greater force was applied.

Finally, the impact of the friction coefficients of the probes was studied. It was calculated that one probe had a greater Young's modulus than the other, which would lead to a larger contact stress. Conversely, this probe also displayed a lower friction coefficient. Upon studying the result of abrasion on the PMC samples it was found that abrasion by the probe with a greater friction coefficient caused significantly greater rupture of PMCs, highlighting the importance of friction between the PMCs and the probe on the survival rate compared to the stress applied to the PMCs.

8.2 Future work

(i) The approach of understanding the effect of structural and physicochemical characteristics of PMCs on the mechanical properties of the samples was based on using samples that P&G provided. This might have been due to economic constraints, or processing constraints, but it limited what could be extracted from the data. In order to gain a deeper understanding in future, full disclosure of processing conditions and formulations would be required, along with thought before synthesising samples to use a design of experiments approach to understand what factors can be sensibly varied in processing, before investigating how this alters structural and physicochemical properties and ultimately mechanical properties. If approached in this manner there would be less speculation associated with hypotheses for changes, and potentially results that could be built into a model to predict future design.

(ii) Compression and relaxation cycles are often repeated once or twice when assessing the viscoelasticity of a microcapsule sample. In reality, especially with PMCs in formulated products and in application in washing machines, there will be repeated instances of compression and relaxation during storage and in use. It would be of interest to invoke a large number of compressions below the failure strain of individual PMCs either using micromanipulation or an AFM to understand whether the PMCs can rupture below expected rupture stress.

(iii) To better understand the relationship between PMCs and Jesmonite resin for fixing in place during friction studies, it would be necessary to characterise the surface roughness of the substrate, using either interferometry or AFM. This would give better information about the asperity sizes and whether the void space was filled with resin, or if a porous network was formed. Once surface roughness was measured, more accurate calculation of real contact area would be possible and more work could be completed on contact stresses between probes and the substrate.

(iv) All PMCs supplied were provided with the same perfume oil core. If a different polymeric core was chosen this may have had an impact on the formation of the polymeric shell, for example how uniform and dense it could be. The perfume within the PAC PMCs was a commercially used variant from P&G, however more learnings could be gained on the PAC PMC architecture synthesised in the same conditions, by choosing more ideal perfume oils, with fewer varieties of hydrophobicities and reactivities between the components. The impact that certain properties of the perfume had on the mechanical properties and olfactive performance properties of the PMCs would have been more discernible in this case.

(v) The development of the ensemble method of assessing rupture of PMCs through friction application by the mini traction machine was a good way of highlighting the potential value in studying friction effects on PMCs, but to provide deeper understanding this would require study on individual PMCs. This would need to fix PMCs on a substrate

in such a way to immobilise PMCs, but to leave them free to deform as naturally as possible. An AFM probe would then compress the PMC to a certain strain and then using carefully controlled lateral movements would apply static and sliding friction forces to see if rupture can be caused at lower applied forces, as observed in the ensemble technique.

(vi) The development of the humidity chamber housing for the micromanipulation rig at the University of Birmingham was a more protracted process than imagined, meaning there was not much opportunity to utilise thoroughly. As such, investigating PMCs mechanical properties under changing humidity took priority, but it would have been beneficial to study the mechanical properties of PMCs in extreme temperatures. This would be relevant for washing process as not only do wash temperatures vary, but many consumers choose to use a tumble dryer, so understanding how PMCs respond in these temperatures would give valuable information on future design and recommended usage.

(vii) The identification of the volume weighted rupture stress as a marker for PMC olfactive performance on damp and dry fabrics was a key finding that enables the manufacturer to be more directed in the PMC synthesis approach. To build more confidence in the relationship, more PMC types would need to be studied. It would also be of interest to understand if the trend of the relationship continued for alternative PMC architectures

such as with melamine formaldehyde and some non-polymeric PMC types that may have a place in the future of the application.

REFERENCES

Adi, S., Adi, H., Chan, H.-K., Young, P. M., Traini, D., Yang, R. & Yu, A. 2008. Scanning White-Light Interferometry as a Novel Technique to Quantify the Surface Roughness of Micron-Sized Particles for Inhalation. *Langmuir,* 24**,** 11307-11312.

Al-Mansoori, T., Micaelo, R., Artamendi, I., Norambuena-Contreras, J. & Garcia, A. 2017. Microcapsules for self-healing of asphalt mixture without compromising mechanical performance. *Construction and Building Materials,* 155**,** 1091-1100.

Al Shannaq, R. & Farid, M. M. 2015. Microencapsulation of phase change materials (PCMs) for thermal energy storage systems. *In:* CABEZA, L. F. (ed.) *Advances in Thermal Energy Storage Systems.* Woodhead Publishing.

Alexandridou, S. & Kiparissides, C. 1994. Production of oil-containing polyterephthalamide microcapsules by interfacial polymerization. An experimental investigation of the effect of process variables on the microcapsule size distribution. *Journal of Microencapsulation,* 11**,** 603-614.

Ali, M., Meaney, S. P., Abedin, M. J., Holt, P., Majumder, M. & Tabor, R. F. 2019. Graphene Oxide–Silica Hybrid Capsules for Sustained Fragrance Release. *Journal of Colloid and Interface Science,* 552**,** 528-539.

Allan-Wojtas, P., Truelstrup Hansen, L. & Paulson, A. T. 2008. Microstructural studies of probiotic bacteria-loaded alginate microcapsules using standard electron microscopy techniques and anhydrous fixation. *LWT - Food Science and technology,* 41 101-108

Andersson Trojer, M., Li, Y., Abrahamsson, C., Mohamed, A., Eastoe, J., Holmberg, K. & Nydén, M. 2013a. Charged microcapsules for controlled release of hydrophobic actives. Part I: encapsulation methodology and interfacial properties. *Soft Matter,* 9 1468-1477

Andersson Trojer, M., Nordstierna, L., Nordin, M., Nydén, M. & Holmberg, K. 2013b. Encapsulation of actives for sustained release. *Physical Chemistry Chemical Physics,* 15**,** 17727-17741.

Andrade, B., Song, Z., Li, J., Zimmerman, S. C., Cheng, J., Moore, J. S., Harris, K. & Katz, J. S. 2015. New Frontiers for Encapsulation in the Chemical Industry. *ACS Applied Materials & Interfaces,* 7**,** 6359-6368.

Appivon Inc. 2014. *Microcapsule Particles*. WO 2014/105440.

Ashraf, M. A., Khan, A. M., Sarfraz, M. & Ahmad, M. 2015. Effectiveness of silica based sol-gel microencapsulation method for odorants and flavors leading to sustainable environment. *Frontiers in Chemistry,* 3**,** 1-15.

Bakry, A. M., Abbas, S., Ali, B., Majeed, H., Abouelwafa, M. Y., Mousa, A. & Liang, L. 2016. Microencapsulation of Oils: A Comprehensive Review of Benefits, Techniques, and Applications. *Comprehensive Reviews in Food Science and Food Safety,* 15**,** 143-182.

Bashaiwoldu, A. B., Podczeck, F. & Newton, J. M. 2004. The application of non-contact laser profilometry to the determination of permanent structural change induced by compaction of pellets: II. Pellets dried by different techniques. *European Journal of Pharmaceutical Sciences,* 22**,** 55-61.

Bintein, S. 2017. Intentionally added microplastics in products. *In:* COMMISSION, E. (ed.). Brussels: Amec Foster Wheeler Environment & Infrastructure UK LTD.

Bogdanowicz, K. A., Tylkowski, B. & Giamberini, M. 2013. Preparation and Characterization of Light-Sensitive Microcapsules Based on a Liquid Crystalline Polyester. *Langmuir*, 29 1601-1608

Bomgardner, M. M. 2019. How perfumers walk the fine line between natural and synthetic. *Chemical & Engineering News.* American Chemical Society

Bône, S., Vautrin, C., Barbesant, V., Truchon, S., Harrison, I. & Geffroy, C. 2011. Microencapsulated Fragrances in Melamine Formaldehyde Resins. *CHIMIA International Journal for Chemistry,* 65**,** 177-181.

Bråred Christensson, J., Hagvall, L. & Karlberg, A.-T. 2016. Fragrance Allergens, Overview with a Focus on Recent Developments and Understanding of Abiotic and Biotic Activation. *Cosmetics,* 3**,** 19-37.

Brooks, B. 2010. Suspension Polymerization Processes. *Chemical Engineering & Technology,* 33**,** 1737-1744.

Bruyninckx, K. & Dusselier, M. 2019. Sustainable Chemistry Considerations for the Encapsulation of Volatile Compounds in Laundry-Type Applications. *ACS Sustainable Chemistry & Engineering,* 7**,** 8041-8054.

Bungenberg De Jong, H. G. 1949. Crystallisation-coacervation-flocculation. *Colloid Science II,* 8**,** 252-258.

Bungenberg, H. G. a. B., O. 1939. Behaviour of microscopic bodies consisting of biocolloid systems and suspended in an aqueous medium. IV. Vacuolation phenomena of complex coacervate drops at a constant temperature. Formation of foam structures and of thin-walled drops with a large central vacuole. . *Proceedings of the royal netherlands academy of arts and science,* 41**,** 643-646.

Butt, H. 1991. Measuring electrostatic, van der waals, and hydration foforces electrolyte solutions with an atomic force microscope. *Biophysical Journal,* 60 1438-1444

Cao, V. D., Pilehvar, S., Salas-Bringas, C., Szczotok, A. M., Rodriguez, J. F., Carmona, M., Al-Manasir, N. & Kjøniksen, A.-L. 2017. Microencapsulated phase change materials for enhancing the thermal performance of Portland cement concrete and geopolymer concrete for passive building applications. *Energy Conversion and Management,* 133**,** 56-66.

Cao, Z., Landfester, K. & Ziener, U. 2012. Preparation of Dually, pH- and Thermo-Responsive Nanocapsules in Inverse Miniemulsion. *Langmuir,* 28**,** 1163-1168.

Caruso, M. M., Blaiszik, B. J., Jin, H., Schelkopf, S. R., Stradley, D. S., Sottos, N. R., White, S. R. & Moore, J. S. 2010. Robust, Double-Walled Microcapsules for Self-Healing Polymeric Materials. *ACS Applied Materials & Interfaces,* 2**,** 1195-1199.

Casanova, F. & Santos, L. 2016. Encapsulation of cosmetic active ingredients for topical application – a review. *Journal of Microencapsulation,* 33**,** 1-17.

Charlon, M., Trachsel, A., Paret, N., Frascotti, L., Berthier, D. L. & Herrmann, A. 2015. "Old" chemistry in a new context: photocleavable 2-oxoacetate-containing latex dispersions and core–shell microcapsules for the controlled release of volatile compounds. *Polymer Chemistry,* 6**,** 3224-3235.

Chatterjee, S., Salaün, F. & Campagne, C. 2014a. Development of Multilayer Microcapsules by a Phase Coacervation Method Based on Ionic Interactions for Textile Applications. *Pharmaceutics,* 6**,** 281-297.

Chatterjee, S., Salaün, F. & Campagne, C. 2014b. Development of Multilayer Microcapsules by a Phase Coacervation Method Based on Ionic Interactions for Textile Applications. *Pharmaceutics,* 6**,** 281-297.

Chen, J., Jo, S. & Park, K. 1995. Polysaccharide hydrogels for protein drug delivery. *Carbohydrate Polymers,* 28 69-76

Chen, K. & Zhou, S. 2015. Fabrication of ultraviolet-responsive microcapsules via Pickering emulsion polymerization using modified nano-silica/nano-titania as Pickering agents. *RSC Advances,* 5**,** 13850-13856.

Choi, I., Malak, S. T., Xu, W., Heller, W. T., Tsitsilianis, C. & Tsukruk, V. V. 2013. Multicompartmental Microcapsules from Star Copolymer Micelles. *Macromolecules,* 46 1425-1436

Chowdhury, R. A., Hosur, M. V., Nuruddin, M., Tcherbi-Narteh, A., Kumar, A., Boddu, V. & Jeelani, S. 2015. Self-healing epoxy composites: preparation, characterization and healing performance. *Journal of Materials Research and Technology,* 4**,** 33-43.

Chung, P.-H., Tregidgo, C. & Suhling, K. 2016. Determining a fluorophore's transition dipole moment from fluorescence lifetime measurements in solvents of varying refractive index. *Methods and Applications in Fluorescence,* 4**,** 045001-045011.

Cordoví, C. M., De Lucas, A., Rodriguez, J. F. & Tejeda, J. 1997. Influence of Stirring Speed on the Suspension Copolymerization of Styrene with Methyl Methacrylate. *Journal of Macromolecular Science, Part A,* 34**,** 1339-1351.

Dardelle, G., Jacquemond, M. & Erni, P. 2017. Delivery Systems for Low Molecular Weight Payloads: Core/Shell Capsules with Composite Coacervate/Polyurea Membranes. *Advanced Materials,* 29**,** 1606099-1606105.

De La Paz Miguel, M. & Vallo, C. I. 2019. Influence of the emulsifying system to obtain linseed oil-filled microcapsules with a robust poly (melamine-formaldehyde)-based shell. *Progress in Organic Coatings,* 129**,** 236-246.

De Loubens, C., Deschamps, J., Georgelin, M., Charrier, A., Edwards-Levy, F. & Leonetti, M. 2014. Mechanical characterization of cross-linked serum albumin microcapsules. *Soft Matter,* 10**,** 4561-4568.

De Vos, P., Van Hoogmoed, C. G., Van Zanten, J., Netter, S., Strubbe, J. S. & Busscher, H. J. 2003. Long-term biocompatibility, chemistry, and function of microencapsulated pancreatic islets. *Biomaterials,* 24 305-312

Dirlik-Uysal, Ç. D., Bou-Belda, E., Bonet-Aracil, M., Belino, N., Diaz-García, P. & Montava, I. 2017. Comparison of Binder Influence and Rigidity on Knitting Fabrics Treated with PCMs by Padding and Coating. *IOP Conference Series: Materials Science and Engineering,* 254**,** 122003.

Dispinar, T., Colard, C. a. L. & Du Prez, F. E. 2013. Polyurea microcapsules with a photocleavable shell: UV-triggered release. *Polymer Chemistry,* 4**,** 763-772.

Dorati, R., Patrini, M., Perugini, P., Pavanetto, F., Stella, A., Modena, T., Genta, I. & Conti, B. 2006. Surface characterization by atomic force microscopy of sterilized PLGA microspheres. *Journal of Microencapsulation,* 23**,** 123-133.

Ducker, W. A., Senden, T. J. & Pashley, R. M. 1991. Direct Measurement of Colloidal Forces Using An Atomic Force Microscope. *Nature,* 353 239-241

Engbrecht, J., Green, D., Hillmyer, M. A., Olson, D. & Todd, E. M. 2013. Positron lifetime spectroscopy in ordered nanoporous polymers. *Journal of Polymer Science Part B: Polymer Physics,* 51**,** 1157-1161.

Fanger, G. O. 1974. Microencapsulation: A Brief History and Introduction. *In:* VANDEGAER, J. E. (ed.) *Microencapsulation: Processes and Applications.* Boston, MA: Springer US.

Fei, X., Zhao, H., Zhang, B., Cao, L., Yu, M., Zhou, J. & Yu, L. 2015. Microencapsulation mechanism and size control of fragrance microcapsules with melamine resin shell. *Colloids and Surfaces A: Physicochemical and Engineering Aspects,* 469**,** 300-306.

Feng, W. W. & Yang, W. H. 1973. On the Contact Problem of an Inflated Spherical Nonlinear Membrane. *Journal of Applied Mechanics,* 40**,** 209-214.

Fery, A. & Weinkamer, R. 2007. Mechanical properties of micro- and nanocapsules: Single-capsule measurements. *Polymer,* 48 7221-7235

Firmenich Sa. 2015. *Polyurea microcapsules*. United States patent application 9034384.

Fukuzumi, H., Saito, T., Iwamoto, S., Kumamoto, Y., Ohdaira, T., Suzuki, R. & Isogai, A. 2011. Pore Size Determination of TEMPO-Oxidized Cellulose Nanofibril Films by Positron Annihilation Lifetime Spectroscopy. *Biomacromolecules,* 12**,** 4057-4062.

Gidley, D. W., Peng, H.-G. & Vallery, R. S. 2006. Positron Annihilation as a Method to Characterize Porous Materials. *Annual Review of Materials Research,* 36**,** 49-79.

Givaudan Sa. 2009. *Product*. WO/2009/100553.

Goldstein, J. I., Newbury, D. E., Echlin, P., Joy, D. C., Lyman, C. E., Lifshin, E., Sawyer, L. & Michael, J. R. 2003. *Scanning Electron Microscopy and X-ray Microanalysis*, Springer.

Gonçalves, O. H., Nogueira, A. L., Araújo, P. H. H. & Machado, R. a. F. 2011. Effects of Operational Parameters on Particle Size Distributions in Methyl Methacrylate Suspension Polymerization. *Industrial & Engineering Chemistry Research,* 50**,** 9116-9122.

Gray, A., Egan, S., Bakalis, S. & Zhang, Z. 2016. Determination of microcapsule physicochemical, structural, and mechanical properties. *Particuology,* 24**,** 32-43.

Groeber, M. A., Haley, B. K., Uchic, M. D., Dimiduk, D. M. & Ghosh, S. 2006. 3D reconstruction and characterization of polycrystalline microstructures using a FIB-SEM system. *Materials Characterization,* 57 259-273

Gutsche, A., Daikeler, A., Guo, X., Dingenouts, N. & Nirsche, H. 2014. Time-resolved SAXS characterization of the shell growth of silica-coated magnetite nanocomposites. *Journal of Nanoparticle Research,* 16**,** 2475-2487.

Haas, D. E., Birnie Iii, D. P., Zecchino, M. J. & Figueroa, J. T. 2001. The effect of radial position and spin speed on striation spacing in spin on glass coatings. *Journal of Materials Science Letters,* 20**,** 1763-1766.

Han, B., Wang, X., Gao, X., Liu, J., Liang, F., Qu, X. & Yang, Z. 2011. Synthesis and characterization of biodegradable microcapsules for the controlled delivery of calcium hydroxide. *Journal of Biomedical Materials Research Part B: Applied Biomaterials,* 99B**,** 120-126.

He, C., Xiong, B., Mao, W., Kobayashi, Y., Oka, T., Oshima, N. & Suzuki, R. 2013. On determining the entrance size of cage-like pores in mesoporous silica films by positron annihilation lifetime spectroscopy. *Chemical Physics Letters,* 590**,** 97-100.

He, L., Hu, J. & Deng, W. 2018. Preparation and application of flavor and fragrance capsules. *Polymer Chemistry,* 9**,** 4926-4946.

He, Y., Bowen, J., Andrews, J. W., Liu, M., Smets, J. & Zhang, Z. 2014. Adhesion of perfume-filled microcapsules to model fabric surfaces. *Journal of Microencapsulation,* 31**,** 430-439.

Hénon, S., Lenormand, G., Richert, A. & Gallet, F. 1999. A New Determination of the Shear Modulus of the Human Erythrocyte Membrane Using Optical Tweezers. *Biophysical Journal,* 76**,** 1145-1151

Herrmann, A. 2007. Controlled Release of Volatiles under Mild Reaction Conditions: From Nature to Everyday Products. *Angewandte Chemie International Edition,* 46**,** 5836-5863.

Hertz, H. 1882. Ueber die Berührung fester elastischer Körper. *Journal für die reine und angewandte Mathematik*

Hitchcock, J. P., Tasker, A. L., Baxter, E. A., Biggs, S. & Cayre, O. J. 2015. Long-Term Retention of Small, Volatile Molecular Species within Metallic Microcapsules. *ACS Applied Materials & Interfaces,* 7**,** 14808-14815.

Hofmeister, I., Landfester, K. & Taden, A. 2015. Controlled Formation of Polymer Nanocapsules with High Diffusion-Barrier Properties and Prediction of Encapsulation Efficiency. *Angewandte Chemie International Edition,* 54**,** 327-330.

Hu, J., Chen, H.-Q. & Zhang, Z. 2009. Mechanical properties of melamine formaldehyde microcapsules for self-healing materials. *Materials Chemistry and Physics,* 118 63-70

Hu, J., Xiao, Z.-B., Zhou, R.-J., Ma, S.-S., Li, Z. & Wang, M.-X. 2011. Comparison of compounded fragrance and chitosan nanoparticles loaded with fragrance applied in cotton fabrics. *Textile Research Journal,* 81**,** 2056-2064.

Huang, Y.-I., Cheng, Y.-H., Yu, C.-C., Tsai, T.-R. & Cham, T.-M. 2007. Microencapsulation of extract containing shikonin using gelatin–acacia coacervation method: A formaldehyde-free approach. *Colloids and Surfaces B: Biointerfaces,* 58**,** 290-297.

International Flavors and Fragrances Inc. 2005. *Melamine-formaldehyde microcapsule slurries for fabric article freshening*. EP20040257187. 2005-05-25.

International Flavours and Fragrances Inc. 2017. *Polyurea capsule compositions*. PCT/US2017/018347. 2017-08-24.

Jain, A., Thakur, D., Ghoshal, G., Katare, O. P. & Shivhare, U. S. 2016. Characterization of microcapsulated β-carotene formed by complex coacervation using casein and gum tragacanth. *International Journal of Biological Macromolecules,* 87**,** 101-113.

Jesmonite Limited. 2017. *Jesmonite AC100 Technical Data Sheet* [Online]. [Accessed July 20 2018].

Jia, X., Sheng, W.-B., Li, W., Tong, Y.-B., Liu, Z.-Y. & Zhou, F. 2014. Adhesive Polydopamine Coated Avermectin Microcapsules for Prolonging Foliar Pesticide Retention. *ACS Applied Materials & Interfaces,* 6**,** 19552-19558.

Jiao, S.-Z., Sun, Z.-C., Li, F.-R., Yan, M.-J., Cao, M.-J., Li, D.-S., Liu, Y. & Li, L.-H. 2018. Preparation and Application of Conductive Polyaniline-Coated Thermally Expandable Microspheres. *Polymers,* 11**,** 22-30.

Juliano, C. & Magrini, G. A. 2017. Cosmetic Ingredients as Emerging Pollutants of Environmental and Health Concern. A Mini-Review. *Cosmetics,* 4**,** 11-29.

Kaufman, G., Mukhopadhyay, S., Rokhlenko, Y., Nejati, S., Boltyanskiy, R., Choo, Y., Loewenberg, M. & Osuji, C. O. 2017. Highly stiff yet elastic microcapsules incorporating cellulose nanofibrils. *Soft Matter,* 13**,** 2733-2737.

Keller, M. W. & Sottos, N. R. 2006. Mechanical properties of microcapsules used in a self-healing polymer. *Exp. Mech.,* 46 725-733

Kleban, M., Weisser, J., Koch, F. & Schwaiger, W. 2004. *Leather finished with scent-containing microcapsules*. US10/887,685. 2004-12-02.

Kleinberger, R. M., Burke, N. a. D., Dalnoki-Veress, K. & Stöver, H. D. H. 2013. Systematic study of alginate-based microcapsules by micropipette aspiration and confocal fluorescence microscopy. *Materials Science and Engineering: C,* 33**,** 4295-4304.

Knoche, S. & Kierfeld, J. 2014. Osmotic buckling of spherical capsules. *Soft Matter,* 10**,** 8358-8369.

Kouisni, L. & Rochefort, D. 2009. Confocal microscopy study of polymer microcapsules for enzyme immobilisation in paper substrates. *Journal of Applied Polymer Science,* 111**,** 1-10.

Kumar, C. S. S. R. 2013. *Transmission Electron Microscopy Characterization of Nanomaterials*, Springer.

L'oréal Sa. 1998. *Composition comprising an aqueous dispersion of lipid vesicles encapsulating a UV screening agent with acidic functionality, and usess in topical application*. US08/755,314. 1998-06-02.

Lardner, T. J. & Pujara, P. 1980. XII - Compression of Spherical Cells A2 *Mechanics Today.* Pergamon.

Lasagni, F., Lasagni, A., Holzapfel, C., Mücklich, F. & Degischer, H. P. 2006. Three Dimensional Characterization of Unmodified and Sr-Modified Al-Si Eutectics by FIB and FIB EDX Tomography. *Advanced Engineering Materials*, 8 719-723

Lasagni, F., Lasagni, A., Marks, E., Holzapfel, C., Mücklich, F. & Degischer, H. P. 2007. Three-dimensional characterization of "as-cast" and solution-treated AlSi12(Sr) alloys by high-resolution FIB tomography. *Acta Materialia,* 55 3875-3882

Latnikova, A. & Jobmann, M. 2017. Towards Microcapsules with Improved Barrier Properties. *Topics in Current Chemistry*, 375**,** 64-81.

Law, D. & Zhang, Z. 2007. Stabilisation and targeted delivery of a fibrinolytic enzyme (nattokinase) by shellac. *Minerva Biotecnologica,* 19**,** 17-26.

Leclercq, S., Harlander, K. R. & Reineccius, G. A. 2009. Formation and characterization of microcapsules by complex coacervation with liquid or solid aroma cores. *Flavour and Fragrance Journal,* 24**,** 17-24.

Lee, H., Choi, C.-H., Abbaspourrad, A., Wesner, C., Caggioni, M., Zhu, T. & Weitz, D. A. 2016. Encapsulation and Enhanced Retention of Fragrance in Polymer Microcapsules. *ACS Applied Materials & Interfaces,* 8**,** 4007-4013.

Lee, H. Y., Lee, S. J., Cheong, I. W. & Kim, J. H. 2002. Microencapsulation of fragrant oil via in situ polymerization: effects of pH and melamine-formaldehyde molar ratio. *Journal of Microencapsulation,* 19**,** 559-569.

Lee, W. L., Tan, J. W. M., Tan, C. N. & Loo, S. C. J. 2014. Modulating Drug Release from Gastric-Floating Microcapsules through Spray-Coating Layers. *PLOS ONE,* 9**,** 1-18.

Lefebvre, Y., Leclerc, E., Barthès-Biesel, D., Walter, J. & Edwards-Lévy, F. 2008. Flow of artificial microcapsules in microfluidic channels: A method for determining the elastic properties of the membrane. *Physics of Fluids,* 20 123102-123112.

Lekka, M., Sainz-Serp, D., Kulik, A. J. & Wandrey, C. 2004. Hydrogel Microspheres: Influence of Chemical Composition on Surface Morphology, Local Elastic Properties, and Bulk Mechanical Characteristics. *Langmuir,* 20 9968-9977

Lengyel, M., Balogh, E., Szerőczei, D., Dobó-Nagy, C., Pápay, Z., Stömmer, V., Klebovich, I. & Antal, I. 2018. Study on process parameters and optimization of microencapsulation based on phase separation. *European Journal of Pharmaceutical Sciences,* 122**,** 273-280.

Lenoir, S., Pagnoulle, C., Galleni, M., Compère, P., Jérôme, R. & Detrembleur, C. 2006. Polyolefin Matrixes with Permanent Antibacterial Activity: Preparation, Antibacterial Activity, and Action Mode of the Active Species. *Biomacromolecules,* 7**,** 2291-2296.

Lensen, D., Gelderblom, E. C., Vriezema, D. M., Marmottant, P., Verdonschot, N., Versluis, M., De Jong, N. & Van Hest, J. C. M. 2011. Biodegradable polymeric microcapsules for selective ultrasound-triggered drug release. *Soft Matter,* 7 5417-5422.

León, G., Paret, N., Fankhauser, P., Grenno, D., Erni, P., Ouali, L. & Berthier, D. L. 2017. Formaldehyde-free melamine microcapsules as core/shell delivery systems for encapsulation of volatile active ingredients. *RSC Advances,* 7**,** 18962-18975.

Levin, I. W. & Bhargava, R. 2005. Fourier transform infrared vibrational spectroscopic imaging: integrating microscopy and molecular recognition. *Annual Review of Physical Chemistry,* 56 429-474

Li, B.-X., Li, X.-X., Liu, Y., Zhang, D.-X., Lin, J., Mu, W. & Liu, F. 2018. Easily Tunable Membrane Thickness of Microcapsules by Using a Coordination Assembly on the Liquid-Liquid Interface. *Frontiers in Chemistry,* 6**,** 1-9.

Li, B., Guan, L., Wang, K., Zhang, D., Wang, W. & Liu, F. 2016. Formula and process optimization of controlled-release microcapsules prepared using a coordination assembly and the response surface methodology. *Journal of Applied Polymer Science,* 133**,** 42865 - 42873.

Li, Y., Ai, L., Yokoyama, W., Shoemaker, C. F., Wei, D., Ma, J. & Zhong, F. 2013. Properties of Chitosan-Microencapsulated Orange Oil Prepared by Spray-Drying and Its Stability to Detergents. *Journal of Agricultural and Food Chemistry,* 61**,** 3311-3319.

Lifshin, E. 1999. *X-ray characterisation of materials,* New York, Wiley VCH.

Liu, H., Wang, X. & Wu, D. 2019. Innovative design of microencapsulated phase change materials for thermal energy storage and versatile applications: a review. *Sustainable Energy & Fuels,* 3**,** 1091-1149.

Liu, K.-K. 2006. Deformation behaviour of soft particles: a review. *J. Phys. D: Appl. Phys.,* 39 188-189.

Liu, M. 2010. *Understanding the Mechanical Strength of Microcapsules and Their Adhesion on Fabric Surfaces.* University of Birmingham.

Long, Y., Liu, C., Zhao, B., Song, K., Yang, G. & Tung, C.-H. 2015. Bio-inspired controlled release through compression–relaxation cycles of microcapsules. *Npg Asia Materials,* 7**,** e148.

Long, Y., Vincent, B., York, D., Zhang, Z. & Preece, J. A. 2010. Organic-inorganic double shell composite microcapsules. *Chemical Communications,* 46**,** 1718-1720.

López Arbeloa, F., López Arbeloa, T. & López Arbeloa, I. 1999. Electronic spectroscopy of pyrromethene 546. *Journal of Photochemistry and Photobiology A: Chemistry,* 121**,** 177-182.

Lu, G. Z., Gray, M. R. & Thompson, B. G. 1992. Physical modeling of animal cell damage by hydrodynamic forces in suspension cultures. *Biotechnology and Bioengineering,* 40 1277-1281

Martins Dos Santos, V. a. P., Leenen, E. J. T. M., Rippoll, M. M., Van Der Sluis, C., Van Vliet, T., Tramper, J. & Wijffels, R. 1997. Relevance of rheological properties of gel beads for their mechanical stability in bioreactors. *Biotechnology and Bioengineering,* 56 517-529

Maybelline Intermediate Corp. 1998. *Skin revitalizing makeup composition*. EP95944158A. 1998-03-04.

Mccoy, M. 2014. Value proposition in the cleaning aisle. *Chemical & Engineering News.* American Chemical Society

Mccoy, M. 2018. How encapsulation is taking root in the laundry room. *Chemical & Engineering News.* American Chemical Society

Mcfarland, B. & Pojman, J. A. 2015. Effects of shell crosslinking on polyurea microcapsules containing a free-radical initiator. *Journal of Applied Polymer Science,* 132**,** 42408-42418.

Mercadé-Prieto, R., Allen, R., York, D., Preece, J. A., Goodwin, T. E. & Zhang, Z. 2012a. Determination of the shell permeability of microcapsules with a core of oil-based active ingredient. *Journal of Microencapsulation,* 29**,** 463-474.

Mercadé-Prieto, R., Allen, R., Zhang, Z., York, D., Preece, J. A. & Goodwin, T. E. 2012b. Failure of elastic-plastic core–shell microcapsules under compression. *AIChE Journal,* 58**,** 2674-2681.

Mercadé-Prieto, R., Nguyen, B., Allen, R., York, D., Preece, J. A., Goodwin, T. E. & Zhang, Z. B. 2011. Determination of the elastic properties of single microcapsules using micromanipulation and finite element modeling. *Chemical Engineering Science,* 66**,** 2042-2049.

Mercadé-Prieto, R., Pan, X., Fernández-González, A., Zhang, Z. & Bakalis, S. 2012c. Quantification of Microcapsules Deposited in Cotton Fabrics before and after Abrasion Using Fluorescence Microscopy. *Industrial & Engineering Chemistry Research,* 51**,** 16741-16749.

Mercadé-Prieto, R. & Zhang, Z. 2012. Mechanical characterization of microspheres – capsules, cells and beads: a review. *Journal of Microencapsulation,* 29**,** 277-285.

Mirabedini, S. M., Dutil, I. & Farnood, R. R. 2012. Preparation and characterization of ethyl cellulose-based core–shell microcapsules containing plant oils. *Colloids and Surfaces A: Physicochemical and Engineering Aspects,* 394**,** 74-84.

Miró Specos, M. M., Escobar, G., Marino, P., Puggia, C., Defain Tesoriero, M. V. & Hermida, L. 2010. Aroma Finishing of Cotton Fabrics by Means of Microencapsulation Techniques. *Journal of Industrial Textiles,* 40**,** 13-32.

Mishra, M. 2015. *Handbook of Encapsulation and Controlled Release,* CRC Press.

Mobus, G. & Inkson, B. J. 2007. Nanoscale tomography in materials science. *Materials Today,* 10 18-25

Mourtzinos, I., Kalogeropoulos, N., Papadakis, S. E., Konstantinou, K. & Karathanos, V. T. 2008. Encapsulation of Nutraceutical Monoterpenes in β-Cyclodextrin and Modified Starch. *Journal of Food Science,* 73**,** S89-S94.

Mukherjee, B., Mahanti, B., Panda, P. & Mahapatra, S. 2005. Preparation and Evaluation of Verapamil Hydrochloride Microcapsules. *American Journal of Therapeutics,* 12**,** 417-424.

Myhra, S. & Rivière, J. C. 2012. *Characterization of Nanostructures,* Taylor & Francis.

Naha, P. C., Kanchan, V., Manna, P. K. & Panda, A. K. 2008. Improved bioavailability of orally delivered insulin using Eudragit-L30D coated PLGA microparticles. *Journal of Microencapsulation,* 25**,** 248-256.

Narayan, P. & Hancock, B. C. 2005. The influence of particle size on the surface roughness of pharmaceutical excipient compacts. *Materials Science and Engineering: A,* 407**,** 226-233.

National Cash Register Company. 1956. *Manifolid Record Material*. US2730456 A.

Naumenko, D., Snitka, V., Duch, M., Torras, N. & Esteve, J. 2012. Stress mapping on the porous silicon microcapsules by Raman microscopy. *Microelectronic Engineering,* 98**,** 488-491.

Neubauer, M. P., Poehlmann, M. & Fery, A. 2014. Microcapsule mechanics: From stability to function. *Adv. Colloid Interfac.,* 207 65-80

Ng, D.-Q., Tseng, Y.-L., Shih, Y.-F., Lian, H.-Y. & Yu, Y.-H. 2017. Synthesis of novel phase change material microcapsule and its application. *Polymer,* 133**,** 250-262.

Nguon, O., Lagugné-Labarthet, F., Brandys, F. A., Li, J. & Gillies, E. R. 2018. Microencapsulation by in situ Polymerization of Amino Resins. *Polymer Reviews,* 58**,** 326-375.

Nguyen, V. B., Wang, C. X., Thomas, C. R. & Zhang, Z. 2009. Mechanical properties of single alginate microspheres determined by microcompression and finite element modelling. *Chemical Engineering Science,* 64**,** 821-829.

Nielsen 2016. The Dirt on Cleaning. UK: Nielsen.

Normand, V., Tang, J. & Struillou, A. 2008. Modelling perfume deposition on fabric during a washing cycle: theoretical approach. *Flavour and Fragrance Journal,* 23**,** 49-57.

O'sullivan, M., Zhang, Z. & Vincent, B. 2009. Silica-Shell/Oil-Core Microcapsules with Controlled Shell Thickness and Their Breakage Stress. *Langmuir,* 25**,** 7962-7966.

Ober, C. K. & Hair, M. L. 1987. The effect of temperature and initiator levels on the dispersion polymerization of polystyrene. *Journal of Polymer Science Part A: Polymer Chemistry,* 25**,** 1395-1407.

Ohtsubo, T., Tsuda, S. & Tsuji, K. 1991. A Study of the Physical Strength of Fenitrothion Microcapsules. *Polymer,* 32 2395-2399

Ozkan, G., Franco, P., De Marco, I., Xiao, J. & Capanoglu, E. 2019. A review of microencapsulation methods for food antioxidants: Principles, advantages, drawbacks and applications. *Food Chemistry,* 272**,** 494-506.

Paini, M., Aliakbarian, B., Casazza, A. A., Lagazzo, A., Botter, R. & Perego, P. 2015. Microencapsulation of phenolic compounds from olive pomace using spray drying: A study of operative parameters. *LWT - Food Science and Technology,* 62**,** 177-186.

Pan, X., Mercade-Prieto, R., York, D., Preece, J. A. & Zhang, Z. 2013a. Preparation and characterisation of user-friendly PMMA microcapsules for consumer care. 1542**,** 1027-1030.

Pan, X., Mercade-Prieto, R., York, D., Preece, J. A. & Zhang, Z. 2013b. Preparation and characterisation of user-friendly PMMA microcapsules for consumer care. *AIP Conference Proceedings,* 1542**,** 1027-1030.

Pan, X., Mercadé-Prieto, R., York, D., Preece, J. A. & Zhang, Z. 2013c. Structure and Mechanical Properties of Consumer-Friendly PMMA Microcapsules. *Industrial & Engineering Chemistry Research,* 52**,** 11253-11265.

Parkinson, D.-R., Barter, D. & Gaultois, R. 2016. Comparison of Spot and Time Weighted Averaging (TWA) Sampling with SPME-GC/MS Methods for Trihalomethane (THM) Analysis. *Separations,* 3**,** 5-21.

Paulose, J. & Nelson, D. R. 2013. Buckling pathways in spherical shells with soft spots. *Soft Matter,* 9**,** 8227-8245.

Percebom, A. M., Ferreira, G. A., Catini, D. R., Bernardes, J. S. & Loh, W. 2018. Phase Behavior Controlled by the Addition of Long-Chain n-Alcohols in Systems of Cationic

Surfactant/Anionic Polyion Complex Salts and Water. *The Journal of Physical Chemistry B,* 122**,** 4861-4869.

Perignon, C., Ongmayeb, G., Neufeld, R., Frere, Y. & Poncelet, D. 2015. Microencapsulation by interfacial polymerisation: membrane formation and structure. *Journal of Microencapsulation,* 32**,** 1-15.

Pirone, D., Marturano, V., Del Pezzo, R., Fernández Prieto, S., Underiner, T., Giamberini, M. & Tylkowski, B. 2019. Molecular Design of Microcapsule Shells for Visible Light-Triggered Release. *Polymers,* 11**,** 904-919.

Polenz, I., Weitz, D. A. & Baret, J.-C. 2015. Polyurea Microcapsules in Microfluidics: Surfactant Control of Soft Membranes. *Langmuir,* 31**,** 1127-1134.

Poncelet, D. & Neufeld, R. J. 1989. Shear Breakage of Nylon Membrane Microcapsules in A Turbine Reactor. *Biotechnology and Bioengineering,* 33 95-103

Pradnya, P., Raghavendra, R. N. G. & Doddayya, H. 2010. Preparation and characterization of mucoadhesive microcapsules of salbutamol sulfate. *Asian Journal of Pharmaceutics,* 4**,** 141-147.

Pretzl, M., Neubauer, M., Tekaat, M., Kunert, C., Kuttner, C., Leon, G., Berthier, D., Erni, P., Ouali, L. & Fery, A. 2012. Formation and Mechanical Characterization of Aminoplast Core/Shell Microcapsules. *ACS Applied Materials & Interfaces,* 4**,** 2940-2948.

Procter & Gamble. 2006. *Microcapsules*. EP1632560.

Procter & Gamble. 2014a. *High-efficiency perfume capsules*. United States patent application 8759275.

Procter & Gamble. 2014b. *High-efficiency perfume capsules*. US8759275.

Procter & Gamble. 2014c. *Laundry scent additive*. EP2496679.

Procter & Gamble. 2015. *Delivery particles*. United States patent application US9186642B2.

Procter & Gamble. 2017a. *Conditioner compositions with increased deposition of polyacrylate microcapsules*. US patent application US 9,561,169 B2.

Procter & Gamble. 2017b. *Methods for making compositions containing multiple populations of microcapsules*. 15/198,248.

Procter & Gamble. 2018. *Benefit Agent Containing Delivery Particle*. WO/2018/052990.

Pybus, D. & Sell, C. 2007. *The Chemistry of Fragrances*, Royal Society of Chemistry.

Qiu, X., Li, W., Song, G., Chu, X. & Tang, G. 2012. Microencapsulated n-octadecane with different methylmethacrylate-based copolymer shells as phase change materials for thermal energy storage. *Energy,* 46**,** 188-199.

Ren, Y. L., Donald, A. M. & Zhang, Z. B. 2007. Investigation of radiation damage to microcapsules in environmental SEM. *Materials Science and Technology,* 23**,** 857-864.

Rocha, G. A., Fávaro-Trindade, C. S. & Grosso, C. R. F. 2012. Microencapsulation of lycopene by spray drying: Characterization, stability and application of microcapsules. *Food and Bioproducts Processing,* 90**,** 37-42.

Rodrigues, S. N., Fernandes, I., Martins, I. M., Mata, V. G., Barreiro, F. & Rodrigues, A. E. 2008. Microencapsulation of Limonene for Textile Application. *Industrial & Engineering Chemistry Research,* 47**,** 4142-4147.

Rokstad, A. M. A., Lacik, I., De Vos, P. & Strand, B. L. 2014. Advances in biocompatibility and physico-chemical characterization of microspheres for cell encapsulation. *Advanced Drug Delivery Reviews,* 67-68 111-130

Røn, T. & Lee, S. 2014. Influence of Temperature on the Frictional Properties of Water-Lubricated Surfaces. *Lubricants,* 2**,** 177-192.

Rosa, N., Martins, G. V., Bastos, M. M. S. M., Gois, J. R., Coelho, J. F. J., Marques, J., Tavares, C. J. & Magalhães, F. D. 2015. Preparation of robust polyamide microcapsules by interfacial polycondensation of p-phenylenediamine and sebacoyl chloride and plasticization with oleic acid. *Journal of Microencapsulation,* 32**,** 349-357.

Rosiñski, S., Grigorescu, G., Lewiñska, D., Ritzén, L. G., Viernstein, H., Teunou, E., Poncelet, D., Zhang, Z., Fan, X., Serp, D., Marison, I. & Hunkeler, D. 2002. Characterization of microcapsules: recommended methods based on round-robin testing. *Journal of Microencapsulation,* 19**,** 641-659.

Rowe, D. 2009. *Chemistry and Technology of Flavours and Fragrances,* Wiley.

Sarrazin, B., Tsapis, N., Mousnier, L., Taulier, N., Urbach, W. & Guenoun, P. 2016. AFM Investigation of Liquid-Filled Polymer Microcapsules Elasticity. *Langmuir,* 32**,** 4610-4618.

Schaffer, M., Wagner, J., Schaffer, B., Schmied, M. & Mulders, H. 2007. Automated three-dimensional X-ray analysis using a dual-beam FIB. *Ultramicroscopy,* 107 587-597

Schermelleh, L., Heintzmann, R. & Leonhardt, H. 2010. A guide to super-resolution fluorescence microscopy. *The Journal of Cell Biology,* 190**,** 165-175.

Sharkawy, A., Fernandes, I. P., Barreiro, M. F., Rodrigues, A. E. & Shoeib, T. 2017. Aroma-Loaded Microcapsules with Antibacterial Activity for Eco-Friendly Textile Application: Synthesis, Characterization, Release, and Green Grafting. *Industrial & Engineering Chemistry Research,* 56**,** 5516-5526.

Shin, S., Warren, P. B. & Stone, H. A. 2018. Cleaning by Surfactant Gradients: Particulate Removal from Porous Materials and the Significance of Rinsing in Laundry Detergency. *Physical Review Applied,* 9**,** 034012-034019.

Shin, Y., Son, K. & Yoo, D. I. 2017. Evaluation of aroma functionality imparted on natural indigo-dyed cotton fabrics. *Fibers and Polymers,* 18**,** 1146-1153.

Shinnar, R. 1961. On the behaviour of liquid dispersions in mixing vessels. *Journal of Fluid Mechanics,* 10**,** 259-275.

Smith, A. E., Zhang, Z. & Thomas, C. R. 2000. Wall material properties of yeast cells: Part 1. Cell measurements and compression experiments. *Chem. Eng. Sci.,* 55 2031-2041

Stora, T., Escher, S. & Morris, A. 2001. The Physicochemical Basis of Perfume Performance in Consumer Products. *CHIMIA International Journal for Chemistry,* 55**,** 406-412.

Sudraud, P. 1988. Focused-ion-beam milling, scanning-electron microscopy, and focused-droplet deposition in a single microcircuit surgery tool. *Journal of Vacuum Science & Technology B: Microelectronics and Nanometer Structures,* 6 234-238.

Sun, J. N., Gidley, D. W., Hu, Y. F., Frieze, W. E. & Yang, S. 2002. Characterizing Porosity in Nanoporous Thin Films Using Positronium Annihilation Lifetime Spectroscopy. *MRS Online Proceedings Library.*

Suresh, S. 2006. Mechanical response of human red blood cells in health and disease: Some structure-property-function relationships. *Journal of Materials Research,* 21**,** 1871-1877.

Tam, S. K., Dusseault, J., Polizu, S., Ménard, M., Hallé, J. P. & Yahia, L. 2005. Physicochemical model of alginate-poly-l-lysine microcapsules defined at the micrometric/nanometric scale using ATR-FTIR, XPS, and ToF-SIMS. *Biomaterials,* 26 6950-6961

Tang, Y.-D., Venkatraman, S. S., Boey, F. Y. C. & Wang, L.-W. 2007. Sustained release of hydrophobic and hydrophilic drugs from a floating dosage form. *International Journal of Pharmaceutics,* 336**,** 159-165.

Tavera, E. M., Kadali, S. B., Bagaria, H. G., Liu, A. W. & Wong, M. S. 2009. Experimental and modeling analysis of diffusive release from single-shell microcapsules. *AIChE Journal,* 55**,** 2950-2965.

Teixeira, C. S. N. R. 2010. *Microencapsulation of Perfumes for Application in Textile Industry.* University of Porto.

Teixeira, C. S. N. R., Martins, I. M. D., Mata, V. L. G., Filipe Barreiro, M. F. & Rodrigues, A. E. 2012. Characterization and evaluation of commercial fragrance microcapsules for textile application. *The Journal of The Textile Institute,* 103**,** 269-282.

Tekin, R., Bac, N. & Erdogmus, H. 2013. Microencapsulation of Fragrance and Natural Volatile Oils for Application in Cosmetics, and Household Cleaning Products. *Macromolecular Symposia,* 333**,** 35-40.

Timilsena, Y. P., Akanbi, T. O., Khalid, N., Adhikari, B. & Barrow, C. J. 2019. Complex coacervation: Principles, mechanisms and applications in microencapsulation. *International Journal of Biological Macromolecules,* 121**,** 1276-1286.

Turin, L. & Sanchez, T. 2010. *Perfumes: The A-Z Guide*, Profile.

Uchic, M. D., Holzer, L., Inkson, B. J., Principe, E. L. & Munroe, P. 2007. Three-Dimensional Microstructural Characterization Using Focused Ion Beam Tomography. *MRS Bulletin,* 32 408-416

Uludag, H., De Vos, P. & Tresco, P. A. 2000. Technology of mammalian cell encapsulation. *Advanced Drug Delivery Reviews,* 42 29-64

Unilever Plc. 2009. *Topical composition comprising coloring antioxidants*. PCT/EP2008/067466. 2009-07-02.

Utama, R. H., Dulle, M., Förster, S., Stenzel, M. H. & Zetterlund, P. B. 2015. SAXS Analysis of Shell Formation During Nanocapsule Synthesis via Inverse Miniemulsion Periphery RAFT Polymerization. *Macromolecular Rapid Communications,* 36**,** 1267-1271.

Vian, A. & Amstad, E. 2019. Mechano-responsive microcapsules with uniform thin shells. *Soft Matter,* 15**,** 1290-1296.

Vishnu, P., Ravindrababu, B., Sudheer, B., Shireesh, K. R. & Naveen Babu, K. 2011. Formulation and optimization of varamamil hydrochloride microcapsules. *International Journal of Pharmacy,* 1**,** 54-58.

Vivaldo-Lima, E., Wood, P. E., Hamielec, A. E. & Penlidis, A. 1997. An Updated Review on Suspension Polymerization. *Industrial & Engineering Chemistry Research,* 36**,** 939-965.

Vöpel, T., Scholz, R., Davico, L., Groß, M., Büning, S., Kareth, S., Weidner, E. & Ebbinghaus, S. 2015. Infrared laser triggered release of bioactive compounds from single hard shell microcapsules. *Chemical Communications,* 51**,** 6913-6916.

Wagdare, N. A., Marcelis, A. T. M., Boom, R. K. & Van Rijn, C. J. M. 2011a. Porous microcapsule formation with microsieve emulsification. *Journal of Colloid and Interface Science,* 355**,** 453-457.

Wagdare, N. A., Marcelis, A. T. M., Boom, R. M. & Van Rijn, C. J. M. 2011b. Microcapsules with a pH responsive polymer: Influence of the encapsulated oil on the capsule morphology. *Colloids and Surfaces B: Biointerfaces,* 88**,** 175-180.

Wang, A., Tao, C., Cui, Y., Duan, L., Yang, Y. & Li, J. 2009. Assembly of environmental sensitive microcapsules of PNIPAAm and alginate acid and their application in drug release. *Journal of Colloid and Interface Science,* 332**,** 271-279.

Wang, C. X., Wang, L. & Thomas, C. R. 2004. Modelling the mechanical properties of single suspension-cultured tomato cells. *Ann Bot-London,* 93 443-453

Wang, Y., Su, C., Schulmerich, M. & Padua, G. W. 2013. Characterization of core-shell structures formed by zein. *Food Hydrocolloids,* 30 487-494

Wang, Y. J. 2000. Development of new polycations for cell encapsulation with alginate. *Materials Science and Engineering: C,* 13 59-63

Werner, J. G., Nawar, S., Solovev, A. A. & Weitz, D. A. 2018. Hydrogel Microcapsules with Dynamic pH-Responsive Properties from Methacrylic Anhydride. *Macromolecules,* 51**,** 5798-5805.

Wirth, R. 2009. Focused Ion Beam (FIB) combined with SEM and TEM: Advanced analytical tools for studies of chemical composition, microstructure and crystal structure in geomaterials on a nanometre scale. *Chemical Geology,* 261 217-229

Xie, H. G., Zheng, J. N., Li, X. X., Liu, X. D., Zhu, J., Wang, F., Xie, W. Y. & Ma, X. J. 2010. Effect of Surface Morphology and Charge on the Amount and Conformation of Fibrinogen Adsorbed onto Alginate/Chitosan Microcapsules. *Langmuir,* 26**,** 5587-5594.

Xu, K., Hercules, D. M., Lacik, I. & Wang, T. G. 1998. Atomic force microscopy used for the surface characterization of microcapsule immunoisolation devices. *Journal of Biomedical Materials Research,* 41 461-467

Xue, J. & Zhang, Z. 2009. Physical, structural, and mechanical characterization of calcium-shellac microspheres as a carrier of carbamide peroxide. *Journal of Applied Polymer Science,* 113 1619-1625

Yow, H. N. & Routh, A. F. 2006. Formation of liquid core–polymer shell microcapsules. *Soft Matter,* 2**,** 940-949.

Yu, S., Wang, X. & Wu, D. 2014. Microencapsulation of n-octadecane phase change material with calcium carbonate shell for enhancement of thermal conductivity and serving durability: Synthesis, microstructure, and performance evaluation. *Applied Energy,* 114**,** 632-643.

Zaleski, R., Maciejewska, M. & Puzio, M. 2015. Mechanical Stability of Porous Copolymers by Positron Annihilation Lifetime Spectroscopy. *The Journal of Physical Chemistry C,* 119**,** 11636-11645.

Zhang, D.-X., Li, B.-X., Zhang, X.-P., Zhang, Z.-Q., Wang, W.-C. & Liu, F. 2016a. Phoxim Microcapsules Prepared with Polyurea and Urea–Formaldehyde Resins Differ in Photostability and Insecticidal Activity. *Journal of Agricultural and Food Chemistry,* 64**,** 2841-2846.

Zhang, G. S. Z. 2001. Mechanical properties of melamine-formaldehyde microcapsules. *Journal of Microencapsulation,* 18**,** 593-602.

Zhang, W., Abbaspourrad, A., Chen, D., Campbell, E., Zhao, H., Li, Y., Li, Q. & Weitz, D. A. 2017. Osmotic Pressure Triggered Rapid Release of Encapsulated Enzymes with Enhanced Activity. *Advanced Functional Materials,* 27**,** 1700975-1700981.

Zhang, Y. & Rochefort, D. 2012. Characterisation and applications of microcapsules obtained by interfacial polycondensation. *Journal of Microencapsulation,* 29**,** 636-649.

Zhang, Y., Song, J. & Chen, H. 2016b. Preparation of polyacrylate/paraffin microcapsules and its application in prolonged release of fragrance. *Journal of Applied Polymer Science,* 133**,** 44136-44143.

Zhang, Z., Ferenczi, M. A., Lush, A. C. & Thomas, C. R. 1991. A novel micromanipulation technique for measuring the bursting strength of single mammalian cells. *Applied Microbiology and Biotechnology,* 36 208-210

Zhang, Z., Saunders, R. & Thomas, C. R. 1999. Mechanical stength of single microcapsules determined by a novel micromanipulation technique. *J. microencapsulation,* 16 117-124

Zhao, D., Jiao, X., Zhang, M., Ye, K., Shi, X., Lu, X., Qiu, G. & Shea, K. J. 2016. Preparation of high encapsulation efficiency fragrance microcapsules and their application in textiles. *RSC Advances,* 6**,** 80924-80933.

Zhao, H., Fei, X., Cao, L., Zhang, B. & Liu, X. 2019. The Fabrication of Fragrance Microcapsules and Their Sustained and Broken Release Behavior. *Materials,* 12**,** 393-407.

Zheng, G., Liu, X., Wang, X., Chen, L., Xie, H., Wang, F., Zheng, H., Yu, W. & Ma, X. 2014. Improving Stability and Biocompatibility of Alginate/Chitosan Microcapsule by Fabricating Bi-Functional Membrane. *Macromolecular Bioscience,* 14**,** 655-666.

Zheng, J., Xie, H., Yu, W., Tan, M., Gong, F., Liu, X., Wang, F., Lv, G., Liu, W., Zheng, G., Yang, Y., Xie, W. & Ma, X. 2012. Enhancement of Surface Graft Density of MPEG on Alginate/Chitosan Hydrogel Microcapsules for Protein Repellency. *Langmuir,* 28**,** 13261-13273.

Zheng, T. & Pilla, S. 2018. Encapsulation of hydrophilic payload by PU-PMF capsule: Effect of melamine-formaldehyde pre-polymer content, pH and temperature on capsule morphology. *Colloids and Surfaces A: Physicochemical and Engineering Aspects,* 542**,** 59-67.

APPENDICES

Appendix A

Method of calculating the Young's modulus of the shell

1. Plot force/size ($N.m^{-1}$) against fractional deformation from the force displacement data from a single PMC compression.

2. Choose suspected contact point of the compression and plot 3rd order polynomial up to $\varepsilon = 0.25$ to find the elastic limit at the inflexion point of the curve. Visually inspect to find the starting point of the real elastic region of compression, disregarding any 'soft spot' initial compression.

3. Plot a 2nd order polynomial between these fractional deformation limits.

4. Calculate the difference between the fitted polynomial and the raw data for each 0.001 increment between the lower and upper force/size values of the elastic region. Sum these values and normalise this total against the number of data point included in the calculation.

5. Use Excel's built in solver to vary the contact point so to minimise the difference between the fitted polynomial and the raw compression data.

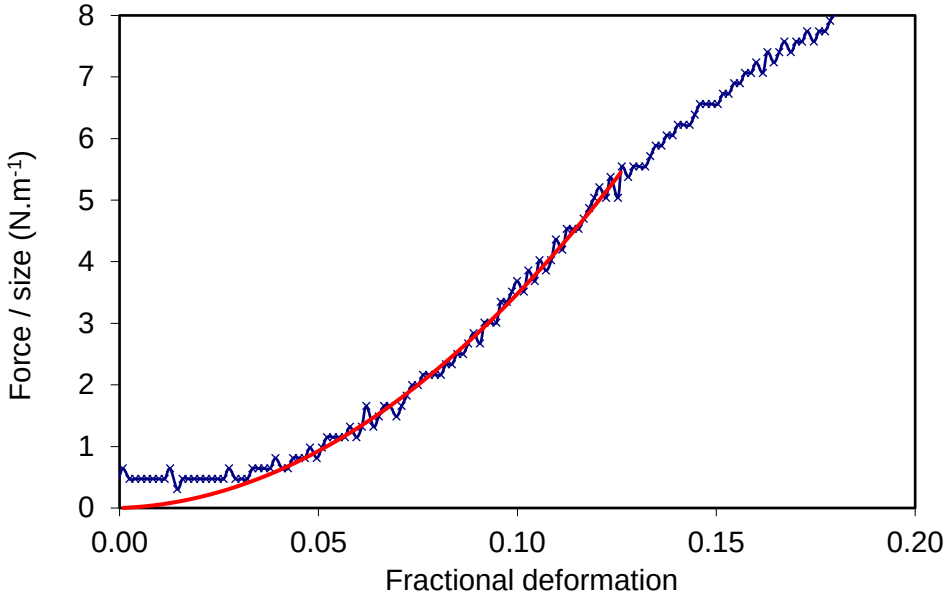

Figure A1: Fitted 2nd order polynomial for a force-fractional deformation curve of a reference sample PMC. The contact point was varied so to minimise the normalised difference between the fitted data and experimental data

6. Using the fitted polynomial calculate $F_\varepsilon/F_{0.1}$ for ε=0.03, 0.04, 0.05, 0.06, 0.07 and 0.08.

7. Estimate h/r at the six deformations using polynomials calculated from FEM by Mercadé Prieto.

Table A1: Polynomials used to estimate h/r at different fractional deformations, ε, using force ratio $F_\varepsilon/F_{0.1}$. Reprinted from *(Mercadé-Prieto et al., 2011)*

***h/r* at ε**	**Polynomial**
0.03	$2782.429x^5 - 2045.506x^4 + 587.033x^3 - 80.603x^2 + 5.544x - 0.14856$
0.04	$710.348x^5 - 758.326x^4 + 320.560x^3 - 65.966x^2 + 6.801x - 0.28041$
0.05	$314.458x^5 - 457.085x^4 + 265.468x^3 - 76.097x^2 + 10.916x - 0.63118$

0.06	$843.351x^5 - 1733.033x^4 + 1419.015x^3 - 577.461x^2 + 116.866x - 9.41587$
0.07	$261.485x^5 - 3350.832x^4 + 3555.599x^3 - 1882.384x^2 + 497.163x - 52.41261$
0.08	$4004.243x^5 - 13404.680x^4 + 17943.898x^3 - 12003.685x^2 + 4012.412x - 536.12401$

8. Calculate coefficient of a, b and c using the average h/r value and the polynomials in table X.

Table A2: Polynomials used to estimate the coefficients a, b, and c for equations X using the calculated average h/r value

Coefficient	**Polynomial**
a	$95071.891x^5 - 28426.030x^4 + 2411.056x^3 - 7.476x^2 - 10.829x + 1.52882$
b	$-318.702x^4 + 120.784x^3 - 11.380x^2 + 2.518x - 0.05792$
c	$-0.004242x + 0.00107$

9. Calculate the average *Eh* value and resulting *E* from Equation A-1.

$$Eh_{\varepsilon} = \frac{F_{\varepsilon}/r}{a\varepsilon^2 + b\varepsilon + c} \quad \text{A-1}$$

Appendix B

Equation B-1 displays the calculation of 95% confidence intervals associated with mass balance of reference on knitted cotton:

$$S_{y/x} = \sqrt{\frac{\sum(y_i - \hat{y}_i)^2}{n-2}} \quad \text{B-1}$$

Where $S_{y/x}$ is the standard deviation of the y values in the calibration curve, y_i is the measured y value and $\hat{y}_i$ is the calculated y value from the calibration curve, with the sum being the residual. n is the number of data points in the calibration curve.

The calculated $S_{y/x}$ value forms part of the calculation of overall standard deviation, S_{x_o}, shown in Equation B-2:

$$S_{x_o} = \frac{S_{y/x}}{b}\sqrt{\frac{1}{N} + \frac{1}{n} + \frac{(y_o - \bar{y})^2}{b^2 \sum_i (x_i - \bar{x})^2}} \quad \text{B-2}$$

Where b is the gradient of the calibration line, N is the number of replicates of the unknown, y_o is the measured value of the unknown, $\bar{y}$ is the mean of the calibration values, x_i is each of the x values for the calibration curve and $\bar{x}$ is the mean of the x values of the calibration points. The 95% confidence interval for a given unknown y value on a calibration curve is calculated using the standard deviation in x of the unknown and the t-statistic for (n-2) degrees of freedom, as seen in Equation B-3:

$$x \pm S_{x_o} t_{n-2} \quad \text{B-3}$$

Confidence intervals are converted to % deposition based on the input of perfume / fluorescent dye. In some situations, such as adding cycle washwater breakage of PMCs to get overall washwater breakage over the course of the wash cycle, or in calculating the % intact deposition by subtracting the broken deposition from total deposition it is necessary to propagate the confidence intervals in the following way:

$$\delta R = \sqrt{(\delta X^2) + (\delta Y^2) + (\delta Z^2)} \qquad \text{B-4}$$

Appendix C

Calculations for number of PMCs deposited on fabric using fluorescence microscopy

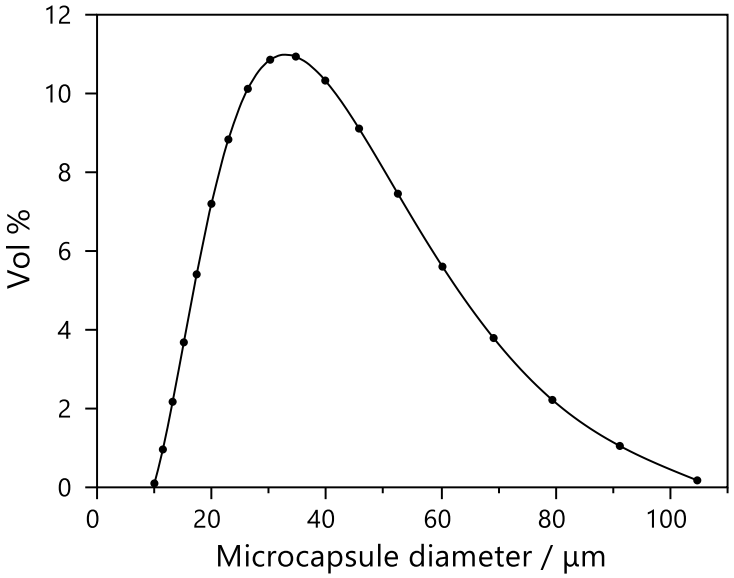

Figure C1: PMC size distribution for reference sample as recorded on the Mastersizer

Based upon the Vol % of each size band of microcapsules in the MF sample in combination with the input mass of slurry in the washing machine, the density and % of PMCs within the slurry itself it was possible to calculate the total number of PMCs added in a wash.

Table C1: Process for converting mass of PMC slurry into total volume

Mass of slurry added / g	1
% PMC solids by mass	37.38
Density of PMC / kg.m^{-3}	925
Volume of PMC in m^3	3.46×10^{-4}

$$Total\ number\ of\ PMCs\ in\ wash = \sum \frac{Total\ Volume\ \ at\ \ specific\ PMC\ diameter}{Volume\ of\ 1\ PMC\ at\ specfic\ PMC\ diameter}$$

Table C2: Calculation of total number of PMCs from a 1 g sample of PMC slurry using mastersizer size distribution data

Size / µm	Vol in %	Total volume / m^3	Volume of 1 PMC of that size / m3	Number of PMCs of that size	Total number of PMCs
10.000	0.100	3.45E-07	5.24E-16	6.59E+08	4.61E+10
11.482	0.962	3.33E-06	7.92E-16	4.20E+09	
13.183	2.172	7.51E-06	1.20E-15	6.26E+09	
15.136	3.681	1.27E-05	1.82E-15	7.01E+09	
17.378	5.408	1.87E-05	2.75E-15	6.80E+09	
19.953	7.199	2.49E-05	4.16E-15	5.98E+09	
22.909	8.832	3.05E-05	6.30E-15	4.85E+09	
26.303	10.118	3.50E-05	9.53E-15	3.67E+09	
30.200	10.857	3.75E-05	1.44E-14	2.60E+09	
34.674	10.937	3.78E-05	2.18E-14	1.73E+09	
39.811	10.328	3.57E-05	3.30E-14	1.08E+09	
45.709	9.109	3.15E-05	5.00E-14	6.30E+08	
52.481	7.455	2.58E-05	7.57E-14	3.41E+08	
60.256	5.604	1.94E-05	1.15E-13	1.69E+08	
69.183	3.791	1.31E-05	1.73E-13	7.56E+07	
79.433	2.219	7.67E-06	2.62E-13	2.92E+07	
91.201	1.051	3.63E-06	3.97E-13	9.15E+06	
104.713	0.177	6.13E-07	6.01E-13	1.02E+06	

Separately it was necessary to calculate the number of PMCs deposited on fabric, as seen in Table C3.

Table C3: Calculation of scale up factor from 100 images to cover the total fabric area of 1 swatch

Area of single image on microscope / m^2	3.49×10^{-7}
Total area covered by 100 images / m^2	3.49×10^{-5}
Mass of 1 swatch in the wash / g	1.5
Area of 1 swatch / m^2	0.2
Mass of ballast / g	3000
Total apparent surface area of ballast / m^2	40
Scale up factor	1.15×10^6

Detailed methodology for quantification of intact and broken PMCs deposited on fabric

To form the FDCC, PMC slurry was first diluted in DI water to facilitate accuracy of deposition and to utilise the water to enable deep penetration of the PMCs into fabric. For a Western Europe front load liquid detergent wash, the dosage of detergent and PMC was as follows:

Table C4: Typical PMC slurry dosage for a Western Europe front load liquid detergent wash cycle

Dosage size / g	65.6
Target perfume oil / %	0.56
Mass oil / g	0.367
Activity of sample / %	21.68
Mass of slurry needed / g	1.69

Table C5: Example composition of a mother solution used for accurate dispensing of known PMC quantities to form the FDCC curve for fluorescent dye quantification

Mother solution	
Mass slurry / g	0.3
Mass DI water / g	300
C (g_{slurry} / g_{sol})	0.0001
Concentration of dye in core / ppm	500

Table C6: Example calculation of mass of mother solution needed to deposit for a theoretical deposition of 60% on a fabric swatch

Theoretical deposition / %	**Mass slurry added to washing machine / g**	**Mass of slurry deposited on all fabric (3 kg) / g**	**Mass of slurry to deposit on 2 g of fabric / g**	**Mass of mother solution to deposit on fabric / g**
60	1.69	1.01	6.95×10^{-4}	0.695

Forced deposition calibration curve (FDCC) for PMCs exposed to Ethanol

Each jar of incremental % deposition was covered in foil to minimise any degradation of fluorescent dye. Each sample jar for the FDCC contained 2 x 1 g pieces of fabric. The required mass of mother solution was deposited onto the fabric pieces in the sample jars and allowed to

dry. 30 g ethanol, enough to cover the fabric was added to each jar and sealed. The samples were placed in a Talboys incubator at 60°C for 60 minutes at 160 rpm to extract dye from intact PMCs. The process was repeated for six replicates of 2 x 1 g pieces of wash fabrics, where the dye was also extracted using the same method. The FDCC and wash fabric jars were removed from heat and the fabric pieces were also removed, leaving the ethanol extract. Analysis of extracts was then conducted using a Spectramax M2e spectrophotometer with an excitation wavelength 488 nm, emission wavelength 507 nm and a cut off filter at 495 nm. 30 lamp flashes per measurement and medium photomultiplier tube gain. See material and methods section for details.

Forced deposition calibration curve for PMCs exposed to hexane

The hexane extraction for forced deposition was conducted using the same protocol as the ethanol extraction with a few minor alterations. Once the mother solution had been deposited on the fabric each 1 g piece was compressed against one another using pneumatic press to break all PMCs, before replacing fabrics in the jars. 20 g of hexane was added to the jars for the extraction. The lower density of hexane accounted for lower mass with respect to the ethanol extraction. The extraction in the incubator was conducted at room temperature rather than at 60°C like with ethanol. For the analysis the emission wavelength was changed to 493 nm, and the emission was changed to 508 nm, as discussed in Section 3.3.7 of the materials and methods.

Detailed methodology for quantification of intact microcapsules in water

The mother solution was created by adding PMC slurry to deionised water to obtain desired concentration. This solution was then further diluted at different levels to create six standard solutions plus a blank. An example is seen in the table below.

Table C7: Example of dilutions of the mother solution required to achieve a range of different dye concentrations for extraction

Concentration of PMC slurry / ppm	Volume of mother solution / mL	Volume of deionised water / mL	Total volume / mL
22.9	25	0	25
11.5	17.5	12.5	25
6.9	7.5	17.5	25
4.6	5	20	25
2.3	2.5	22.5	25
1.2	1.25	23.75	25
0	0	25	25

The volume of water added had no impact on the deposition concentration, but it did serve to disperse the PMC, enabling an easier deposition onto the filter paper.

Each standard solution and wash solution were stored in foil to ensure no degradation of the fluorescent dye over time through light exposure.

1. 15 mL of hexane was added to each standard solution and washwater prior to filtration. This ensured that any dye from any residual broken capsules dissolved in the hexane, so that it would pass through the filter paper.

2. Standard solution with hexane was carefully dispensed dropwise from the jar onto the 90 mm diameter filter paper (2.5 µm pore size) under vacuum setup. 5 mL of DI water was added to empty jars to ensure all residual intact PMCs were recovered. This was repeated for all standard solutions and washwater samples.

3. The filter paper was carefully removed from the Buchner funnel and replaced in the jar, to which 15 g ethanol was added and then extraction at 60°C for 60 minutes in the incubator with an agitation speed of 160 rpm was conducted before filter paper was removed.

4. Analysis of the extracts was then conducted using a Spectramax M2e spectrophotometer with an excitation wavelength 488 nm, emission wavelength 507 nm and a cut off filter at 495 nm. 30 lamp flashes per reading and medium photomultiplier tube gain.

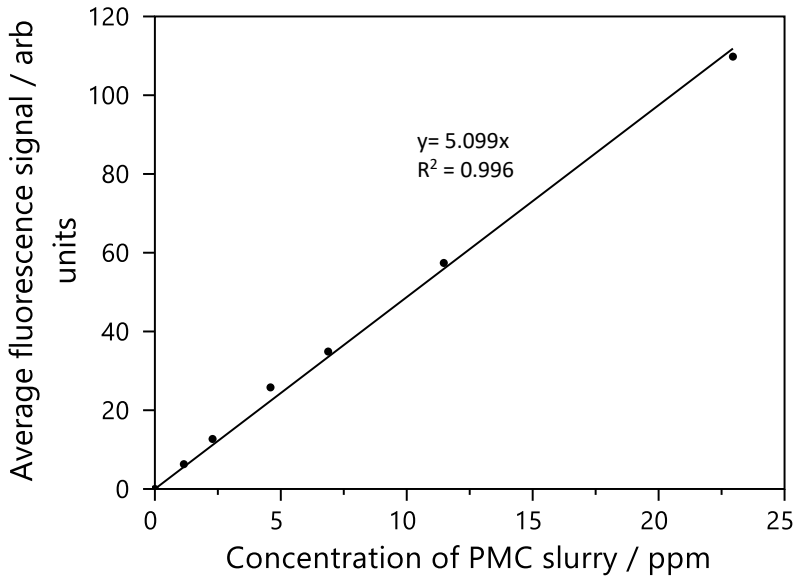

Figure C2: Example forced deposition calibration curve formed for the calculation of the percentage of intact PMCs in washwater

Table C8: Calculation of intact PMCs using the average fluorescence intensity from unknown wash samples and fitting to the forced deposition calibration curve to calculate the percentage if intact PMCs in washwater

Wash cycle	Average fluorescence intensity	Concentration of perfume in collection / ppm	Volume of washwater removed / L	Mass of perfume in washwater / mg	Total perfume input / mg	% intact PMC
Main wash	27.8	5.5	7.0	38.2	367.4	10.4
Rinse 1	11.1	2.2	15.4	33.6		9.2
Rinse 2	7.1	1.4	15.1	21.1		5.8

Detailed methodology for quantification of broken perfume microcapsules in water

Preparation of standard solutions

Neat perfume was added to ethanol and mixed for 5 minutes before being subsequently diluted in washwater, essentially spiking washwater with known amounts of perfume. An example of two concentration setup is seen below:

Table C9: Preparation of two standards to form the calibration curve for quantification of perfume from broken PMCs using headspace GC-MS

Standard number	Mass perfume oil / mg	Volume of ethanol / L	Concentration of perfume / PPM	Volume of perfume and ethanol added / mL	Volume of washwater added / mL	Final Concentration of perfume / PPM
1	14.5	0.1	145	0.15	10	2.14
2	26	0.025	1040	0.05	10	5.17

1 mL of this solution was pipetted to 20 mL headspace vials and this was repeated with 1 mL of washwater samples to get the final samples for headspace GC-MS analysis, the specific parameters of which are proprietary to P&G

Analysis of calibration curves

There was a trade-off between obtaining larger numbers of standards for the calibration curve and more washwater samples to get greater accuracy in this estimate as the apparatus only had a finite number of sample holders and there was often a time limit on how long the machine could be run for.

As such two replicates were run for each standard concentration, giving four points on the calibration curves. An example work through of % breakage is shown below:

Table C10: Formation of the calibration curve for quantity of perfume in washwater from a rinse 2 cycle

	Concentration / ppm	**Sum peak area / arb units**	**Average washwater sum peak area from 6 reps / arb units**	**Sum standard peak area – washwater peak area / arb units**
Standard rinse 2	2.14	1367119	437091	930028
	2.14	1369308		932217
	5.17	2713095		2276004
	5.17	2591235		2154144

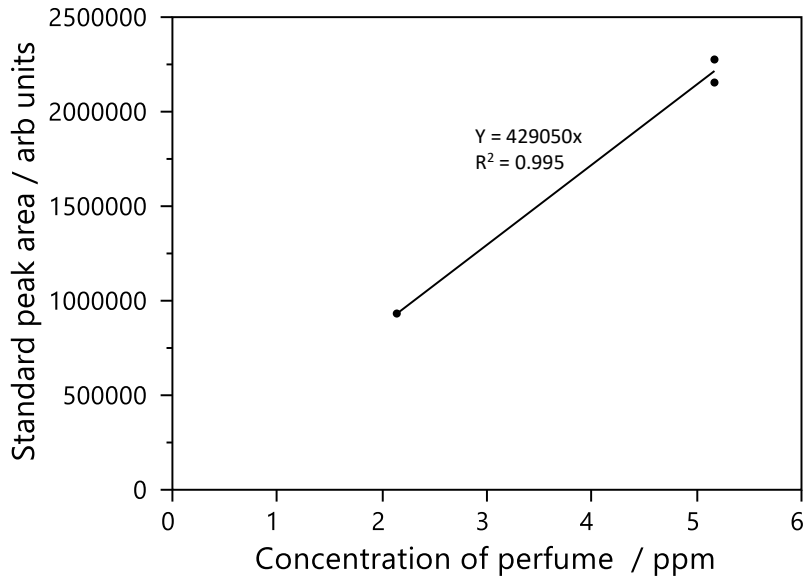

Figure C3: Example calibration curve for known quantities of perfume in washwater from a rinse 2 cycle

$$Gradient\ of\ calib\ line = \frac{Standard\ Peak\ Area}{Concentration\ of\ perfume}$$

$$Concentration\ of\ perfume = \frac{Washwater\ Peak\ Area}{Gradient\ of\ calib\ line}$$

$$Mass\ perfume\ in\ washwater/(mg) = Concentration\ of\ perfume\ (ppm)\ \times$$

$$volume\ of\ washwater\ removed\ (L)$$

$$\%\ Breakage\ of\ total\ input = \frac{Mass\ of\ perfume\ in\ washwater/mg}{Total\ Perfume\ input/mg}$$

Table C11: Calculation of the percentage of broken PMCs in washwater from a rinse 2 cycle by relating calibration curve to measured average fluorescence intensities from unknown concentrations

Gradient of fitted line	Concentration of perfume in washwater / ppm	Volume of water removed at this stage / L	Mass of perfume in washwater / mg	Total perfume input at start of wash / mg	% breakage of input PMC
429050	1.02	15.1	15.4	376.4	4.2

Appendix D

ImageJ protocol for quantifying PMC breakage before and after rupture.

ImageJ macro

1. Set the scale of the image – 1 pixel = 0.6127 µm for the 20x objective lens used in the experiments
2. Change image type to 8-bit black and white
3. Set threshold (23,255)
4. Run “Make binary”
5. Run “Fill holes” (Seeks to obtain correct area)
6. Run “watershed” (Separates PMCs that appear joined under a binary image)
7. Run “analyse particles”; 30 μm^2 < area < Infinity; 0.75 < Circularity < 1, show outlines